UNIVERSITY OF SOUTHAMPTON

The Analysis of Partially Separated Flow on Sail Systems Using A Sectional Method

by

Augusto Elisio Lessa Veiga

Fluid Structures Research Group

School of Engineering Sciences

November 2006

UNIVERSITY OF SOUTHAMPTON

ABSTRACT

SCHOOL OF ENGINEERING SCIENCES

Doctor of Philosophy

THE ANALYSIS OF PARTIALLY SEPARATED FLOW ON SAIL SYSTEMS USING A SECTIONAL METHOD

by Augusto Elisio Lessa Veiga

Yacht sail systems are subjected to low speed and transitional flow. Because of the supporting structure (mast and boom) of the sail system and the curvature of sail membrane, sail systems also have a partially separated flow.

In this work, it is introduced the sectional method as a sail system flow analysis tool. The sectional method uses the surface discretization and it is based in the simultaneous approach for viscous-inviscid interaction but, it works independently to the initial panel mesh and inviscid panel method calculation, permitting the adjustment of sectional points to have a better local convergence.

The sectional method is applied to the detection of separated flow regions by means of integral boundary layer parameters investigation. The investigation is used in cases of weak separation and strong separation, when analysing mast and sail configurations. The weak separation detection is applied to a three-dimensional sail shape in a sail design problem: the study of parameters such as twist and section curvature in order to control separation on the sail.

Contents

List of Tables

List of Figures

Acknowledgements

Many people contributed to this thesis in many ways. I would like to thank my supervisor, Dr. Stephen Turnock for his support to this work and his patience; To Professor Philip Wilson for his invitation and offering of a studentship at the University of Southampton; To Ian Campbell for his great support on experimental data for sails; To Professor Molland for his support that was right in the spot when I was believing that this work would not get any further; To Mingyi Tan, who was promptly available to any doubt on mathematics, computers and any other complicated questions; To all the School of Engineering staff.
I would also like to thank my dad Claudio Veiga who supported me and helped in questions of computer facilities and travels. Thanks to my friends Israel Vieira, who created this thesis format, and Bernardo Carmo for their incentive; To Professor Mark Drela from the M.I.T. for his prompt e-mail when I had questions about his method; To Ricardo Lobato (Blu) and Eduardo Penido from Quantum Sails Latin America for their support on sail making experience; To Maria Tereza Moreira for her support and last corrections.
Last but not least I would like to thank all my friends and colleagues who were living at the same time in Southampton, a city that hosted wicked people who were living a magic moment that will be difficult to be repeated in any other place and at the same time. Thanks to all those people who made between hard studies and social life this magic moment that will be rare to happen again.

Nomenclature

A	Surface area
A_R	Aspect ratio
B	Transpired source influence coefficient
c	Chord length
C_D	Drag coefficient
C_{Df}	Frictional drag coefficient
C_{Di}	Induced drag coefficient
C_{diss}	Dissipation coefficient
C_E	Entrainment coefficient
C_f	Friction coefficient
C_L	Lift coefficient
C_{Li}	Inviscid lift coefficient
C_{Lv}	Viscous lift coefficient
C_{Lt}	Theoretical lift coefficient
C_P	Pressure coefficient $\left(1 - \left(\frac{u}{U_\infty}\right)^2\right)$
C_R	Camber ratio
C_τ	Wall shear coefficient
$C_{\tau_{eq}}$	Wall equilibrium shear coefficient
D	Dipole vortex influence coefficient or drag force
d	distance between points
G	Nodal transpired source influence coefficient
h	Height function from matching surface to original surface

H	Shape parameter $\frac{\delta^*}{\theta}$
H_k	Kinematic shape parameter
H^*	Kinetic energy shape parameter
H^{**}	Density shape parameter
L_w	Surface length inside matching surface
l	Thwaites parameter for skin friction
M	Mach number
m	Thwaites parameter for external pressure
m_d	Mass defect $(u_e \cdot \delta^*)$
N	Number of body nodes
N_w	Number of nodes on wake
$\mathbf{n}$	Surface normal vector (direction)
$\tilde{n}$	Amplification ratio
$\tilde{n}_{crit}$	Critical amplification ratio
q	$q = \sqrt{v_y^2 + v_y^2 + v_z^2}$ - tangential velocity modulus
Q_∞	$Q_\infty = \sqrt{U_\infty^2 + V_\infty^2 + W_\infty^2}$ - freestream velocity
R	Radius
R_Z	Residuals
Re	Reynolds number
Re_θ	Reynolds number in relation to momentum thickness
Re_∞	Freestream Reynolds Number
S	Source induced coefficient
s	Distance along surface or streamline
t	Thickness
t_{nm}	Thickness of numerical method
u	Tangential streamwise velocity
u_e	Edge tangential velocity
u_i	Inviscid tangential velocity
U	$U = u/U_\infty$
U_∞	Freestream speed
v	Normal velocity
V	Volume or velocity vector (v_x, v_y, v_z)
V_∞	Freestream normal velocity
V_{CP}	Vertical centre of pressure
x	cartesian coordinate streamwise direction
x_{tr}	chordwise position of transition point
y	cartesian coordinate normal direction
z	cartesian coordinate on spanwise direction
W	Wake dipole or $W = w/U_\infty$
W_∞	Crossflow freestream velocity
w	tangential crossflow velocity

α	Angle of incidence
α_{io}	Optimal or ideal angle of incidence
Γ	Circulation
γ	Vortex strength
δ	Thickness of boundary layer
δ^*	Displacement thickness
δ^{**}	Density thickness
φ	Airfoil leading or trailing edge angle
η	Normal distance to surface
μ	Dipole strength
ξ	Parametric distance
κ_w	Curvature of wall
κ^*	Curvature of displacement thickness
ν	Kinematic viscosity
ρ	Density
σ	Source strength
θ	Momentum thickness
θ^*	Kinetic energy thickness
τ	Shear stress
Φ	Velocity potential
Φ_∞	Freestream potential

Subscripts

I	Value in equivalent inviscid flow
(i)	Inviscid flow
(v)	Viscous flow
w	Value near wall
W	Value on wake
u, l	Upper, lower
eq	Equilibrium values
e	Outer edge of shear layer
se	Separation
tr	Transition
TE	trailing edge

Chapter 1

Introduction

Much of the existing technology developed to flow analysis has been applied to supposedly rigid structures such as aircraft. Aircraft aerodynamics has a set of specifications according to: velocity of vehicle (airplane) and height of operation. These two characteristics are typically constant for most of the duration of flight.

Sailing yachts operate in different flow conditions. Flow is considered low speed, with wind speed commonly in the range from zero to 20 m/s where, according to Gad-el-Hak [1], it lies in the transitional flow range. Sailing flow characteristics also cannot be considered constant during sailing. Yachts can sail with different headings to true wind velocity and, this true wind velocity is also subjected to changes in atmospheric conditions. Hence, yacht sails have to be adjusted in order to have a better yacht performance or control when sailing.

In order to allow a better adjustment, sails have a flexible membrane instead of a rigid wing shape. However, they can only resist to surface tensions. As they can only resist to tensions, they need supporting structures at their edges (mast and boom). This structures are, on modern racing yachts, slender in order to keep flow disturbance to a minimum and, they have a certain degree of elasticity to allow shape adjustment.

In account of the flexible membrane supported by elastic structures, sail yacht design have a complex flow analysis, that normally depends on fluid-structures interactions. In these interactions, it is necessary a flow analysis which can be performed by experimental or computational fluid dynamics (CFD) methods.

Experimental methods, according to Van-Oossanen [2], Larsson and Eliasson [3], are considered as the most accurate methods for flow analysis, however there are some details, mainly on sails, that their assessment in experimental analysis is difficult. For example, the distribution of pressure on a sail surface varying its angle of incidence.

The CFD can provide pressure distribution information on a sail surface at discrete points using a simple model of the sail surface. The experimental method can also provide this information but, experiments need a series of instruments and complex automated devices to capture this information, as discussed in Wilkinson [4].

Experimental methods are commonly used in the global analysis, where particularities of sail shape variation are not the focus of the study but, forces acting on a sail

system of a yacht sailing in determinate conditions. The global analysis is applied in works of Poor and Sironi [5] and Campbell [6]. However, information about changes in sail shape and its relation to yacht performance cannot be easily evaluated.

The study of sail shape variation and its influence to the yacht performance is still a challenge and involves other multi-parameter interactive analysis, such as aeroelastic analysis, shape optimization and performance prediction. The use of computational fluid dynamics can aid in the sail shape design, giving detailed information and avoiding complex experiments already in the earlier design phases.

There are two basic groups of computational fluid dynamic methods:

- Finite volume analysis methods, that depends on the modelling of body control volume. Euler potential equations, which have a inviscid flow calculation and Reynolds averaged Navier-Stokes solvers (RANS) are based in this analysis, which requires heavy computational facilities and a very refined mesh modelling;

- Surface Methods, that are based in the panel method solution. They require the modelling of body and wake surface just. Corrections to viscous flow can be introduced in the panel method solution. Surface methods are reported to be faster and requires a less detailed mesh than finite volume methods, with the disadvantage of the increasing reliance in empiricism.

Even with the continuing advancement of computing techniques and the increasing availability of powerful information technology hardware, the solution of multi-parameter interactive analysis, such as the performance prediction or aeroelastic analysis of sail shapes using finite volume methods is still expensive in terms of time and computing power. Examples are given by Date [7] and Camponetto and co-authors [8]. This discards the first group of methods for practical design studies in the short to medium terms.

In the second group of methods, most of their theory is based in the inviscid flow. There are only limited surface methods that incorporate the influence of viscous flow by means of a coupling scheme between perturbation potential equation (panel method) with integral boundary layer equation, referred to as viscous-inviscid interaction methods, according to Lock and Williams [9]. Their use has been restricted to aircraft aerodynamics and ship propeller hydrodynamics, with little use on yacht sails yet. Surface methods are reported to be very accurate for streamlined bodies.

The main objective of this work is the creation of the sectional method, which is based in the surface method, to viscous flow analysis. It is mainly discussed its application to sail yacht membranes acting as lifting surfaces, regarding the low speed flow with transitional characteristics and partially separated flow.

It is the intention to create a surface method for two and three-dimensional viscous flow analysis that allows a simple mesh modelling with lower computational requirements than RANS, permitting its use as a module in other multi-parameter interactive analysis of flexible sails.

This work is divided as follows:

- Chapter two - Background to sail systems. It is reviewed the contributions from many important references and the problem of sail flow analysis is stated in more details;

- Chapter three - Inviscid flow analysis. It is reviewed the basic theory to two and three-dimensional surface inviscid flow, that is the base for surface viscous flow methods. Later, it is discussed the use of this inviscid methods to very thin foils and to mast and sail configurations;

- Chapter four - Viscous flow and Separation. It is discussed the boundary layer theory and the development of integral boundary layer methods used in laminar, transition and turbulent flows. Based in the observation of some integral boundary layer parameters, it is introduced a classification of flow separation between weak and strong separation. This classification is intended to be used to model the partially separated flow on sail systems;

- Chapter five - Coupling of inviscid to viscous flow. It is reviewed the most used techniques for viscous-inviscid interaction (VII) methods, the direct approach and the simultaneous approach using two-dimensional flow. It is evaluated their convergence and accuracy. Techniques to use viscous-inviscid interaction methods in partially separated flow problems are discussed later in the Chapter;

- Chapter six - The three-dimensional coupling. It is discussed existent VII methods used on three-dimensional flow and proposed a new one, the sectional method, with an independent solution to panel method. This method is tested on NACA four digit profile three-dimensional wings, where it is evaluated its solution symmetry, convergence and mesh limitations;

- Chapter seven - Case studies. Numerical results for two and three-dimensional methods are discussed and compared qualitative and quantitatively to experimental data. The investigation of H boundary layer shape parameter distribution on sail membrane sections is introduced in order to avoid separated regions;

- Chapter eight - Conclusion. It is discussed the main contributions of this work and further research.

Chapter 2

Background to Sail Systems

In this Chapter it will be discussed the theories from various sources that contribute to the sail system flow analysis. It is the intention to create a theoretical background revising the state of art of yacht sail system design, the influences of flow, working conditions, principles and issues considering viscous flow, such as separation and transitional flow.

All this discussion will contribute to establish the objectives and considerations of this dissertation that will guide its work theoretical discussion.

2.1 Definition of a Sail System

According to Marchaj [10], sails are membranes with essentially no thickness attached to a slender structure (mast). The sloop configuration, showed in Figure 2.1 is the most usual on sail yachts, including the racing ones. The basic configuration comprises a mainsail, mast, jib and rigs which provide part of mast strength and fixing to the boat. For improving offwind performance, a Spinnaker is used.

The tensioning of the membrane is very important, as described by Marchaj [11] and Jackson [12], for sail performance. By varying the tension, it is possible to vary the curvature of membrane (camber), showed in Figure 2.2, improving aerodynamical performance. Also, as discussed by Marchaj [11], Whidden and Levitt [13], sails are built with predefined sections in such a way that, their performance can be adjusted for a determinate condition. For example, if a designer wants to make a sail for lightwinds, he or she will choose larger cambers on sails. If the sail is intended for stronger winds, the camber can be reduced.

When a boat is sailing the tensioning is given by the wind and the structures attached to sail membrane (mast and boom, for example). As showed by Marchaj [11], on the structures attached, there are many devices to aid on the tensioning. A sketch of the main tensions in a simple sail system is shown in Figure 2.3.

On a yacht, the sail foot is supported by the boom and the forehead of sail (leading edge) is supported by the mast. According to Sugimoto [14], with the wind action, the unsupported part, that is the leech side near top, have a trend to follow the wind

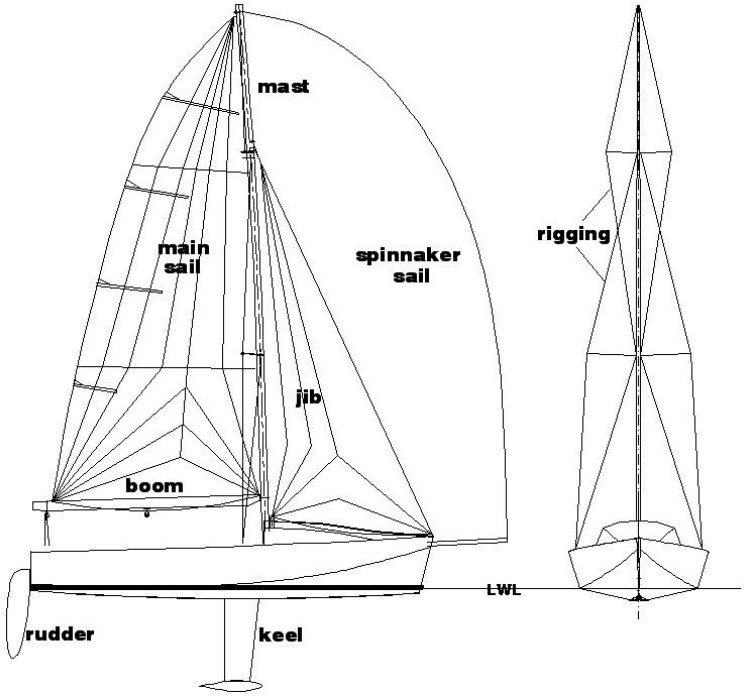

Figure 2.1: A typical sloop sail system

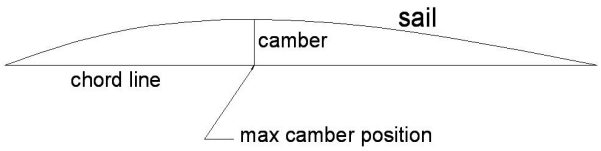

Figure 2.2: A sail crossection

direction thus a twist on the sail surface can be expected.

According to Marchaj [11], the sail twist also influences in many ways the yacht performance. Twist is always present on sail membrane but it can be reduced or increased by controlling the leech tension. In small dinghies, the device that normally controls leech tension is the vang. On yachts, the leech tension is adjusted by controlling tension on rigging. When tensioning the leech, for example, twist is decreased.

The mast supports the head tension and the tack tension. These tensions control the camber size and position relative to chord, as shown in Figure 2.2.

As sail yachts have many directions relative to wind, the sail system has to be pivoted in order to maintain an ideal angle of incidence of flow on membrane shape. In sloop sail yachts, this is done by sail sheets that control the opening angle of boom relative to yacht centreline.

The combination of clew and tack tension modifies the position of the maximum camber along the sail chord. This position varies into a limit that is given by the strength and directions of fibres on sail (sail cloth), which is, at last, controlled by the

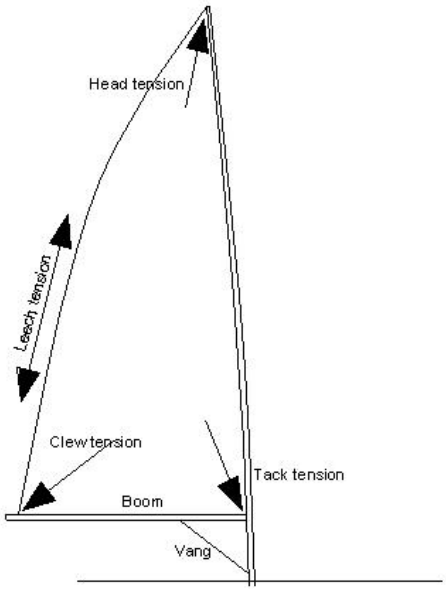

Figure 2.3: The basic sail system and main tensions on its membrane

sailmaker.

Besides this basic points of tensions, on modern yachts there are other devices on rigging such as: stays and runners, that control mast bending, reducing or increasing membrane tensions in different parts.

The tensions can also be adjusted for different wind forces, during navigation, by crew so, performance can be optimized at any moment. All these subjects turn the problem of real sail flow analysis into a difficult task.

2.2 Review of Previous Work

2.2.1 The Classical Wind Heading Dynamics

According to Herreshoff [15] and considering that, *a priori*, there is no wind action when a yacht is moving with a velocity V_B, the yacht displaces air against the its movement with the same velocity V_B. If this V_B is added vectorially to wind velocity or, true wind velocity V_{TW}, the resultant is the apparent wind velocity V_{AW} which has the same direction and intensity of flow that acts on sail system. Figure 2.4 shows the wind velocity diagram.

Sails are operated from upwind, with very large angles of incidence of flow, showed in Figure 2.5a, until upwind, showed in Figure 2.5b. Although the true wind heading can vary in a wider range, sails operate most of the time with relative small angles of incidence due to the resultant direction of flow acting on sails and the constant adjustments made by crew during navigation. The downwind sailing, with large incidence angles, have a different nature, according to Marchaj [11]. On this wind heading, flow is separated and sails act as bluff bodies.

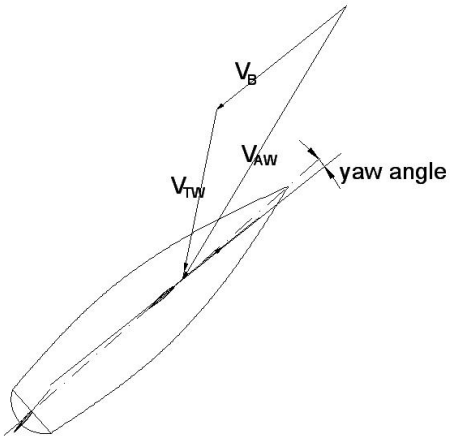

Figure 2.4: Wind velocities acting on a sail yacht

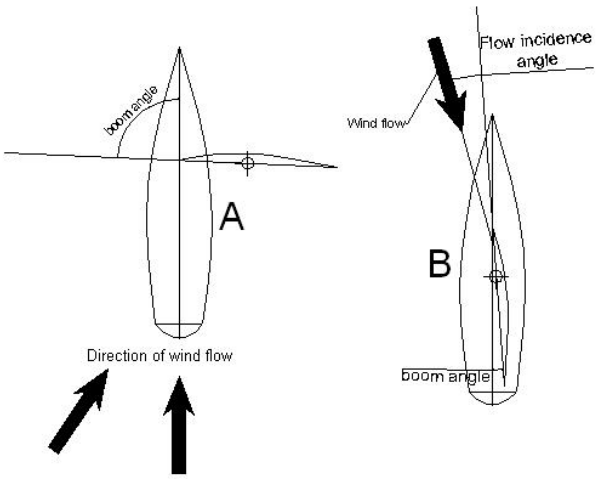

Figure 2.5: Scheme of a sail boat downwind (a) and offwind (b)

There is a heading limit in which sail is considered to be working as a lifting surface and starts to work as a bluff body. This limit, according to Marchaj [10], is the "broad reach" heading, that has a heading approximately $135^o$to the true wind direction. In this heading, depending on boat velocity, the apparent wind direction can be moved to a nearly $90^o$to the centreline of the boat, according to Figure 2.6, where sail will act as a lifting surface. If velocity of boat is small enough, the apparent wind direction will not change much in relation to the 135^otrue wind direction and sail will work as a bluff body.

2.2.2 The Wind Structure

According to Flay and Jackson [16], the sail boat operates inside the atmospheric boundary layer with waves playing the major part of surface roughness. The atmospheric boundary layer, likewise the classical Prandtl boundary layer, has a velocity

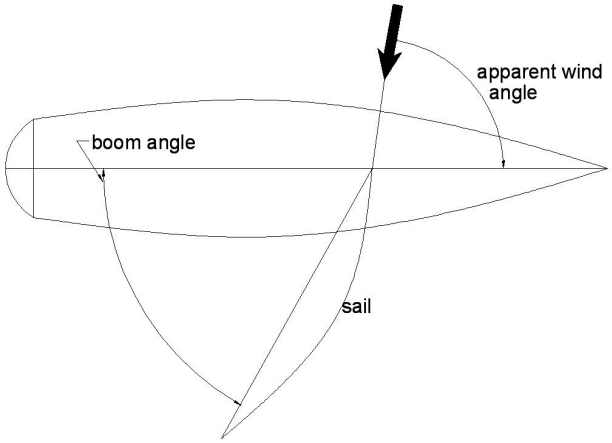

Figure 2.6: A yacht on reaching position

profile that changes in height. Because of wind velocities and roughness of surface, the boundary layer is normally turbulent and fully developed when it reaches a boat.

If the boundary layer is turbulent and fully developed, the airflow is not steady inside and it comes in periodic gusts. According to Flay and Jackson [16], the average frequency of gusts are very low, in the order of 10^{-2} Hz but, it changes with boat movement and heading to wind. Then, the sail flow nature is unsteady.

Regarding the previous discussion about classical wind heading dynamics, considering a velocity profile that changes in height, the incident flow on sails will be twisted. It has different angle of incidence from foot to top of sail and the gradient of wind direction will vary according to yacht performance. The twist varies with mast height, boat velocity and wind intensity.

Figure 2.7 illustrates the wind variation by height and compares apparent wind velocities (V_{AW}) in two distinct heights from sea level. The heading angle with true wind velocity, considered in Figure 2.7, is typical of an upwind sailing and the difference on A_{WA} is small from foot to top.

2.2.3 Sail Yacht Flow Analysis

If considerations of wind flow were taken strictly as discussed before, sail analysis could be the most difficult fluid dynamics problem to solve. The analysis of real sailing conditions is only possible by measuring all the wind flow effects. Peters [17] created a sailing dynamometer for studying the dynamics of sailing yacht in real conditions. The apparatus included a prototype yacht with a frame inside where all forces could be measured by means of strain gauges. According to Peters [17] the apparatus could measure tensions on boat frame however, the tension on sails and pressure distribution on its surface could not be evaluated properly.

When it turns to sail design, some approximations have to be made. According to Flay and Jackson [16], as turbulent gusts have very low frequency, sail flow can be

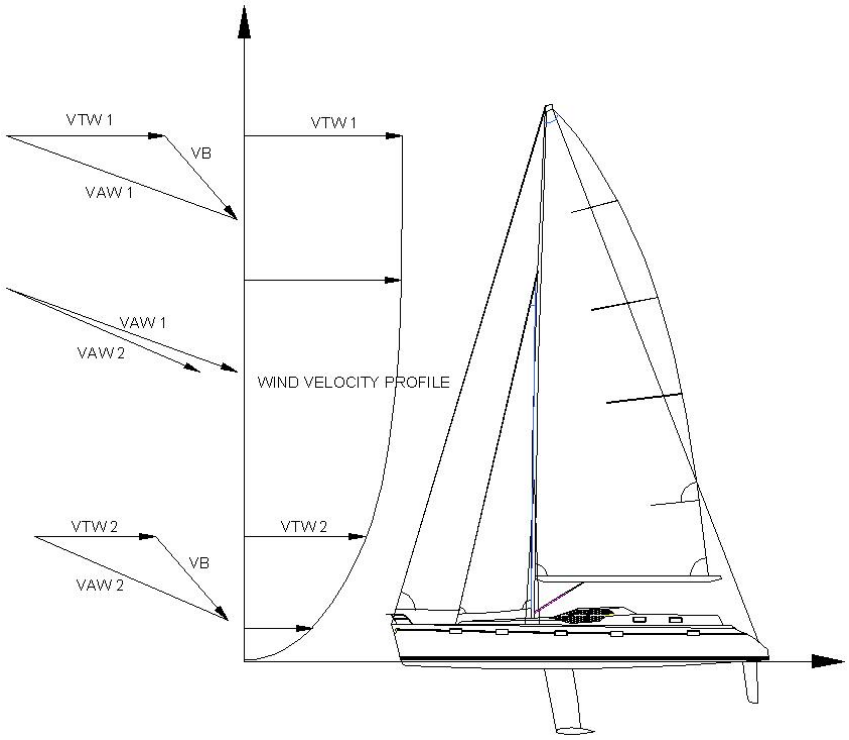

Figure 2.7: The wind velocity profile and its influence on apparent wind velocity

approximated by a series of steady flows, and this simplifies the analysis so that low speed wind-tunnel testing can produce accurate results.

The twisted flow approximation, discussed by Flay [16], is more difficult to consider. According to Flay [16], it has to take into account boat velocity, which suffers from limited space inside a wind-tunnel testing section.

An alternative approach for sail analysis on wind tunnel, discussed by Flay [18] and Flay and et al [19] uses twisted blades that theoretically twists the incident flow on sails, approaching the wind velocity spectrum relative to the yacht.

According to Poor [5] and Campbell [6], wind tunnel testing has been made with a fixed yacht in front of a straight flow, producing results sufficiently accurate.

The commonly accepted method for aerodynamic tunnel test analysis, according to Larsson [20] and Campbell [6], uses a fixed sail with untwisted and steady flow on sail rig, that simplifies the problem and has been producing satisfactory results.

2.2.4 Sail System Aeroelasticity

According to Flay and Jackson [16], another important characteristic of sail flow is the aeroelastic number which represents the ratio of the sail material stiffness to the incident dynamic pressure. The exact formulation is well discussed by Jackson [12] and Newman [21] where they used a simple model of a two-dimensional membrane to establish a method for sail analysis. The overview of this method is shown in the diagram of Figure 2.8.

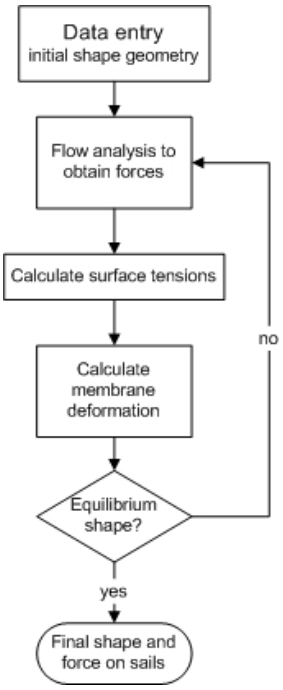

Figure 2.8: The scheme of flow and tension analysis for finding the flying shape

According to both authors [12] and [21], the aerodynamic response of a sail will depend on the shape of the membrane which is deformed by the wind. To do so, there is an interactive procedure where, at first, the sail surface geometry is considered rigid for flow analysis. Then, loads on surface are obtained. If the membrane mechanical properties are known then, membrane stretching is calculated and so the final shape. The interaction will go successively until the stretch of the membrane is balanced to the determined load caused by the wind. This final shape is the so called "flying shape".

In an experimental point of view, the correlation between model and prototype, requires keeping the aeroelastic number constant. Unfortunately this requires a very elastic membrane on model, which would complicate its manufacture. Hence, model sails are made with inelastic materials such as mylar films.

Widden and Levitt [13] describe the process of sail manufacture. Sail membranes today are mostly laminated rather than stitched. This allows the optimization of fibres on both characteristics: directions and materials, in order that sail membrane deformation is very small and sails will "fly" mostly with little difference to the previously designed rigid shape.

2.2.4.1 The Sail Membrane Luffing

The theory for sail analysis as a lifting body implies that sail membrane is always curved. According to Newman [21], when sail is approaching wind direction, the upper surface of membrane is subjected to positive pressure and the tensioning system cannot maintain membrane with its original shape thus creating a collapsed region on

membrane. It is called, according to Newman [21], luffing of sail.

This same observation can be used in a separation bubble that will produce a positive pressure region on sail membrane upper surface. If separation occurs on a membrane, it will collapse. On experimental testing, luffing of sail membranes is simple to check as sail flattens or start to oscillate but, on numerical analysis, it is a difficult problem. When using numerical methods, an useful avoidance of luffing would be the identification of separated flow regions.

2.2.4.2 The Three-dimensional Aeroelastic Problem

Jackson [12] and Newman [21] created analytical methods to calculate two-dimensional membrane stretching. For the three-dimensional problem, both flow and stress analysis are more complicated to calculate analytically and, there is a need for numerical procedures.

Jackson and Christie [22], solved the same scheme proposed earlier by Jackson [12] for hang-gliders, using a finite element analysis coupled with a perturbation potential method (panel method). The authors also showed that their analysis was in good agreement with experiments.

One of the characteristics of hang-gliders is their relatively low aspect ratio if compared to sails. Also, sails can be adjusted when "flying", which is different from hang-gliders.

Hobbs [23] used finite element analysis (FEA) for stress and a panel method for flow analysis. The procedure, as reported by the author gave good results, reaching the equilibrium shape in about 10 iterations for a one sail system (mast and sail).

According to Widden and Levitt [13], the aeroelastic analysis leads to: materials choice, place of reinforcements, fibre direction (when sail is laminated) and sail performance prediction.

All authors, Jackson [12], Newman [21], Jackson and Christie [22] and Hobbs [23] agreed that the surface geometry for flow analysis must be rigid. Later, for stress analysis, then sail surface is considered again as an elastic membrane. All of them also used surface computing methods for flow analysis, due to its faster calculation in relation to other more complex flow analysis methods.

2.2.5 Performance Prediction

If the sail shape is known in determined condition of a boat then, it is possible to predict forces with accuracy and, having hull data, it is possible to calculate the final equilibrium position and velocity. Then, knowing the aeroelastic behaviour of a sail system, the global performance of a yacht can be accurately evaluated.

The most used tool to analyse the global performance of a yacht design is the VPP (velocity prediction program). According to Van Oossanen [2], the VPP has data for hull and appendage lift and drag, mostly obtained from experimental testing and

transformed into semi-empirical relations, that calculates forces from each part of the yacht and gives the global performance.

Sails have the same kind of approach in a VPP, as discussed by Poor and Sironi [5]. Sail data and hydrodynamic data interact until an equilibrium of forces and momentum is reached. The final result presents an averaged boat velocity, heel and leeway. The proposed scheme of a VPP, according to Van Oossanen [2], is shown in Figure 2.12.

According to Larsson [20] and Oliver et al [24], the VPP calculation is based on a database obtained from experimental results for one specific series of hull, appendage or sails. For hull resistance, for example, as described by Gerritsma et al [25] and Veiga [26], forces are obtained according to systematic series of hull. If a hull does not have the same characteristics of a determinate series (Delft series, for example), there is no guarantee that it will perform what is predicted.

The sail model used initially in the Offshore Racing Council (ORC) VPP [27] was the Poor and Sironi [5] model, with data obtained from wind tunnel tests. The data in Poor and Sironi [5] is presented in a series of wind heading angles, starting from 27^oup to $180^o$and considers which sails are up and the number of reefs. For each heading angle there is a lift and drag coefficient. This model considers that sail is perfectly adjusted to each heading and other parameters such as camber position, camber size for sail sections and twist are not taken into account.

According to Oliver et al [24] and Larsson [20], there has been more research on substituting the database of VPP to other sources of mathematical model, in order to make VPP more accurate for any kind of yacht. This has been done by two means:

- Experimental data, which has been proving accurate although expensive and time consuming;
- Computational flow analysis, which has been improving in accuracy and on computing requirements lately.

In the computational field, a remarkable work for improving sail data on VPP was done by Couser [28] for upwind sails. Couser used a vortex lattice method for predicting lift and induced drag for sails, varying parameters such as reef, rake and camber of sections, improving the prediction of sail forces. Couser's [28] work is an example of a particular flow analysis applied to sails, aiding in the global analysis performed by a VPP.

However, the particular analysis of sails using computational fluid dynamics has improved little in downwind sailing. According to Ranzenbach and Teeters [29] and [30] little has been improved in downwind sail modelling in the last 25 years and just experimental data has been producing satisfactory results.

Hedges et al [31] discuss the modelling of downwind sails using PHOENIX, a CFD package based on Reynolds Averaged Navier-Stokes (RANS) solver. In some angles ($90^o$to 120^o), the RANS did not converge. However, lift and drag curves had the same

trend to the ones measured experimentally, although with a considerable discrepancy. In Hedges et al [31] solution time for each heading was reported to be approximately twelve hours.

The use of particular and detailed computational analysis to aid a VPP is still time consuming and limited to upwind sailing. VPP data for downwind sails, according to Ranzenbach and Teeters, [29] and [30], are still based in experimental results.

2.2.6 Experimental Analysis of Flow on Sails

In the works made by Wilkinson [4] and [32], it was studied experimentally a cylinder and membrane configurations that approximated a sail system. Wilkinson made an experimental apparatus, shown in Figure 2.9, with different cylinder diameters attached to a rubber membrane. Data along membrane was obtained by means of an automated device called "mouse". This device was equipped to measure the pressure at different heights within the boundary layer. Experiments were performed for different angles of incidence. The apparatus of Figure 2.9 could adjust the entire system to a defined angle of incidence, where angles varied from $2.5^o$to 10^o.

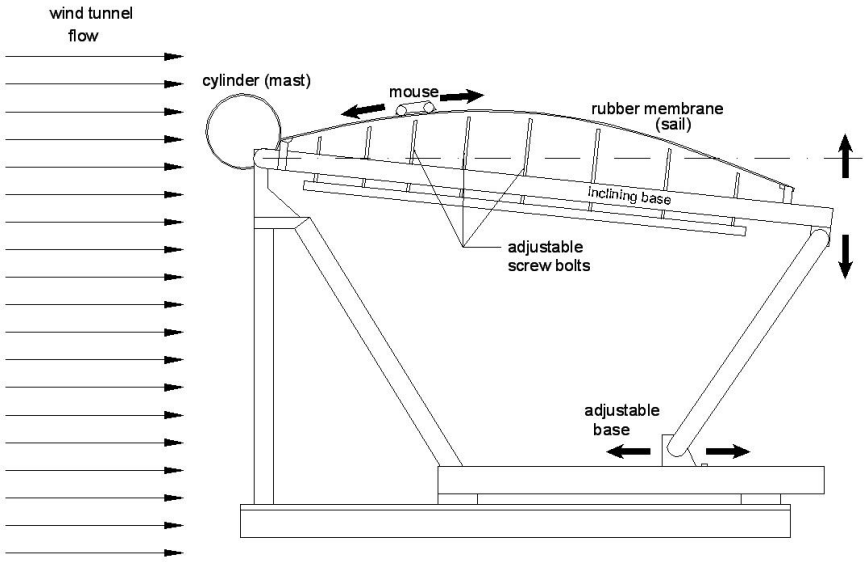

Figure 2.9: Schematic profile of experimental apparatus used by Wilkinson

Although most of the work reported by Wilkinson [4] was about the development of the automated device, it is the only one of the few known sources of experimental data for sail systems that describes in detail the partially separated flow in two regions: leading edge, where mast is attached to sail surface, and trailing edge where, generally, separation occurs in a turbulent flow.

2.2.6.1 Differences Between Wilkinson and Campbell Experiments

Experimental data in Campbell [6] and Poor and Sironi [5] were obtained by testing a model of the entire sail yacht inside the wind tunnel. This testing technique, according to Campbell [6], allowed a proper sail adjustment to each heading.

Lift coefficient for Campbell's [6] case, for example, will consider an entire sail yacht with heel, leeway and some boom angle that was not measured. So, Campbell [6] and Poor and Sironi [5] works, consider the global effects of sails, without detailing the effects that sail geometry parameters can produce in the flow.

In Wilkinson's [4] tests, sail was considered rigid so its shape could not change to the different angles of incidence. In Wilkinson [4] work, due to the small angles of incidence considered, sail was working basically as a lifting surface. Figure 2.10 shows a scheme of a Wilkinson´s sail system configuration.

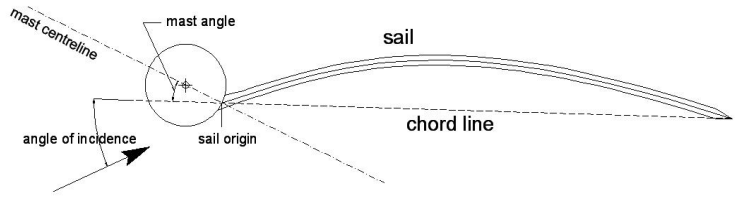

Figure 2.10: The reference system used for experimental data

Wilkinson [4] experiments have a consideration of some two-dimensional sail geometry parameters and takes into account its effects in the viscous flow, such as: separation and reattachment points, transition of flow and the qualitative relation between reattachment and transition by varying mast diameter, camber of section an Reynolds number (Re).

2.2.7 Viscous Effects and Separation

Gad-el-Hak [1] studied the low speed flow aerodynamics and observed that most of the human scale flying objects like: birds, fish, manpowered flying machines and remote controlled airplanes lie in a range of Reynolds numbers from 10^4 to 10^6. Yachts are also included in this low speed range. At this speeds, flow is predominantly laminar and, unless there is an adverse pressure region, a rough surface or any other kind of interference in flow, the transition to turbulence may not even occur on body surface.

As observed by Gad-el-Hak [1], if the transition to turbulence is delayed in this range of Reynolds numbers, there will be a substantial reduction on drag. According to Gad-el-Hak [1], the turbulent flow dissipates more kinetic energy in the formation of small eddies increasing the drag. In spite of the drag increase, as discussed in the same reference [1], in turbulent flow, because of its higher momentum level, flow is less

susceptible to separation. An earlier transition may be desired for an airfoil so, flow will be more difficult to separate and there will be a gain in lifting force.

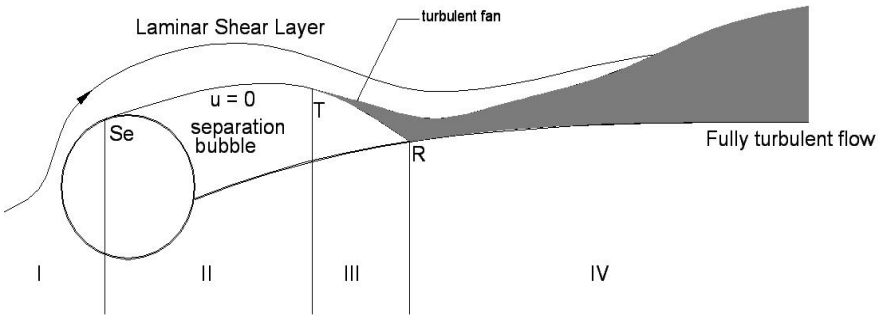

Figure 2.11: The boundary layer profile evolution on a mast and sail section

In Wilkinson [4] experimental data, bubbles of separation, shown schematicaly in Figure 4.7, formed between mast and sail membrane. Se, T and R in Figure 4.7 are separation, transition and reattachment points respectively.

Turbulence is triggered at the transition point where a turbulent fan develops until it becomes a fully turbulent flow. As observed by Wilkinson [4], when transition happens, the separation bubble has a sudden decrease in slope, re-attaching sooner to the sail membrane.

When Reynolds number is increased, keeping the incidence angle constant, there is an earlier reattachment and, consequently an increase in lifting force. This was observed on Wilkinson´s [4] experiments when the same mast and sail section was compared for different Reynolds numbers. When Reynolds numbers were increased, transition occurred earlier and the separation bubble was smaller. Consequently, Wilkinson [4] data has a close agreement to some of Gad-el-Hak [1] observations.

2.2.8 The Computational Analysis of Viscous Flow

According to Ferziger and Peric [33], numerical methods for flow analysis are divided as follows:

- Surface methods for inviscid flow;
- Surface methods for viscous flow;
- Inviscid finite volume methods;
- Viscous finite volume methods.

Inviscid surface methods are generally known as panel methods and, according to Katz and Plotkin [34] they have been used for computational flow analysis for the last 40 years. Panel methods consider tangential and attached flow all around and calculate velocity distribution on a body by means of an appropriate distribution of singularities.

Surface methods for viscous flow, discussed later in this section, use viscous corrections and couple them with the inviscid panel method, according to Lock and Williams [9].

Inviscid finite volume methods applies the Euler potential equations on small cells. Potential flow is calculated to the centre of each cell volume, according to Drela [35]. As discussed by Ferziger and Peric [33], Euler equations are considered high fidelity computational method, because they need a refined finite volume mesh discretization.

Lately, many studies have used codes based in the numerical solution of Reynolds averaged Navier-Stokes equations (RANS), which is a viscous finite volume method. Theoretically, according to Ferziger and Peric [33], RANS approach has the most complete flow solution and it is a high fidelity computational method.

Considering a finite volume mesh developed for a RANS application, as discussed by Ferziger and Peric [33], the Navier-Stokes equations are solved at the centre of each cell. For an accurate prediction of flow, the computational mesh should be sufficiently refined, depending on the characteristics of the geometry to be analysed.

The three-dimensional sail geometry, considering that sail is rigid and will not deform with flow, the mesh utilized must be very refined in order to capture most of the viscous effects using RANS. As an example, Camponetto et al [8] used about 1.5 to 2 million cells to analyse flow of the entire three-dimensional sail system of an America´s Cup yacht.

On Date´s work [7], it was used a IRIX workstation with 32 RISC based processors at the University of Southampton to solve some NACA three-dimensional foils. In the work of Camponetto et al [8], there were used 64 processors of a Silicon Graphics Origin 2000. Just one analysis took about 5 hours to solve.

RANS approach applied as a flow analysis module of an aeroelastic interaction, as made by Hobbs [23], an optimization procedure as mentioned by Day [36] or a VPP, as discussed by Couser [28], is practically discarded if computational time and requirements are taken into account.

Also, sails lie in the transitional Reynolds number range and, as reported by Foussekis and et al [37], the transition analysis with RANS is still difficult. Flows are analysed either using laminar flow or turbulent flow. If both flows are present on the same surface, according to Foussekis and et al [37], it will need a substantial increase in the number of cells in order to model the transition accurately. These issues make RANS approach too slow for multiple design parameters problems.

In terms of costs, sail yacht design offices are small companies with limited resources. When looking at the computing facilities used by authors like Foussekis [37], Camponeto [8] and Date [7], it is easy to conclude that this kind of flow analysis does not yet comply with the economic reality of most offices.

2.2.9 Surface Methods for Computational Fluid Dynamics

In sail system analysis, most authors [36], [38], [28], [39], [23] and [22] used some kind of inviscid surface flow analysis method. One advantage about using the surface method is its relatively easier mesh modelling and fast calculation when compared to more complex methods such as Navier-Stokes or Euler potential equations solvers.

Using a three-dimensional panel method to analyse a NACA 0012 foil with aspect ration of 3.0, on a PC with 128 Mbytes RAM and with a mesh size of 1000 panels, for example, it takes about 30 seconds. As the panel method is fast, it can be used interactively many times. This is also good for optimization problems, as described by Day [36].

Day [36] made the optimization study of a yacht sailplan using a genetic algorithm and a panel method. As Day's work was an optimization with many parameters, variations on sailplan were reduced then, characteristics such as section cambers were considered constant. Also, the number of panels was kept constant.

Day [36] reported that the solution for the genetic algorithm took a large amount of hours in a UNIX based RISC machine and then, the lattice method was chosen due to its fast solution and modelling.

Surface methods use only surface elements to discretize body and wake, making it easier to correct and to check about problems of wrong modelling or poor mesh refinement.

According to Katz and Plotkin [34], the biggest problem of using panel method for flow analysis is its consideration of just potential flow tangential to the surface. This makes the flow to have zero viscous drag and, on big angles of attack, flow will still be tangential to surface. Any lifting curve obtained with panel method will be a diagonal straight line, meaning that a foil, when analysed with a inviscid panel method, will never have a position where flow will separate and cause a stall.

However, panel method is still today considered as a fast and reliable tool and with a good accuracy level to foils at small angles of incidence, as reported in references [34] and [40].

2.2.9.1 An Alternative Surface Method for Viscous Flow Solution

Surface methods are applied mostly in inviscid flow problems. However, it is possible to use corrections to an inviscid surface method for calculating viscous flow. The main theory, discussed by Lock and Williams [9], considers the classical integral boundary layer momentum equation which has its main parameters, the displacement and momentum thicknesses, related to a normal displacement of the original surface, in order to have an equivalent inviscid flow.

This principle can similarly be transformed into an extra distribution of sources on body surface where their strengths are functions of the integral boundary layer variables so, panel method can be used to solve surface viscous flow.

This theory, called as viscous-inviscid interaction (VII), discussed in Lock and Williams [9], demands lower computational effort but, depends on a series of empirical relations to calculate viscous flow.

There are two successful approaches for the VII. One is the direct approach, discussed by Eça and Falcão de Campos [41], where it is assumed that the viscous corrections are small, compared to the initial inviscid velocity. This direct approach uses normally a inviscid panel method and a integral boundary layer method such as Thwaites [42] to calculate the viscous correction.

The simultaneous approach is other successful approach for VII. It considers an initial inviscid velocity calculated by panel method, that is considered incorrect and uses the potential equation with the integral boundary layer equation to calculate the source strengths, which correct interactively the viscous flow. Methods using the simultaneous approach are also called "two equation" methods, due to the need of using the potential and viscous equations, as discussed by Katz and Plotkin [34].

Simultaneous approach, according to Drela [43] can use more sophisticated integral boundary layer methods, such as the lag-entrainment method, discussed by Green et al [44], to turbulent flow.

In order to have a smooth and continuous transition in the simultaneous approach, Drela [43] also introduced to the boundary layer solution, the Tollmein-Schlichting waves amplification theory.

Drela et al [35], [43], [45] and [46] published a series of works improving the Lag-Entrainment method, adding new closure relations to transition flow and introducing a Newton-Raphson procedure to solve the equations simultaneously. In Drela´s work [43], it was proposed a two-dimensional coupling of his boundary layer solution with panel method, creating the code XFOIL.

Hufford et al [45] proposed the strip theory, which uses the two-dimensional lag-entrainment method divided into panel strips to approach the three-dimensional flow. The strip theory was applied to marine propellers. The method of Hufford et al [45] was reported to have a close agreement with experimental data of foils tested. Strip theory was also reported to converge quickly, just adding a few more seconds to the primary inviscid solution. The authors [45] even suggest the possibility of coupling the method with unsteady panel methods, as the one developed by Hsin [47].

In a later work, Drela [46] derived the two-dimensional lag-entrainment method creating a three-dimensional method. Milewski [48] developed a simultaneous coupling of a surface panel method with Drela´s [46] three-dimensional boundary layer method. As reported by Milewsky [48], the coupling needs more computational effort for reaching convergence. The method presented an enormous sparse block matrix to be solved and, as reported by Hufford et al [45], the results are very similar between the three-dimensional method and the strip theory.

2.3 Objective and Considerations

In this Chapter it was discussed that yacht sail systems work in a low speed flow and low altitude, which is subjected to near floor viscous flow effects. The low speed operation and size of sails impose a transitional flow that can have some complexity due to the three-dimensional geometry of sail membranes.

Sails are thin membranes that are only capable to resist to surface tension. Yacht sails have the characteristic to be thin and flexible but, they operate as lifting surface when they assume a curved shape with wind action. The maintenance of this curved shape is dependant on sail surface tension and a certain angle of incidence to wind.

The angles of incidence where sails have a lifting surface effect are considered small in relation to the broad range of headings sail can operate, however by adjusting the boom angle, for most of the headings until 135^o, sails can be considered to operate as lifting surfaces.

Considering that sails have a momentarily rigid shape, so the surface tensioning issue can be isolated, the angle of incidence that keeps sail curved has to be in such way that flow separation is avoided on all sail surface. The avoidance of separation will contribute that, in a second moment of the aeroelastic analysis, when surface is not rigid, flow will not collapse the membrane.

In the next chapters, it will be investigated the surface method for viscous flow analysis, with the intention to use it in sail systems. The main theory of panel method will be reviewed, since surface methods for viscous flow are based in the panel method. There will be a discussion of the different tangential boundary conditions involved in the panel method problem, regarding the inclusion of transpired source sheets to the viscous-inviscid interaction coupling to sail membrane analysis.

Methods to solve laminar and turbulent integral boundary layers are studied as components of the numerical coupling between inviscid and viscous flows. The study of boundary layer methods also includes the typification of flow separation, that can be weak or strong, based in some of Gad-el-Hak [1] and Gad-el-Hak and Bushnel [49] observations. This typification will be helpful on developing a criteria to identify separation on foils.

Hence the numerical coupling of viscous and inviscid methods is studied in two-dimensions, exploring the differences between direct and simultaneous approaches. In the end, it is intended to create a three-dimensional sectional method to analyse viscous flow. With this method, three-dimensional sail shapes will be tested, varying their geometries, where flow separation can be checked using the criteria developed in this work.

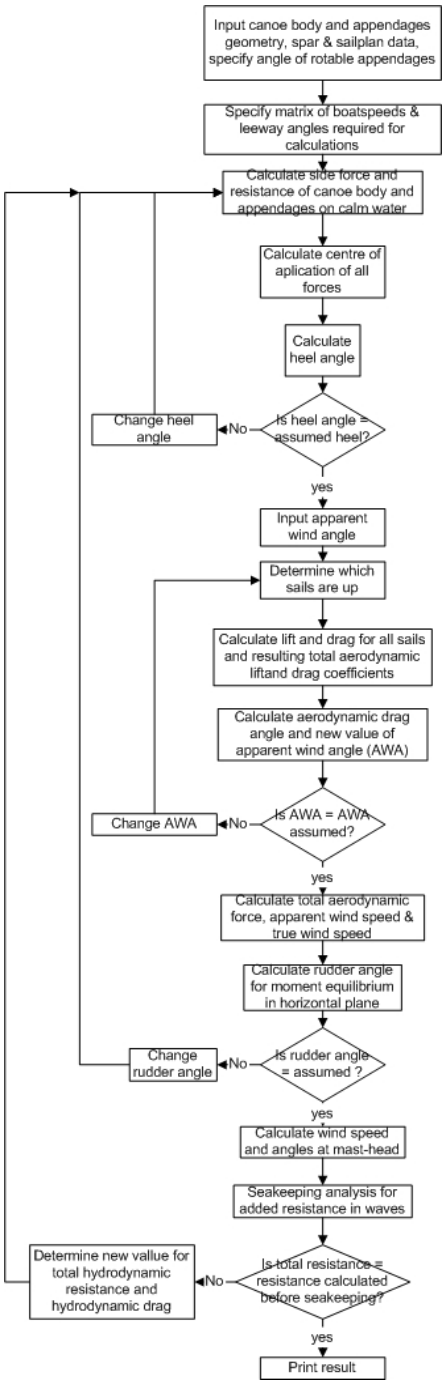

Figure 2.12: The VPP calculating scheme

Chapter 3

Inviscid Flow Analysis

Inviscid flow has been commonly applied to sail yacht flow analysis, as reported by Hoghton [50], Milgram [51] and, Larsson and Eliason [3], by means of the panel method. Panel method has its basic theory derived from the inviscid flow but, with a few more considerations it can also be used in some cases of viscous flow analysis, as it will be discussed later in this work using viscous-inviscid interaction.

Authors such as Hess [40], classify panel method as a highly accurate method for lifting bodies flow. It can even calculate drag force inherent of inviscid flows as in the case of induced drag force due to finite aspect ratio wings, as it will be seen in this Chapter.

As panel method will be used extensively in other methods presented along this work, the basic theory for two and three-dimensional flows is discussed here. Panel method limitations concerning its application in very thin membranes and on body surfaces with sudden changes in curvature are also presented.

As in flow analysis of sail systems it is common to have very thin membranes or a mast attached to the sail, the discussion of panel method limitations is helpful to create approximations or guidances for an accurate analysis.

3.1 The Panel Method

Panel method is based in surface flow and assumes that flow is potential and, by considering small incidence angles and a thin body in relation to its chord, its solution is approximated by a linear system using a superposition of singularities, positioned at discrete points on body surface and wake (panels).

In this section it is discussed the basic assumptions, considerations and solution of potential flow lifting surfaces using panel method.

3.1.1 The Potential Flow

It is assumed that foil is moving at a constant speed (steady flow) in an undisturbed fluid. It is considered a foil frame of reference with Cartesian coordinates, where its x

axis in the direction of foil chord, the y axis following camber distance and z following the height of foil, as shown in Figure 3.1.

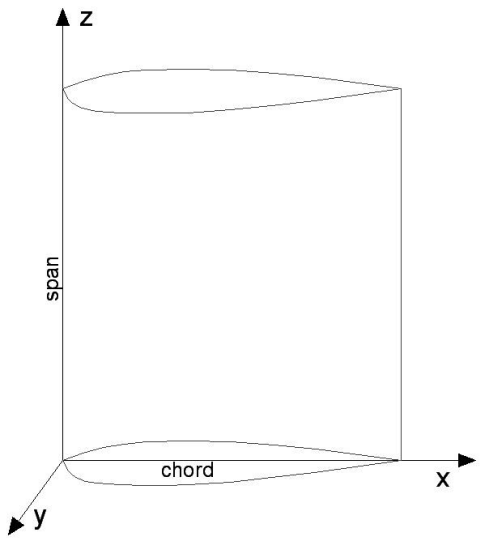

Figure 3.1: Cartesian frame of reference for wing

The freestream velocity Q_∞ has its components in the frame of reference as U_∞ in x axis, V_∞ in y axis and W_∞ for z axis. The angle of incidence α is given by equation (3.1)

$$\alpha = \tan^{-1} \frac{V_\infty}{U_\infty} \tag{3.1}$$

where, for the sake of simplicity at this point, $W_\infty \equiv 0$. The respective components of velocity field in the foil Cartesian frame of reference are u, v and w

According to Hess [40] and Katz and Plotkin [34], a flow to be potential must be inviscid, incompressible and irrotational. The governing equations of potential flow are: the equation (3.2), which accomplishes for continuity;

$$\nabla \cdot \Phi = 0 \tag{3.2}$$

and Laplace's equation (3.3), derived from (3.2), which also accomplishes for irrotationality.

$$\nabla^2 \Phi = 0 \tag{3.3}$$

For a body submerged in fluid with impervious surface, it is assumed, in the inviscid flow, that the velocity component normal to surface must be zero in a body fixed coordinate system. Hence,

$$\nabla \Phi \cdot \mathbf{n} = 0 \tag{3.4}$$

If flow is potential, it is assumed that the velocity field due to motion of foil can be obtained by solving Laplace's equation (3.3). The velocity field is obtained by

equations (3.5), (3.6) and (3.7).

$$\frac{\partial \Phi}{\partial x} = u \tag{3.5}$$

$$\frac{\partial \Phi}{\partial y} = v \tag{3.6}$$

$$\frac{\partial \Phi}{\partial z} = w \tag{3.7}$$

The principle of superposition, according to Katz and Potkin [34], can be applied to potential flow so,

$$\Phi = \sum_{k=1}^{n} c_k \Phi_k \tag{3.8}$$

and Laplace's equation (3.3) can be

$$\nabla^2 \Phi = \sum_{k=1}^{n} c_k \nabla^2 \Phi_k$$

Hence, potential flow can be described by a sum of potentials, permitting a discretization of body surface into singularities (sources, doublets and vortices) that satisfy Laplace's equation (3.3).

3.1.2 Potential Singularities

Considering a foil given in Figure 3.2 with its internal potential Φ_0, the difference of the potential Φ at a point on the surface and the internal potential Φ_0 is given by a doublet $\mu = \Phi - \Phi_0$.

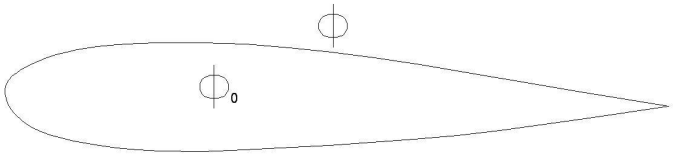

Figure 3.2: Scheme of surface and internal potentials

The difference of normal velocities inside the body and on its surface is given by a source σ.

$$-\sigma = \frac{\partial \Phi}{\partial \mathbf{n}} - \frac{\partial \Phi_0}{\partial \mathbf{n}}$$

The general solution of Laplace's equation (3.3), according to Katz and Plotkin [34], consists in doublets and sources distributions only. However, other solutions to Laplace's equation, as discussed by Katz and Plotkin [34], are possible and based on vortex flow.

The use of vortex singularity, as discussed by Katz and Plotkin [34], uses the Biot-Savart law. The formulation considers a point vortex with zero radial velocity q_r and a tangential velocity q_θ that depends on the distance from singularity r:

$$q_r = 0$$

$$q_\theta = q_\theta(r)$$

Thus, the magnitude of velocity varies with $1/r$, similar to the radial velocity variation of a source singularity.

Vortex singularities have strengths related to circulation Γ, defined in equation (3.9), rather than difference between internal and external potentials as it was defined for doublets and sources.

$$\Gamma = \oint q \cdot dl \tag{3.9}$$

3.1.3 Tangential Flow Boundary Condition

The superposition of discrete singularities using equation (3.8) allows the linearization of problem. However, as it is a linear system with the main equation being Laplace's equation (3.3), and the unknowns being c_k and Φ_k from equation (3.8), a boundary condition is needed for the solution of problem.

According to Katz and Plotkin [34], the potential flow solution uses a linearization of the equation (3.4). To do so with tangential boundary condition, it is considered small angles of incidence, so that $\tan\alpha \ll 1$ and, geometry restrictions for normal coordinates on body surface η as follows:

$$\left|\frac{\partial \eta}{\partial x}\right| \ll 1$$

and

$$\left|\frac{\partial \eta}{\partial z}\right| \ll 1$$

or, a thin body in relation to its chord.

There are two basic approaches to use a tangential flow boundary condition in panel method. The Neumman and Dirichlet conditions which are discussed here later.

3.1.4 Potential Lifting Surface Problem

According to Katz and Plotkin [34], the potential lifting surface problem can be divided into three subproblems, with its respective potentials Φ_1, Φ_2 and Φ_3, as follows:

1. Straight mean-line foil shape, as shown in Figure 3.3 with internal finite volume, at zero incidence angle, with the main equation $\nabla^2\Phi_1 = 0$ and the boundary

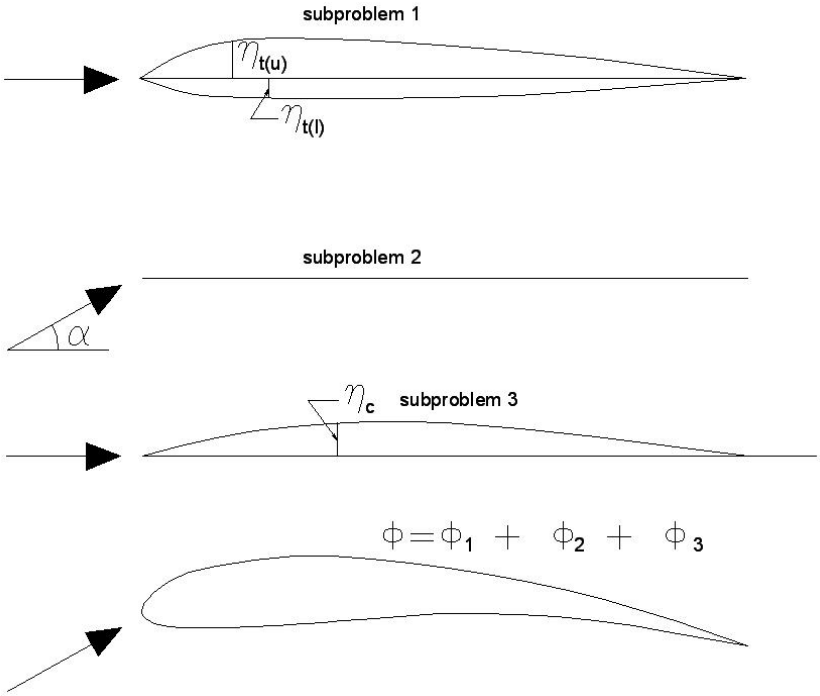

Figure 3.3: Scheme of the perturbation potential Φ and its subproblems Φ_1, Φ_2 and Φ_3

condition given by equation (3.10)

$$\frac{\partial \Phi_1}{\partial y} = \pm \frac{\partial \eta_t}{\partial x} Q_\infty \tag{3.10}$$

where η_t accounts for the normal surface coordinate of uncambered non-zero thickness foil with signs + for the upper surface $\eta_{t(u)}$ and − for the lower surface $\eta_{t(l)}$;

2. Zero-thickness, uncambered foil mean-line at an incidence angle with main equation $\nabla^2 \Phi_2 = 0$ and the boundary condition given by equation (3.11);

$$\frac{\partial \Phi_2}{\partial y} = -Q_\infty \alpha \tag{3.11}$$

3. Zero-thickness cambered foil mean-line at zero incidence angle, with main equation $\nabla^2 \Phi_3 = 0$ and the boundary condition given by equation (3.12)

$$\frac{\partial \Phi_3}{\partial y} = \frac{\partial \eta_c}{\partial x} Q_\infty \tag{3.12}$$

where η_c accounts for the normal surface coordinate of the cambered thin foil.

The solution of the potential subproblem 1 can be done by the distribution of source singularities in two ways: By distributing sources on body surface, as shown in Figure 3.4 for surface distribution, where the source strengths are given by the difference of the internal and external potentials or; by distributing sources along the meanline of

body, as shown in Figure 3.4, and the source strengths are given by the difference in η_t between upper and lower potentials of surfaces.

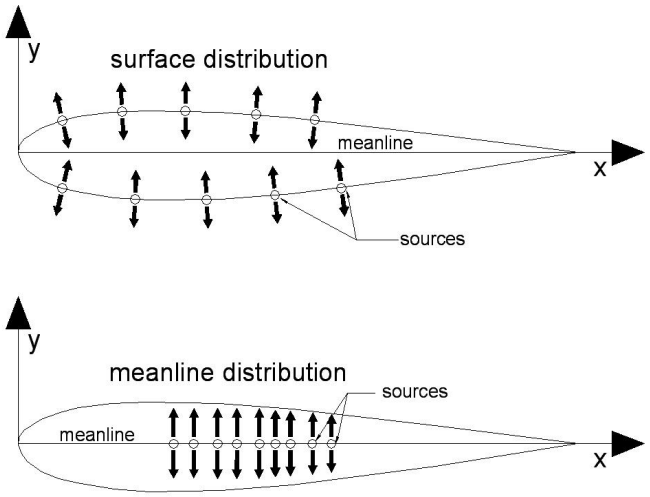

Figure 3.4: Scheme of possible configurations for source distributions

Subproblems 2 and 3 can be solved together, becoming one non-symmetric subproblem: zero-thickness cambered airfoil at an incidence angle. Two kinds of singularities can be used to model the problem: doublet and vortex. A more common approach considers that singularities are related to the potential jump between the upper and lower sides of the thin foil. However, the distribution of doublets or vortex on a thick body surface is possible and will be discussed later in this section.

According to Katz and Plotkin [34], the perturbation potential is derived following Green's identity and it is given in equation (3.13) for any point on body surface S_B, where σ is the source and μ the dipole strengths.

$$\Phi = \frac{-1}{4\pi} \int_{S_B} \left[\sigma \left(\frac{1}{r} \right) - \mu \mathbf{n} \cdot \nabla \left(\frac{1}{r} \right) \right] ds + \Phi_\infty \tag{3.13}$$

In the equation (3.13), inside the brackets, the subproblem 1 corresponds to the left hand side, while subproblems 2 and 3 correspond to the right hand side.

3.1.4.1 The Application of Tangential Boundary Condition

The basic approaches to apply tangential boundary condition on body surface are Neumman and Dirichlet.

The Neumman Boundary Condition The Neumman boundary condition is simply the consideration of zero normal velocity on body surface $\partial\Phi/\partial\mathbf{n} = 0$. It implies on evaluating the resulting velocity field generated by the contribution of potential subproblems, meaning the entire solution of equation (3.13). Katz and Plotkin [34] call it as direct boundary condition. It is given by equation (3.4).

The Dirichlet Boundary Condition The Dirichlet boundary condition considers that at a distance r far from body, the flow disturbance is zero.

$$\lim_{r\to\infty} \nabla\Phi = 0$$

If the condition $\partial\Phi/\partial\mathbf{n} = 0$ on body surface is required then, potential inside body (without internal singularities) will not change ($\Phi_0 = constant$). This constant can be specified as zero. Applying Neumann condition, as discussed by Katz and Plotkin [34], solution will be equivalent to equation (3.14).

$$\frac{\partial\Phi}{\partial\mathbf{n}} = -\mathbf{n}\cdot Q_\infty \tag{3.14}$$

Considering

$$-\sigma = \frac{\partial\Phi}{\partial\mathbf{n}} - \frac{\partial\Phi_0}{\partial\mathbf{n}}$$

and $\Phi_0 = 0$, with a constant potential function then, $\frac{\partial\Phi_0}{\partial\mathbf{n}} = 0$ too. the Dirichlet boundary condition will be given in equation (3.15), where σ is a source strength and $\mathbf{n}$ points inside the body.

$$\sigma = \mathbf{n}\cdot Q_\infty \tag{3.15}$$

Dirichlet boundary condition is applied to source singularities, implying that body needs a finite volume inside so, the constant potential can be adopted. By establishing the constant potential, the condition of tangential flow on surface is satisfied indirectly so, it is called by Katz and Plotkin [34] as indirect method.

The Dirichlet boundary condition, for viscous-inviscid interaction, as it will be seen in Chapter 5, allows a split solution for inviscid and viscous flows and the viscous part can be inserted as a separate module in calculation.

3.1.4.2 Surface and Lattice Methods

The source singularity modelling, discussed before, can be done by two approaches: Using a distribution of sources on a meanline inside surface or, by distributing them on wing surface. The same approaches can be used for doublet or vortex singularities. The difference between them is the tangential flow boundary condition used. The distribution of singularities on a body surface (surface panel method) uses normally the Dirichlet boundary condition, as an internal potential has to be specified.

The problem of singularities distributed on a meanline does not need a specification of an internal potential but, the boundary condition has to be satisfied at the body surface points then, Neumman condition is applied. The combination of potentials of all singularities involved has to satisfy the tangential flow condition. The meanline distribution of singularities is also known as lattice methods, according to Couser [28].

One advantage of lattice methods over the surface panel method is the number of panels involved in calculation as described in works of Greeley and Cross-Whiter [52]

and Couser [53]. Lattice methods (LM) use fewer panels but, according to Hess [40], LM has less accuracy than surface method due to small oscillations between lattices. Hess [40] obtained 20% of error comparing the LM and his own surface panel method.

3.1.4.3 The Kutta Condition

According to Hess and Smith [54], describing flow over thick and non-lifting bodies with source singularities distribution is sufficient. However, for the lifting cases, a boundary condition has to be specified at the trailing edge, in order to have for resulting body circulation Γ an unique solution and a finite value for velocity at this region.

The Kutta boundary condition states that: "The flow leaves the sharp trailing edge of an airfoil smoothly and the velocity there is finite". This is interpreted by Katz and Plotkin [34] as a trailing edge flow with the following characteristics:

- Flow leaving sharp trailing edge along the bisector line there;
- The normal component of trailing edge velocity must vanish for both sides of foil (upper and lower);
- The pressure jump at trailing edge is zero;

$$\Delta p_{TE} = 0$$

- If circulation is modelled by a vortex distribution, pressure jump can be expressed as

$$\gamma_{TE} = 0$$

where TE subscripts mean trailing edge region.

3.1.4.4 The Wake Modelling

Doublets or vortices are used to solve the subproblems 2 and 3 discussed before: zero thickness cambered foil at an angle of attack. The most important variable for subproblems 2 and 3 is the amount of circulation Γ generated by the body. In two-dimensional flow, a trailing vortex segment of wake is not necessary since it has zero vorticity and it is sufficient to specify the location of trailing edge where Kutta condition has to be satisfied.

In three-dimensional flow, according to Katz and Plotkin [34], if wing is looked at a distance, it can be modelled as a vorticity segment producing a determinate circulation. According to the Helmholtz theorem [34], vorticity segments cannot begin and end in the fluid. After reaching the surface limits, vorticity vector turns to be parallel to the local velocity vector and they shed at some length into flow, as shown in Figure 3.5.

If foil is discretized into many spanwise lines of vorticity, these lines will come out of wing in different points along the trailing edge and form the wake. As wake cannot

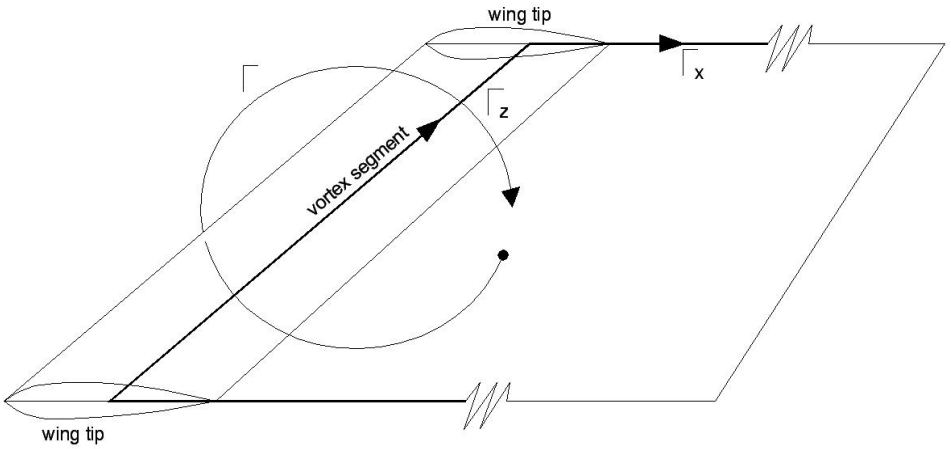

Figure 3.5: Scheme of vortex segment development in a finite wing according to Helmholtz theorem

generate force in the fluid, the lines coming out of trailing edge should be parallel to the local flow direction at any point and, as observed by Katz and Plotkin [34], the vortex singularity strength γ_W along this line or, the doublet strength μ_W, must be constant.

According to Hess [40] and Katz and Plotkin [34], the wake modelling is part of the solution and, the disturbed potential equation (3.13) should take into account the wake vorticity. Then, equation (3.13) becomes (3.16) for three-dimensional flow.

$$\Phi = \frac{1}{4\pi} \int_{body+wake} \mu \mathbf{n} \cdot \nabla \left(\frac{1}{r} \right) dS - \frac{1}{4\pi} \int_{body} \sigma \left(\frac{1}{r} \right) dS + \Phi_\infty \tag{3.16}$$

3.1.5 Numerical Solution Method

The influences of each singularity for the three numerical subproblem is calculated at a collocation point on panel with singularities positioned at each vertex of panel. The collocation point, according to Hess and Smith [54] is a point on panel where normal velocities generated by its singularities positioned on vertices vanish. It is usually approximated, according to Hess and Smith [54], as the centre point of panel.

Panel methods use normally quadrilateral panels for three-dimensional surfaces and line segments for two-dimensional surfaces.

3.1.5.1 Two-dimensional Flow

The influence of singularities are calculated at point P, as shown in Figure 3.6.

On a wing, singularities are distributed all around the contour of body. Half distance between two singularities there are the collocation points, as exemplified in Figure 3.7.

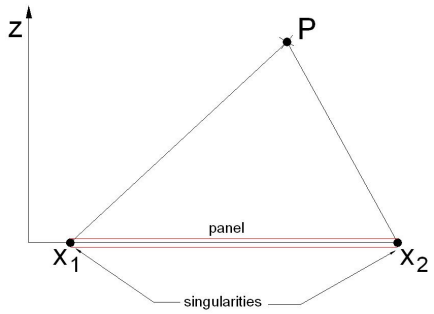

Figure 3.6: Scheme of a local coordinate for a panel and the singularity distribution

As the collocation point is a place where induced potential of local singularities vanishes, the resultant potential is just dependent on the other body singularities induced potentials.

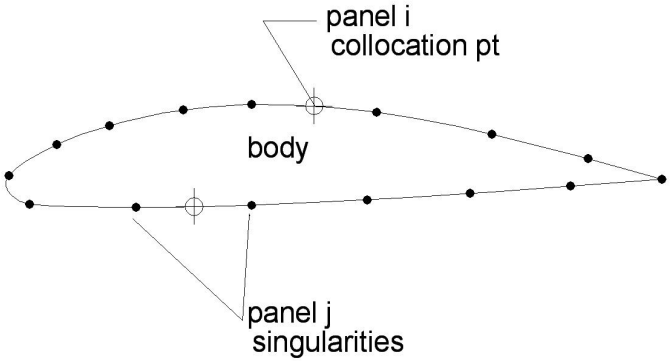

Figure 3.7: Scheme of influence of j panel singularities at i panel collocation point

Hence, at a collocation point i, the resulting potential is dependant on the other j influences of other panels singularities. For subproblem 1, as it has zero circulation, there is an $N \times N$ matrix. However, for the subproblems 2 and 3, the Kutta condition must be taken into account, adding one more row and one more column to the solution system, according to Katz and Plotkin [34]. Their values will depend on the numerical approach used where, the most common is the Kutta-Morino [40] numerical condition. Formulae for two-dimensional induced potentials are described in more detail in Appendix A.

The general linear system is given by equation (3.17),

$$[D] \cdot [\Phi] = [S] \cdot \left[\frac{\partial \Phi}{\partial \mathbf{n}}\right] \tag{3.17}$$

where $[D]$ is the dipole (or vortex) influence matrix with the Kutta condition and $[S]$ is

the source influence matrix which multiplies the tangential boundary condition vector $\left[\frac{\partial \Phi}{\partial \mathbf{n}}\right]$.

3.1.5.2 Three-dimensional Flow

The calculation for three-dimensional flow has an additional system due to wake vorticity panels. A similar numerical approach to two-dimensional linear system is used to take into account the Kutta condition for doublet or vortex distribution on body. The linear system is given by equation (3.18),

$$[D] \cdot [\Phi] + [W] [\Delta \Phi_w] = [S] \cdot \left[\frac{\partial \Phi}{\partial \mathbf{n}}\right] \tag{3.18}$$

where $[D]$ is the dipole or vortex influence matrix on body with Kutta condition and $[W]$ is the wake vorticity influence matrix. $[\Phi]$ accounts for body potential and $[\Delta \Phi_w]$ is the potential jump on wake. $[S]$ is the source influence matrix that multiplies the vector of tangential boundary condition $\left[\frac{\partial \Phi}{\partial \mathbf{n}}\right]$ on surface.

Formulae for three-dimensional induced potentials for some singularities are shown in Appendix A.

3.1.6 Numerical Panel Methods

The general linear system for panel methods discussed before is the basis of the calculation. However, the construction of influence coefficients given by a singularity allows the use of the following approaches:

- Piecewise constant potentials, where potential is constant anywhere on panel apart from the vertices;
- Linear potential, where potential has a linear function between collocation points of panels;
- Higher order potential, where potential has a second order or even a third order function between collocation points of panels.

In this work, the methods used for two and three-dimensional flows are piecewise constant surface panel methods using source and vortex singularities. Both use Neumann tangential boundary condition. The two-dimensional panel method code is shown in Appendix E and the three-dimensional panel method used was PALISUPAN, developed by Turnock [55].

3.1.7 Force Calculation

In inviscid flow there are two forces acting on wing surface: lift force that is caused by asymmetrical flow on body and, for three-dimensional flow only, the induced drag, that is caused by vorticity development for a finite wing span.

3.1.7.1 Lift Force

Lift force F_L is calculated in relation to the angle of incidence vector. It has a perpendicular direction to the undisturbed flow. Pressure is integrated on body surface as in equation (3.19), where s is body surface.

$$F_L = -\int_{wing} p \cdot \mathbf{n} ds \tag{3.19}$$

Lift force is generally presented as the non-dimensional value C_L, which is given by:

$$C_L = \frac{F_L}{0.5\rho Q_\infty^2 A}$$

for three-dimensional flow, where A is the total area of body surface or,

$$C_L = \frac{F_L}{0.5\rho Q_\infty^2 c}$$

for two-dimensional flow, where c is the chord length.

In literature it is preferred to show pressure as pressure coefficient as in equation (3.20), where p_∞ is the freestream pressure.

$$C_P = 1 - \left(\frac{q}{Q_\infty}\right)^2 = \frac{p - p_\infty}{0.5\rho Q_\infty^2} = \frac{\Delta p}{0.5\rho Q_\infty^2} \tag{3.20}$$

Using singularity potential, Δp is given by equation (3.21), where Φ reefers to the potential between upper and lower surfaces in the case of a thin foil or, between inner and surface edge potential, for thick foils.

$$\Delta p = \rho Q_\infty \frac{\partial \Phi}{\partial x} \tag{3.21}$$

Hence, for doublet singularity that has its influence on x-z plane,

$$\Delta p = \rho Q_\infty \frac{\partial \mu(x,z)}{\partial x}$$

and for vortex singularity on x-z plane too:

$$\Delta p = \rho Q_\infty \gamma(x,z)$$

Considering circulation Γ, defined in equation (3.9), as the total circulation on a wing, the lift force coefficient C_L is given by equation (3.22). In two-dimensions A is substituted by c.

$$C_L = \frac{\rho Q_\infty \Gamma}{\frac{1}{2}\rho Q_\infty^2 A} = \frac{2\Gamma}{A Q_\infty} \tag{3.22}$$

3.1.7.2 Induced Drag

Induced drag is obtained by means of the far-field integration on Trefftz plane, as proposed by Giles et al [56] and [57], for incompressible flow. It consists in integrating the potential jump on a plane perpendicular to wake surface, as indicated on equation (3.23), where dy and dz refer to Cartesian coordinates.

$$D_i = \int\int_S \Delta p \cdot dydz \tag{3.23}$$

At some distance from trailing edge, on wake surface, streamwise velocity u is negligible and does not contribute to induced drag then,

$$D_i = \int\int_S \left(v^2 + w^2\right) dydz$$

But

$$D_i = \int\int_S \left(v^2 + w^2\right) dydz = \int\int_S \left[\left(\frac{\partial\phi}{\partial y}\right)^2 + \left(\frac{\partial\phi}{\partial z}\right)^2\right] dydz$$

Using the divergence theorem to transfer a surface integral to a line integral:

$$\int\int_S \left[\left(\frac{\partial\phi}{\partial y}\right)^2 + \left(\frac{\partial\phi}{\partial z}\right)^2 + \phi\left(\frac{\partial^2\phi}{\partial y^2} + \frac{\partial^2\phi}{\partial z^2}\right)\right] dydz = \oint \Phi \frac{\partial\Phi}{\partial\mathbf{n}} dl$$

where l refers to the line resulting from the intersection of wake surface to the Trefftz plane. If wake is modelled parallel to x axis and singularity distributions are continuous then:

$$D_i = -\frac{\rho}{2}\int_{-b_w/2}^{b_w/2} \Delta\Phi dz = -\frac{\rho}{2}\int_{-b_w/2}^{b_w/2} \Gamma(z)_{wake} \cdot w dz \tag{3.24}$$

where z is the axis where a sail, fin keel or rudder is developed.

3.2 The Close Approach Problem

Sail membranes have essentially no thickness but, when surface panel methods are used for their flow analysis, there is a need to model sails with a small volume inside. One common problem, according to Wilkinson [4], Hoghton [50] and C. Elstub[58], is the close approach between lower and upper surfaces when modelling sail membranes. A minimum thickness has to be established so that there will be a finite volume inside the foil and method will not break.

Lattice methods in this case would be more suitable as there is no need to establish a minimum internal volume. However, in viscous-inviscid interaction methods, the use of a Dirichlet boundary condition allows a split solution between viscous and inviscid

problems, as it will be discussed in Chapter 5. The consideration of a Dirichlet boundary condition, as discussed before, needs an internal finite volume in order to have the constant internal potential.

Wilkinson [4] introduced some approximations for increasing sail model internal volume, based in average thickness of boundary layer around sail. This process, as reported by Wilkinson [4], improved the numerical solution using surface panel methods for two-dimensional sail membranes without having a significative influence in the accuracy of flow analysis.

In more recent studies, Hoghton [50] and C. Elstub[58], sails were analysed considering a thickness of 2.5% to 3.0% of chord. Both authors used a three-dimensional piecewise constant potential surface panel method (PALISUPAN).

3.2.1 Mesh Modelling

The solution performance for surface panel methods when using very thin foils is directly dependant on the surface mesh modelling. Assuming an equally spaced panel mesh, there is a relation between the panel size to the distance that separates the other panel on the opposite side of surface, as illustrated in Figure 3.8. This distance $2t$ should be enough so singularity strengths of both panels do not affect each other.

For unequally spaced panel mesh, as in the case of sinusoidal mesh distributions or a mesh distribution given by functions, as the case of ADAPTIFLEX [59], more care should be given to the spacing between panels. The relation should be evaluated for each panel spacing. For the sake of simplicity, this case will not be discussed here.

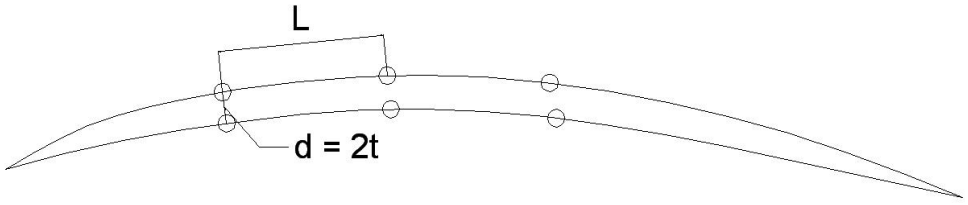

Figure 3.8: Relative distance $2t/L$ between upper and lower surfaces for a thin foil

Unfortunately, as far as this work is concerned, there is not a formal approach to determine the minimum distance. The calculation process is also highly influenced by the matrix solver precision, which is set by computing hardware.

3.2.2 The Solution Matrix Investigation

The solution matrix investigation can show the behaviour of thickness reduction. When two singularities of opposite sides are closer enough, there should be a high influence on each, approaching the self induced coefficient of a singularity. The other surface singularities, as they are relatively far, will have a small effect and their influence coefficients in matrix will be closer to zero.

The effect of close approach is better observed by considering a hypotetical body and decreasing its thickness to small values. The matrix coefficients should approximate a system with no solution (singular matrix). The considered part of solution matrix is related to body influence coefficients only, without taking into account the Kutta condition.

In order to observe what happens in solution matrix when body thickness is reduced, it was used a two-dimensional surface panel method with piecewise constant source and vortex strengths distribution. A set of runs were done for the body in Figure 3.9 considering symmetrical flow and decreasing the foil thickness. The body geometry had a non dimensional length of 1.0.

Just eight nodes equally spaced were used to discretize the body so, results could be shown in Tables (3.2),(3.3) and (3.4), representing the solution matrix.

Calculations were ran for a series of different thicknesses $2t$. It used a PC Pentium III with 128 Mbytes RAM and 330 MHz clockspeed for analysis. The processing time was much less than one second because of the small number of nodes. Table (3.1) gives some different thicknesses, panel spacing and the ratio between panel spacing and thickness used ($2t/L$).

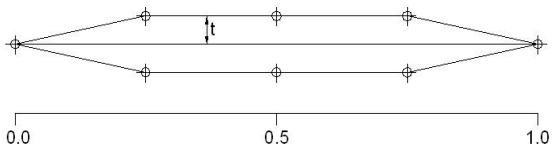

Figure 3.9: The eight nodes simple body used in calculations varying the thickness $2t$

$\frac{1}{2}$**Thickness**	**Panel Spacing**	**Ratio**
0.500	0.25	4.0
0.125	0.25	1.0
0.010	0.25	0.08
$1.0 \cdot 10^{-6}$	0.25	$8.0 \cdot 10^{-6}$

Table 3.1: Table of body thicknesses

Results for solution matrices are presented in Tables (3.2) to (3.4). In all of them, it was observed the predominance of the main diagonal terms and the cross diagonal terms. In the first two matrices, represented by Tables (3.2) and (3.3), the half thicknesses for each problem was 0.5 and 0.125 respectively. It can be noticed the increase on diagonal and cross diagonal terms, while outside this region, terms have a trend to smaller values. For the limiting case of a very small thickness, like $2.0 \cdot 10^{-6}$, showed in Table (3.4), the off diagonal terms vanish while both main and cross diagonal terms approach the value -0.5, thus turning the determinant of this matrix progressively close to zero or, a system with no solution.

The reduction of thickness produces a matrix with no solution as the case when it

-.32379	0	0	-.06056	-.13943	-.19290	-.23021	-.27628
-.08262	-.50000	0	-.03302	-.03678	-.03731	-.03958	-.04751
-.03302	0	-.50000	-.08262	-.04751	-.03958	-.03731	-.03678
-.10485	-.10739	-.14758	-.50000	-.1008	-.08262	-.08551	-.09514
-.09514	-.08551	-.08262	-.1008	-.50000	-.14758	-.10739	-.10485
-.03678	-.03731	-.03958	-.04751	-.08262	-.50000	0	-.03302
-.04751	-.03958	-.03731	-.03678	-.03302	0	-.50000	-.08262
-.27628	-.23021	-.19290	-.13943	-.06056	0	0	-.32379

Table 3.2: Solution matrix for half thickness of 0.5

-.42621	0	0	-.01586	-.04639	-.09358	-.17621	-.27628
-.04751	-.50000	0	-.01042	-.02741	-.08262	-.14578	-.08262
-.01042	0	-.50000	-.04751	-.08262	-.14578	-.08262	-.02741
-.02721	-.03142	-.05121	-.50000	-.26979	-.12500	-.06217	-.03504
-.03504	-.06217	-.12500	-.26979	-.50000	-.05121	-.03142	-.02721
-.02741	-.08262	-.14578	-.08262	-.04751	-.50000	0	-.01042
-.08262	-.14578	-.08262	-.02741	-.01042	0	-.50000	-.04751
-.27628	-.17621	-.09358	-.04639	-.01586	0	0	-.42621

Table 3.3: Solution matrix for half thickness of 0.125

-.50000							-.50000
	-.50000					-.49999	
		-.50000			-.49999		
			-.50000	-.49999			
			-.49999	-.50000			
		-.49999			-.50000		
	-.49999					-.50000	
-.50000							-.50000

Table 3.4: Solution matrix for half thickness of 1.0E-06

is very thin $2t = 2.0 \cdot 10^{-6}$. However, before reaching the limiting case, solution could be achieved without numerical problems. The minimum thickness relation in which calculation worked was $2t/L = 8\%$. As the close approach problem depends on other parameters that are mostly particular for each case, this 8% relation value will be used as a guidance for mesh modelling.

3.2.2.1 The Three-dimensional Case

In three-dimensional surface panel methods, the same conclusions can be applied. However, there are two directions to optimize the distance ratio and, according to Kervin et al [60], other aspects of surface geometry may influence in solution, such as: skew and twist. Hence the determination of a suitable thickness would also depend on variables that are specific for each case.

In the two-dimensional solution matrix investigation, the minimum thickness ratio (d/L) used was 8%. Based in this guidance, the adopted ratio value for three-dimensional cases will also be 8%. As panel surface has two characteristic lengths: chordwise L_1 and spanwise L_2, L should be given by equation (3.25). However, the performance of three-dimensional panel method should always be checked for the chosen thickness, mainly for twisted surface geometries.

$$L = \sqrt{L_1^2 + L_2^2} \tag{3.25}$$

3.3 The Attached Flow Condition

As discussed in the first section, the tangential flow boundary condition is linearized based in certain assumptions, as the thin body in relation to its chord and small angles of incidence. The thin body consideration has two derivative conditions: $|\partial\eta/\partial x| \ll 1$ and $|\partial\eta/\partial z| \ll 1$. The first derivative condition is called here as the chordwise condition. By analysing the chordwise condition, sudden changes on body surface normal coordinate η may result in relatively large slope relations and the chordwise condition will not be valid.

Then, panel method body surface geometries must be thin on chordwise direction and smooth.

On highly curved regions, if the condition of tangential flow is imposed, the potential flow will be accelerated on convex regions (less pressure) and will be subsequently decelerated on concave regions (more pressure).

If sail is perfectly attached to mast, *i.e.* no flow is allowed to pass between mast and sail surfaces, sail system will be a typical case of a thin membrane with a high curvature change at its leading edge, as illustrated in Figure 3.10. The chordwise condition will not be valid but pressure changes can still be observed with low pressure on convex and high pressure on concave regions. The attachment point of the membrane with

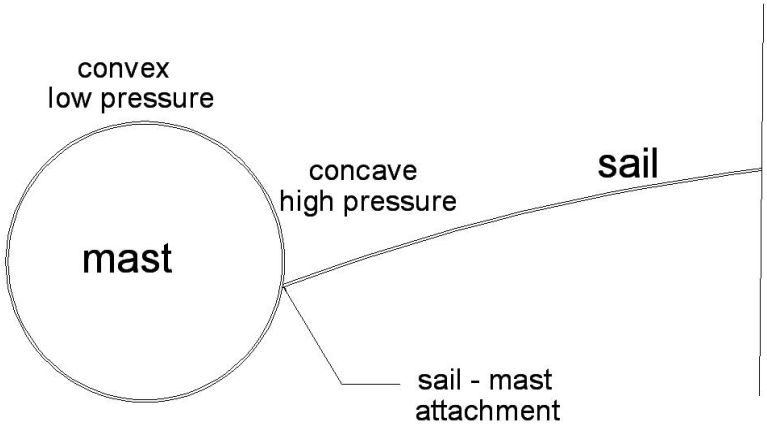

Figure 3.10: Mast and sail geometry with convex and concave regions

mast, due to its discontinuity in surface curvature, will create another point of zero velocity besides the leading edge stagnation point.

According to Wilkinson [4], the effect of flow acceleration will increase if mast sectional radius is decreased, while on the attachment region, flow will have zero velocity, becoming a singular point.

As the chordwise condition is not valid, the region between mast and sail is highly curved and flow on mast surface will normally have its velocity overpredicted by panel method, unless a matching surface or some modification in geometry is adopted to overcome this problem.

3.3.1 Wilkinson Mast/Sail Configurations

Wilkinson [4] used a series of NACA $a = 0.8$ mean lines varying cambers from 7.5% to 12.5% c, with a circular mast attached on the leading edge. The NACA mean line series, according to Abbot and Van Doenhoff [61], were not developed to represent a sail shape profile. Other profile series, as the elastic membranes used by Jackson [12] are more suitable for this purpose.

However, the behaviour of a NACA a mean line series is evaluated here using a two-dimensional piecewise constant surface panel method. Two models are discussed: the membrane of a NACA $a = 0.8$ with 10% c camber alone and a circular mast with 10% c diameter attached to its leading edge. Numerical results for inviscid flow could be compared with test 73 of Wilkinson's [4] work.

3.3.1.1 NACA a Mean Line Series Membrane

The main theory for a NACA a mean line series, according to Abbot and Van Doenhoff [61], considers an optimal angle of incidence where upper surface pressure is uniformly distributed along the line until a point a that is specified to be at 80% of c. Equation (3.26) gives ordinates of NACA mean lines, from parameters a and the theoretical

inviscid lift C_{Lt}.

$$\frac{y}{c} = \frac{C_{Lt}}{2\pi\,(a+1)} \left\{ \frac{1}{1-a} \left[\frac{1}{2} \left(a - \frac{x}{c}\right)^2 \ln\left|a - \frac{x}{c}\right| - \frac{1}{2} \left(1 - \frac{x}{c}\right)^2 \ln\left(1 - \frac{x}{c}\right) \right.\right.$$

$$\left.\left. + \frac{1}{4} \left(1 - \frac{x}{c}\right)^2 - \frac{1}{4} \left(a - \frac{x}{c}\right)^2 \right] - \frac{x}{c} \ln\left(\frac{x}{c}\right) + g - h\frac{x}{c} \right\} \tag{3.26}$$

where

$$g = \frac{-1}{1-a} \left[a^2 \left(\frac{1}{2} \ln(a) - \frac{1}{4} \right) + \frac{1}{4} \right]$$

$$h = \frac{1}{1-a} \left[\frac{1}{2} (1-a)^2 \ln(1-a) - \frac{1}{4} (1-a)^2 \right] + g$$

Equation (3.27) gives the ideal angle α_{io} in radians.

$$\alpha_{io} = -\frac{C_{Lt} \cdot h}{2\pi\,(a+1)} \tag{3.27}$$

Table 7.28 shows the NACA $a = 0.8$ mean line series with the range of cambers used by Wilkinson [4], the theoretical lift C_{Lt} and its ideal incidence angle α_{io} in degrees, calculated by equations (3.26) and (3.27).

Camber (%c)	$\mathbf{C}_{Lt}$	α_{io}
7.5	1.105	1.7
10.0	1.473	2.3
12.5	1.768	2.7
15.0	2.209	3.4
17.5	2.578	4.0

Table 3.5: NACA a=0.8 mean line and its optimal properties

Figure 3.11 shows the pressure distribution for a NACA $a = 0.8$ mean line foil with 10% c of camber. This figure was obtained by a two-dimensional analysis using a piecewise constant surface panel method with vortex and source singularities. Body was discretized using 150 points equally spaced and thickness of body was 0.5% c. According to Abbot and Van Doenhoff [61], the pressure distribution on a NACA $a = 0.8$ mean line foil should be uniform until $x/c = 0.8$. In this Figure 3.11, as analysis was performed using a panel method, the distribution approaches an uniform distribution, mainly on the lower surface. When $x/c = 0.8$ the distribution assumes a different slope and goes down to trailing edge C_P that is close to zero.

3.3.1.2 Attaching a Circular Mast to a Membrane Profile

The attachment of a circular mast at the membrane leading edge will modify the pressure distribution and the attachment point will generate a discontinuity on curvature of surface. Up and downstream from this singular point, numerical pressure distribution

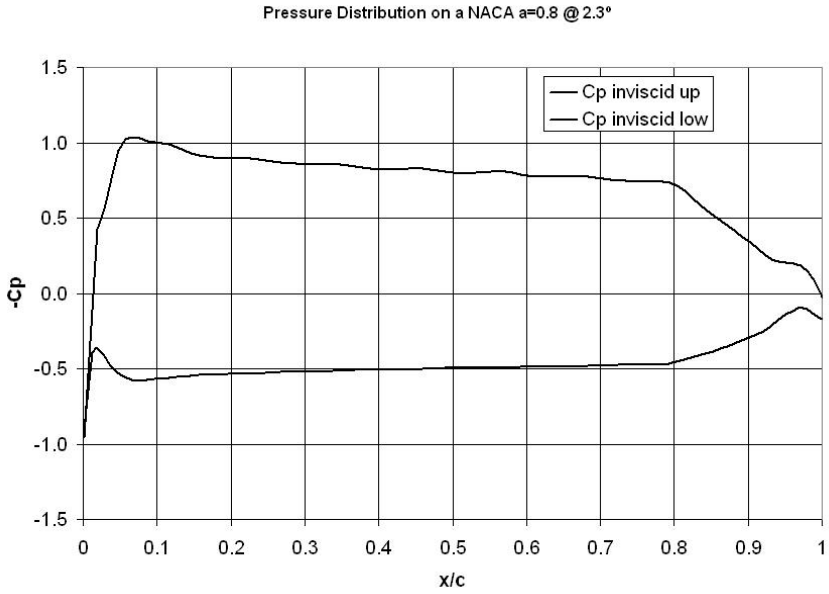

Figure 3.11: Pressure distribution on a NACA $a = 0.8$ mean line with 10% c camber on its optimal angle of incidence

will suffer influence, presenting a shape that has an exaggerated negative pressure on mast upper surface, as it can be observed in the inviscid C_P distribution of Figure 3.12.

Experimental data for Figure 3.12 was obtained from Wilkinson [4] test number 73, with its respective testing parameters shown in Table 3.6. Inviscid flow was calculated using a two-dimensional vortex panel method.

	$\mathbf{Re}_\infty$	α_i	Diam ratio (%)	mast angle
Test 73	$0.6 \cdot 10^6$	2.5^o	10.0	10^o

Table 3.6: Wilkinson's test 73 settings

In Wilkinson's [4] work, the same minimum pressure peak was obtained with values of $C_P = -7.0$ for the same sail system configuration. According to Wilkinson [4], it was used a two-dimensional piecewise constant lattice panel method with distribution of source and doublet singularities.

Observing Figure 3.12, where $x/c = 0$ is the attachment point, the sail membrane surface pressure distribution has a good agreement with the NACA $a = 0.8$ mean line foil, analysed before. On mast surface, mainly on its upper part, the shape of experimental points suggests that viscous flow has an effect of damping the low pressure peak until a point, already on sail surface, where pressure recovers to the attached flow model.

At the attachment region ($x/c = 0$), experimental data has an approximately uniform pressure distribution, as observed by Wilkinson [4]. In this region, real flow is separated, according to Wilkinson [4].

Hence, the panel method theory is limited to smooth surfaces and inviscid flow.

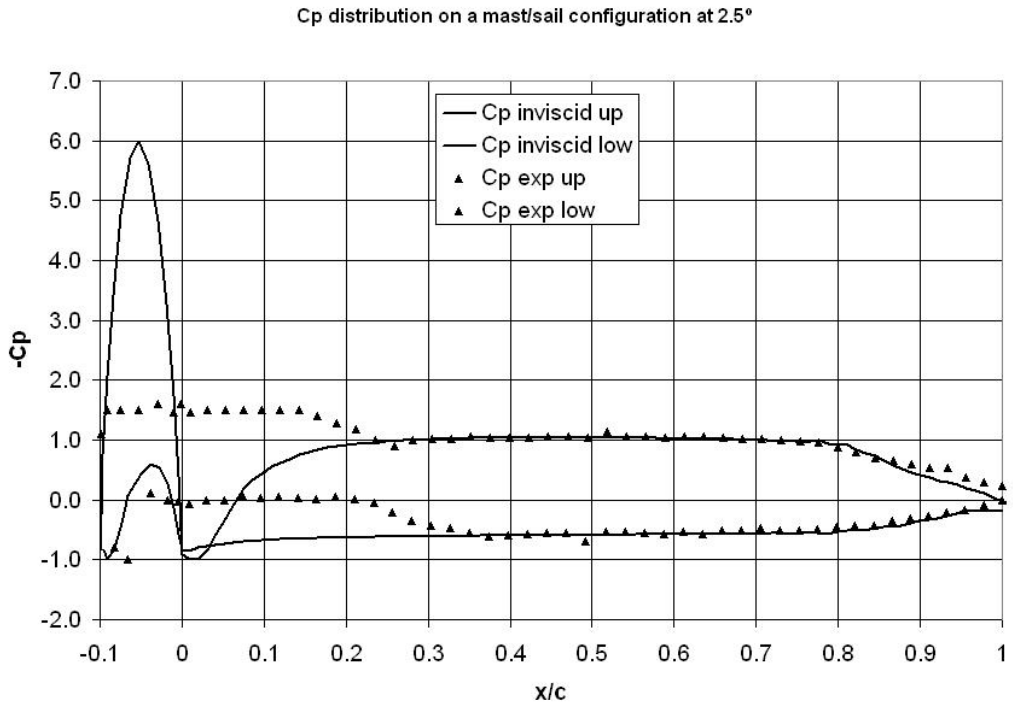

Figure 3.12: The C_P distribution on a Wilkinson test 73 configuration.

The separation is a viscous effect and it can just be detected by means of a viscous flow analysis. In the next Chapters, it will be discussed the viscous flow and methods to add viscous effects in the analysis.

3.4 Summary

In this chapter it was presented the inviscid method based on perturbation potential. According to Hess [40], panel method falls into the category of high accuracy flow analysis and then, it is extensively used in major flow analysis problems. The first section presented the basic theory and assumptions used in panel method.

Sail systems presented two challenges for panel method application. The first one is their very small thickness. In order to use a surface panel method which allows the application of a Dirichlet tangential boundary condition, sail membrane numerical model has to be "cheated" with a finite thickness. This thickness, as numerical solution is dependent on many parameters which are particular of each case, does not have a formal method to predict. So it was established a relation guidance for a minimum thickness between upper and lower surfaces of body. The guiding value is 8% and it was taken observing two-dimensional solution matrix.

The second challenge for a sail system model is the introduction of a mast at the membrane leading edge. Masts have small diameter relations compared to sail

membrane chord, creating a region with sudden changes on surface curvature. Panel methods work with the assumption of smooth and thin surfaces. The region of sudden curvature will produce inaccurate pressure distributions that are not easy to overcome with inviscid theory.

In the next Chapters, it will be discussed the effect of the introduction of a bluff body (mast) on a membrane leading edge. Its effect on real flow will create separation, which is a particular feature of viscous flows. On a real flow, a particle will not be retarded by the sudden convex curvature. It will simply continue its movement by separating from body. This will originate other complex problems like the appearance of flow vorticities and turbulence.

Then, panel method is accurate when surface curvature is smooth and small. A viscous flow analysis must be employed to study the behaviour of flow otherwise. The next chapters will present a discussion about computational methods that can cope with some viscous effects, as well their limitations.

Chapter 4

Viscous Flow and Separation

In the last Chapter it was discussed the inviscid flow and its application by means of panel method to inviscid surface flow problems, mainly sail systems. Sail systems, as discussed in the previous Chapter, have a very thin membrane which is difficult to model using surface panel methods. They also present a partially separated flow, that when panel method is used, it has a peak of negative pressure and the point at the attachment between mast and sail has zero velocity.

This Chapter discusses the viscous flow and presents some methods applied to surface modelling, based on integral boundary layer. The objective is to introduce integral boundary layer methods, showing the one parameter based integral method such as Thwaites and entrainment method and, show the lag-entrainment method and its solution by basically two non-linear equations. Later in this work, it will be discussed the coupling of an integral boundary layer to the inviscid method, producing a viscous-inviscid interaction method for viscous flow analysis.

The use of integral methods permits a series of advantages on sail flow analysis:

- Simple mesh, depending only on surface modelling;
- Laminar and turbulent flow can be analysed on the same body with this simple mesh;
- Indication of flow separation;
- Relatively simple calculation, compared to Navier-Stokes solution.

However, integral methods have a difficult solution in separated flow regions, mainly because basic considerations of boundary layer flow are not valid, such as the thin boundary layer. Then, its solution in the separated flow region is only possible by using empirical methods.

This Chapter investigates the laminar separated region on a sail and mast surface, which is critical due to the transitional flow and establishes a method to identify separation, transition and the bubble end (re-attachment point) using a laminar integral boundary layer method (Thwaites).

With the use of experimental data, empirical formulae will be discussed and a surface envelope will be created on the laminar separation bubble, in order to apply the tangential flow condition to a separated region and make sail and mast surfaces suitable for viscous-inviscid interaction analysis using surface methods.

4.1 Boundary Layer Theory

4.1.1 The General Boundary Layer Equations

Considering a two-dimensional, incompressible and laminar flow, the Navier-Stokes equations, also the basis for the boundary layer equations, are presented in equations (4.1), (4.2) and (4.3) for steady flow, according to Duncan et al [42]. Equation (4.1) is the continuity equation. The other two equations, (4.2) and (4.3), are the momentum equations for two-dimensional incompressible steady flow in Cartesian coordinates.

$$\frac{\partial u}{\partial x} + \frac{\partial v}{\partial y} = 0 \tag{4.1}$$

$$u \cdot \frac{\partial u}{\partial x} + v \cdot \frac{\partial u}{\partial y} = -\frac{1}{\rho} \cdot \frac{\partial p}{\partial x} + \nu \frac{\partial^2 u}{\partial y^2} \tag{4.2}$$

$$u \cdot \frac{\partial v}{\partial x} + v \cdot \frac{\partial v}{\partial y} = -\frac{1}{\rho} \cdot \frac{\partial p}{\partial y} + \nu \frac{\partial^2 v}{\partial x^2} \tag{4.3}$$

Alternatively, momentum equations can be rewritten in the notation used by Ferziger and Peric [33], considering $u = u(x, y)$. Thus:

$$u \cdot \nabla u = -\frac{1}{\rho} \cdot \nabla p + \nu \nabla^2 u \tag{4.4}$$

4.1.2 Navier-Stokes Solution

The solution is done by a discretization of the control volume that defines the problem. *i.e.* in the case of a sail system, the control volume would comprise mast and sail membrane surface with an additional part for wake development. The space surrounding these surfaces has also to be discretized in order to form a control volume. This control volume is subdivided into N small cells where Navier-Stokes equations are solved at the centre of each cell. This process is called as finite-volume analysis, according to Ferziger and Peric [33].

The number of cells involved on solution will depend on convergence and accuracy of calculation. According to Date [7] the number of cells for solving a three-dimensional NACA 0012 foil with $A_R = 3$, is in the order of 10^5.

For turbulent flows, in addition to the solution of the continuity and momentum equations, it is necessary a closure equation based on turbulence statistics or, semi-empirical methods, for solving the Reynolds stress part.

4.1.3 The Integral Boundary Layer Equations

Integral boundary layer is a simplification of Navier-Stokes equations applied to surface flow. It considers that flow is comprised into a thin boundary layer with thickness δ, where u_e is the velocity at the boundary layer edge. Figure 4.1 shows an illustrative scheme of the boundary layer.

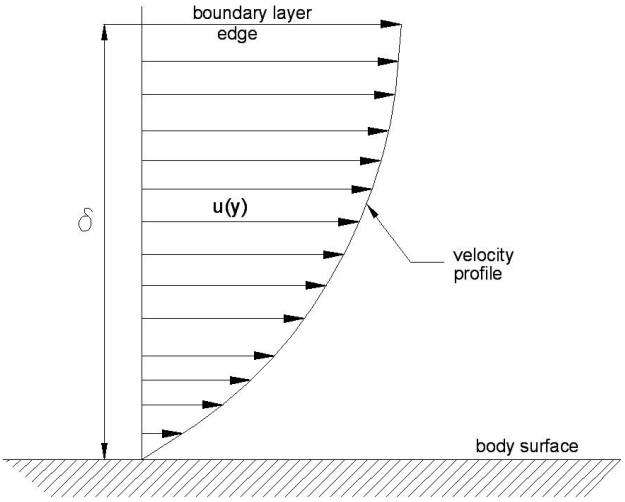

Figure 4.1: The boundary layer and velocity profile

According to Duncan et al [42], δ^* is the displacement thickness. It is a variable, shown in equation (4.5) that measures the distance from the original body that surface had to be displaced in order to have an equivalent inviscid flow.

$$\delta^* = \int_0^\delta \left(1 - \frac{u}{u_e}\right) dy \tag{4.5}$$

θ is the momentum thickness. It is the distance from original body that surface should be displaced in order to have the same momentum in an equivalent inviscid flow. It is a variable that, when multiplied by the square of edge velocity u_e, it equals the integral of momentum defect inside boundary layer or,

$$\theta u_e^2 = \int_0^\delta u(u_e - u) dy$$

as shown in equation (4.6).

$$\theta = \int_0^\delta \frac{u}{u_e}\left(1 - \frac{u}{u_e}\right) dy \tag{4.6}$$

H is the shape parameter, presented in equation (4.7) and relates δ^* to θ. In the next sections, it will be discussed its values associated to separation of flow and how it can indicate a separation of boundary layer.

$$H = \frac{\delta^*}{\theta} \tag{4.7}$$

By integrating the momentum equation (4.2), considering a small thickness δ in relation to body and low fluid viscosity, it is developed the momentum integral equation:

$$\frac{d\theta}{ds} + \frac{1}{u_e}\frac{du_e}{ds}\theta(H+2) = \frac{\tau_w}{\rho u_e^2} = \frac{C_f}{2} \tag{4.8}$$

4.1.4 Viscous Flow Conditions on Sails

The previously assumed considerations for integral boundary layer theory do not make the problem unrealistic. Some of them may be observed when a yacht is sailing: the thin boundary layer condition, for example, is most of the time true, as sails can be adjusted constantly by the crew to reach the best angle of attack with apparent wind. If flow separates from sail surface, forming a thicker boundary layer, regions of strong adverse pressure gradients and unsteady flow will be formed, making the sail membrane to collapse and produce no lifting force.

4.1.5 Integral One Parameter Boundary Layer Method

The boundary layer solution methods, according to Duncan et al [42], concentrate in the solution of the momentum equation (4.8). According to Duncan et al [42] most steady integral boundary layer methods simplify the solution to a one-parameter problem.

Young's method [42] is one of them and it was the first to introduce the parameters l and m, from equations (4.9) and (4.10) to calculate the boundary layer.

$$l = \frac{\theta}{u_e} \cdot \left(\frac{\partial u}{\partial y}\right)_w \tag{4.9}$$

$$m = \frac{\theta^2}{u_e} \cdot \left(\frac{\partial^2 u}{\partial y^2}\right)_w \tag{4.10}$$

Young's method [42] considers that velocity profile is given by a polynomial dependent of a variable λ. This λ is function of m and, it develops empirical relations with other boundary layer variables in order to solve the momentum equation for laminar flow.

4.1.5.1 Thwaites Method

The Thwaites method, developed from the Young's method [42], is similar to its predecessor with slightly differences in the empirical formulae used. It is regarded, according to Duncan et al [42] as accurate for predicting flow separation. Because of its application as a major method for identifying transition and separation points, as discussed by Drela [62] and Gad-el-Hak [1], this method is revised here.

In Thwaites method, parameter l, from equation (4.9), is directly related to the skin friction, whilst m, from equation (4.10) is related to the external pressure gradient. The subscript w in equations (4.9) and (4.10) means near wall values.

The momentum equation (4.8) can be rewritten as equation (4.11), where $\lambda(m)$ is the right hand part.

$$u_e \cdot \frac{\partial(\theta^2)}{\partial s} = 2\nu \cdot [m \cdot (H+2) + l] = \nu \cdot \lambda(m) \tag{4.11}$$

$$\lambda(m) = 2 \cdot [m \cdot (H+2) + l]$$

Using experiments and calculations, it was found that λ has a empirical relationship given by equation (4.12)

$$\lambda(m) = 0.45 + 6 \cdot m \tag{4.12}$$

Equation (4.11) can be written as

$$u_e \cdot \frac{\partial(\theta^2)}{\partial s} - 0.45\nu + 6\frac{\partial u_e}{\partial s} \cdot \theta^2 = 0$$

with some algebraic manipulation followed by integration,

$$\left[\theta^2\right]_{s_1} = \frac{0.45\nu}{(u_e^6)_{s_1}} \cdot \int_0^{s_1} u_e^5 ds$$

If a previous velocity distribution on body surface is known, the Thwaites method is applied to evaluate boundary layer parameters for the next node downstream. The order of accuracy of the method varies with the order of the integration method used, as discussed on Cebeci and Bradshaw [63] so, it is dependant on last nodes boundary layer parameters. The first node needs an initial solution to begin the process so, Hiemenz solution is applied.

4.1.6 The Hiemenz Solution

The Hiemenz solution, according to Cebeci and Bradshaw [63], is an initial solution used near the stagnation point. It is derived from the Navier-Stokes equations for laminar flow and it basically considers that, at large but finite Reynolds numbers, the boundary layer variables (H, θ and δ^*) near the stagnation point are constant and have finite values.

The Hiemenz solution considers a cylinder with radius R submerged in a steady flow. The attachment length ξ is the length that flow is considered to be normal to cylinder section, according to Cebeci and Bradshaw [63]. According to Cebeci and Bradshaw [63], for a bluff body, it is recommended that ξ have large values (mast diameter, for example), while, for sharp nosed bodies (flat plate, for example), boundary layer at the stagnation point is zero, according to Cebeci and Bradshaw [63].

Equations (4.13) and (4.14) shows the exact formulas derived by Hiemenz [64].

In later works, Drela and colleagues [35], [46] and [45] used $C_\theta = 0.38574$, $C_{\delta^*} = 0.90649$ and $H = 2.35$ for a better correlation to experimental results. It is applied at the first node of the boundary layer solution, where θ_1 and δ_1^* are respectively the initial momentum and displacement thicknesses. The velocity u_ξ is approximated as the velocity calculated for the first positive tangential velocity near leading edge, as discussed by Milewsky [48].

$$\theta_1 = C_\theta \cdot \sqrt{\frac{\xi}{Re_\infty \cdot u_\xi}} \tag{4.13}$$

$$\delta_1^* = C_{\delta^*} \cdot \sqrt{\frac{\xi}{Re_\infty \cdot u_\xi}} \tag{4.14}$$

As foil sections or two-dimensional bodies are inclined by an arbitrary angle, sometimes it is difficult to evaluate the attachment length. In these cases, the attachment length was considered to be the distance from the stagnation point to the next node downstream. This consideration can be bypassed by inputting an arbitrary length.

4.2 Turbulent and Transitional Integral Boundary Layer Methods

4.2.1 Reynolds Averaged Navier-Stokes Equations

When flow is turbulent, there is still a component of flow in the streamwise direction but, there is also a chaotic movement of particles of flow. According to Ferziger and Peric [33], the flow velocity has two parts: a mean velocity in streamwise flow that is steady and a fluctuation part that is time dependant. So equation (4.15) substitutes u in the momentum equation (4.2) and equation (4.16) substitutes v in momentum equation (4.3). According to Ferziger and Peric [33], on streamlined bodies with thin boundary layers, the fluctuation (u' and v') parts are very small.

$$u(x,t) = \overline{u}(x) + u'(x,t) \tag{4.15}$$

$$v(y,t) = \overline{v}(y) + v'(y,t) \tag{4.16}$$

All equations (4.1), (4.2) and (4.3) can be rewritten for these new functions u and v, becoming, using Ferziger and Peric [33] notation:

$$\nabla \cdot u = 0$$

$$u \cdot \nabla u = -\frac{1}{\rho} \cdot \nabla p + \nu \nabla^2 u + \frac{1}{\rho} \nabla \cdot t \tag{4.17}$$

When derived from the original momentum equations, the averaged momentum

equation (4.17) has one more part with a new variable $t = -\rho\overline{u'u'}$, called as the Reynolds stress tensor. The mean value $\overline{u'u'}$ is understood as $\overline{q^2}$ in Green et al [44] notation.

According to Ferziger and Peric [33], t represents the mean rate of momentum transfer through the control volume boundaries due to turbulence. This term is unknown and is a function of formulas based on statistics for turbulence or, the so called "closure" equations, according to Ferziger and Peric [33].

4.2.2 The Entrainment Method

Head and Patel [63] created a method to correct the integral boundary layer for Reynolds stress tensor influence. It was called as the entrainment method. This method, used for incompressible flow, considers an entrainment coefficient C_E that relates the velocity v_e, which is the velocity that the outer flow penetrates in the turbulent boundary layer, with the edge velocity u_e. C_E is given by equation (4.18).

$$C_E = \frac{1}{\rho_e u_e} \cdot \frac{\partial}{\partial s} \int_0^\delta (\rho u) dy \tag{4.18}$$

The original entrainment equation is given by (4.19)

$$\theta \frac{dH}{ds} = \frac{dH}{dH_1} \left(C_E - H_1 \frac{1}{u_e} \frac{d}{ds} (u_e \theta) \right) \tag{4.19}$$

where H_1 is defined by equation (4.20)

$$H_1 = \frac{\delta - \delta^*}{\theta} \tag{4.20}$$

If a turbulent boundary layer is in equilibrium *i.e.* if the shape of the mean velocity profile is invariant on the streamwise direction, C_E will be function of only constant parameters that have empirical relations. For Head's method [63], C_E is given by equation (4.21), where v_e is the entrainment velocity.

$$C_E = \frac{v_e}{u_e} = \frac{1}{u_e} \cdot \frac{\partial}{\partial s} \left[u_e \cdot (\delta - \delta^*) \right] = F(H_1) \tag{4.21}$$

$F(H_1)$ has its empirical relation given by equation (4.22)

$$F(H_1) = 0.036 \cdot (H_1 - 3.0)^{-0.6169} \tag{4.22}$$

The calculation method, according to Cebeci and Bradshaw [63], uses an initial solution placed at an initial point, where it is believed turbulent flow starts. It calculates boundary layer variables for the next node. The initial solution uses a laminar flow value for H where a function G which is the velocity defect shape parameter is used

to relate H to H_1 in two cases: the first if $H < 1.6$

$$G = \frac{H-1}{H}\sqrt{\frac{2}{C_f}} = 1.5501\,(H - 0.6778)^{-3.064}$$

or, if $H > 1.6$

$$G = 0.8234\,(H - 1.1)^{-1.287}$$

The initial turbulent solution is given by: if $H < 1.6$

$$H_1 = 1.5501\,(H - 0.6778)^{-3.064} + 3.3$$

or, if $H > 1.6$

$$H_1 = 0.8234\,(H - 1.1)^{-1.287} + 3.3$$

The procedure marches on by calculating a the entrainment velocity v_e, here adapted for a linear solution, as suggested by Cebeci and Bradshaw [63]:

$$[v_e]_{in} = H_1 u_e \theta$$

where subscript in means initial turbulent value. Then for the next node downstream v_e is calculated:

$$v_e = [v_e]_{in} + F(H_1) u_e \Delta s$$

A similar procedure, adapted for a linear solution, is used for θ calculation, using the initial node i to predict θ_{i+1} using the momentum equation:

$$\frac{d\theta}{ds} = \frac{C_f}{2} - (H+2)\,\frac{\theta}{u_e}\frac{du_e}{dx}$$

and

$$\theta_{i+1} = \theta_i + \frac{d\theta}{ds}\Delta s$$

H_1 initial value is calculated for the next node:

$$[H_1]_{i+1} = \frac{v_e}{\theta_{i+1} u_e}$$

if $H_1 < 5.3$ then the inverse of function G is used again for calculate H for the next node:

$$H_{i+1} = 0.6778 + \left(\frac{[H_1]_{i+1} - 3.3}{1.5501}\right)^{-0.326}$$

or, if $H_1 > 5.3$

$$H_{i+1} = 1.1 + \left(\frac{[H_1]_{i+1} - 3.3}{0.8234}\right)^{-0.777}$$

C_f uses a formula, given on Cebeci and Bradshaw [63]:

$$C_f = 0.246 \cdot 10^{-0.678H} \cdot Re_\theta^{-0.268}$$

4.2.3 The Lag-entrainment Method

The lag-entrainment method, discussed by Green and co-authors [44], is considered an improvement of the entrainment method. It is composed by a system of three equations: the momentum equation, the original entrainment equation (4.19) and a "lag" equation, as called by Green and co-authors [44], that has its embryo in the kinetic energy equation (4.23), derived from the Reynolds averaged Navier-Stokes equations for two-dimensional flow,

$$\frac{1}{2}\rho\left(\overline{u}\frac{\partial\overline{q^2}}{\partial x} + \overline{v}\frac{\partial\overline{q^2}}{\partial y}\right) - \tau\frac{\partial\overline{u}}{\partial y} + \frac{\partial}{\partial y}\left(\overline{pv} + \frac{1}{2}\rho\overline{q^2}\overline{v}\right) + \rho\varepsilon = 0 \tag{4.23}$$

where $\overline{q^2}$, according to Green et al [44], is denominated as the mean fluctuating velocity and ε is the dissipation coefficient.

Equation (4.23), from left to right hand sides, is understood by authors [44] as separate terms responsible for advection, production, diffusion and dissipation of kinetic energy respectively. In the development of this equation, authors [44] used empirical formulas and made the assumption that flow was on equilibrium *i.e.* shape of velocity and shear-stress profile in the boundary layer did not vary with x so, equation (4.23) could be rewritten as:

$$\frac{\delta}{C_\tau}\frac{dC_\tau}{dx} = 2a_1\frac{u_e\delta C_{\tau eq}^{1/2}}{u} - 2a_1\frac{u_e\delta C_\tau^{1/2}}{u} + \left(\frac{2\delta}{u_e}\frac{du_e}{dx}\right)_{eq} - \frac{2\delta}{u_e}\frac{du_e}{dx} \tag{4.24}$$

Again, equation (4.24) on equilibrium can be read from left to right hand sides in separate terms for advection, production, diffusion and dissipation. C_τ and $C_{\tau eq}$ are respectively mean shear stress and mean equilibrium shear stress coefficients on wall. They will form the lag equation discussed later.

Hence, equation (4.24) has its terms approximated by parameters with known empirical relations.

Most of this theory was revised by Drela et al [35], [46] considering its application on airplane foils with compressible flow, subsonic and transonic velocities. Thus, equations are presented here on their general formulation for compressible flow.

The general equation (4.27) for integral boundary layer was derived combining the momentum equation (4.25) with the kinetic dissipation equation (4.26), derived from the entrainment equation (4.19), where C_{diss} is the dissipation coefficient.

$$\frac{d\theta}{ds} + \frac{1}{u_e}\frac{du_e}{ds}\theta(H + 2 - M^2) = \frac{C_f}{2} \tag{4.25}$$

$$\frac{d\theta^*}{ds} + \left(\frac{\delta^{**}}{\theta^*} + 3 - M^2\right)\frac{\theta}{u_e}\frac{du_e}{ds} = 2C_{diss} \tag{4.26}$$

$$\frac{1}{H^*}\cdot\frac{dH^*}{ds} + \left[2H^{**} + (1-H)\right]\frac{1}{u_e}\frac{du_e}{ds} = \frac{2C_{diss}}{H^*\cdot\theta} - \frac{C_f}{2\theta} \tag{4.27}$$

δ^{**} is the density thickness and it is defined on equation (4.28). For an incompressible flow, δ^{**} is zero as the density of fluid is invariant. θ^*, defined on equation (4.29), is the kinetic energy thickness. H^* is the kinetic energy shape parameter and $H^* = \theta^*/\theta$. It has an empirical relation, detailed in Appendix C, with M, Re_θ and the parameter H_k.

H^{**} is the density shape parameter, $H^{**} = \delta^{**}/\theta^*$ and it is has a empirical function with parameters H_k and M. For incompressible flow, where M is very small, H^{**} is zero.

$$\delta^{**} = \int_0^\delta \left(\frac{u}{u_e}\right)\cdot\left[1 - \frac{\rho}{\rho_e}\right]dy \tag{4.28}$$

$$\theta^* = \int_0^\delta \frac{\rho u}{\rho_e u_e}\left[1 - \left(\frac{u}{u_e}\right)^2\right]dy \tag{4.29}$$

H_k is the kinematic shape parameter. It relates δ^{**} with θ^*. H_k has an empirical relation between H and M, given by equation (4.30), from references [44] and [35]. For low velocity condition, as M is considered zero, $H_k = H$.

$$H_k = \frac{H - 0.290M^2}{1 + 0.113M^2} \tag{4.30}$$

Coefficients C_f and C_{diss} are also given as functions of H_k by empirical relations [35]. C_{diss} dissipation coefficient is derived from shear work integral equation (4.31)

$$C_{diss} = \int_0^\delta \left(\frac{\tau}{\rho_e u_e^3}\cdot\frac{\partial u}{\partial y}\right)\cdot dy \tag{4.31}$$

where

$$C_\tau = \frac{\tau_w}{0.5\cdot\rho\cdot U_\infty^2\cdot A} = C_f \tag{4.32}$$

τ_w is the wall shear stress and it is only computed when flow is attached to body surface.

4.2.3.1 The Turbulent Closure Equation

The closure equation for turbulent boundary layer, also named by Green et al [44] as the "lag" equation is given by (4.33). This equation (4.33) is derived from the

equilibrium kinetic energy equation (4.24).

$$\frac{\delta}{C_\tau} \cdot \frac{dC_\tau}{ds} = 4.2 \cdot (C_{\tau_{eq}}^{1/2} - C_\tau^{1/2}) \tag{4.33}$$

4.2.4 The Transitional Flow

Integral boundary layer methods such as Thwaites and entrainment methods when used together in one surface, provide a steep transition between laminar to turbulent flows. As an example, considering a transitional flow fully attached to body surface, in the laminar regime, H ranges between 2.35 to 3 using a Thwaites method. Turbulent flow has H increasing smoothly from 1.9 to 3 using the entrainment method.

According to Drela and Giles [35], the transition from laminar to turbulent flow has to be smooth. Steep boundary layer variables distributions only happens in separated flows. Hence, another calculation method was introduced by Drela and Giles [35] to the lag-entrainment method, in order to make a smooth transition. The main theory is based in Tollmein-Schlichting waves formed in a transitional flow on a flat plate, with the use of some wind tunnel testing data.

4.2.4.1 Tollmein-Schilichting Waves

Figure 4.2 illustrates the development of flow on a flat plate. After a critical Reynolds number, flow starts to be unstable and some waves form in the transverse direction across the surface of a plate.

As discussed by Neto [65], because of the initial low momentum, laminar flows are unstable and, the oscillation of Tollmein-Schilichting waves also becomes progressively unstable. After some point, according to observations made by Neto [65], waves disintegrate and form small high energy turbulent spots with a wake, in the format of a hairclip, as shown schematicaly in Figure 4.2. According to Neto [65], instabilities keep on growing transforming progressively into a fully turbulent flow.

The complete understanding of the transition is still very difficult and, according to Foussekis and co-authors [37], numerical methods available do not yet incorporate all main factors involved in transition.

The theory applied by Drela and Giles [35] considers that transition occurs when the most unstable wave in the boundary layer has grown by some factor, usually taken to be $e^9 = 8100$, mostly known as the e^9 method. Drela and Giles [35] introduced in the lag-entrainment equations an empirical formula relating the critical amplification of the Tollmein-Schilichting wave, here represented as $\tilde{n}$.

Hence, the boundary layer lag entrainment method has three simultaneous equations to be solved: (4.25), (4.26) and (4.33). For laminar flow and transition, the equation (4.34) given on [35] substitutes the equation (4.33). $m(H_k)$ and $\ell(H_k)$ are

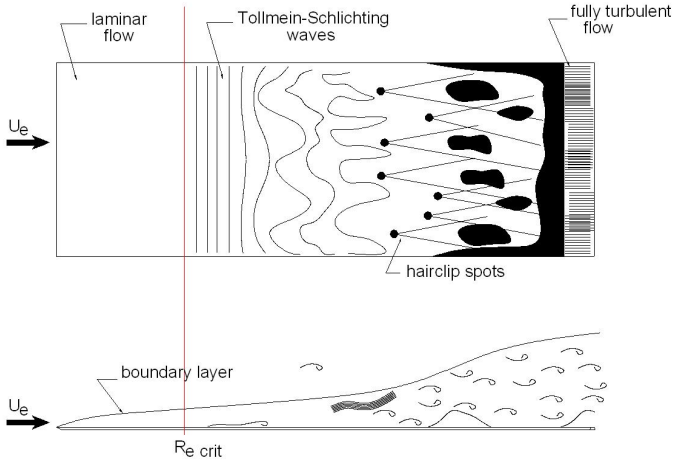

Figure 4.2: Development of flow on a flat plate

two parameters dependent on H_k. Their formulae are given in Appendix C.

$$\frac{\partial \tilde{n}}{\partial s}(H_k, \theta) = \frac{\partial \tilde{n}}{\partial Re_\theta}(H_k) \cdot \frac{m(H_k)+1}{2} \cdot \frac{\ell(H_k)}{\theta} \tag{4.34}$$

4.2.4.2 The Critical Amplification Ratio

In the XFOIL code documentation [62], distributed as part of the GNU project by the Massachusetts Institute of Technology (MIT), there is an empirical table of values for critical amplification ratio. According to this documentation, for each flow situation there is a critical amplification, as shown in Table 4.1 that, after the point where $\tilde{n} = \tilde{n}_{crit}$, turbulent flow starts.

Situation type	**min.** $\tilde{n}_{crit}$	**max.** $\tilde{n}_{crit}$
Sailplane	12	14
Motorglider	11	13
Clean wind tunnel	10	12
Average wind tunnel	$<= 9$	e^9 method
Dirty wind tunnel	4	8

Table 4.1: Typical critical amplifications for different situations

In Table 4.1, a sailplane, for example, is one of the "cleannest" vehicles. It works at considerably high altitudes and there is no engines to disturb flow. Then, transition is delayed and it is necessary higher critical amplifications for turbulence to occur.

A wind tunnel has its walls with some roughness and much of the transition will depend on how smooth they are and the interference of support apparatus for the experiment.

A sail system for a yacht has many interferences from diverse sources:

- Sea waves;

- Atmospheric boundary layer;
- Hull, deck and other sails;
- Mast, boom, shrouds, stays and cables;
- Interference from crew.

Hence, all those items make flow "dirty". In table 4.1, the dirty wind tunnel refers to a wind tunnel experiment that has many sources of interference in the flow and the $\tilde{n}_{crit}$ adopted for sail systems should have a similar range for dirty wind tunnel, meaning an earlier transition point.

So the lag-entrainment method can provide a smooth transition from laminar to turbulent flow. The main change in the boundary layer integral theory is that a three equation system has to be solved now, instead of a one equation method, as in Thwaites and entrainment methods.

4.2.5 Drag Force Coefficient

Drag force has three basic components: induced drag, which is originated by the finite wing span on three-dimensional foils; frictional drag and viscous pressure drag, this last one is related to separation and it is more difficult to evaluate numerically.

On three-dimensional streamlined bodies, frictional drag is normally smaller, compared to induced drag. In two-dimensional flow, induced drag is zero then, frictional drag plays a main whole in total drag.

Drag forces, as for lifting forces, are represented as non-dimensional coefficients and are given by equation (4.35) for two-dimensional flow, where L is the length of surface and ρ_s is surface density of fluid. In three-dimensional flows, L is substituted by area A, as in equation (4.36) and ρ is the volumetric density of fluid.

$$C_D = \frac{f_D}{0.5\rho_s \cdot U_\infty^2 \cdot L} \tag{4.35}$$

$$C_D = \frac{f_D}{0.5\rho \cdot U_\infty^2 \cdot A} \tag{4.36}$$

4.2.5.1 Frictional Drag

According to Drela and Youngreen [62], the frictional drag can be calculated by two methods as follows:

- The Squire-Young formula, presented on XFOIL documentation [62] for two-dimensional flow analysis. It is given by equation (4.37), where θ, u_e and H are taken at wake last point. The Squire-Young formula extrapolates the momentum thickness to downstream infinity. Its drag calculation near the trailing edge is

always questionable, as discussed by Drela [62], because of presence of separation but, it can be reasonable in a distance far from the airfoil;

$$C_{Df} = 2 \cdot \theta \cdot u_e^{0.5 \cdot (H+5)} \tag{4.37}$$

- Direct integration of wall shear stress, given on equation (4.38); it is preferred for three-dimensional flows as it gives a more accurate result. For turbulent flows, C_f uses the identity on equation (4.32) instead of using directly C_f from momentum equation (4.8). In laminar and transitional flows C_f is taken directly from the momentum equation (4.8).

$$C_{Df} = \int_S C_f \cdot ds \tag{4.38}$$

In separated regions, wall shear stress is considered to be zero as there is no surface for friction to act.

4.2.5.2 Viscous Induced Drag

The inviscid induced drag, discussed in Chapter 3 is particular for finite span foils. However, its computation is related to the inviscid flow which, according to Hufford et al [45] and Katz and Plotkin [34], has a slightly higher pressure distribution.

The viscous induced drag $C_{D_{i(v)}}$ is a correction of inviscid induced drag for viscous flow. It is presented in equation (4.39) and it was developed by Milewsky [48]. C_{Lv} and C_{Li} are viscous and inviscid lift coefficients respectively and $C_{Di(i)}$ is the inviscid induced drag.

$$C_{Di(v)} = C_{Lv}^2 \cdot \frac{C_{Di(i)}}{C_{Li}^2} \tag{4.39}$$

4.3 Aspects of Flow Separation

Separation happens when flow streamline detaches from body surface. The intensity of the detachment can promote strong changes in pressure distribution, as in a severe separation or, it can cause only a slightly decrease in pressure distribution on body surface when separation is weak.

Usually, the separation on foil occurs because of adverse pressure gradients or a sharp edge. This situation is present mainly on high lifting bodies.

On sail systems, according to Wilkinson [4], there are two main regions of flow separation. One at the leading edge, behind the mast and, another one near trailing edge. The trailing edge separation is normally a turbulent separation and happens mainly because of sail surface curvature and the pressure jump between upper and lower surfaces at this region. The leading edge separation here is a case for study due to the implications in transitional flow and, because of the mast surface, it has a severe separation behaviour.

4.3.1 The Separation and Transition

Observing the experiments made by Wilkinson [4] and the work of Gad-el-Hak [1], in the Re_∞ range of 10^4 to 10^6. If a laminar separation occurs, there will be a transition to turbulence due to the instability of laminar boundary layer. This transition will force flow to have a higher momentum downstream and flow will re-attach, forming a separation bubble.

According to Gad-el-Hak [1], the length of separation bubble modifies the pressure distribution. At high Re_∞ the bubble is short, with an earlier transition and C_P viscous distribution has little difference to the viscous distribution. At lower Re_∞, the bubble is longer, with a later transition and the C_P viscous distribution has significative difference to the inviscid flow. For an even lower range of Re_∞ transition may not occur and flow will not re-attach. This last range is not discussed here as transition is considered to occur somewhere on body surface and laminar separation bubble length is considered small, compared to the body length.

A rough rule presented by Gad-el-Hak [1] is based in chord Reynolds number. A foil with chord Reynolds number less than $5 \cdot 10^4$ will experience laminar separation with no subsequent re-attachment. For chord Re slightly higher than $5 \cdot 10^4$ there will be a long bubble. Increasing Re from $5 \cdot 10^4$ bubble becomes shorter.

4.3.2 Severity of Separation

Gad-el-Hak [1] classifies separation in two types: the severe and weak separation. According to Figure 4.3, the weak separation has its pressure distribution closer to the inviscid one but, with slightly smaller values and a continuous distribution. When separation is severe, pressure distribution is discontinuous, presenting a region with constant pressure after separation, as illustrated in Figure 4.3.

The weak separation, Gad-el-Hak [1] called it as "short" separation bubble and a severe separation it was named as "long" separation bubble, due to their physical identities with the different bubble lengths from the rough rule discussed before.

4.3.3 Flow Separation Using the Integral Approach

For a flow about separation, the left hand side of equation (4.2) at the wall must be zero, then:

$$\left[\frac{1}{\rho} \cdot \frac{\partial p}{\partial x}\right]_w = \left[\nu \frac{\partial^2 u}{\partial y^2}\right]_w$$

where the subscript w denotes values near wall.

$[\partial^2 u/\partial y^2]_w > 0$ is a necessary condition for a steady two-dimensional boundary layer to separate and the contrary is also a necessary condition for flow to stay attached, as discussed by Gad-el-Hak and Bushnell [49]. Then $[\partial^2 u/\partial y^2]_w$ should be kept as negative as possible to avoid separation.

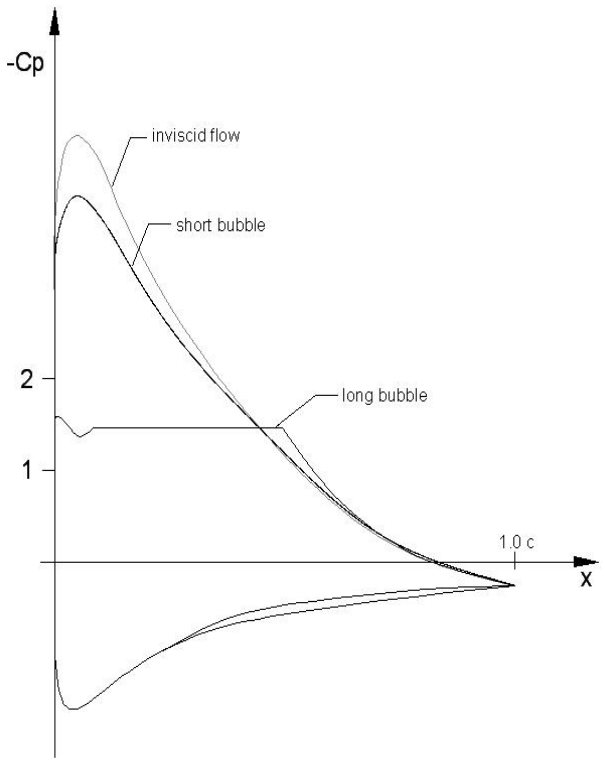

Figure 4.3: Illustration of a short and long separation bubbles with inviscid flow -Cp distributions

The observation of $[\partial u/\partial y]_w$, as reported by Gad-el-Hak and Bushnell [49] can tell if flow is about to separate or not. If $[\partial u/\partial y]_w = 0$, it means that separation is about to start.

Analysing terms l and m from Thwaites method, in equations (4.9) and (4.10), the first one (l) is the slope of boundary layer profile near the wall. l must be zero at the separation point. The second term (m) is basically the pressure gradient and it is related to the curvature of velocity profile. Using the same correlation of equation (4.11) and comparing with the integral equation (4.8), the following can be concluded:

$$\frac{\theta^2}{u_e} \cdot \left[\frac{\partial^2 u}{\partial y^2}\right]_w \equiv \frac{1}{u_e}\frac{\partial u_e}{\partial s}\theta$$

and

$$\left[\frac{\partial^2 u}{\partial y^2}\right]_w = \frac{1}{\theta} \cdot \frac{\partial u_e}{\partial s} \tag{4.40}$$

also, using the empirical equation (4.12) l value is obtained by equation (4.41).

$$l = 0.225 - m \cdot (H - 1) \tag{4.41}$$

Then, observing equation (4.41), flow will separate when $m \cdot (H - 1)$ approaches 0.225 using Thwaites method.

4.3.3.1 H Shape Parameter Investigation

H, according to Gad-el-Hak [1] is an important parameter to identify laminar flow separation. Drela [35] and Gad-el-Hak [1] presented different limits of H where separation is considered to occur based in wind tunnel experiments. In Drela's [35] work, separation was considered to occur when $H = 2.5$, while in Gad-el-Hak [1] it was considered $H = 3.7$.

Here the H laminar distribution downstream the separation point is considered to be valid for engineering purposes, although it must be clear that H laminar distribution cannot be used to compare with real flow boundary layer in separated flow regions.

Using a Thwaites method in a laminar separated region, as discussed by Duncan et al [42], H increases from 2.5 to values near 10 asymptotically, decreasing sharply to values near 2. When H decreases to a value near 2, although it is in a separated flow region, it approaches the initial turbulent boundary layer values, according to Cebeci and Bradshaw [63].

If the point on surface where $H \approx 2$ after the peak region is close to the place on surface where transition is detected in experimental data then, the H distribution can be used as an estimate for the transition point in partially separated flows.

4.3.3.2 The Criteria to Identify Transition after Laminar Separation

Existent methods used to identify transition, such as the criteria of Cebeci and Smith [63] and Wazzan et al [66] do not consider separated flow. The objective of the investigation of H after the separation point is the creation of an estimate for transition in partially separated flows.

A first step of H shape parameter investigation is the observation of its behaviour using an initially attached inviscid flow on a body that presents a separated flow in real conditions. The circular cylinder flow is a classical case of a bluff body separated flow. An inviscid attached flow will be used to illustrate H shape parameter development on this circular cylinder.

A two-dimensional potential flow is used to calculate the initial velocity distribution. A Thwaites method will be applied to this potential flow, considering $Re_\infty \geq 5 \cdot 10^4$. Inviscid velocity u/U_∞ is obtained by equation (4.42). Transforming s/R into degrees, Figure 4.4 shows the inviscid pressure distribution on the cylinder surface.

$$\frac{u}{U_\infty} = 2 \cdot \sin\left(\frac{s}{R}\right) \tag{4.42}$$

For boundary layer calculation, it was considered that, *a priori,* all cylinder flow was laminar and attached to body. The initial H is calculated using the Hiemenz solution $H = 2.35$.

In Figure 4.5, H was set to zero in the last 25% of circle length, near trailing edge region, in order to avoid numerical problems with very small inviscid velocities. It does not interfere in calculations as, according to Parkinson and Jandali [67], real flow

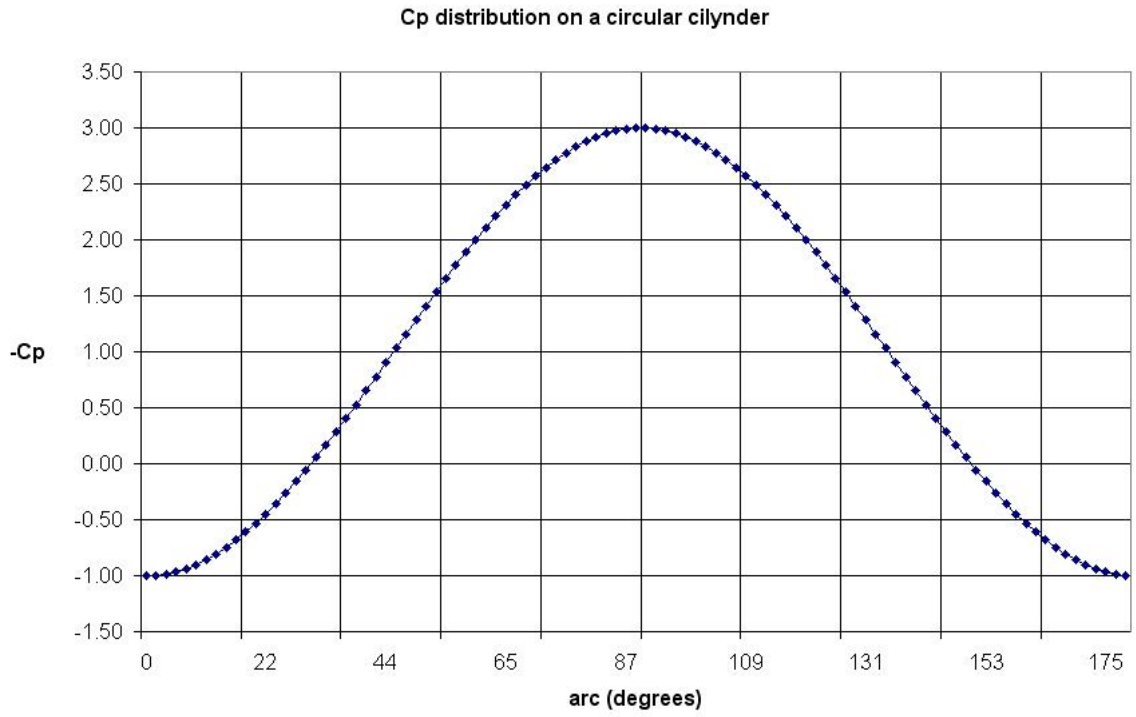

Figure 4.4: Inviscid Cp distribution on a circular cylinder

in this part of the circle would be completely separated and integral methods are not valid.

Observing figures 4.4 and 4.5, while $-C_P$ is growing, H hardly changes. When $-C_P$ starts to decrease, H starts the asymptotical growth.

If $H = 2.5$ is the value where separation occurs, according to Drela [62], then Table 4.2 shows the separation points for different Re_∞.

Re_∞ $(\times 10^5)$	**Separation angle**
0.50	90.9^o
5.00	87.3^o
10.0	83.6^o
15.0	78.2^o

Table 4.2: Separation points on an infinite cylinder section varying Re

Further downstream, H will make a sharp peak with high values approaching 10 and decreasing to values near 2, as predicted. By increasing Re_∞, it can be noticed in Figure 4.5 that the sharp peaks appear more downstream, leading to the previous conclusion that it has a different trend than the rough rule for separation, discussed before, where transition would be expected to occur nearer the separation point.

However, the circle, as discussed by Parkinson and Jandali [67], is a case of a bluff body separation where flow will continue separated. As the method for transition detection has to be applied to regions where flow will reattach to surface at some length, according to Wilkinson [4], sail and mast configurations should be used as examples of

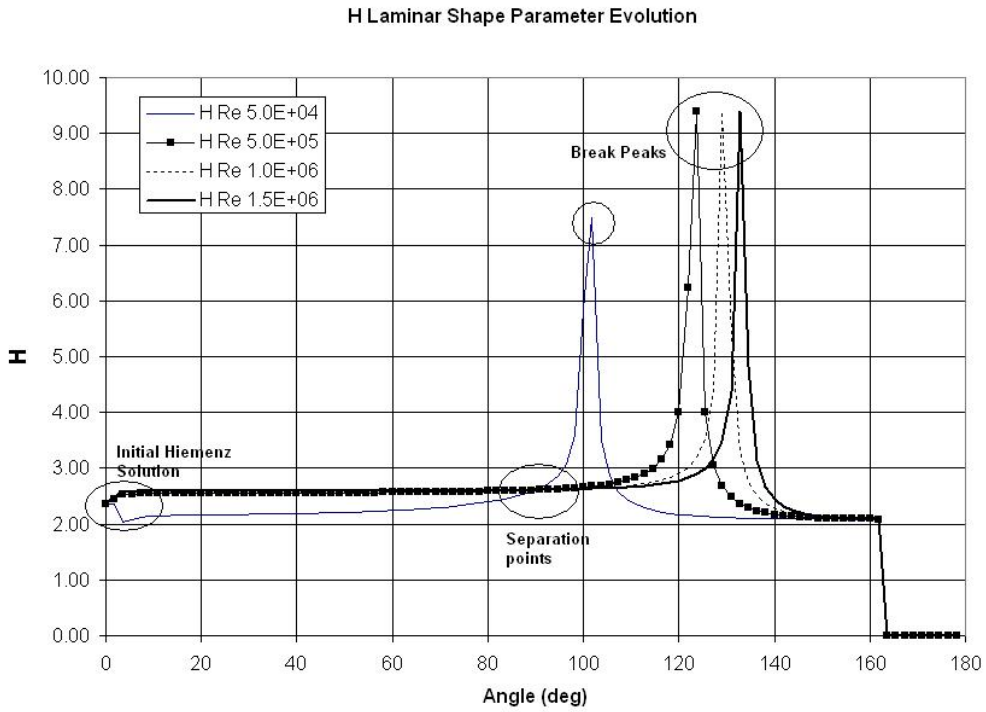

Figure 4.5: H variation with Re_∞ on a circular cylinder

partially separated flow instead.

4.3.4 Numerical Identification of Separation and Reattachment on Sail and Mast Configurations

Sail and mast configurations are consisted of a bluff body (mast) at the leading edge, attached to a membrane. The mast and membrane attachment will produce a singular point with zero inviscid velocity, as it was observed in Chapter 3. In this case, if Thwaites method is applied to this inviscid velocity distribution, the H distribution will also have a singular point.

After the singular point, H laminar distribution decreases sharply to turbulent values again. If the point where H decreases to turbulent values coincides with the experimental data, then it can be created a criteria for transition point location.

Figure 4.6 shows the C_P and H distributions on the upper surface for a sail and mast configuration. The cylindrical mast has a relative diameter of 16.5% c and it is attached to a membrane in a format of a circular arc with 12.5% c of camber. The angle of incidence is 7.5^o.

Flow was set for $Re_\infty = 3.0 \cdot 10^5$ and transition was forced to occur initially at 75% of total length (mast and chord) so, laminar flow development could be better observed.

The initial velocity distribution was calculated by a two-dimensional piecewise con-

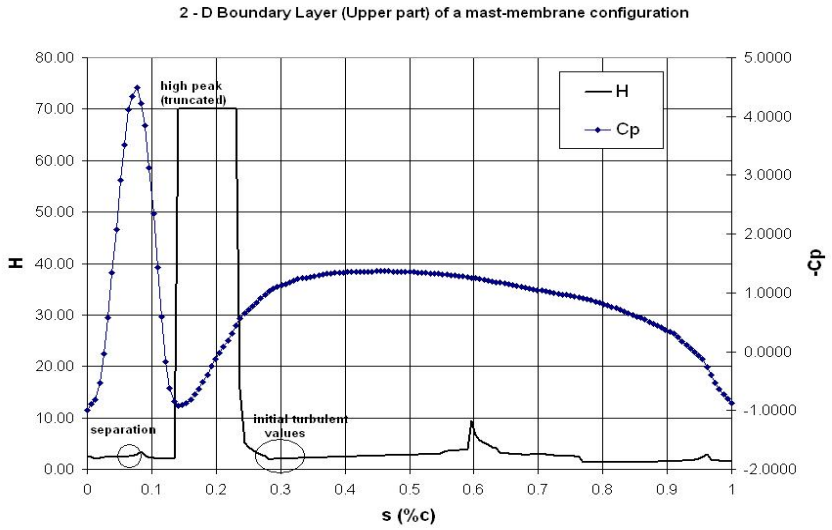

Figure 4.6: H and Cp distribution for a Wilkinson sail/mast configuration at 7.5^o and $Re = 1.0 \cdot 10^6$

stant potential surface panel method with 300 points.

According to Figure 4.6, there is an initial smooth increase of H on mast surface (laminar flow), where H reaches for the first time 2.5 and separation occurs. It is followed by a first sharp peak with $H = 4.0$ and a second peak at the attachment point, here truncated to 70, in order to scale the graphic, but with original values in the order of 10^9 due to the singular point created by the sail and mast attachment. After the singular peak, as shown in Figure 4.6, there is a recovery of H but with typical turbulent values ($1.94 \leq H \leq 2.0$).

The region where H recovers to typical turbulent values coincides with the region where slope of inviscid velocity ($du_{(i)}/ds$) smooths down and presents values approaching the membrane inviscid attached flow.

Some configurations of mast and sail used by Wilkinson [4] were also tested, leading to the first overall conclusions:

- Separation can be identified by potential flow at the maximum of velocity distribution, which is localized on the mast surface;
- On the sail membrane surface, the inviscid velocity distribution in some extent after separation, produces a region of recovering of suction pressure. In this same region, marked with a circle, observing the curve for H in Figure 4.6, it assumes initial turbulent values. The same behaviour was observed for θ and δ^*.

4.3.4.1 Numerical Transition Point Behaviour

If configurations of test numbers 4, 14, 28, 45, 49 and 67 of Wilkinson's experiments [4] are analysed here and there is the assumption of transition occurring after the mast

and sail attachment, at the point where initial H turbulent values (1.94) are obtained, Table 4.3 shows the calculated points compared to the experimental results found by Wilkinson [4]. Subscripts t stands for transition and r for re-attachment in Table 4.3.

Variables					**Experimental**		**Calculated**
test n^o	$Re_\infty \times 10^5$	α (deg)	diam. (%c)	mast angle (deg)	x_t/c	x_r/c	x_t/c
4	3.5	5.0	17.5	15	0.21	0.36	0.153
14	6.0	2.5	16.8	15	0.18	0.37	0.128
28	6.0	5.0	10.3	10	0.16	0.28	0.093
45	10	7.5	16.5	15	0.19	0.39	0.133
49	6.0	2.5	10.2	10	0.13	0.24	0.087
67	10	7.5	4.3	5.0	0.08	0.16	0.048
70	10	10	4.3	5.0	0.13	0.30	0.090

Table 4.3: Table comparing numerical laminar approach to experimental analysis for transition

Experimental data, according to Wilkinson [4] were taken from upper surface. Calculated results are also evaluated on the upper surface. Numerical results for transition points x_t are shown in the last column of Table 4.3. Chord c has its origin at sail membrane attachment point to mast, as well as in the experiments [4].

Reynolds number for tests varied between $3.5 \cdot 10^5$ and $10.0 \cdot 10^5$. Flow was, *a priori*, considered laminar with its transition forced to occur at 75% c. For numerical calculations, the disretization used 300 points equally spaced, with a membrane thickness of 2.0% c.

The flow analysis used a two-dimensional piecewise constant strength surface panel method based in vortex and source distribution. The laminar flow was calculated using the Thwaites method, while for the last 25% chord it was used the entrainment method.

Although Table 4.3 presents some discrepancies between experimental and calculated results, it can be noticed that numerical results have approximately the same behaviour of experimental data.

4.3.4.2 Localization of Re-attachment Point Using Statistical Treatment of Numerical Data

According to Gad-el-Hak [1], it is difficult to predict with a reasonable accuracy the point where re-attachment occurs after separation. Its location is dependant on many factors and even experimentally, according to Gad-el-Hak [1] and Wilkinson [4], it is difficult to repeat experiments with the same re-attachment point locations. In Cook and McDonald [68] work, for example, re-attachment was calculated using empirical approach.

Once the location of numerical transition behaves approximately as the experimental values, an approximation can be applied to numerical transition point, in order to locate the re-attachment point. The approximation can use some basic statistics involving experimental data from Wilkinson [4] work and calibrate the method for

placing the bubble end point accurately.

According to Wilkinson [4], laminar separation bubbles presented some regularity in shape depending on transition point location. This regularity, according to Wilkinson [4], had a similar behaviour on upper and lower surfaces. In Wilkinson [4] work, even some rough geometrical relations, that will be discussed later, could be established to find the bubble shape but, data were not treated statistically to give a more accurate location of the bubble end (re-attachment point).

Considering that the re-attachment (x_{rc}) always happens after the transition point, the proposed statistical formula for this point, using the numerical result for transition is presented in equation (4.43).

$$x_{rc} = (x_{tc} \cdot \overline{Rx}_t) \cdot \left(1.0 + \overline{\frac{x_{tex}}{x_{rex}}}\right) \tag{4.43}$$

where:

- x_{tc} is the numerical transition point of the sail and mast configuration;
- x_{tex}, the experimental transition point, taken from Table 4.3;
- x_{rex}, the re-attachment point taken from Table 4.3;
- $\overline{Rx}_t$, the average of relations (x_{tc}/x_{tex}) using the calculated and experimental values from Table 4.3;
- The value $\overline{\frac{x_{tex}}{x_{rex}}}$ is the average of x_{tex}/x_{rex} using the experiments from Table 4.3.

$\overline{Rx}_t = 1.512$ with its standard deviation 0.131. $\overline{\frac{x_{tex}}{x_{rex}}} = 0.528$ and standard deviation of 0.053. Table (4.4) shows the experimental and calculated re-attachment points using the equation (4.43).

	Experimental	**Calculated**
test n^o	x_{rex}/c	x_{rc}/c
4	0.36	0.353
14	0.37	0.296
28	0.28	0.215
45	0.39	0.307
49	0.24	0.201
67	0.16	0.112
70	0.30	0.209

Table 4.4: Table with experimental and calculated values using the calibration

4.4 Modelling Partially Separated Flow on Sails

In the previous Section, it was discussed a method to identify the transition point and calculate the bubble re-attachment point, based in experimental data. In this section,

the method will be applied to model the bubble shape using the overall conclusions about separation bubble shape from Wilkinson [4] work.

4.4.1 Characteristics of Wilkinson Experiments

Wilkinson [4] made a physical model of sails attached to cylindrical masts for wind tunnel tests. The mast crossections were constant, using circular cylinders with diameters ranging from 4.1% to 17.1% of sail membrane chord length.

According to Wilkinson [4], sail membranes were built in small transversal rubbered strips and an automated device called "mouse" could measure boundary layer velocities at different levels from surface. The shapes used were the mean camber lines NACA $a = 0.8$ and NACA 63.

The objective of Wilkinson's experiments was the reproduction of a two-dimensional flow around a sail system. According to Wilkinson's [4] description, the test section of the wind tunnel was 5 feet high and 7 feet wide (1.52 × 2.13 m). The sail system model was as wide as the test section in order to avoid leakage at the tips.

The maximum velocity in the wind tunnel working section was 40 m/s and the lengths of the system were chosen in order to simulate a sail in real operating conditions *i.e.* Re_∞ between $0.2 \cdot 10^6$ to $2.0 \cdot 10^6$. Then, to satisfy dimensioning and flow velocity conditions, the chord length used for sail membrane was 0.70 m.

4.4.1.1 Qualitative Analysis of Experimental Data

Observing the data from Wilkinson's work [4], the laminar separation bubble on sail system has the general characteristics as illustrated in Figure 4.7:

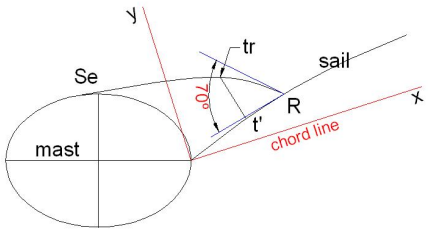

Figure 4.7: The laminar separation bubble profile

- The initial separation point (S_e) takes place smoothly along a line tangential to the local surface (mast body);
- Sudden reduction in the bubble thickness occurs in the last 25% of its length. The slope of C_p coefficient at the reattachment point (R) presents large values. According to the pressure distribution graphics presented by Wilkinson [4], C_p slope was approximately -70^o, as shown in figure 4.7;

- If laminar separation occurs at S_e, a free shear layer remains laminar up to the point t_r in figure 4.7. At this point, transition begins and starts a spreading "fan" of turbulence to the rest of the sail and wake;

- The bubble between mast and sail at the lower surface has the same characteristics to the upper one, as observed by Wilkinson [4]. Differences between bubbles are on sizes: the lower surface bubble is smaller than the upper, as flow was observed to re-attach earlier on the lower surface;

- Trailing edge presents also a separation region that varied in place with geometry and Re_∞. In average, as reported by Wilkinson [4], trailing edge separation happened from 75% c and it was always turbulent, as shown in Appendix D, in the last column;

- According to Wilkinson [4], pressure distribution between points t' and S_e in Figure 4.7 can be approximated by a constant distribution with good agreement with the real flow. After the transition point, the pressure coefficient assumes values determined by the local tangential flow. This was called by Wilkinson as recovery region.

4.4.2 Construction of the Bubble Surface Geometry

The attachment of mast to sail membrane produces a strong separation and, as discussed in Chapter 3, inviscid velocity has a singular point in this region. The objective here is the creation of a surface envelope on the laminar separation region where, on its edge, tangential flow condition is valid.

This kind of surface is called as "matching surface", according to Lock and Williams [9]. It is created numerically over the existent discontinuous surface by establishing a function and applying certain boundary conditions to it, in order to fit the shape of function to experimentally measured conditions.

For reference, it will be used the following notation:

- x_{se} - Separation length, where H reaches for the first time 2.5;

- x_{tr} - Transition length, where after the attachment point, $H = 1.94$;

- x_{re} - Re-attachment length, calculated using $x_{tr} = x_{tc}$ in equation (4.43), with values taken from the statistical approximation using experimental data from Table 4.3.

Boundary conditions are:

- Coordinate y_{se} on mast surface at x_{se};

- Slope of mast surface at separation point y'_{se};

- Coordinate y_{re} on membrane surface at x_{re}.

The end of the bubble, although Wilkinson [4] proposes a sharp end with a slope approximating -70^o, it cannot be used as, it will create another discontinuous point for the attached flow condition. Hence, it will be considered that the bubble end has a smooth surface with the membrane. This is only possible if one more boundary condition is considered: Slope of bubble end point y'_{re} should be the same as membrane surface.

With four boundary conditions established, the polynomial that best fits the separation bubble model should be third order. However, the area between mast and membrane surface presents big changes in surface curvature. If a third order polynomial is used, with its coefficients directly calculated from the boundary conditions, it can have oscillations between separation and re-attachment points.

4.4.2.1 Cook and McDonald Matching Surfaces

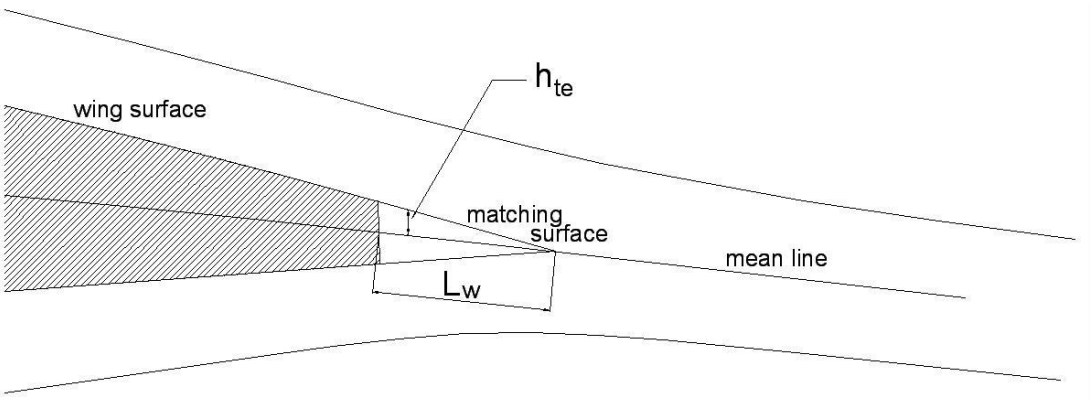

Figure 4.8: Blunt trailing edge matching surface scheme

Cook and McDonald [68] proposed a matching surface generated by a third order polynomial for separation at wing blunt trailing edges, also used by Drela [43]. Although this surface was applied to transonic blunt trailing edges, it does not present oscillations and its shape approaches the bubble separated flow region. The development of this matching surface is illustrated in Figure 4.8 and the polynomial is given in equation (4.44)

$$\eta_w = h_{te} \cdot \left\{ 1 + \left[2 + \frac{L_w}{h_{te}} \cdot \frac{\partial t_{te}}{\partial s} \right] \cdot \xi \right\} \cdot (1 - \xi)^2 \tag{4.44}$$

where, η_w is the normal coordinate from wake mean line to matching surface edge and ξ is given by equation (4.45) using the surface coordinate s. Subscripts te stand for trailing edge station.

$$\xi = \frac{s - s_{te}}{L_w} \tag{4.45}$$

The polynomial proposed by Cook and McDonald [68] starts with an initial height h_{te} and tangential to wing surface ($\partial t_{te}/\partial s$), becoming parallel to wing meanline axis at $\xi = 1$.

If sail system is divided longitudinally from mast leading edge to sail trailing edge, a similar polynomial could be applied to the separation bubble between mast and sail membrane. h_{te} would be the distance from mast surface to this line but, with the fourth boundary condition of the bubble polynomial yet unsatisfied on membrane surface.

However, if a "relative" plane is created *i.e.* a plane that ends tangential to the sail membrane and is extrapolated upstream, meeting the mast surface, as shown in Figure 4.9, then, the matching surface could be developed with the fourth boundary condition satisfied.

Using the relative plane principle, h_{te} could be measured as the distance from the separation point on mast surface to the relative plane. The normal coordinates η_w would be in relation to this plane and the initial mast surface slope $\partial t_{te}/\partial s$ would have to be transformed to this coordinate system.

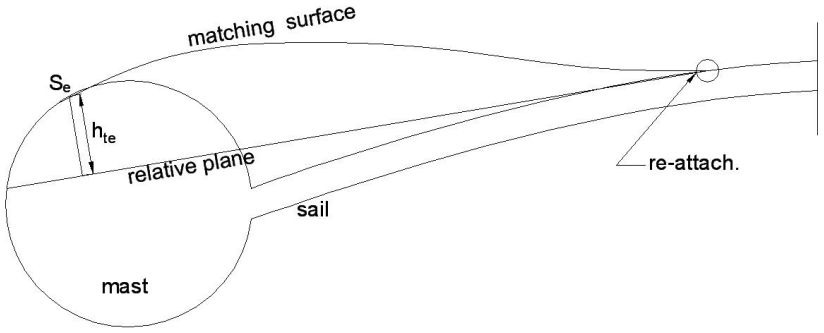

Figure 4.9: Matching surface for a mast and sail separation bubble

4.4.2.2 Separation Bubble Mesh Modelling

The typical mesh modelling for a mast and sail configuration consists on equally spaced points distributed in different regions, according to Figure 4.10. This distribution was chosen because of the new surface added to the system (matching surface) and the difficulty to model mast with a smooth surface by choosing just one general mesh distribution for the entire system.

The equally spaced points allowed a simpler way to control points distribution regionally, without the complexity of using other higher order functions, such as the ones applied by ADAPTIFLEX [59].

Mast and sail surfaces are divided at the stagnation point in two distinct surfaces: the upper and lower. The upper surface, as the experimental data [4], presents a more severe separation and the numerical implementation of matching surface can be used.

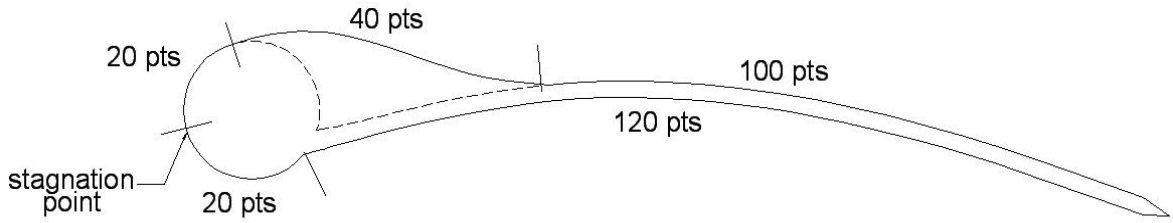

Figure 4.10: Typical mesh points distribution on mast and sail configuration with separation bubble.

On the lower surface, depending on the rotation angle of sail membrane at the attachment point, mast and sail membrane presents most of the time a smoother surface. If mesh distribution is applied according to Figure 4.10, the mast lower surface region approximates a continuous curvature for panel method. This makes velocity distribution on the lower surface to be continuous without presenting low velocities as the upper surface attachment region. In this case, separation is considered to be weak and matching surface is not created.

4.4.2.3 Numerical Implementation of Mast and Sail Matching Surface

According to Figure 4.11, the construction of the matching surface starts with the input of geometry and flow conditions, then a surface panel method is used to calculate the initial inviscid velocity distribution. From the initial inviscid velocity, a Thwaites method is applied to the first 75% length of each surface (upper and lower), considering that flow is laminar up to this length.

In the initial inviscid velocity distribution, if points which are not in the stagnation region but present small velocities, such as $u/Q_\infty < 0.2$, then u/Q_∞ is set to the minimum of 0.2. This will avoid that Thwaites method breaks down with numerical overflow at the mast and sail attachment point.

With boundary layer parameters calculated by Thwaites method, searching routines are applied to H distribution where it is possible to identify the transition point and apply the approximation for the re-attachment point.

Searching routines are applied to identify the separation point and calculate the local mast surface slope, as well as the re-attachment point and the local membrane slope. Figure 4.11 shows a diagram of the process.

In case of relative plane does not intersect mast surface, there is a process that considers the relative plane being from the stagnation point at mast surface to the re-attachment point. This consideration occurs for mast models of small relative mast diameters of less than 10% c and it may create a discontinuity at the re-attachment point. However, this discontinuity is still small in relation to the panel mesh size and final mesh will be smooth for panel method.

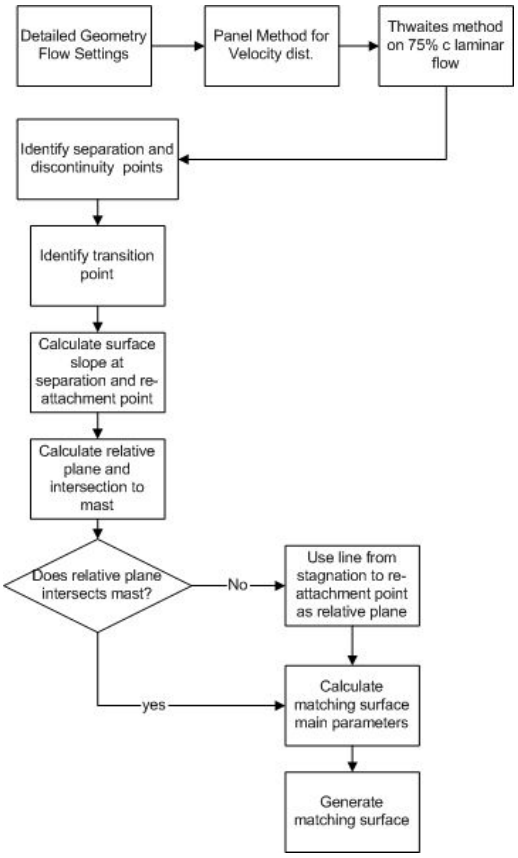

Figure 4.11: Diagram showing the main steps of the matching surface construction process

Figures 4.12 and 4.13 shows the original mast and sail surfaces for Wilkinson [4] tests 4 and 45 with their respective versions with the separation bubble.

4.5 Summary

This Chapter discussed the viscous flow modelling using the surface tangential approach and its application to transitional and partially separated flows. The basis of this viscous theory is the classical equations of Navier-Stokes but, derived for its use with body surface modelling, instead of volume modelling.

The surface modelling permits a simpler solution of viscous flow and, even a transitional flow can be solved, as it was discussed for the lag-entrainment method. However, the solution simplification brings a higher reliance on empirical formulae.

Because integral methods work with surface modelling, it is difficult to analyse accurately viscous phenomena such as separation and re-attachment of flow. However, as integral methods, such as Thwaites, depend only on a few previous points and the local tangential velocity, it was possible to create a method to numerically estimate the transition point and, with the use of some experimental data analysis, to evaluate the flow re-attachment point.

The estimate of transition and re-attachment points may not be enough to describe

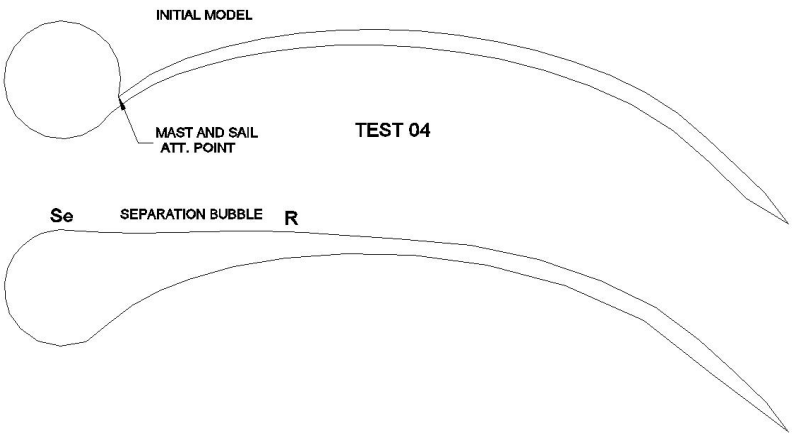

Figure 4.12: Test 04 showing initial model and the version with separation bubble matching surface, with their main points identified.

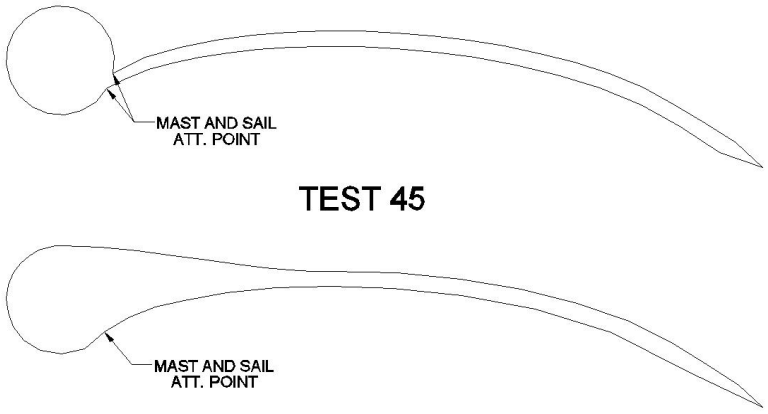

Figure 4.13: Test 45 with initial model and the version with separation bubble matching surface.

flow inside the bubble in detail but, it is sufficient to create an approximate surface involving the separation region and having tangential flow condition on its edge. Then, it permits other surface methods to be applied to evaluate viscous flow.

In the next Chapter it will be discussed the coupling of inviscid method to the integral boundary layer methods discussed here, in order to create a flow analysis tool to be applied to sail surfaces, which is capable to predict separation bubbles.

Chapter 5

The Coupling Scheme for Viscous-Inviscid Interaction

In the previous Chapter, it was introduced the integral boundary layer theory and its basic parameters δ^* and θ that are related to an equivalent displacement of the body surface in normal direction, in order that inviscid flow has an equivalent mass displacement or a momentum displacement respectively.

The equivalent inviscid flow concept leads to the viscous-inviscid interaction or, methods that uses inviscid flow to simulate a viscous flow.

There are basically two principles which are equivalent for viscous-inviscid interaction:

- Methods that consider a displacement in the normal direction from the body surface to δ^*, according to Lock and Williams [9] and Dvorak et al [69];
- Methods that use sources with transpired velocity on the initial body surface mesh and correct its strength according to equation (5.1), as the works of Drela et al [35] and Eça and Falcão de Campos [41].

$$\sigma = \frac{1}{u_e} \cdot \frac{d(u_e \cdot \delta^*)}{ds} \tag{5.1}$$

In this Chapter it will be discussed the approaches for two-dimensional flow that use these two principles mentioned above, their differences and the coupling scheme. The objective is the introduction of simultaneous approach as a stable numerical method to couple to a surface inviscid velocity distribution, permitting a solution of viscous flow, including the solution with flow separation.

The development of the coupling scheme also concerns about its portability and the capacity of being independent of the initial inviscid flow calculation. Hence, inviscid flow can be performed in any existent panel method code and imported to the method, in order to calculate the viscous correction.

Later in this Chapter there will be the study of the coupling scheme and its limitations to flow separation, regarding the discussion of long and short separation bubble

behaviour from the previous Chapter.

5.1 Interactive Approaches

The main characteristic of an viscous-inviscid interaction method is an initial inviscid flow on a body surface that is corrected to the viscous flow. The modelling of both flows can be volumetric as in Drela et al [35] or, surface modelling, as in Eça and Falcão de Campos [41] and [62]. In this work, just the surface modelling is discussed. In this surface modelling, the initial inviscid flow uses a surface panel method and viscous flow uses integral boundary layer methods such as Thwaites, entrainment method or lag-entrainment method.

For a simplified calculation, tangential velocities are related to the freestream velocity, then:

$$U_e = \frac{u_e}{Q_\infty}$$

for viscous flow, and

$$U_I = \frac{u_I}{Q_\infty}$$

for inviscid flow.

Using surface methods, there are basically two kinds of approaches for viscous-inviscid interaction: Direct and simultaneous.

5.1.1 The Direct Approach

The direct approach assumes that inviscid flow is predominant and the viscous flow is a small correction in relation to the inviscid flow, calculated in an one-step interaction. This approach is used mainly in the coupling of panel method to one parameter integral boundary layer methods.

According to the Figure 5.1, inviscid flow is used to calculate the initial velocity distribution. An integral boundary layer method such as Thwaites or entrainment method is applied to this initial inviscid velocity distribution. With the boundary layer parameters calculated, surface panels are moved in the normal direction from the original surface to a distance δ^* or, transpired sources have their strengths corrected to the equation (5.1). Inviscid flow is run again, where this process is called by authors [41] as edge velocity correction. Then the resultant inviscid flow is assumed to be corrected to viscous effects.

According to Lock and Williams [9] and Eça and Falcão de Campos [41], methods using the direct approach are difficult to be applied to separated regions and wakes. According to Drela et al [35], their transition to turbulent flows are normally discontinuous and sharp.

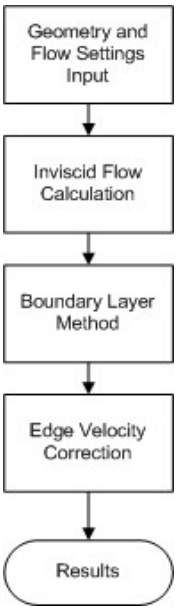

Figure 5.1: The direct approach for viscous-inviscid interaction.

5.1.2 The Simultaneous Approach

The simultaneous approach starts from an inviscid flow, that is presumed incorrect, and uses the viscous flow to successively correct it. According to Drela et al [35], this approach considers an inviscid flow equation to be solved simultaneously to the viscous flow equation or equations, as in the case of the lag-entrainment method.

Because flow is successively corrected, the simultaneous approach considers a residual for each equation involved, a tolerance and it is subjected to a numerical solver. According to Drela et al [35], numerical solution uses a Newton-Raphson solver, in the case of the lag-entrainment method.

The diagram in the Figure 5.2 shows the simultaneous method. It starts with an initial inviscid velocity distribution, where the first integral boundary layer parameters are calculated. This first application of integral boundary layer calculation is called by authors Drela et al [35], Milewski [48] and Drela and Youngreen [62] as the "solution seeding". The code used to the solution seeding of the lag-entrainment method is shown in Appendix E.

After the solution seeding, transpired source strengths are evaluated and residuals are calculated using the linear equation (3.18) for panel method, and boundary layer integral equations. With a Newton-Raphson solver these residuals are driven to zero or, to a specified tolerance.

5.1.2.1 The Surface Displacement with The Simultaneous Approach

It was discussed that the viscous-inviscid interaction can be done by two principles: The normal displacement of surface or; the consideration of transpired sources with

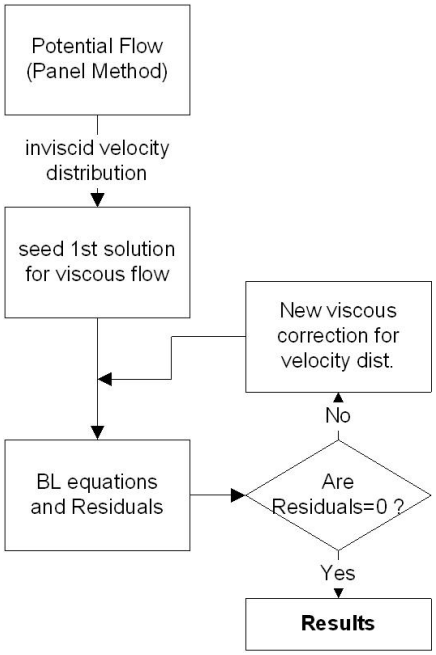

Figure 5.2: The simultaneous approach for viscous-inviscid interaction.

their strengths as function of boundary layer parameters, in order to make inviscid flow equivalent to the viscous flow.

The first principle is difficult to use in a simultaneous approach. The surface displacement configures another body geometry and the problem has to restart from the geometry input in each iteration, which is not practical for complex surface geometries. Another problem is related to the panel method solution: As boundary layer variables have a trend to increase near the trailing edge region, panels have to be modelled making a blunt trailing edge when displaced. Unless some kind of correction is applied, panel method will not work in the next iteration because the Kutta condition will not be satisfied. The Kutta condition has to be applied to sharp trailing edges, which is not the case when a blunt trailing edge appears.

With source distribution, it is possible to use the initial inviscid velocity and correct it to the new source strengths without changing the initial surface geometry. Its panel method solution is also possible because, as it was discussed in Chapter 3, the source distribution and doublet or vortex distributions are separated in different subproblems. Hence, in this work, it will be preferred the source distribution as the main principle for viscous-inviscid interaction.

5.2 The Coupling of Viscous and Inviscid Flows Using the Simultaneous Approach

Many approaches have been developed to solve the integral non-linear boundary layer equations from lag-entrainment method and simultaneously couple them with the in-

viscid flow solution. Drela and Giles [35] coupled the boundary layer formulation to the steady Euler equations, while in a later work of Drela [43], it was coupled a linear vorticity panel method to the same boundary layer formulation.

The use of panel method in viscous-inviscid interaction coupling is a faster alternative for engineering design purposes. It demands lower computational effort with the disadvantage to calculate flow only on body surface, different than Euler potential equations, that needs finite volume modelling, according to Drela and Giles [35].

Drela [43] developed the coupling of a two-dimensional linear surface panel method, based in the distribution of vortex and source singularities to the lag-entrainment method. The coupling scheme used a Newton method to solve the variables (θ, m_d, C_τ or $\tilde{n}$), where m_d was the mass defect given in equation (5.2).

$$m_d = U_e \cdot \delta^* \tag{5.2}$$

The mass defect variable was used to obtain the correction of the initial inviscid velocity U_I, calculated by panel method. Using a distribution of transpired sources on surface, U_e was obtained after some iterations, depending on the body and mesh distributions, according to Drela [43].

5.2.1 The Use of Panel Method in Simultaneous Solution Approach

The potential equation (5.3) for viscous-inviscid interaction includes an extra sheet of transpired sources on body and wake surfaces, where its source strengths are dependent only on boundary layer variables. Then, the perturbation potential will be the sum of the perturbation inviscid potential $\phi^{(I)}$, calculated by panel method plus a potential part for viscous correction $\phi^{(V)}$, calculated by the integral boundary layer equation.

$$\phi = \phi^{(I)} + \phi^{(V)} \tag{5.3}$$

Equation (3.18), discussed in the Chapter 3, was a linear system for perturbation potential flow. The viscous-inviscid interaction equation (5.4) considers the linear system for potential equation plus a viscous part, given by matrices $[B]$ of influence coefficients for transpired source distribution at body surface and $\left[\widetilde{B}\right]$ for transpired source distribution on wake. $[B]$ matrix of influence coefficients will have the same size and values as source influence coefficient matrix $[S]$.

$$[D] \cdot [\Phi] + [W]\,[\Delta\Phi_w] = [S] \cdot \left[\frac{\partial \Phi}{\partial \mathbf{n}}\right] + [B] \cdot [\sigma] + \left[\widetilde{B}\right] \cdot [\sigma_w] \tag{5.4}$$

Recording the potential subproblems discussed in Chapter 3, the viscous correction adds one more subproblem.

5.2.1.1 The Dirichlet versus Neumann Boundary Conditions

Using a Neumann boundary condition, the coupling, instead of presenting a zero normal velocity, has now a non-zero velocity for each panel, as shown in equation (5.5).

$$\frac{\partial\left(\phi+\phi_{\infty}\right)}{\partial \mathbf{n}}=-\sigma \tag{5.5}$$

If a Dirichlet boundary condition is used , then each source strength on body and wake σ_s is given by equation (5.6).

$$\sigma_s=\mathbf{n}\cdot Q_{\infty}-\sigma \tag{5.6}$$

The potential problem using Dirichlet boundary condition, discussed in Chapter 3, considers that, in equation (3.18), the right hand part is already known and the free variables are the potential vectors $[\Phi]$ and $[\Delta\Phi_w]$. The source influence makes a constant vector which characterizes the volume of body and it does not contribute to the tangential direction, just normal direction.

The viscous contribution is summed to the potential solution and, using the Dirichlet boundary condition, the viscous part can be completely independent to the inviscid part $\phi^{(I)}$ and the total potential flow will be given by equation (5.7).

$$\phi=\phi^{(I)}+\sum_{j=1}^{N+N_w} B_{ij}\cdot\sigma_j \tag{5.7}$$

If a Neumann boundary condition was used, the total potential ϕ would have to be solved, implying that the viscous contribution would also have to be considered in the solution process. This means that panel method would have to be run in each iteration, considering the viscous corrections.

With the Dirichlet boundary condition, the inviscid part is solved in the beginning and the coupling depends on successive corrections dependent on the boundary layer variables.

5.2.1.2 The Mass Defect and Source Strength Discretization

The transpired source strength σ is evaluated at collocation point, according to Katz and Plotkin [34]. However, boundary layer variables are calculated at panel nodes.

Considering a distance Δs between panel nodes and using the Hess and Smith [54] approximation of a collocation point at the centre of panel then, collocation point has a distance of $\Delta s/2$ from each node. If a source strength evaluated at panel collocation point is influenced by mass defects m_{d_i} and $m_{d_{i+1}}$, evaluated at panel nodes then, a second order mid-difference will lead to equation (5.8)

$$\sigma=\frac{m_{d_{i+1}}-m_{d_i}}{s_{i+1}-s_i} \tag{5.8}$$

Considering a two-dimensional flow and differentiating equation (5.7) in s surface direction then:

$$U_{e_i} = U_{I_i} + \sum_{j=1}^{N+N_w} K_{ij} \cdot \sigma_i$$

where,

$$K_{ij}\sigma_i = \frac{K_{ij} \cdot m_{d_{i+1}} - K_{ij} \cdot m_{d_i}}{s_{i+1} - s_i}$$

Considering an equally spaced mesh and introducing a new coefficient G:

$$G_{ij} = \frac{K_{ij} - K_{ij+1}}{s_{i+1} - s_i}$$

The general equation for the coupling is given in equation (5.9), where j varies with the number of panels and i with the number of nodes involved.

$$U_{e_i} = U_{I_i} + \sum_{j=1}^{N} (G_{ij}) \cdot m_{d_j} + \sum_{k=N+1}^{N_w} \left(G_{w_{ij}}\right) \cdot m_{dw_k} \tag{5.9}$$

5.2.1.3 The Independence of Viscous and Inviscid Solutions

The equation (5.9) has to be solved simultaneously to the integral boundary layer equations. U_I is evaluated once in the beginning using the panel method. G coefficients are also evaluated once when calculating source influence coefficients for panel method and m_d is evaluated at each iteration from boundary layer variables.

Observing equation (5.9), an arbitrary inviscid surface velocity distribution can be previously input and used to the solution scheme, once G influence coefficients of body and wake can be evaluated. Hence, viscous and inviscid solutions can be completely independent.

5.2.1.4 The Wake coefficients and Boundary Layer Variables

The wake modelling in the inviscid flow, as discussed in Chapter 3, is necessary because of the Helmholtz theorem when using three-dimensional lifting bodies with a finite span. In two -dimensional inviscid flow, there is no need to model wake surface, as its vorticity should be zero.

However, in two-dimensional flow, using the simultaneous method, that needs a continuity of boundary layer variables and edge velocity distribution, the wake needs to be modelled using transpired sources. According to Green et al [44], the wake source distribution will give a more accurate trailing edge velocity. Also, far field boundary layer variables on wake are used for viscous drag calculation, according to Drela and Youngreen [62].

On wake surface, the shear coefficient C_τ should be zero and, according to Green et al [44], the wake is considered to be turbulent.

Green et al [44] and Drela et al [45] developed the formulation for boundary layer variables using a split approach. *i.e.* wake surface is divided in two parts: the upper and lower surfaces. Boundary layer variables on wake surface are presented in equations (5.10), (5.11) and (5.12), where the subscripts L and U indicate lower and upper parts at the trailing edge respectively.

$$\theta_{wake} = \theta_U + \theta_L \tag{5.10}$$

$$\delta^*_{wake} = \delta^*_U + \delta^*_L \tag{5.11}$$

$$C_{\tau_{wake}} = \frac{C_{\tau U} \cdot \theta_U + C_{\tau L} \cdot \theta_L}{\theta_U + \theta_L} \tag{5.12}$$

σ is given by equations (5.13) as function of U_e and δ^*, and (5.14) as function of m_d where the subscript L for the lower side just is exemplified.

$$\sigma_L = \frac{1}{U_{e_L}} \cdot \frac{d(U_{e_L} \cdot \delta^*_L)}{ds} \tag{5.13}$$

$$\sigma_L = \frac{d(m_{d_L})}{ds} \tag{5.14}$$

The potential jump on wake surface, using the source distribution is:

$$\Delta\sigma_{wake} = \sigma_U - \sigma_L = \sigma_w$$

5.2.2 Solution Procedure of the Two-Dimensional Coupling

The solution of the two-dimensional case has the following steps:

1. Seed the first guess, considering $U_i = U_e$. The first boundary layer calculation uses a similar approach to Thwaites method but with some modifications for the calculation of lag-entrainment turbulent variables. This procedure code, that is used in XFOIL [62], is shown in Appendix E;

2. Obtain the first residuals using the discrete equations (5.15) or (5.16), (5.17) and (5.18);

3. With residuals, build the Newton-Raphson solution system: The symbol Δ followed by a boundary layer variable represents the discrete difference, that can be first, second order or biasing. Each boundary layer variable in equations (5.15) or (5.16), (5.17) and (5.18) is represented by its mean value. Q is the vector of these boundary layer variables;

4. After the Newton-Raphson solver, the inviscid velocity is corrected using equation (5.9), when a new edge velocity is obtained;

5. With the new edge velocity, the boundary layer equations are evaluated again and the residuals are calculated. If the root mean squared (rms) of residuals is less than an user specified tolerance, the method stops and prints out the results of flow analysis.

$$2\delta_i \cdot \frac{\Delta(C_\tau^{1/2})}{C_\tau^{1/2}} - 4.2 \cdot \left(C_{\tau eq}^{1/2} - C_\tau^{1/2}\right)_i \cdot \Delta s = R_{C_\tau} \tag{5.15}$$

$$\Delta\tilde{n} - \frac{\partial\tilde{n}}{\partial Re_\theta}(H_k) \cdot \frac{m(H_k)+1}{2} \cdot \frac{\ell(H_k)}{\theta} \cdot \Delta s = R_{\tilde{n}} \tag{5.16}$$

$$\frac{\Delta\theta}{\theta} + (H+2)\frac{\Delta U_e}{U_e} - \frac{C_f}{2\theta} \cdot \Delta s = R_m \tag{5.17}$$

$$\frac{\Delta H^*}{H^*} + (1-H) \cdot \frac{\Delta U_e}{U_e} + \left(C_f - \frac{2C_{diss}}{H^*}\right) \cdot \frac{\Delta s}{\theta} = R_k \tag{5.18}$$

5.2.2.1 The Newton-Raphson Method

Newton Raphson Method is a system with two basic equations (5.19) and (5.20), where F is considered to be zero ($F = 0$) and superscripts indicate the iteration number n. For one iteration of simultaneous method, F is the vector of residuals, shown in equation (5.21) and Q is the vector of free variables, shown in equation (5.22). In each iteration, the Newton-Raphson method calculates the correction δQ for the free variables to satisfy the condition of $F = 0$.

$$F^n + \left[\frac{\partial F}{\partial Q}\right]^n \cdot \delta Q^n = 0 \tag{5.19}$$

$$Q^{n+1} = Q^n + \delta Q^n \tag{5.20}$$

$$F = (R_{C_\tau}, R_m, R_k) = (R_1, R_2, R_3) \tag{5.21}$$

$$Q = (C_\tau, \theta, m_d) \tag{5.22}$$

5.2.2.2 The Solution Matrix

F is the vector of discrete boundary layer equations (5.15) or (5.16), (5.17) and (5.18). The derivatives of function F will imply in the differentiation of the residual equations in respect to all boundary layer variables. This differentiation implies in a chain rule involving the closure relations described in Appendix C.

The main equations involved in the calculation are:

$$U_e = U_I + \sum_{l=1}^{N+N_w} (G_i) \cdot m_{d_i}$$

$$H = \frac{\delta^*}{\theta}$$

$$H^* = f_1(H)$$

$$C_f/2 = \frac{1}{Re_\theta} f_2(H)$$

$$\frac{2C_{diss}}{H^*} = \frac{1}{Re_\theta} f_3(H)$$

where, f_1, f_2 and f_3 plus turbulent or transition closures are functions to be differentiated in respect to each boundary layer free variable. The differentiations involving m_d uses a chain rule exemplified in equation (5.23), where () represents a function. $\partial\delta^*/\partial m_d$ and $\partial U_e/\partial m_d$ are given by equations (5.24) and (5.25).

$$\frac{\partial()}{\partial m_d} = \frac{\partial()}{\partial \delta^*} \cdot \frac{\partial \delta^*}{\partial m_d} + \frac{\partial()}{\partial U_e} \cdot \frac{\partial U_e}{\partial m_d} \tag{5.23}$$

$$\frac{\partial \delta^*}{\partial m_d} = -\frac{m_d}{U_e} \cdot \frac{\partial U_e}{\partial m_d} \tag{5.24}$$

$$\frac{\partial U_{ei}}{\partial m_{dl}} = G_{ij} \tag{5.25}$$

The differentiation scheme uses a downwind linear difference. The solution uses the variables on nodes i and $i+1$ for the derivatives, as shown in matrix of equation (5.26), where A represents the part of differentiation scheme at node i and, B at node $i+1$. All the other nodes contribute with a mass defect influence, shown in the matrix of equation (5.27) and are represented by the letter m.

$$\begin{bmatrix} \frac{\partial R_1}{\partial C_\tau} & \frac{\partial R_1}{\partial \theta} & \frac{\partial R_1}{\partial m_d} \\ \frac{\partial R_2}{\partial C_\tau} & \frac{\partial R_2}{\partial \theta} & \frac{\partial R_2}{\partial m_d} \\ \frac{\partial R_3}{\partial C_\tau} & \frac{\partial R_3}{\partial \theta} & \frac{\partial R_3}{\partial m_d} \end{bmatrix} = A, B \tag{5.26}$$

$$\begin{bmatrix} 0 & 0 & \frac{\partial R_1}{\partial m_d} \\ 0 & 0 & \frac{\partial R_2}{\partial m_d} \\ 0 & 0 & \frac{\partial R_3}{\partial m_d} \end{bmatrix} = m \tag{5.27}$$

This will form a full matrix with 3 by 3 block coefficients. In the main diagonal, there will be the differentiation of boundary layer equations at the current node. Equation (5.28) shows schematicaly the solution matrix.

$$\begin{bmatrix} A & m & m & m & m \\ B & A & m & m & m \\ m & B & A & m & m \\ m & m & B & A & m \\ m & m & m & B & A \end{bmatrix} \cdot \begin{Bmatrix} \delta Q_1 \\ \cdot \\ \delta Q_i \\ \cdot \\ \delta Q_N \end{Bmatrix} = - \begin{Bmatrix} R_1 \\ \cdot \\ R_i \\ \cdot \\ R_N \end{Bmatrix} \tag{5.28}$$

5.2.3 Initial Solution Considerations

At the stagnation point, residuals of momentum and kinetic energy equations were derived by Milewski [48] and are shown in equations (5.29) and (5.30).

$$R_m = \theta - 0.38574\sqrt{\frac{\xi}{Re_\infty \cdot u_\xi}} \tag{5.29}$$

$$R_{k.e} = \delta^* - 0.38574\sqrt{\frac{\xi}{Re_\infty \cdot u_\xi}} \tag{5.30}$$

5.2.3.1 Initial Turbulent Solution

At the transition point, the amplification $\tilde{n}$ has reached its specified critical value (usually 9) and there is a change of boundary layer variables. $\tilde{n}$ is no longer used downstream and it is substituted by $C_\tau^{1/2}$ with the first value given by equation (5.31), according to Milewski [48]. Then residuals are forced to be: $R_{\tilde{n}} = 0$ and $R_{C_\tau} = 0$ at transition point, according to Drela and Youngreen [62].

$$C_\tau^{1/2} = 1.8 \exp\left(-\frac{3.3}{H-1}\right) \cdot C_{\tau eq}^{1/2} \tag{5.31}$$

5.3 Comparison Between Direct and Simultaneous Approaches

In this section, the two-dimensional NACA 0012 foil is analysed with direct and simultaneous method in order to show the differences of both methods in relation to convergence and behaviour of boundary layer variables with a popular foil series.

The NACA four digit series, which includes NACA 0012 foil, according to Abbott and Doenhoff [61], is a relatively thick foil with a blunt trailing edge. This blunt trailing edge is transformed into a sharp end by extending foil 1% c after the trailing edge and applying a matching surface as described by Cook and McDonald [68] and discussed in the previous Chapter.

The simultaneous approach uses the viscous-inviscid interaction module of Drela and Youngreen [62] XFOIL code. The direct approach uses a two-dimensional piecewise constant strength surface panel method with source and vortex distributions for inviscid flow, coupled to a Thwaites method for laminar flow and the entrainment method for viscous turbulent flow.

5.3.1 Flow and Mesh Settings

Flow was set for $Re_\infty = 6.0 \cdot 10^5$, with $\tilde{n}_{crit} = 9.0$. Two different points of transition were chosen (25% c and 50% c) in order to have a better observation of boundary layer variables development.

By using the simultaneous method, convergence depends on an interactive scheme. According to Drela and Youngreen [62], the interactive scheme will have its convergence according to mesh density. For the case of a NACA 0012 foil, Figure 5.3 shows the convergence of method for 100, 200 and 300 points.

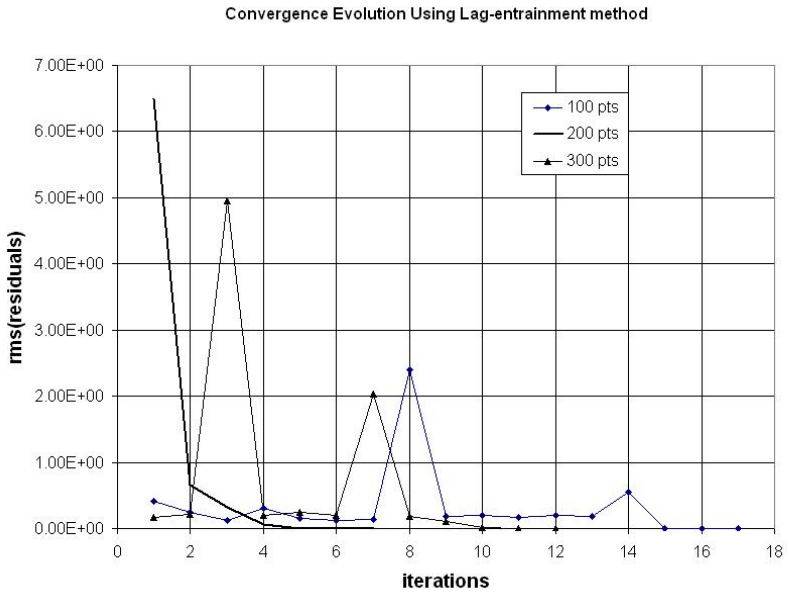

Figure 5.3: Lag-entrainment method convergence evolution with different number of points for a NACA 0012 foil.

According to Drela and Youngreen [62], the convergence in the simultaneous method is dependent on mesh modelling. Using the example of a NACA 0012 mentioned before, Figure 5.3 shows the convergence of method using 100, 200 and 300 points equally spaced. In order to compare direct and simultaneous approaches, it was used the same mesh modelling for both.

In the simultaneous approach, it was established that rms of residuals should be less than 10^{-5} for convergence criteria. The maximum number of iterations was 17 with 100 points and, the best convergence was reached with 200 points, rms of residuals of $6.0 \cdot 10^{-7}$ and 7 iterations. The mesh with 300 points presented convergence in the eleventh iteration.

Hence, the chosen mesh has 200 points with 100 points equally spaced on upper and lower surfaces.

5.3.2 Pressure Distribution

The two-dimensional pressure distribution with 200 points for a NACA 0012 foil at $\alpha = 0$ is shown in Figure 5.4. Experimental data for NACA 0012 were obtained in Abbott and Doenhoff [61]. It can be observed that the direct, simultaneous and inviscid distributions have a close agreement with experimental data. The differences in pressure between methods are small.

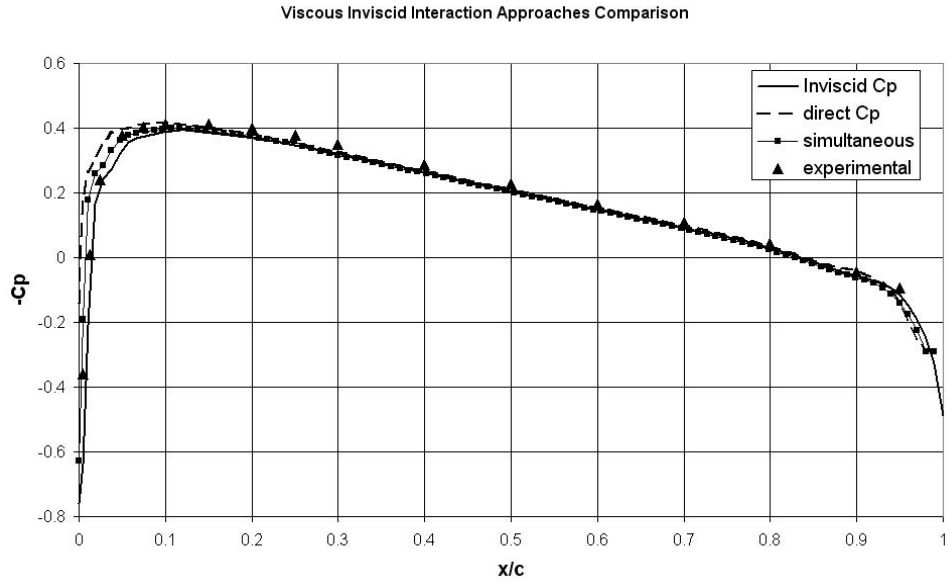

Figure 5.4: C_P distribution using direct and simultaneous approaches

5.3.3 Shape Parameter

Figure 5.5 shows H shape parameter calculated by both approaches at zero incidence angle. The simultaneous approach presents a smoother distribution of boundary layer variables with an initial laminar oscillation.

The direct approach has an almost constant distribution in the laminar regime while simultaneous approach has an approximately linear increase. Direct approach H curves have a sharp transition as discussed before, causing a discontinuity at transition point.

Increasing the incidence angle to 5^o, the shape parameter calculated by direct method presents higher values at the trailing edge region, according to Figure 5.6.

According to Green et al [44] and Katz and Plotkin [34], the direct approach ties the boundary layer variables to the inviscid velocity. The simultaneous approach eliminates the link between the initial inviscid velocity and boundary layer variables, making the approach more stable in separated regions, as the case of the trailing edge separation in Figure 5.6.

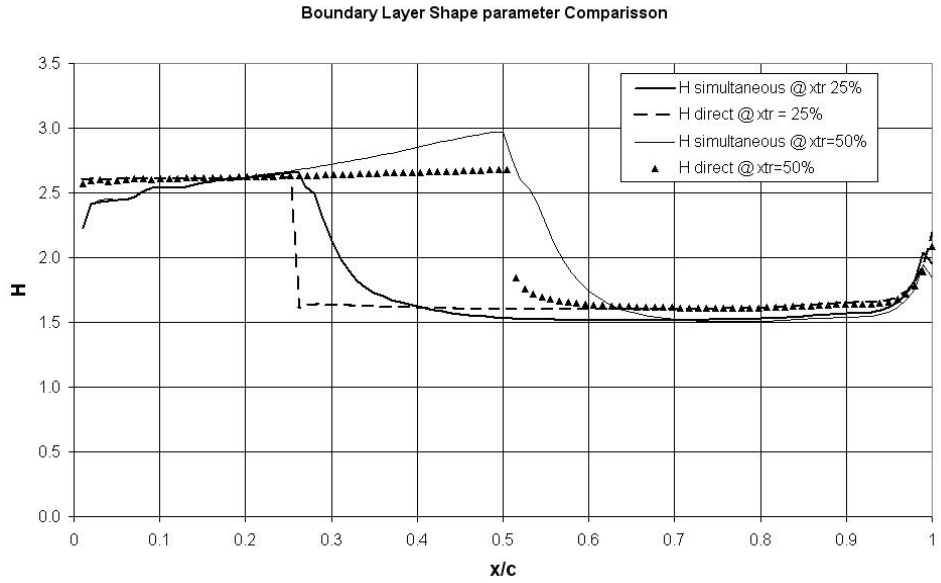

Figure 5.5: H Shape parameter comparison for a NACA 0012 foil using transition (xtr) in two different places for direct and simultaneous approaches

Hence, the simultaneous approach is a more stable method in separated regions, since velocity distribution is sufficiently continuous, characterizing a weak separation.

5.4 Modelling of Strong Separation Bubble Using Surface Flow Analysis

According to Gad-el-Hak [1], flow separation has two types of behaviour: long and short bubble behaviour. The short bubble behaviour is also called as weak separation by Lock and Williams [9] and, as discussed in the previous Chapter, it does not modify significantly the initial inviscid pressure distribution.

The long bubble behaviour or, strong separation, has a flat shaped pressure distribution on the separated region where, according to Wilkinson [4], C_P has a constant value ranging from -1.5 to -2.0.

As observed by Lock and Williams [9], a body with a step on its surface will create a discontinuous point on the surface velocity distribution, as well as the insertion of a high surface curvature as a mast at membrane leading edge. This discontinuous point in velocity distribution starts a strong separation region.

The steeped body surface and mast and sail configurations are examples related to the strong separation which was introduced in the previous Chapter. The strong separation imposes a limitation to viscous-inviscid interaction methods and it is only possible to overcome it by using empirical methods, which their theories will be discussed in this Section.

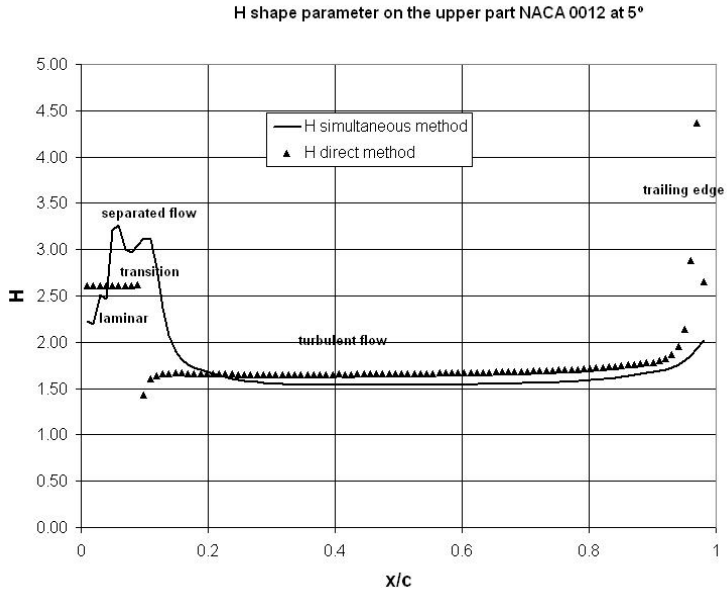

Figure 5.6: H shape parameter on upper surface comparisson for lag-entrainment and direct (entrainment) methods on a NACA 0012 foil at 5^o

5.4.1 Long and Short Bubble Behaviours

By having a continuous initial velocity distribution in the viscous-inviscid interaction and if a short bubble region is detected then, the continuity in velocity distribution will be preserved.

According to the documentation of XFOIL [62], and some observations made by Lock and Williams [9], the maximum difference between viscous and inviscid C_p using a viscous-inviscid interaction method is 5%.

Variations of C_p in short separation bubbles are inside this limit but for strong separation, 5% is well below to what is measured experimentally, regarding Figure 4.3 and the observations of Wilkinson [4].

The long bubble presents a discontinuous region that is difficult to treat using the viscous-inviscid interaction. According to Drela [43], the analysis of a separation region due to high curvature using a surface based method (panel method or viscous-inviscid interaction) is only possible in case there is some interference from user in flow modelling such as a matching surface over the separation zone or a velocity correction.

5.4.2 The Viscous Correction Considering Wall Curvature

According to Lock and Williams [9], the pressure gradient inside boundary layer can vary from the wall to the edge. Lock and Williams [9] also showed that the difference in pressure, in equation (5.32), vary with the streamline curvature (κ^*). Δp_w is defined by authors [9] as the difference between the inviscid wall pressure to the real flow wall

pressure.

$$\frac{\Delta p_w}{\rho \cdot U_{iw}^2} = \kappa^* \cdot (\theta + \delta^*) = \Delta C_p \tag{5.32}$$

κ^*, from equation (5.33) is function of the wall curvature κ_w, defined on equation (5.35), and the first derivative of the transpired source. The equation (5.33), called as Le Balleur approach by the authors Lock and Williams [9], gives the streamline curvature in terms of transpired source.

$$\kappa^* = \kappa_w + \frac{d\sigma}{ds} \tag{5.33}$$

or alternatively:

$$\kappa^* = \kappa_w + \frac{d^2 m_d}{ds^2} \tag{5.34}$$

The wall curvature in surface coordinates is given by equation (5.35), where $r(s)$ represents the line function vector $r = r\,[x(s), y(s), z(s)]$ described, in this work, by a cubic spline.

$$\kappa_w(s) = \frac{\left|\frac{dr}{ds}\right| \cdot \frac{d^2 r}{ds^2}}{\left|\frac{dr}{ds}\right|^3} = \frac{1}{R} \tag{5.35}$$

According to Lock and Williams [9], when flow is near separation ($H \simeq 3$), the correction using the curvature effect for the pressure coefficient will be about 5% to 10%, not larger.

5.4.3 Matching Surfaces

Matching surfaces are smooth surfaces placed over blunt or highly curved regions, in order to have a tangential flow along this region. It is used on steeped or blunt surfaces, where the most applied case is the blunt trailing edge of foils, as the NACA four digit series.

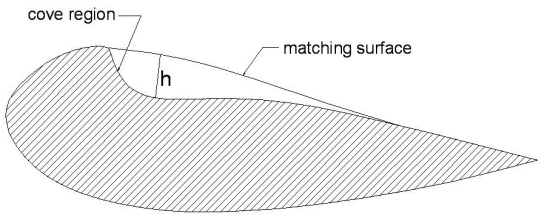

Figure 5.7: The h parameter for a matching surface approach, considering a cove region

Lock and Williams [9], used the cove region, as shown in Figure 5.7, to exemplify the matching surface. Equation (5.36) gives the curvature correction due to the matching surface. h is the parameter that measures the local height between original surface and matching surface. h should be continuous inside the separation bubble. In cases discussed by Lock and Williams [9], equation (5.36) gives the pressure correction in the

range of 5% to 10%.

$$\Delta C_p = \kappa^* \cdot (\theta + \delta^* - h) \tag{5.36}$$

5.4.3.1 The Use of Viscous-Inviscid Interaction on a Mast and Sail Configuration with a Matching Surface

By using some few modifications, the concept of matching surface was applied to sail configurations in the previous Chapter. It was developed the methodology to create a surface enveloping the separation area. However, the use of viscous-inviscid interaction methods with matching surface in the case of mast and sail configurations is far from being accurate for the following reasons:

- The strong separation, as discussed by Parkinson and Jandali [67] and Gad-el-Hak [1], does not have a continuous velocity distribution. In Figure 4.3, strong separation presents a flat part, recovering sharply to the normal attached flow after some length. This was also observed experimentally by Wilkinson [4];
- Although simultaneous viscous-inviscid interaction methods have a relative numerical stability, they need a continuity in velocity distribution, what makes them not converge for an edge velocity distribution with the shape of Figure 4.3.
- Even with a matching surface being continuous to the existent surface, panel method is very sensitive to surface curvature and, in concave regions, inviscid velocity decreases in these places, as shown in Figure 5.8 for test 45 with a matching surface. The velocity decrease may create regions with velocities near stagnation points and the initial seeding solution method will break down.

5.4.4 The Inviscid Velocity Correction

Alternatively to matching surfaces, there is the inviscid velocity correction. Wilkinson [4] developed this correction for panel method using the experimental results obtained in his work. The use of the method was dependent on the input of the separation, transition and the reattachment points by the user. Then, a sheet of sources with unknown strength was superposed to the panel method singularities (doublets, in Wilkinson´s case) as shown in Figure 5.9.

The condition imposed to sources was a velocity distribution between the specified separation and reattachment points as constant, while inside bubble, at the doublet (or vortex) singularities, it was imposed zero tangential velocity. The modified influence coefficients are solved together with the original singularities of the panel method, resulting in a constant pressure distribution in the separation bubble region.

The approach proposed by Wilkinson [4] was dependent on experimental results. It did not take into account any viscous effects that may have occurred inside the separated regions.

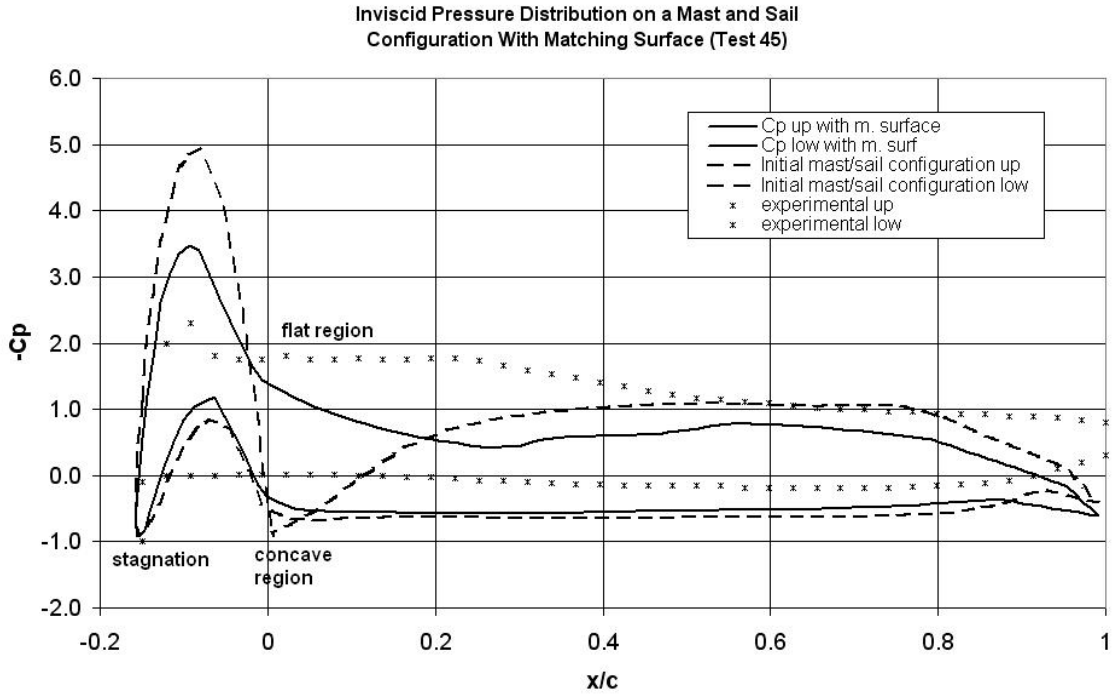

Figure 5.8: C_P distribution for test 45 with and without matching surface

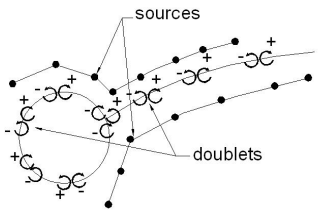

Figure 5.9: Scheme of doublets and sources distribution for sail and mast

5.5 Summary

In this Chapter was discussed the main principles of viscous-inviscid interaction method and the basic approaches to solve flow: Direct and simultaneous. The direct approach ties the boundary layer variables to the initial inviscid velocity, correcting flow by inserting transpired sources or dislocating original body surface. The simultaneous method solves two basic equations to calculate the strength of transpired sources: the inviscid and the viscous flow where, in this work, they are, the panel method linear system and the integral momentum equation, by means of the lag-entrainment method.

The direct approach has a simple implementation and it is dependant on an initial inviscid velocity and a one-parameter boundary layer method. The simultaneous approach has a more complex coupling but it is more stable and more suitable for analysing bodies with weak separation.

By using the Dirichlet boundary condition in the simultaneous coupling scheme, it

is possible to solve the viscous correction independent to the inviscid flow, what allows the use of pre-calculated inviscid velocity for the same problem.

The simultaneous approach presented a stable numerical solution with weak separation. However, for strong or severe separation, viscous-inviscid interaction methods are limited. Some approaches to overcome these limitations were introduced and their effect on flow calculation was discussed.

The theory presented in this chapter was also limited to two-dimensional flow. The foil used (NACA 0012) is considered a thick foil with a significative internal volume. Sails are three-dimensional surfaces and flow also suffers three-dimensional effects such as cross-flow.

In the next Chapter, it is discussed the use of three-dimensional simultaneous methods on thick and thin foils, in order to develop a surface method for three-dimensional viscous flow analysis.

Chapter 6

A Surface Method for Three-dimensional Viscous-Inviscid Interaction

In the last Chapter, it was introduced the viscous-inviscid interaction coupling theory in two-dimensions. The simultaneous coupling presented a more stable solution, even in separated regions, since velocity distribution on body is continuous.

In the present Chapter, it is intended to use the original simultaneous coupling in two-dimensions to approximate a three-dimensional solution by dividing the body into chordwise sections and applying the boundary layer calculation to each section. This process is called here as sectional method.

There are other existing methods for calculating three-dimensional flow and their theory will be discussed here. The most complex, the Milewski's [48] method, considers a three-dimensional boundary layer theory coupled to a piecewise constant panel method. Other more simple but, with a reported high accuracy, divides the original panel method mesh into chordwise strips and apply a two-dimensional boundary layer calculation on each one, thus called the "strip theory". This last method, was first developed by Dvorak et al [69] where it was used a direct coupling with the normal dislocation of surface principle for correcting flow. Another strip theory method which uses the simultaneous coupling was developed by Hufford et al [45].

The three methods for three-dimensional viscous flow solution discussed before are dependant on the original three-dimensional panel method, since the mesh, up to the calculated influence coefficients matrix. There are many existing three-dimensional panel method codes and they are in their finest state of art. Many of them do not have their codes available to the public because they are already commercial softwares.

Based on this existing panel method codes which have many features available to aid in inviscid flow analysis, it would be better to create a separate routine for the three-dimensional viscous flow calculation using the simultaneous coupling which panel method calculated inviscid velocity distribution could be input to this routine.

In the previous Chapter, it was shown that it is possible to separate the viscous

to the inviscid solution by means of a numerical approach using Dirichlet boundary condition. By having a detailed body geometry mesh, imported from panel method, it is possible to use the sectional method with the initial inviscid velocity input from panel method code results.

The sectional method is discussed in more detail, including a method adapted from XFOIL [62] for identifying transition and separation using the simultaneous approach and the interpolation process using an available surface panel method, PALISUPAN [70]. A three-dimensional NACA 0012 foil is used with method, in order to evaluate its convergence and solution symmetry. At last, there will be a discussion on wake positioning using the simultaneous coupling to three-dimensional flow.

6.1 The Three-dimensional Boundary Layer Coupling

The approach presented by Milewski [48] couples a piecewise constant singularity strength panel method to a three-dimensional integral boundary layer method, introduced by Drela and Mughal [46].

The boundary layer method considers that boundary layer variables develop in two surface directions: streamwise (1) and crossflow (2). Both directions are related linearly, based on a linear simplification of Johnston's [71] model. If flow is assumed to be incompressible and irrotational, this linearity is valid and dependant only on constant parameters that leads to the assumption of a boundary layer "resultant" on stream direction that has an unique solution at each node of the discretized surface.

Hence, integral boundary layer momentum equation becomes equation (6.1) for streamwise flow direction and equation (6.2) for crossflow direction. s and t are stream and crossflow directions respectively, u_e is streamwise edge velocity and w_e crossflow edge velocity, where q_e is their resultant modulus.

$$\frac{\partial}{\partial s}\left(\rho q_e^2 \theta_{11}\right) + \frac{\partial}{\partial t}\left(\rho q_e^2 \theta_{12}\right) + \rho q_e \delta_1^* \frac{\partial u_e}{\partial s} + \rho q_e \delta_2^* \frac{\partial u_e}{\partial t} = \tau_{12} \tag{6.1}$$

$$\frac{\partial}{\partial s}\left(\rho q_e^2 \theta_{21}\right) + \frac{\partial}{\partial t}\left(\rho q_e^2 \theta_{22}\right) + \rho q_e \delta_1^* \frac{\partial w_e}{\partial s} + \rho q_e \delta_2^* \frac{\partial w_e}{\partial t} = \tau_{21} \tag{6.2}$$

Using the Johnston [71] linear approximation, variables θ_{12}, θ_{21} and θ_{22} are all functions of streamwise momentum thickness θ_{11}. Mass defects are given in equations (6.3) and (6.4).

$$m_1 = \rho q_e \delta_1^* \tag{6.3}$$

$$m_2 = \rho q_e \delta_2^* \tag{6.4}$$

$$q_e^2 = u_e^2 + w_e^2$$

The solution considers the variables in a pre-defined computational domain. The residuals are discretized using the finite element theory. The solution matrix for the Newton solver will be a big and sparse block matrix with blocks of 4 by 4 coefficients, as shown in equation (6.5), occupying the main diagonal of the general solution matrix. R_1 in equation (6.5) is the residual of the two-dimensional turbulence or laminar closure equations; R_2 is the residual of the streamwise kinetic energy equation; R_3 is the residual of momentum equation in crossflow direction and R_4 is the residual of momentum equation in streamwise direction.

$$A = \begin{bmatrix} \frac{\partial R_1}{\partial C_\tau^{1/2}} & \frac{\partial R_1}{\partial \theta_{11}} & \frac{\partial R_1}{\partial m_1} & \frac{\partial R_1}{\partial m_2} \\ \frac{\partial R_2}{\partial C_\tau^{1/2}} & \frac{\partial R_2}{\partial \theta_{11}} & \frac{\partial R_2}{\partial m_1} & \frac{\partial R_2}{\partial m_2} \\ \frac{\partial R_3}{\partial C_\tau^{1/2}} & \frac{\partial R_3}{\partial \theta_{11}} & \frac{\partial R_3}{\partial m_1} & \frac{\partial R_3}{\partial m_2} \\ \frac{\partial R_4}{\partial C_\tau^{1/2}} & \frac{\partial R_4}{\partial \theta_{11}} & \frac{\partial R_4}{\partial m_1} & \frac{\partial R_4}{\partial m_2} \end{bmatrix} \tag{6.5}$$

The neighbouring nodes, contribute with the mass defect influences, as shown in the block matrix of equation (6.6).

$$B = \begin{bmatrix} 0 & 0 & \frac{\partial R_1}{\partial m_1} & \frac{\partial R_1}{\partial m_2} \\ 0 & 0 & \frac{\partial R_2}{\partial m_1} & \frac{\partial R_2}{\partial m_2} \\ 0 & 0 & \frac{\partial R_3}{\partial m_1} & \frac{\partial R_3}{\partial m_2} \\ 0 & 0 & \frac{\partial R_4}{\partial m_1} & \frac{\partial R_4}{\partial m_2} \end{bmatrix} \tag{6.6}$$

The general solution is solved at once for each node and the general solution matrix is presented schematicaly in equation (6.7).

$$\begin{bmatrix} \cdot & & \cdot & \cdot & & \cdot & \cdot & & & \\ \cdot & \cdot & & \cdot & \cdot & & \cdot & \cdot & & \\ B & A & A & B & A & A & B & A & A & B \\ & & \cdot & \cdot & & \cdot & \cdot & & \cdot & \cdot \\ & & & \cdot & \cdot & & \cdot & \cdot & & \cdot \end{bmatrix} \cdot \begin{Bmatrix} \delta U_1 \\ \cdot \\ \delta U_i \\ \cdot \\ \delta U_N \end{Bmatrix} = - \begin{Bmatrix} R_1 \\ \cdot \\ R_i \\ \cdot \\ R_N \end{Bmatrix} \tag{6.7}$$

Although solution is done at once by the Newton solver for all the nodes involved, the solution of this kind of matrix demands high computational time because of the sparsity of general solution matrix, as reported by Milewski [48]. Convergence, for some of Milewski [48] results, were reported to be difficult.

6.2 The Strip Theory

A simpler approach for solving three-dimensional viscous flow is the strip theory, first developed by Dvorak et al [69]. The strip theory considers that on a strip of panels on a wing surface, as illustrated in Figure 6.1, viscous flow develops predominantly

in chordwise direction. Then, integral boundary layer methods are used in this flow direction. In Dvorak et al [69] work, it was used the direct approach and it was based on the normal surface displacement principle for viscous-inviscid interaction.

In another work from Hufford et al [45], it was used the strip theory with a three-dimensional linear strength panel method with a two-dimensional simultaneous coupling, using the lag-entrainment method.

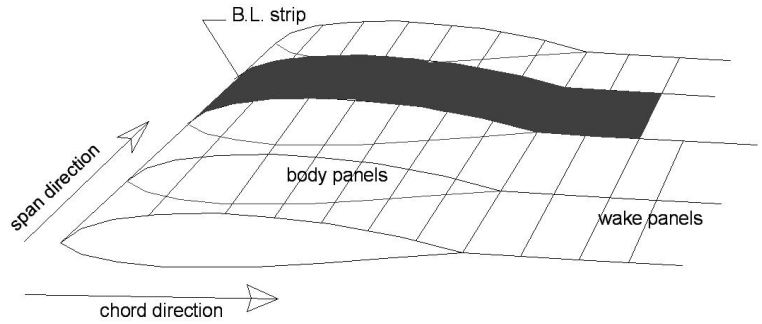

Figure 6.1: Scheme of chordwise strip used on strip theory

Viscous solution is calculated on chordwise strips of panels from the initial panel model. For calculations, it is assumed that viscous flow develops in chordwise direction and neighbouring strips sources cannot have influence on the current strip, avoiding the crossflow effect.

The Hufford et al [45] method and the coupling of viscous to inviscid solution uses basically the same formulae and considerations to the two-dimensional coupling discussed in the previous Chapter. The only difference is the use of quadrilateral panels from the original panel method mesh.

According to Hufford and colleagues [45], strip theory approaches with good agreement the three-dimensional calculation and has the advantage of fast processing time, compared to Milewski's [48] method.

6.3 The Sectional Velocity Method (VIX Code)

In the previous Chapter, it was shown that the viscous solution can be run entirely independent to the inviscid solution using the Dirichlet boundary condition. The objective of this Section is the use of this independent solution to create a separate routine for viscous correction based on simultaneous coupling, using an initial surface inviscid velocity distribution, calculated by panel method.

The routine is similar to the strip theory discussed by Hufford et al [45] but, it

divides the body into chordwise sections and not strips, which were dependant on an initial panel mesh. On each section, the tangential chordwise velocity U_I is corrected to the viscous flow, assuming that viscous flow develops just in chordwise direction. It is assumed that crossflow velocities, compared to chordwise direction are small and, consequently, viscous effects are negligible in this direction.

If the assumption above is true, streamwise viscous boundary layer approaches the real three-dimensional viscous flow and there will not be significative differences to a three-dimensional method, such as the one developed by Milewski [48], provided that freestream velocities are small (incompressible and irrotational flow).

The initial inviscid velocity can be calculated by a three-dimensional surface panel method and its results are interpolated at nodes of sections, obtaining a continuous velocity distribution. A two-dimensional boundary layer calculation is applied to each section using the interpolated velocity. The Figure 6.2 shows the diagram of the calculation process.

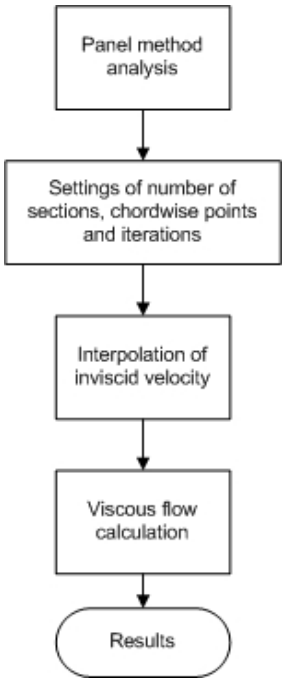

Figure 6.2: Calculation process on VIX method

6.3.1 Interpolation Scheme

The initial inviscid velocity on surface and wake can be calculated by any surface panel method. In this work, it was used PALISUPAN code [70]. According to Turnock [70], PALISUPAN is a surface piecewise constant strength panel method that uses vortex and source singularities. For its use with a method that divides surface into chordwise sections, it needs an interpolation scheme to transform these piecewise constant velocities into a continuous distribution of velocities on panels for boundary layer calcu-

lation. Figure 6.3 shows schematicaly the velocity interpolation over piecewise constant singularity strength distribution, original from a panel method.

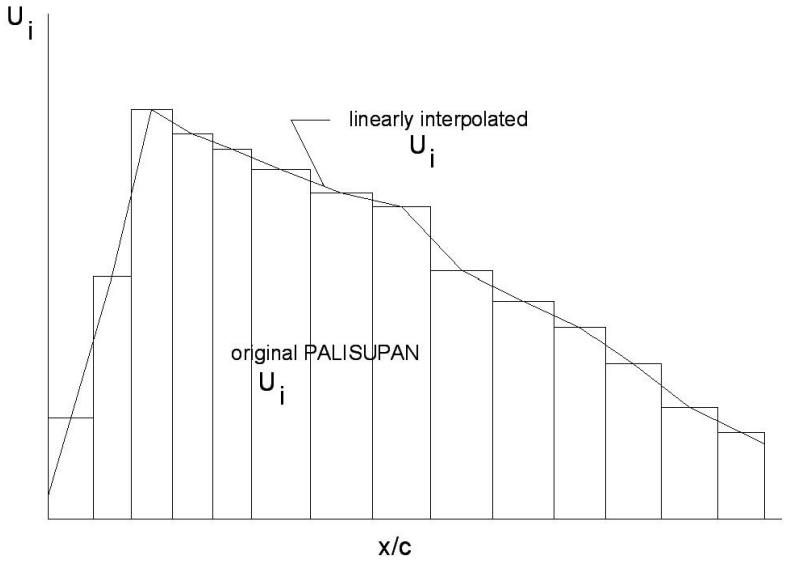

Figure 6.3: The piecewise constant U_i interpolated by a linear scheme

The bi-linear interpolation, presented in Appendix B, was chosen because it does not present oscillations between original points, as it would be the case of other higher order interpolation methods, such as bi-cubic.

Inviscid tangential velocities V_x, V_y and V_z in Cartesian coordinates, calculated for each panel collocation point by PALISUPAN are interpolated and transformed into surface velocities U_I, in chord and, W_I in span direction.

In U direction, only, it is based the viscous flow and U_I is used as a first guess for boundary layer calculation. Later, after interaction, viscous U_e and inviscid W_I are summed again, thus obtaining the three-dimensional pressure distribution on foil surface, lift and drag forces.

6.3.1.1 Special Considerations in Velocity Interpolation Scheme

The interpolation uses the velocities calculated by panel method at the panel collocation point, which is in the centre of panel, according to Hess and Smith [54]. The centres surrounding a panel vertex forms a cell, as shown in Figure 6.4.

It is difficult to interpolate velocities at nodes on body edges, such as trailing, tip or root edges then, there is a special interpolation scheme.

Using the trailing edge as an example, special panels are created at the edge with zero length, denominated as "ghostcells". Velocities that were calculated initially by panel method, are extrapolated using a linear approximation from the last existing collocation point to the centre of the ghostcell, presented in Figure 6.5.

The values on edges are evaluated considering these different regions:

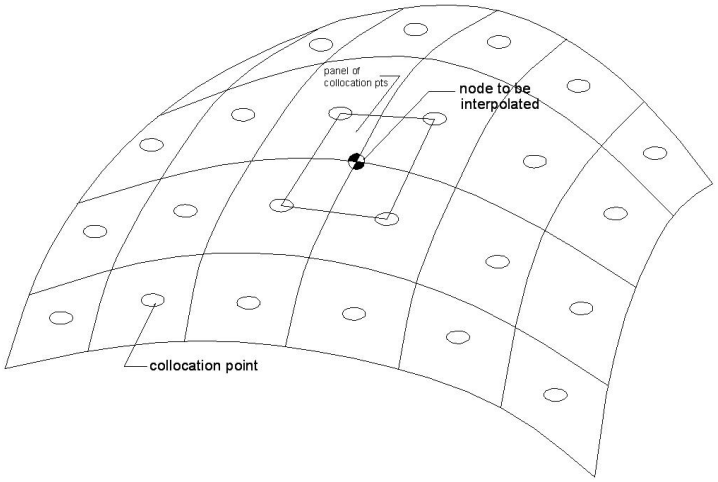

Figure 6.4: The scheme of interpolation on nodes when values are given on collocation points

- Trailing edge: upper panels have the same velocity on upper and lower surfaces (Kutta condition). The corner values are the average between the first ghostcell on chord direction, the first ghostcell on span direction and the corner panel centre as shown in Figure 6.5.

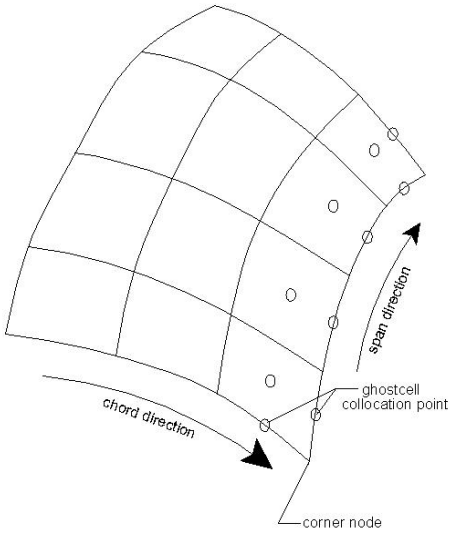

Figure 6.5: The scheme of interpolation on edges using a ghostcell scheme

- Far field wake: ghostcells have its velocities set to the previous chordwise cell value (constant velocity);

The interpolation scheme code, made in FORTRAN 95 language, uses an object structure of nodes, panels and sections. The main parts of this code are shown in Appendix E.

6.3.2 Construction of Sectional Influence Coefficients

The source influence coefficients are calculated according to sectional geometry. It is used a two-dimensional linear source distribution. The matrix construction is dependant on the location of the stagnation point, which defines where upper and lower surfaces begin.

In two-dimensional methods, using surface vortex distribution, the location of the stagnation point is not a difficult task as γ, the vortex strength, changes sign at stagnation point. In three-dimensional interpolation scheme, this is not possible because data available does not show γ, but velocities V_x, V_y and V_z. Hence, it was developed a FORTRAN 95 subroutine, called STAGPOINT that searches velocity distribution near leading edge of each section and locates the stagnation point at the closest chordwise U_I value to zero.

For use with membranes, STAGPOINT identifies the membrane type and places the stagnation point at the very leading edge of membrane.

The influence coefficient matrix is calculated using a routine adapted from XFOIL, here named as AIJCALC. Both subroutines AIJCALC and STAGPOINT are shown in Appendix E.

In order to guarantee two-dimensional flow, neighbouring section sources were not allowed to have influence on present section, as discussed by Dvorak et al [69] and Hufford et al [45].

6.3.3 The Coupling Scheme

The derivations made to the coupling scheme for two-dimensional flow in Chapter 5 are valid for the sectional velocity method. Then, the same equation for two-dimensional flow can be repeated here.

$$U_e = U_I + \sum_{i=1}^{N+N_w} G_{ij} \cdot m_{d_i}$$

Different than methods developed by Milewski [48] and Hufford et al [45], the sectional velocity method does not depend on quadrilateral panels. This makes the numerical solution simpler and gives more freedom for user to increase the number of nodes per section, improving the solution for viscous flow.

The computing time will depend on the number of streamlines and the number of nodes chosen to each of them.

6.4 Transition and Separation Identification Using Sectional Method

In Chapter 4 it was introduced a method to identify transition in a strong separation, for the specific case of mast and sail configurations. However, the identification of transition and separation with simultaneous method in continuous velocity distribution, with the method discussed in Chapter 4 is not applicable because it is based in the discontinuous velocity distribution at the mast and sail membrane attachment.

XFOIL code, which is based in the simultaneous approach, uses another routine to identify transition and separation points, called SETBL, developed by Drela and Youngreen [62]. The SETBL has a very complex interaction scheme that will not be detailed here. The original SETBL FORTRAN code, which was used in the sectional method is shown in Appendix E. Just the basic principle of the routine method will be discussed.

The SETBL routine is based in the similarity station principle. It considers a two-dimensional panel i, as illustrated in Figure 6.6, from a section of the body. This panel has two nodes: node 1 is the current node which all boundary layer variables Q and derivatives ∂Q were calculated; and node 2 where, using a linear approximation, boundary layer variables will be evaluated.

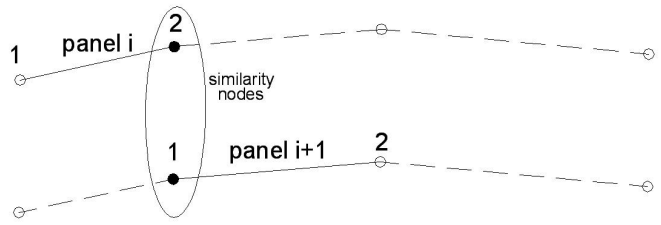

Figure 6.6: The similarity nodes principle from SETBL routine

The routine marches downstream to the next panel $i+1$ where now the node 1 of panel $i+1$ is the node 2 of panel i. The routine will test if the approximated variables to node 2 are similar to the current node 1. If not, residuals will be calculated and a Newton-Raphson method will be applied to drive residuals to zero and a continuity between panels can be guaranteed.

In SETBL routine, there is a percentage of section chord input where, *a priori,* transition is considered to happen. There are two conditions for transition:

- If transition is forced to happen at the specified percentage of chord;
- If the input percentage is an upper limit for transition but its place is determined by the boundary layer development from the interaction, based on $\tilde{n}$ search. This second condition is called by Drela and Youngreen [62] as "free transition".

While the SETBL is marching each panel, $\tilde{n}$ and its derivatives are being evaluated. When using a free transition condition, if $\tilde{n}$ reaches a critical value $\tilde{n}_{crit}$ then transition is set at the current node, as shown in Figure 6.7. If forced condition is used, as shown in Figure 6.8, SETBL will arrange $\tilde{n}$ distribution in order to the specified $\tilde{n}_{crit}$ happen at the specified transition point.

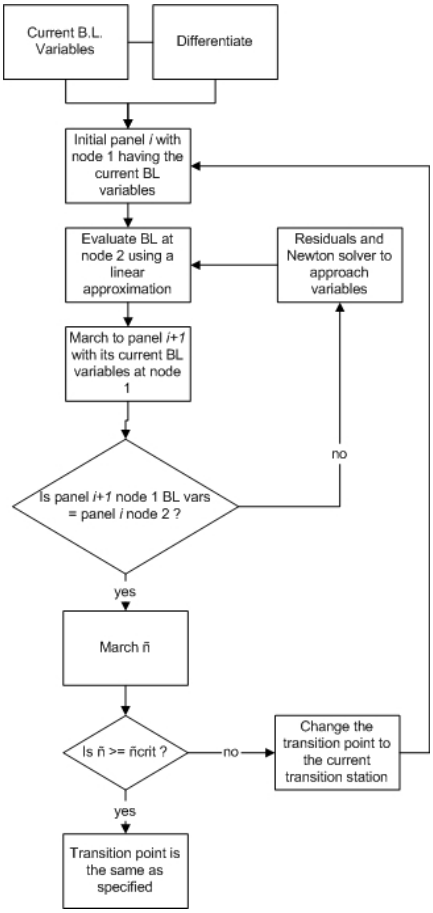

Figure 6.7: SETBL routine with free transition condition

SETBL also searches the H distribution to identify regions of weak separation and give a continuous and smooth treatment to boundary layer variables inside the separated region. This last procedure was called "inverse mode" by Drela and Youngreen [62]. The inverse mode assumes a continuous boundary layer variable distribution inside the separation region, and interpolates its values from boundary layer variables at nodes outside the separated region.

6.5 Convergence and Limitations of Sectional Method

The VIX sectional method uses the approximation of two-dimensional boundary layer flow on each section to evaluate the three-dimensional flow. The initial evaluation of program used a $A_R = 3$ NACA 0012 foil with $Re_\infty = 6.0 \cdot 10^5$ and incidence angle

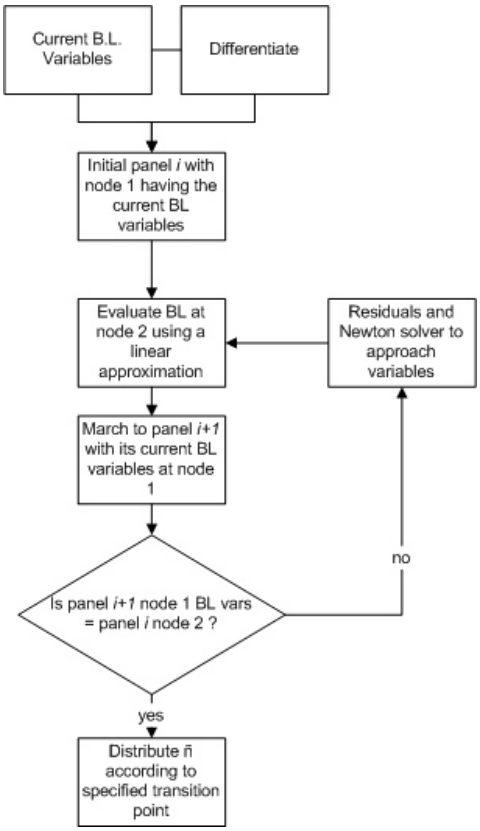

Figure 6.8: SETBL diagram with forced transition condition

$\alpha = 10^o$. Forced transition condition was used with $x_{tr} = 25\%\ c$ on upper and lower surfaces. The initial inviscid solution was obtained using PALISUPAN with a mesh of 2964 body panels, showed in Figure 6.9. There are 38 panels in spanwise direction and 78 in chordwise direction, with an uniform spacing distribution. Just the inviscid solution took 166 seconds of processing time in a PC Pentium IV with 528 MB RAM and 1.4 GHz clockspeed.

6.5.1 Numerical interpolation

The initial inviscid lift coefficient (C_{Li}) was obtained by integrating pressure using trapezoidal rule on panels from PALISUPAN results. Applying the interpolation scheme with 40 sections and 80 points, approximately the same number of panels, lift coefficient obtained was $C_{Li} = 0.484$. Doubling the number of points per section in chordwise direction, lift obtained was $C_{Li} = 0.486$.

Table 6.1 presents lifting force comparison between different distributions of points. The reported experimental value, presented by Turnock and Wright [72] is $C_L = 0.50$.

The interpolation with 300 points in chordwise direction presented a faceted velocity distribution as shown in Figure 6.10, where a tip section inviscid velocity distribution of the NACA foil is presented. The faceted distribution create points of discontinuity and VIX code may not converge. This distribution shape happens because the spacing

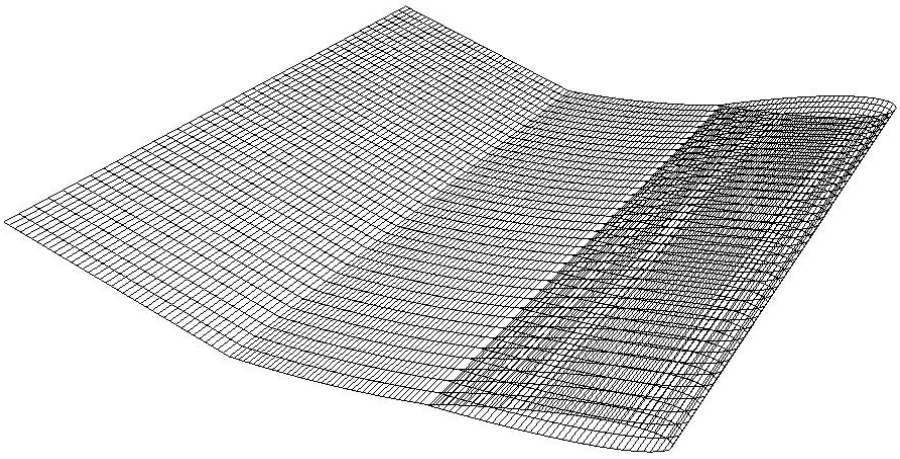

Figure 6.9: Panel mesh of a $A_R = 3$ NACA 0012 foil at 10^o used in PALISUPAN

Mesh Distribution			**Lift coefficient**
Method	span	chord	C_{Li}
PALISUPAN	38	78	0.485
VIX	40	80	0.484
VIX	40	160	0.486
VIX	20	160	0.485
VIX	15	300	0.491

Table 6.1: Table of three-dimensional lifting coefficient using different distribution of points

is so small that interpolation becomes sensitive to the original panel method velocity distribution.

6.5.2 Convergence of Viscous Coupling

The convergence of boundary layer method is reached for each section separately. In average, the sectional method for $A_R = 3$ NACA 0012 foil, takes 7 iterations to converge. Figure 6.11 shows the convergence per section using 40 sections with 80 points each. Doubling the number of chordwise points to 160, the shape of convergence shown in Figure 6.12, assumes a more symmetrical distribution.

The criteria of convergence was set to be the rms of residuals of less than $1.0 \cdot 10^{-4}$. In Figure 6.13 it is shown the sectional viscous lift distribution using different number of points and the original inviscid sectional distribution, calculated by PALISUPAN. z/h is the distance from one tip to another, where h is the total foil width.

It can be concluded that the increase on section points gives a more symmetrical convergence and a more accurate pressure calculation. The limit to the increase of section points is the effect of the faceted mesh and velocity distribution, where discontinuous points can appear and spoil the convergence.

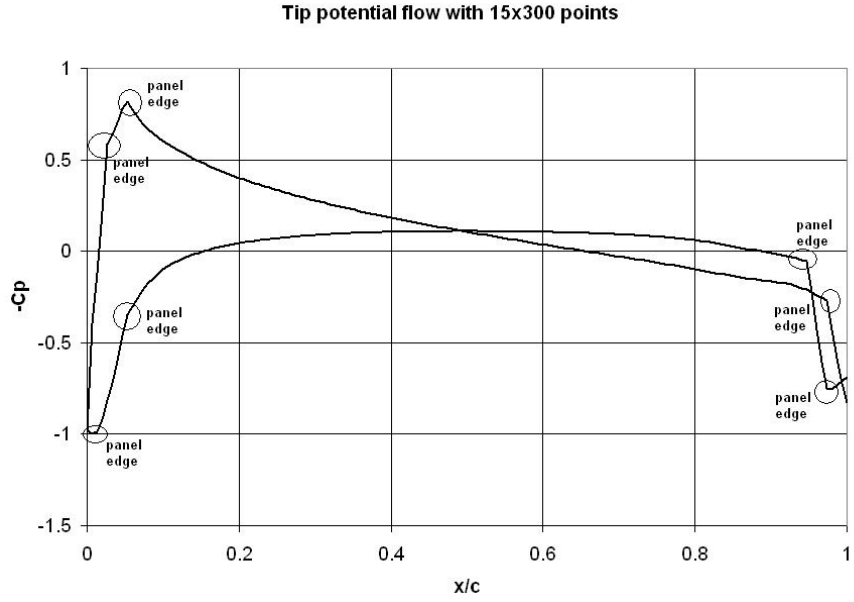

Figure 6.10: Faceted C_P distribution on the tip section of a three-dimensional NACA 0012 foil

6.5.2.1 Tip Section Convergence

As discussed by Hufford et al [45] tip and root regions have a difficult convergence when using the strip theory. With the sectional method, using the example of a $A_R = 3$ NACA 0012 foil, tip regions did not converge, presenting high residuals, in the order of 10^6.

Tip region is where flow is mostly affected by three-dimensional effects and, according to Figure 6.10, it is more likely to present regions with discontinuity in the initial velocity distribution, leading to a difficult convergence. The other sections present a more smooth velocity distribution.

In order to avoid the diverging U_e calculation of the tip section affecting the lift calculation of the other converged sections, boundary layer calculation on this section was not carried out. For lift calculation, just the inviscid pressure distribution was taken into account.

6.5.2.2 Section Frictional Drag Distribution

The objective of section frictional investigation on a symmetrical foil is to show that viscous flow calculation is also symmetric without the consideration of singularities from neighbouring sections influencing the current section. The section frictional drag distribution (C_{Df}), given by equation (6.8) has its distributions for different number of points shown in Figure 6.8.

In Figure 6.8, drag on first and last sections (tip sections) were modified to $8.4 \cdot 10^{-3}$ in order to fit in the graphic. Their values on tip were assumed to be zero on

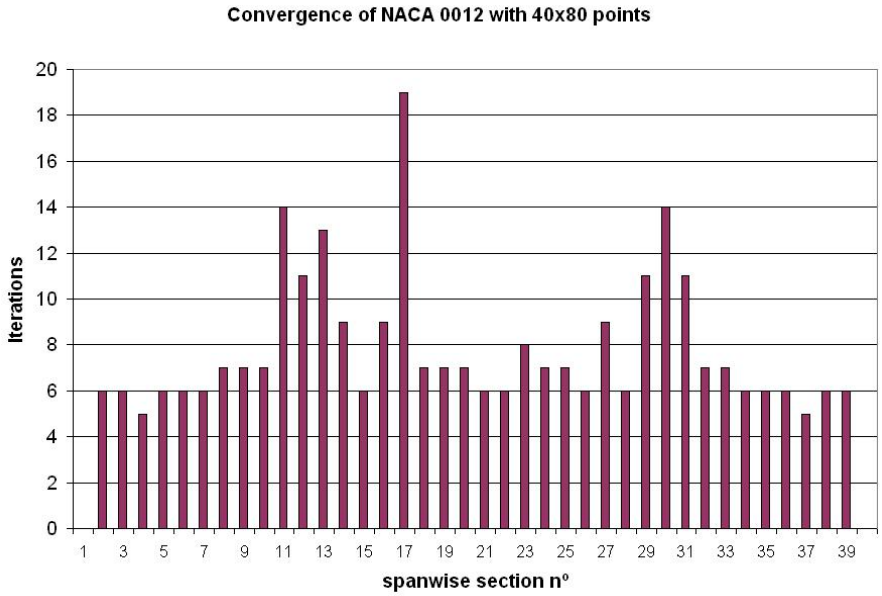

Figure 6.11: Sectional convergence with 40 sections of 80 points each on a $A_R = 3$ NACA 0012 foil at 10^o

calculations.

$$C_{Df} = \int C_\tau dx \tag{6.8}$$

In principle, the biggest number of points gives more details of viscous drag on sections. However, using fewer sections (20) but keeping the doubled number of chordwise points (160), results approach well the finest mesh (40x160 points). This reduction of sections is possible because of the smooth behaviour of sectional velocity distribution.

Errors in velocity interpolation are in the order of 10^{-5} and viscous calculation is assumed symmetrical, showing that the method can be applied successfully in low velocity fluid dynamic problems without considering neighbouring sections influence.

6.6 Wake Adjustment by Means of Viscous-Inviscid Interaction

It was discussed in the previous Chapter, that wake for simultaneous approach needs to be modelled using a distribution of sources with transpired velocities. According to Katz and Plotkin [34], in the inviscid flow, wake should be parallel to the freestream flow, what also needs to be true for the wake modelled with source singularities in the viscous-inviscid interaction, according to Lock and Williams [9].

As discussed by Katz and Plotkin [34], in the general case of wake adjustment wake mesh rolls up near tip regions, simulating a tip vortex. According to Katz and Plotkin [34] this process is called as wake "roll up" but, according to authors [34], it does not bring significative improvement in accuracy to the inviscid flow calculation.

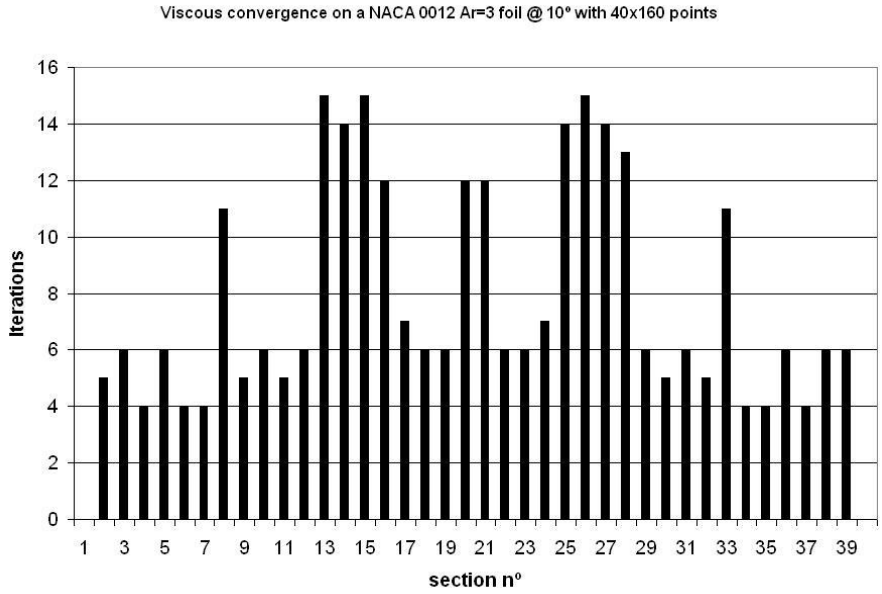

Figure 6.12: Sectional convergence with 40 sections and 160 points of a $A_R = 3$ NACA 0012 foil at 10^o

The wake adjustment discussed in this Section regards only the longitudinal position of wake using transpired sources leaving the trailing edge. It is not considered wake roll up at this point.

Lock and Williams [9] introduced a theory to automatically adjust the wake using the viscous-inviscid interaction method in two-dimensional flow. The process involved another interactive process using more than once the panel method calculation as, the wake adjustment changes the solution.

The method considers the definition of boundary layer variables for wake presented in Chapter 5 and a split solution for lower and upper parts of wake. Wake adjustment may involve discontinuous jumps and some steep boundary layer variables on wake surface, as reported by Lock and Williams [9].

Equation (6.9) gives the jump on inviscid transpired velocity on wake, where W_I is the induced inviscid velocity on wake. U_I is calculated at trailing edge and subscripts l and u stand for lower and upper parts respectively. The sign convention for transpired sources on upper part of wake is positive and on lower part is negative.

$$\Delta W_{Iw} = W_{Iu} - W_{Il} = \sum_{u,l} \frac{\partial \left(U_I \delta^* \right)}{\partial s} = \sum_{u,l} U_I \cdot \sigma \tag{6.9}$$

The main theory of the wake adjustment is based on having the potential jump $\Delta\sigma$ as closer to zero as possible. Considering the transpired source σ on each side of wake (lower and upper), the equation (6.10) is applied on each panel. If φ, in Figure 6.15, is the angle between the matching surface not converged TP to the correct wake dividing

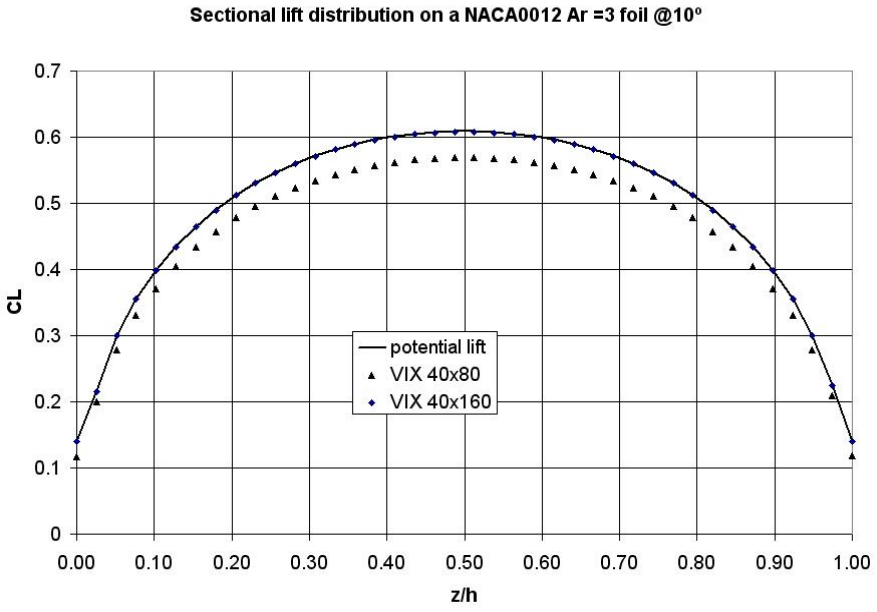

Figure 6.13: C_L distribution using different number of points on viscous flow calculation for a $A_R = 3$ NACA 0012 foil at 10^o

surface $TP\prime$ and, if φ is small, then

$$\frac{W_{Iu}}{U_{Iu}} = \sigma_u, \frac{W_{Il}}{U_{Il}} = \sigma_l \tag{6.10}$$

the following approximation can be considered:

$$\varphi = \tan^{-1}\left(\frac{\partial(\delta_{Zw})}{\partial s}\right) \simeq \frac{\partial(\delta_{Zw})}{\partial s}$$

and so, equation (6.11) can be written.

$$\frac{\partial(\delta_{Zw})}{\partial s} = \frac{\left(\frac{W_{Iu}}{U_{Iu}} - \sigma_u\right)}{1 + \sigma_u^2} \tag{6.11}$$

The same equation (6.11) is applied to the lower side, which has an analogue treatment to the upper part. $\frac{W_{Iu}}{U_{Iu}} - \sigma_u$ is defined here as the wake transpired residual. Considering that σ^2 on lower or upper part will always be very small, it can be neglected in equation (6.11), and it follows that the wake transpired residual must be driven to zero in order to have the correct adjustment of wake.

Interactive process of wake adjustment is presented in Figure 6.16. The first guess for wake considers that, at trailing edge, the wake starts with its bisector and a function guides the wake downstream to the freestream flow direction.

For the sake of simplicity, it was chosen an initial longitudinal wake shape, given by a quadratic function that has an end boundary condition parallel to freestream flow,

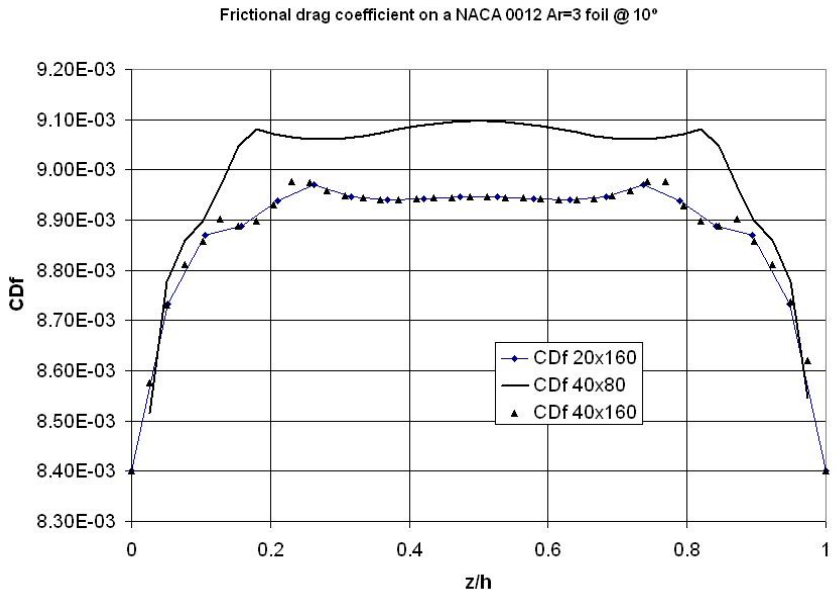

Figure 6.14: Frictional drag distribution on a $A_R = 3$ NACA 0012 foil at 10^o using different number of points

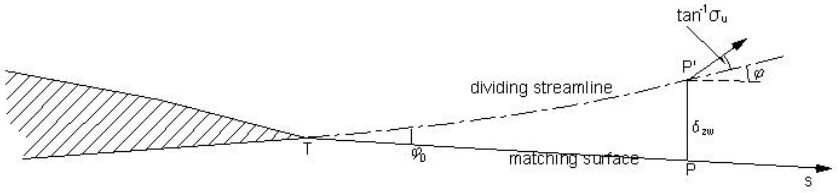

Figure 6.15: The wake adjustment using viscous-inviscid interaction

as shown in Figure 6.17 for 30^oangle of incidence on a F-40 sail. From this quadratic distribution, follows successive interactions with viscous-inviscid interaction method until the wake transpired residuals converge.

The successive use of a three-dimensional viscous-inviscid interaction scheme to correct the wake path in three-dimensions is time consuming because panel method has to be run many times. Two-dimensional cases are faster, because of the smaller number of points and the simpler flow considerations.

Another issue of the longitudinal wake adjustment in three-dimensional flow is the adjustment near tip sections, where simultaneous approach has problems with velocity continuity and the real wake would have a trend to roll up. Hence, the longitudinal wake adjustment was disabled due to difficult convergence. The initial shape generated by a quadratic function was used instead.

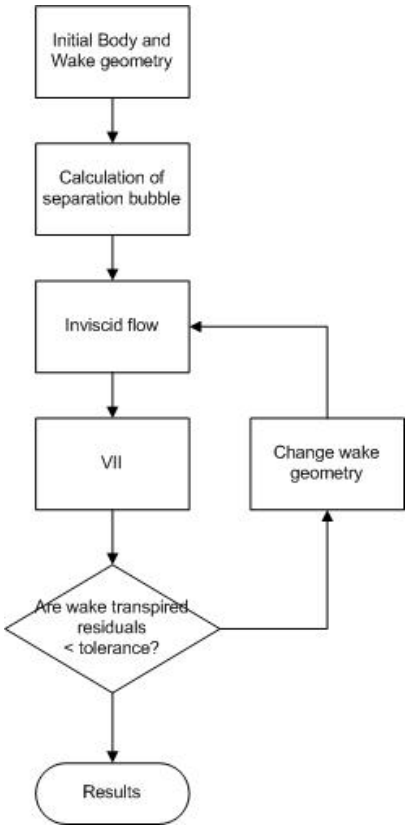

Figure 6.16: The wake adjustment scheme

α(deg)	$\mathbf{C_L}$ **Straight**	$\mathbf{C_L}$ **Quadratic**
3	0.154	0.155
5	0.249	0.253
7	0.351	0.353

Table 6.2: Inviscid lift varying wake shape

Table 6.2 shows lift coefficients from inviscid calculation, comparing a model of a NACA 0012 wing with $Ar = 3$, using a straight wake leaving with the bisector of trailing edge and the quadratic wake shape.

6.7 Summary

In this chapter it was presented the sectional method as an alternative to approximate the three-dimensional viscous flow solution. The advantage of the sectional method is its application as an independent routine to the three-dimensional panel method. The three-dimensional panel method is only used once, in order to obtain initial inviscid velocity distribution and the panel mesh, which will be used in an interpolation scheme to divide body into sections.

A NACA 0012 foil with $A_R = 3$ was used as example, with forced transition condition, in order to investigate the convergence and the solution symmetry, according

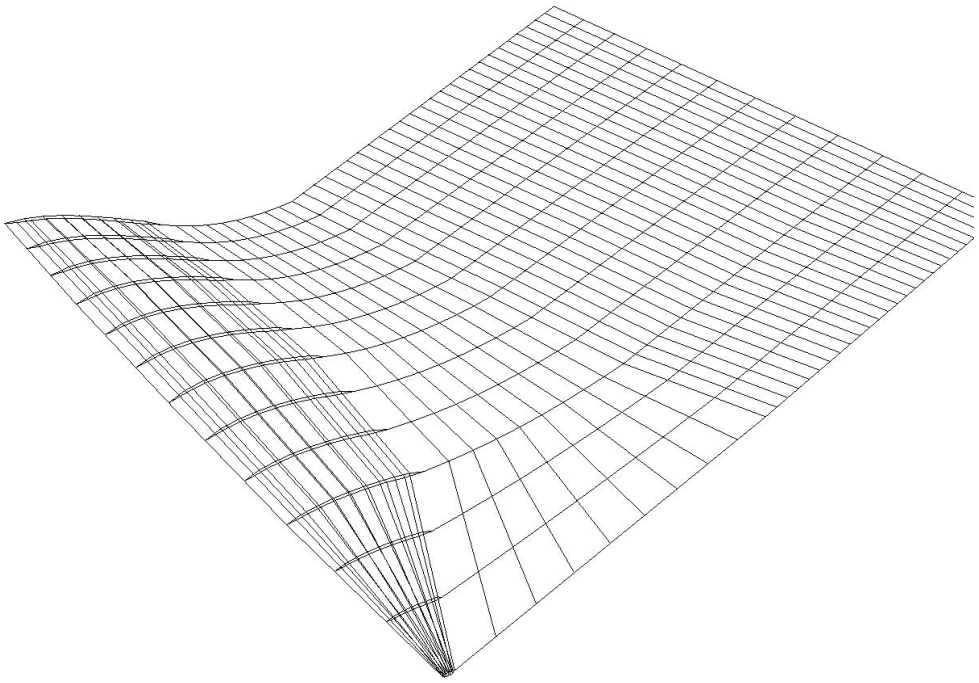

Figure 6.17: A sail with the quadratic sectional wake

to the mesh distribution: distribution of sections and nodes on each section. It was shown that an increase in chordwise points to approximately the double of panels will increase the symmetry of convergence and produce better results.

Convergence problems were detected at tip sections, due to the initial inviscid velocity distribution have presented points with discontinuity. The adopted procedure was the consideration of only inviscid flow at tip sections.

Lately, it was discussed the longitudinal adjustment of wake and its influence to results, without considering more complex three-dimensional effects such as wake roll up. The adjustment of wake using two-dimensional viscous-inviscid interaction methods can be fast, as reported by Drela and Youngreen [62]. However, the adjustment with three-dimensional viscous-inviscid interaction method will demand more computational time as the change in wake geometry configures another panel method solution. Wake longitudinal adjustment may also have some convergence problems at tip sections, due to the trend of wake mesh to roll up.

An alternative was proposed by using a quadratic function to consider wake leaving trailing edge with its bisector and finishing parallel to the freestream flow. The length of wake model has to be adjusted for each case by the user.

In the next Chapter, it will be discussed some cases using simultaneous coupling in two and three-dimensions, where it is intended to study their application with sail membranes.

Chapter 7

Case Studies

In the previous Chapter it was introduced the sectional method for calculating three-dimensional viscous surface flow. As an example it was used the NACA 0012 foil with $A_R = 3$ at $\alpha = 10^o$. The NACA four digit foil has a finite volume inside, where surface panel method and the Dirichlet boundary condition can be applied. The previous Chapter results pointed to a symmetrical convergence for finite span foil and, convergence problems were detected at tips due to velocity distribution discontinuity caused by crossflow.

In this Chapter, it is intended to investigate some three-dimensional foil geometries using the sectional method developed in this work and observe boundary layer characteristics such as flow separation and transition. The sectional method (VIX) is first applied to thick foils, from the NACA four digit series, in order to assess its boundary layer variable H behaviour, by changing some flow settings. It is intended to check qualitatively if boundary layer variables have their behaviour as predicted in works of Gad-el-Hak [1], Gad-el-Hak and Bushnell [49] and Drela [35].

In order to assure that sectional method has the same trend and a good accuracy, it is used the NACA 0020 rudder, with experimental data taken from Turnock and Wright [72] in the analysis.

Once it is shown that sectional method has a close agreement to experimental data, it is the intention to use it to three-dimensional sail membrane analysis. However, three-dimensional membranes have a set of parameters that should be controlled for method convergence and accuracy. The first one, discussed in Chapter 3, is the numerical thickness. In the case of a thin membrane, method convergence and accuracy are dependant on the determination of a suitable thickness that will be adopted to other membrane cases in this Chapter.

Other parameters that should be controlled are the curvature of membrane and flow separation. The NACA $a = 0.8$ meanline series, studied by Wilkinson [4] and Milgram [73] may not be the ideal shape for sails, as it presents flow separation, according to Wilkinson [4].

Most of the experimental data for rigid membranes using the NACA $a = 0.8$ meanline series available are based on two-dimensional flow and a comparison with these data

should be done with a two-dimensional method. Hence, membranes are investigated with the two-dimensional viscous-inviscid interaction method using the simultaneous approach, the XFOIL.

The two-dimensional boundary layer on NACA $a = 0.8$ meanline foils are investigated, in order to detect separation and it is proposed an alternative to NACA $a = 0.8$ meanline series, the Jackson [12] "simple" model for sails.

At last, three-dimensional sail membrane models can be analysed but, other geometry parameters still have to be controlled. Real sails have triangular or trapezoidal shape, twist and variation of sections. Appart from that, the difficulty to find experimental data to compare, makes the analysis more qualitative than quantitative.

Sail membranes are studied using the sectional method by first considering an extruded membrane. From the extruded membrane, three dimensional geometry parameters are gradatively introduced and sails are evaluated at tip and mean sections, with regard to boundary layer development, lift and drag. The investigation of boundary layer development will help on choosing a sail shape that avoids flow separation.

7.1 Three-dimensional NACA Four Digit Foils

Wings using NACA four digit profiles are examples of foils with significative internal volume, where sectional method have normally a fast convergence. It will be used two NACA four digit foils in this Section. The first one, the NACA 0012 with aspect ratio $A_R = 3.0$ foil, will be analysed with the sectional method. Boundary layer variables will be evaluated at the midspan section with the purpose of showing the numerical behaviour of boundary layer with free transition condition, and compare it qualitatively to the observations of Gad-el-Hak [1].

The second foil is the NACA 0020 foil with $A_R = 1.5$, where sectional method, Inviscid, RANS solution and experimental method can be compared in terms of lift and total drag.

7.1.1 The NACA 0012 foil

It was discussed in the previous Chapter that on NACA 0012 foils, apart from tip region, convergence is reached in an average of 7 iterations, using 20 sections and 160 nodes on each section, with the same panel mesh used in Chapter 6. The flow characteristics for NACA 0012 foil are listed in Table 7.1.

Aspect Ratio	3.0
Re_∞	$6.0 \cdot 10^5$
$\tilde{n}_{crit}$	9.0
Range of α	0 to 10^o

Table 7.1: Characteristics of NACA 0012 foil problem

It was used a free transition condition with its limit at 90% c.

7.1.1.1 Varying the Angle of Incidence of the foil

The increase in the angle of incidence, according to Gad-el-Hak [1] and Drela and Giles [35], makes laminar flow to be increasingly more unstable. Then numerically, the increase in incidence angle should contribute to an earlier transition to turbulence.

The objective of the following numerical analysis is to show qualitatively, by means of graphics obtained from VIX analysis, that the increase in the angle of incidence will move the transition upstream, meaning an earlier transition. The transition point can be identified at the maximum of H shape parameter distribution.

Figure 7.1 shows H shape parameter distribution on the upper surface at midspan section, for three different angles: zero, $5^o$and 10^o. The distribution presents a continuous curve, starting with a small oscillation near leading edge and increasing smoothly to a peak where transition happens. After the peak, H decreases smoothly to turbulent values, increasing later, near the trailing edge.

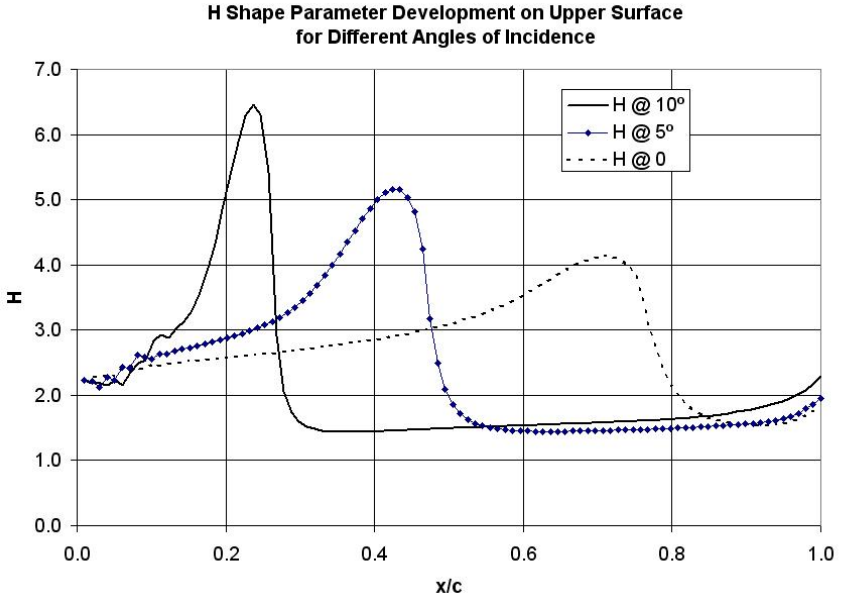

Figure 7.1: H shape parameter behaviour for different angles of incidence on a NACA 0012 foil

In this work, regions with $H > 2.5$ are considered separated flow regions. Table 7.2 shows α and the point of transition, taken at the maximum H.

In Figure 7.1, the transition peak moves upstream with the increase in the angle of incidence. The peak also increases in height and decreases in width. H also an increases near the trailing edge when the incidence angle is increased.

With peaks becoming progressively narrower and higher as α increases, there is a trend to a discontinuous peak if α is large. In a limiting inclination, the appearance of a discontinuous and sharp peak can be understood as a stall.

α **degrees**	**Average Upper Transition (%c)**
0	75
2	63
3	58
5	45
7	34
9	25
10	21

Table 7.2: Variation of transition and frictional force

7.1.1.2 Variation of Critical Amplification Ratio

According to Drela and Youngreen [62], the decrease on the amplification ratio $\tilde{n}_{crit}$ has an effect of shortening the laminar length by imposing a lower limit for laminar momentum instability. In this test, using the NACA 0012 mesh at $\alpha = 0$, it was used the free transition and $\tilde{n}_{crit}$ was reduced.

Table 7.3 shows the transition point on a chord percentage and the frictional drag coefficient C_{Df} adopting two values for $\tilde{n}_{crit}$.

Due to the difficulty to obtain experimental frictional drag data in which $\tilde{n}_{crit}$ is controlled, just a qualitative analysis is performed. According to Drela and Youngreen [62], devices to force turbulence such as, turbulators or sand sheets on the leading edge of a wing, have a similar effect of reducing $\tilde{n}_{crit}$ and, according to Gad-el-Hak [1], it is expected that frictional drag will increase.

$\tilde{\mathbf{n}}_{crit}$	**Average Transition (% c)**	$\mathbf{C}_{Df}$
4.0	64	$5.999 \cdot 10^{-3}$
9.0	80	$4.657 \cdot 10^{-3}$

Table 7.3: Flow characteristics varying amplification ratio

Figure 7.2 shows the comparison of H shape parameter using $\tilde{n}_{crit} = 4.0$ and $\tilde{n}_{crit} = 9.0$. In Figure 7.2 H peak is reduced and transition is moved upstream when using a lower amplification ratio. In this case, $\mathbf{C}_{Df}$ increases, as shown in Table 7.3, because transition length is shortened and separation bubble is reduced or, in some cases, eliminated due to the higher momentum of flow when $\tilde{n}_{crit}$ is decreased.

7.1.2 NACA 0020 Rudder

A NACA 0020 rudder of $A_R = 1.5$ was investigated in order to compare with data from the work of Turnock and Wright [72]. The rudder model is shown in Figure 7.3. In the work [72], authors used a coupled and uncoupled inviscid panel method, the PALISUPAN, to a finite element method (FEA) to analyse flow on a rudder. RANS analysis, uncoupled to the structural model was also done by the authors [72] and it is shown in Figures 7.4 and 7.5.

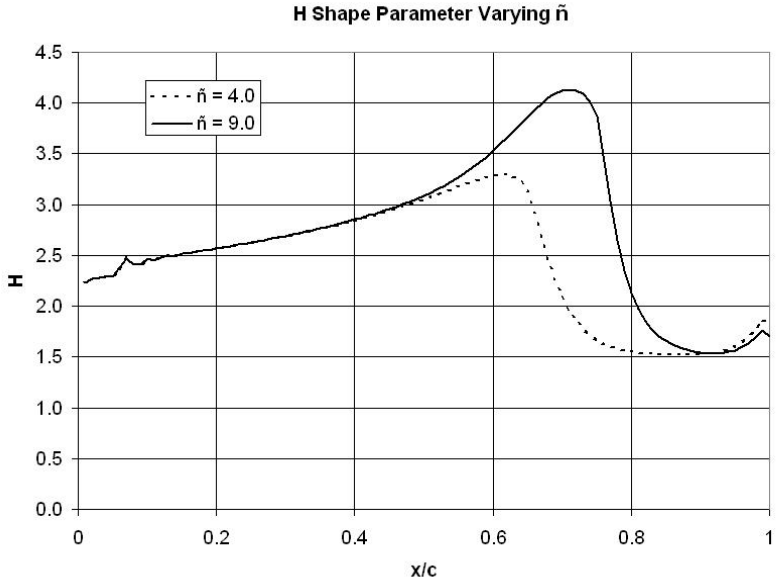

Figure 7.2: H shape parameter varying $\tilde{n}_{crit}$ on a NACA 0012 foil at zero angle of incidence

At rudder's root, it was imposed a reflection condition in order to simulate wind tunnel wall. The VIX analysis was run using $Re_\infty = 1.0 \cdot 10^6$; $\tilde{n}_{crit} = 9.0$ and a free transition condition with $x_{tr} = 90\%\ c$. Figures 7.4 and 7.5 show lift and drag for the rudder model compared to experimental results. Just data from the uncoupled model presented by Turnock and Wright [72] was considered.

At 12.5 degrees, VIX viscous flow did not converge so it is shown the underconverged data at the twentieth iteration.

7.2 Two-dimensional Membrane Analysis

In this section, the two-dimensional simultaneous approach is used in the analysis of membrane profiles. In the first analysis, it is investigated numerically the section thickness reduction and its convergence to a NACA $a = 0.8$ meanline, in order to reach a thickness that is close to the theoretical lift of mean line, discussed in Chapter 3.

A second analysis compares the numerical results from the simultaneous approach to the experimental data from Milgram [73] using NACA $a = 0.8$ meanline profiles. Numerical results are discussed and compared to other foil shapes, such as the cubic foils from Jackson [12] work, in terms of flow separation. It is intended to use the two-dimensional simultaneous viscous-inviscid interaction approach to choose a profile to the three-dimensional analysis performed later in this Chapter.

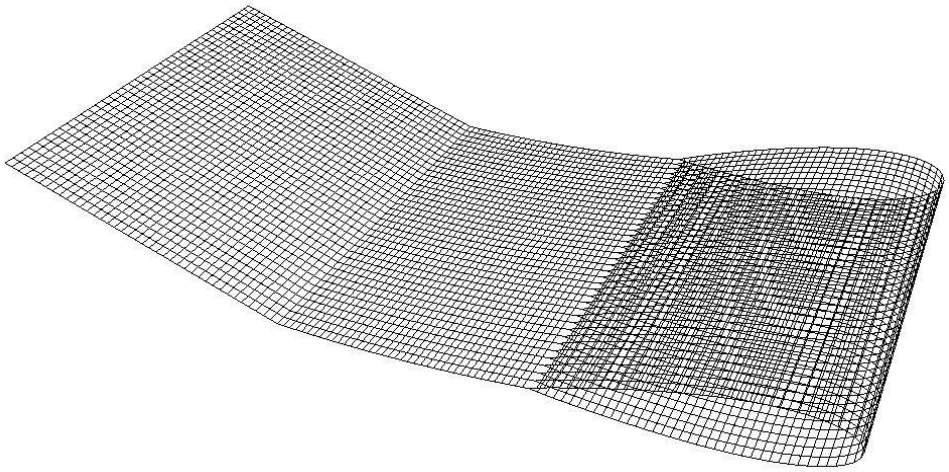

Figure 7.3: NACA 0020 rudder model with $A_R = 1.5$ and 5928 panels used for VIX simulations.

Thickness (%c)	$\mathbf{C}_{Lv}$	$\mathbf{C}_{Li}$	Iterations
2.0%	—	1.126	40 (limit)
1.0%	0.960	1.111	22
0.5%	1.073	1.104	6

Table 7.4: Numerical lift coefficient for NACA a=0.8 mean line at optimal angle

7.2.1 Convergence to Thickness Investigation

Using a two-dimensional simultaneous viscous-inviscid coupling and a NACA $a = 0.8$ membrane with 7.5% c of camber, membrane thickness was successively reduced and compared to the theoretical lift coefficient, given by Abbott and Doenhoff [61]. The starting thickness was chosen to be 2% c, the same thickness used by Elstub [58] in three-dimensional sail flow analysis.

According to Table 7.28, the theoretical optimal lift coefficient (C_{Lt}) for a NACA $a = 0.8$ mean line with 7.5% c of camber and $\alpha_{io} = 1.70^o$, is $C_{Lt} = 1.105$. It was used a free transition condition with $x_{tr} = 90\%\ c$ and a critical amplification $\tilde{n}_{crit} = 9.0$.

Table 7.4 shows the lift calculated by VIX (C_{Lv}) for this NACA mean line at the optimal angle, their respective numerical thickness relative to chord and the number of iterations to convergence. It was used a two-dimensional mesh with nodes equally spaced and a total of 200 nodes.

With 2% thickness, viscous inviscid interaction did not converge, presenting high residuals, in the order of 10^2 at the 40^{th} iteration.

Reducing thickness to 1%, solution converges but, just for some small angles and with 22 iterations. When using a thickness of 0.5% c, the best results were obtained.

The difficult convergence with higher thicknesses is attributed to the leading and trailing edge solutions. A membrane with a large thickness will have a faceted surface

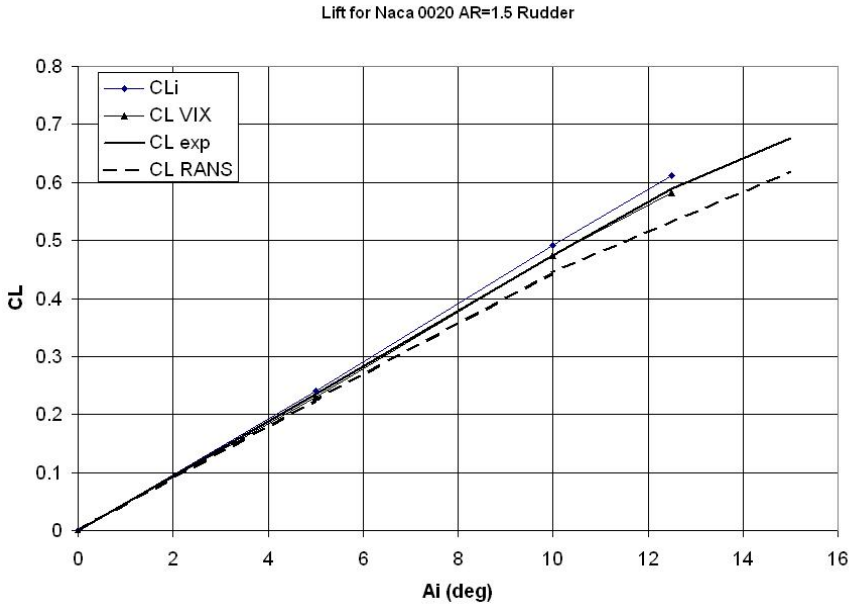

Figure 7.4: Lft coefficient for a NACA 0020, $A_R = 1.5$ rudder on freestream

mesh that will form a bump, and produces high initial velocities. Then, this faceted region will produce, numerically, a strong separation. The separation generates high shape factors (H) and solution does not converge.

With thin thicknesses, the bump effect is minimized and solution converges faster. The problem of using very thin thicknesses, as discussed on Chapter 3, is the close approach problem that can generate a singular panel solution matrix. Thus, the use of very thin thicknesses requires an initial panel mesh more refined.

7.2.2 Comparison with Milgram's Experiments

In Milgram [73] work, it was used rigid foils with the NACA $a = 0.8$ meanline shape and camber ratios: 12% c and 15% c. The objective of the work was the study of the effect of a mast attached to a sail membrane (the NACA $a = 0.8$) in lift and drag. However, data for rigid foils without mast were also provided.

In the experiments of foil without mast, Milgram [73] used rigid NACA $a = 0.8$ profiles made of bronze, spanning a wind tunnel section.

According to Chapter 3, the theoretical lift coefficients, and optimal incidence angles to the studied membranes are:

- Camber ratio 12% c: $\alpha_{io} = 2.72^o$, $C_{Lt} = 1.77$;
- Camber ratio 15% c: $\alpha_{io} = 3.40^o$, $C_{Lt} = 2.21$.

Two-dimensional Inviscid Flow Analysis Applying a two-dimensional panel method calculation to a NACA $a = 0.8$ profile with camber of 12% c, with a mesh of 200 nodes

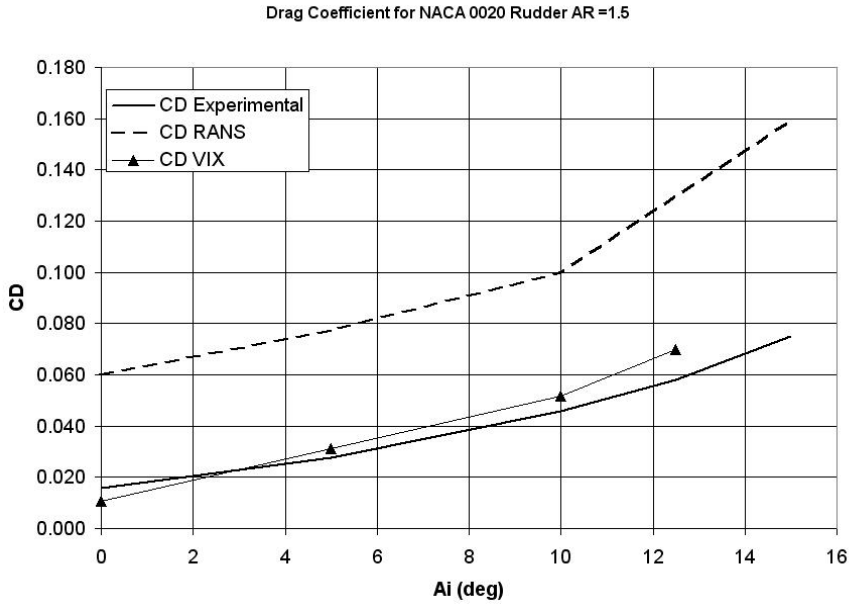

Figure 7.5: Drag coefficient for a NACA 0020, $A_R = 1.5$ rudder

and a numerical thickness of 0.5% c, with zero angle of incidence, the inviscid lift coefficient C_{Li} is 1.52. The same mesh with $\alpha = 2.72^o$ gives $C_{Li} = 1.75$.

According to Milgram [73], the same profile was tested in a range of C_L from 0.5 to 2.2. Then, it is concluded that a C_L of less than 1.52 is only possible if profile had a negative angle of incidence, given, from previous NACA $a = 0.8$ $C_R = 7.5\%$ c panel method analysis, that inviscid panel method calculation does not have a large discrepancy from experimental data.

Separation Detection According to Milgram [73], the rigid sail has a sharp leading edge and, at negative angles of incidence, the lower surface would present separation in this region thus, the simultaneous method may encounter difficulties to converge.

Using the simultaneous approach for the NACA $a = 0.8$ profile at zero angle of incidence, the underconverged H distribution on lower surface is showed in Figure 7.6. In most part of lower surface H reaches values near 10.

The numerical analysis with the simultaneous method failed with the Milgram's [73] profiles. From negative angles to $\alpha = 2^o$ because of the sharp leading edge separation on the lower surface and, up to the optimal angle of incidence because profile also presents a strong separation near trailing edge due to its curvature.

Figure 7.7 shows the underconverged H distribution on upper surface to angles $\alpha = 1.0$, 1.5, 2 and 2.7. H distribution was taken from the 10^{th} iteration of simultaneous approach using XFOIL.

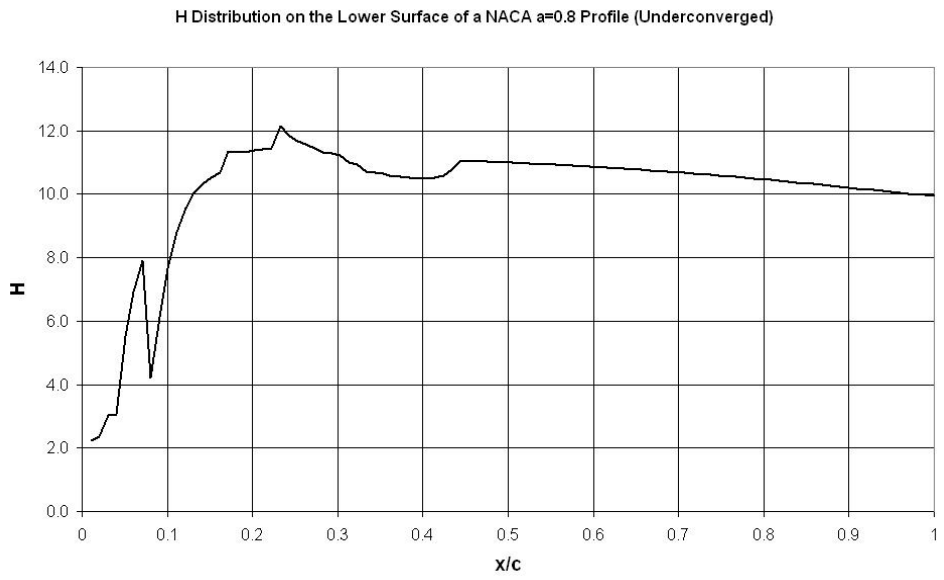

Figure 7.6: H distribution on the lower surface of a NACA $a = 0.8$ $C_R = 12\%$ c foil at 0^o

7.2.3 NACA $a = 0.8$ Partially Separated Flow

In two dimensional flow, the drag of a foil is only influenced by viscous effects and it can be divided in two parts: drag due to viscous pressure, which is related to flow separation and, frictional drag C_{Df}, which is dependant on skin friction. According to Drela and Youngreen [62], once flow is separated, C_{Df} is zero and viscous pressure plays the whole of drag increase.

The NACA $a = 0.8$ $C_R = 12\%$ c profile presents a lift and drag curve taken from Milgram [73] results and showed in Figure 7.8. Comparing to the VIX underconverged results, it leads to the conclusion that experiments had a strong component of partially separated flow. In Milgram [73] work, drag for both foils varied between 0.1 and 0.2 while numerical underconverged frictional drag to the same profile varied between 0.008 and 0.010.

Surface integral boundary layer methods do not have a method to calculate drag with partially separated flow. Hence, drag curves of experimental and numerical methods have such a discrepancy showed in Figure 7.8.

7.2.4 An Alternative to NACA $a = 0.8$ Profiles

As discussed by Wilkinson [4], the NACA $a = 0.8$ profile is not the ideal shape for sails. It presents separation at the trailing edge at its theoretical angle of incidence α_{io} using larger camber ratios ($C_R > 10\%$ c). An alternative to NACA $a = 0.8$ mean line series is the use of Jackson [12] simple sail model. This model permits a direct adjustment of section angles at leading and trailing edges thus, with a control of curvature at these regions. The control of curvature will permit a control of flow separation.

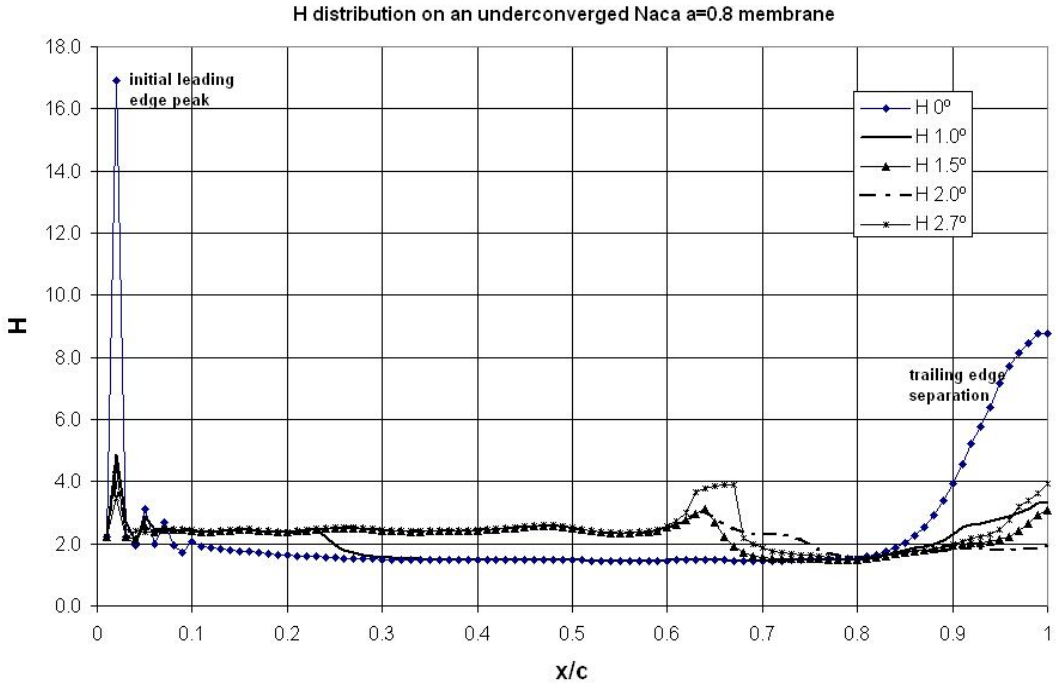

Figure 7.7: H shape parameter distribution for different incidence angles on a NACA $a = 0.8$ membrane and 12% c of camber

However, as far as this work is concerned, there is a lack of experimental data about this foil shape and, in Jackson [12] work, the foil theory was based on the inviscid flow.

7.2.4.1 The Jackson Sail Section Profiles

According to Jackson [12], if trailing and leading edges are fixed to points $(b, 0)$ and $(-b, 0)$ respectively and φ_1 and φ_2 are leading and trailing edge angles of membrane, as shown in Figure 7.9, then profile equation is given by (7.1),

$$\frac{y}{b} = \frac{1}{4}\left[1 - \left(\frac{x}{b}\right)^2\right] \cdot \left[A + \frac{Bx}{b}\right] \tag{7.1}$$

where

$$A = \varphi_1 + \varphi_2$$

and

$$B = \varphi_2 - \varphi_1$$

The lift coefficient, which is inviscid according to Jackson [12], is given by equation (7.2).

$$C_{Li} = 2\pi\left(\alpha + \frac{A}{4} + \frac{B}{8}\right) \tag{7.2}$$

Figure 7.10 shows the lift coefficient to a Jackson profile with $\varphi_1 = 21.5^o$ and

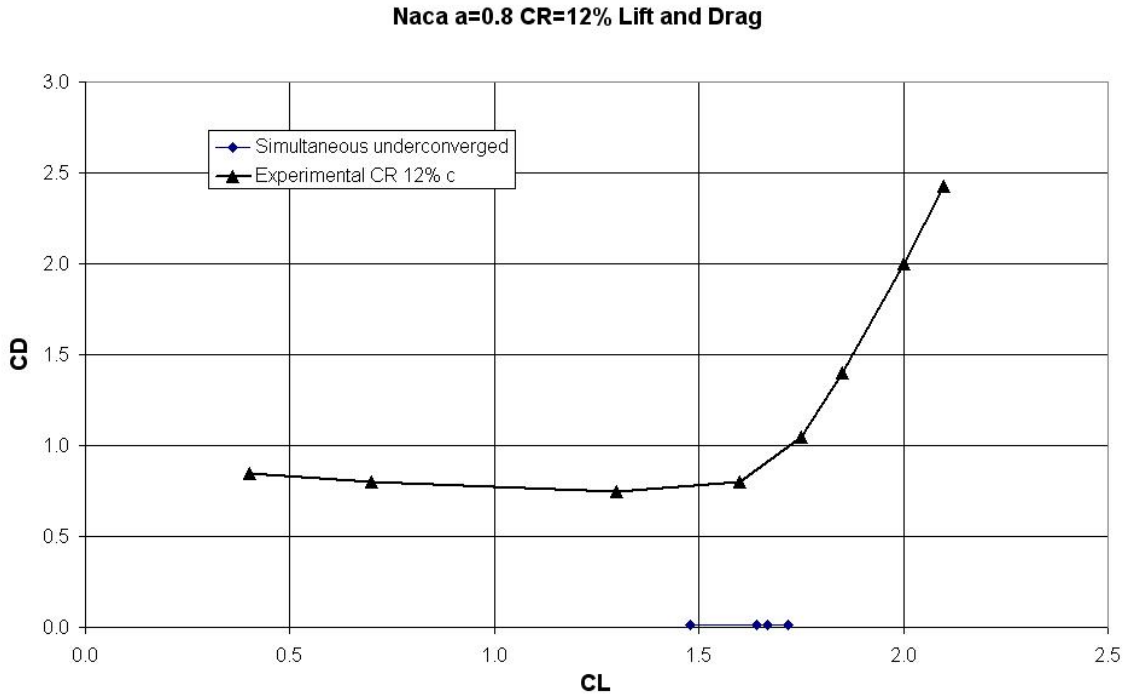

Figure 7.8: Experimental lift and drag curve compared to the underconverged simultaneous approach analysis

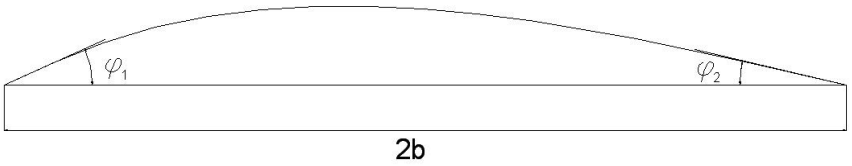

Figure 7.9: Schematic view of Jackson's simple sail profile

$\varphi_2 = 17^o$, comparing with panel method calculation and the adapted simultaneous approach from the XFOIL [62] code. The panel method used is a two-dimensional surface piecewise constant strength with vortex and source singularities. The mesh used for panel method and the simultaneous approach (XFOIL) had 200 nodes equally spaced on foil surface with 0.5% c of numerical thickness.

It was set $\tilde{n}_{crit} = 4.0$ to simultaneous approach analysis (XFOIL) to minimize the high H peaks on the lower surface when $\tilde{n}_{crit}$ is higher. x_{tr} was set to 75% c with a free transition condition. In Figure 7.10 panel and XFOIL curves were plotted from 0.3^o. It was the smallest angle where convergence could be reached to the Jackson foil.

7.2.4.2 Comparison to a NACA $a = 0.8$ Sail Profile

The Jackson is compared to a NACA $a = 0$ profile in order to choose a membrane shape that is less susceptible to separation. The numerical analysis considered a NACA

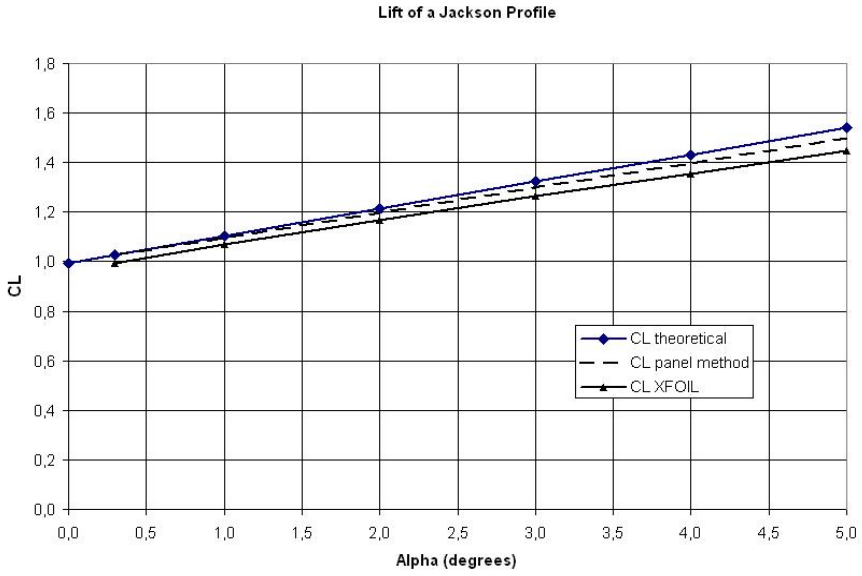

Figure 7.10: C_L comparison of a Jackson profile using the theoretical, panel method and XFOIL calculation

$a = 0.8$ profile that had converged then, it was chosen the $C_R = 7.5\%$ c.

The Jackson profile was considered to be rigid with $\varphi_1 = 21.5^o$ and $\varphi_2 = 17^o$, that corresponds to a $C_R = 8.4\%$ c. The angles of incidence varied from zero to 5^o. The same flow and mesh settings used in the previous analysis of NACA $a = 0.8$ shapes were used to this analysis.

At angles of incidence near zero, the convergence using the simultaneous approach is difficult due to the lower surface separation near leading edge. Convergence is faster to angles from $1^o$to $5^o$where, in general, it is reached with 6 to 7 iterations to both foil shapes.

Figure 7.11 shows the lift calculated by panel method and simultaneous approach (XFOIL) to both foils.

Shape Parameter Distribution on Both Foils H shape parameter distribution is shown in Figure 7.12 to the Jackson profile and, Figure 7.13 to the NACA $a = 0.8$ profile. The Jackson profile presents a H distribution reminding the shape of the NACA four digit foil discussed previously: there is a laminar flow which is characterized by small oscillations and a peak where transition occurs. This peak moves upstream with the increase in the angle of incidence. The peak also shows a small separation bubble when $H > 2.5$. At trailing edge region, H presented values below 2.0, what meant numerically, a flow without turbulent separation at this region.

The NACA $a = 0.8$ profile H distribution, shown in Figure 7.13, has a different shape. It does not present a transition peak. While flow is laminar, there is a small oscillation in H distribution with a practically constant rms with values above 2.5.

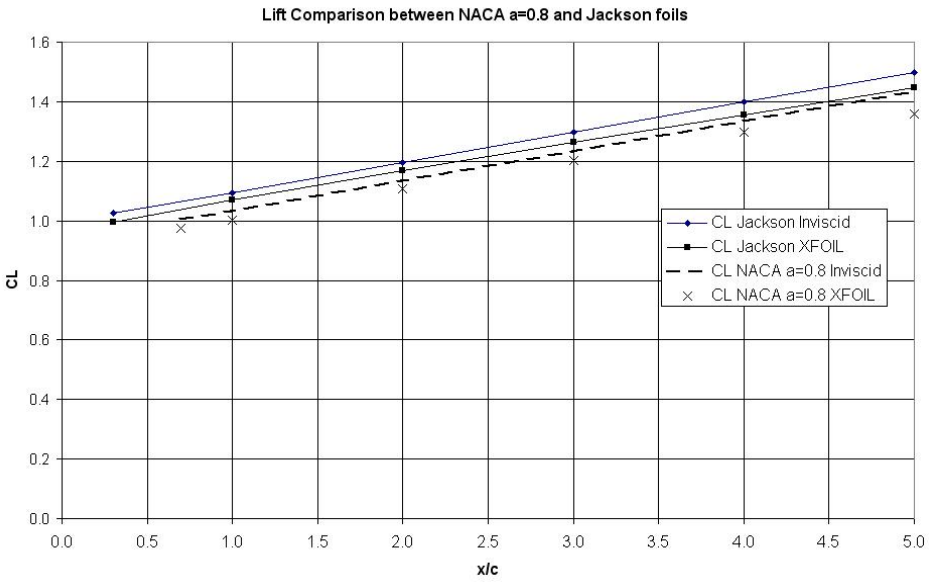

Figure 7.11: NACA $a = 0.8$ $C_R = 7.5\%$ c and a Jackson foil lift comparison

The transition point presents a negative slope where H distribution presents a valley, with turbulent flow and values near 1.5. H increases again at trailing edge region.

The negative slope at transition point, showed in Figure 7.13 moves upstream and, at the trailing edge region, distribution approaches values of $H = 2.5$ when the angle of incidence increases, meaning a trend for trailing edge separation.

Hence, the NACA $a = 0.8$ profile presents two regions with flow separation: the laminar region, where flow has a H distribution above 2.5 and, at the trailing edge where H also starts to increase to values near 2.5. These observations are in accordance to Wilkinson [4] work where two regions with separation bubbles were also detected but, the near leading edge bubble had the influence of mast.

The numerical analysis was done using a NACA $a = 0.8$ profile with a considerable small camber ratio $C_R = 7.5\%$ c. Although results using the Milgram [73] NACA $a = 0.8$ profiles had higher camber ratios, it can be concluded from Figure 7.13 that the laminar region presented a higher H distribution on a long portion of chord length, what characterizes a long separation bubble thus, simultaneous approach could not converge.

7.3 Three-dimensional Sail Membrane

In the previous Section, it was discussed the two-dimensional membrane viscous flow analysis and the limitations of the simultaneous approach to two-dimensional flow. Simultaneous approach cannot calculate drag due to separation and, if separation bubble is long enough, as in the case of Milgram [73] profiles, simultaneous approach does not converge.

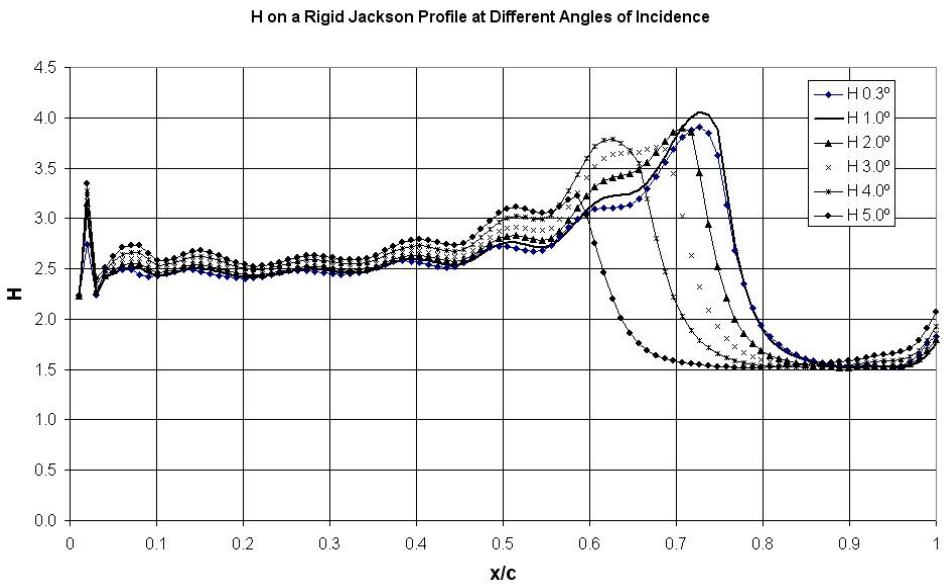

Figure 7.12: H distribution on a Jackson profile at different angles of incidence

The simultaneous approach presented a high sensitivity to flow separation, what should not be understood as a problem. As sail membranes cannot stand separated flow, so they will collapse, the ability to identify a separation before the real sail is built is an advantage.

However, real sails have a complex three-dimensional geometry with variations of section camber from foot to top and its natural twist to wind direction. The investigation of this complex geometry needs a three-dimensional flow analysis tool to identify regions where separation can happen. The identification of separation can aid on minimizing this viscous effect.

In this Section, it will be used the sectional method (VIX), introduced in the previous Chapter, to analyse the viscous flow of three-dimensional membranes, considering the main geometry features such as: reduction of section from foot to top (triangular shape) and variation of section camber and twist. Sails are considered rigid and inextensible throughout all numerical analysis. Results will be discussed qualitatively due to the lack of experimental data to compare.

7.3.1 Extruded Membrane

The extruded membrane is studied here, in order to have a control surface to show how boundary layer behave in a sail without twist and reduction of section. It is the intention to add gradatively the three-dimensional geometry features later and investigate the boundary layer behaviour by means of H distribution curves from selected sections.

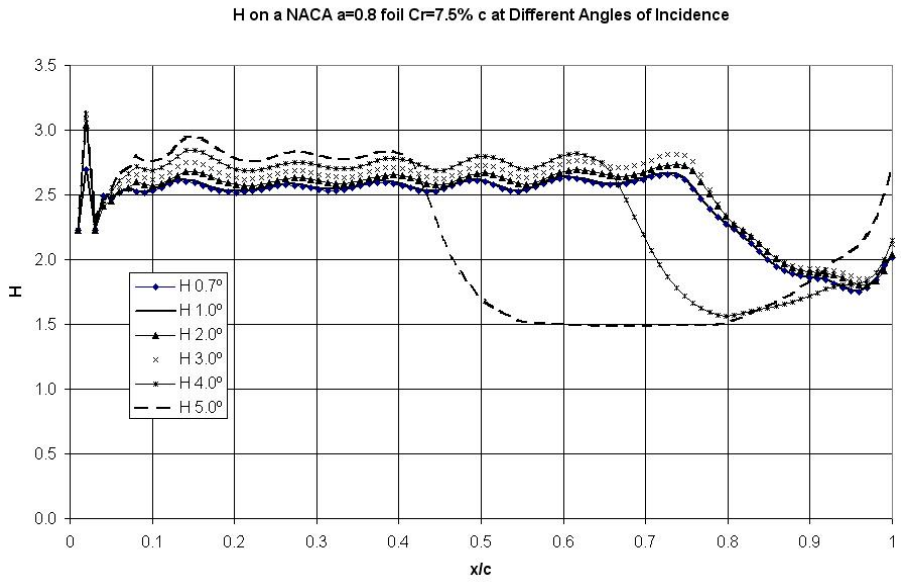

Figure 7.13: H distribution on a NACA $a = 0.8$ $C_R = 7.5\%$ c profile at various incidence angles

7.3.1.1 NACA $a = 0.8$ Extruded Membrane

It was used a NACA $a = 0.8$ membrane with camber of 7.5% c and $A_R = 1.5$. The initial body panel mesh had 2646 with 27 panels spanwise and 98 panels chordwise with a numerical thickness (t_n) of 0.5% c, as shown in Figure 7.14. Membrane data is shown in Table 7.5. It was used the free transition condition but, to force a faster sectional method convergence, x_{tr} was set to 20% c. For viscous-inviscid interaction calculation membrane was modelled using 15 sections with 200 nodes each.

Membrane Data	
A_R	1.5
Re_∞	10^6
$\tilde{n}_{crit}$	4.0
t_n	0.5% c
x_{tr}	20% c

Table 7.5: Extruded membrane data

Convergence to this membrane model is limited to higher angles, however from 1.7 to 7.5, convergence was reached for most of sections in an average of 7 to 8 iterations. Figures 7.15 and 7.16 shows the viscous C_P distribution at the tip and midspan sections. Figures 7.17 and 7.18 shows the H distribution at these two sections.

The C_P viscous distribution presented some oscillations, that are caused due to the proximity of singularities of upper and lower surfaces. On tip section, in Figure 7.15, this oscillation is more visible.

The three-dimensional extruded membrane has a different convergence than the NACA four digit foil. Tip sections have a faster convergence than midspan sections.

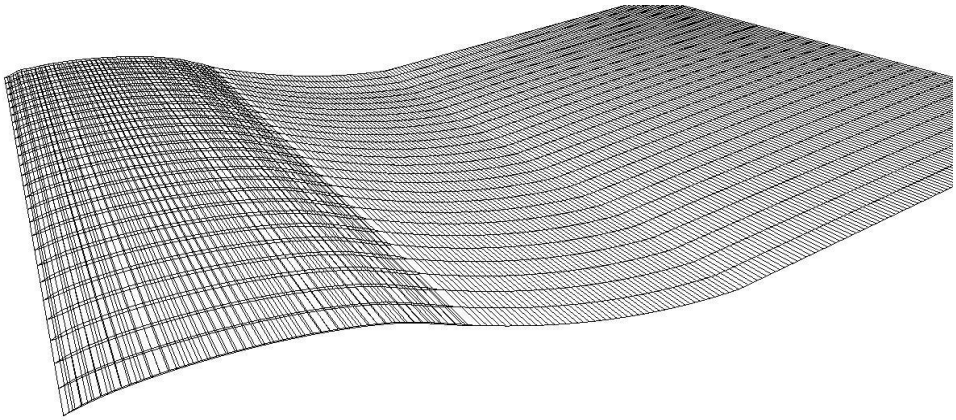

Figure 7.14: Extruded mean line mesh with 2646 panels and 0.5% c thickness used for VIX analysis

For the incidence angles tested, midspan section reach convergence in an average of 15 iterations while near tip sections converged in an average of 7 iterations.

In Figure 7.19, it is shown the development of crossflow velocity W on spanwise direction, on stations at 25% c, 50 % c and 75% c to the NACA $a = 0.8$ foil at $\alpha = 5^o$. Figure 7.20 shows the crossflow development of a NACA four digit foil (NACA 0012) at the same stations, angle of incidence and aspect ratio.

The faster convergence at tips is because crossflow velocity difference between upper and lower surfaces on a thin foil are smaller than a thick symmetrical NACA four digit foil, as shown in Figures 7.19 and 7.20. This difference creates a circulation at tip and it has an influence on streamwise flow. In the case of the membrane, as the difference is small, the influence on streamwise velocity is also smaller, resulting on a smoother and a continuous pressure distribution so, simultaneous method can be applied.

Besides the oscillation produced by numerical effects, observing Figures 7.15 and 7.16, the smaller pressure distribution on tips are the cause that H distribution has smaller values near trailing edge, as shown in Figure 7.17, when compared to a midspan section H distribution, shown in Figure 7.18.

7.3.1.2 The Jackson Extruded Membrane

Using now an extruded Jackson profile with $\varphi_1 = 21.5^o$ and $\varphi_2 = 17^o$, $A_R = 1.5$ and the same mesh and flow settings as the case before, showed in Figure 7.21, the results obtained had the same trend of the NACA $a = 0.8$ foil studied before.

The Jackson extruded profile was analysed at 5^o, $7.5^o$and 10^o. At $\alpha = 1.7^o$, sectional method did not converge because of separation on the lower surface, near leading edge. Pressure distribution is shown in Figures 7.22 and 7.23 for tip and midspan sections respectively.

Midspan sections from the extruded profile were more difficult to converge as expected. However, H distribution, even using higher angles of incidence than the NACA

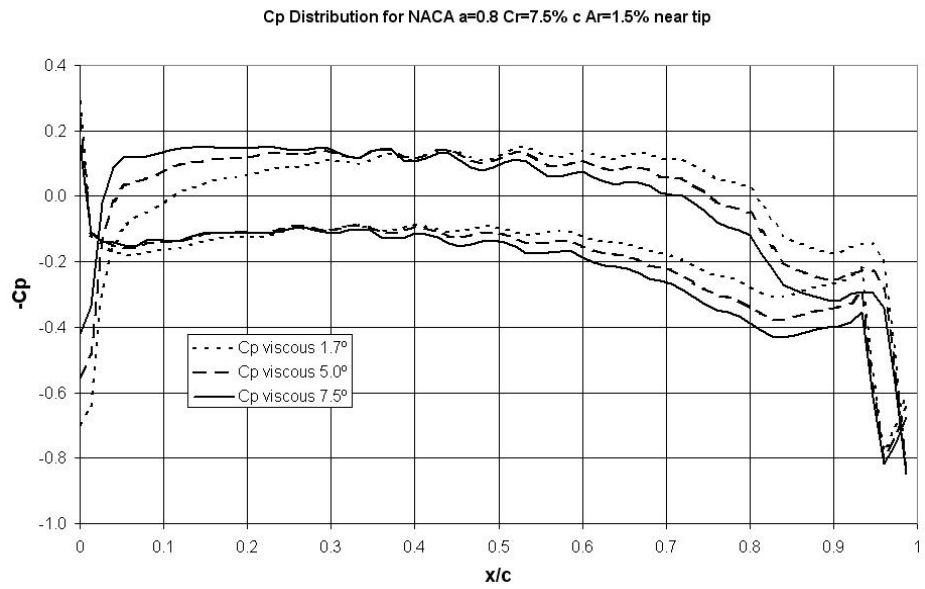

Figure 7.15: C_P distribution for a NACA $a = 0.8$ foil near tip region at various angles of incidence

$a = 0.8$ profile, presented smaller values near trailing edge, as shown in Figures 7.24 and 7.25.

7.3.2 The Real Sail Model

The previous flow analysis case used a rectangular ($A_R = 1.5$) extruded sail membrane. The analysis was applied on extruded NACA $a = 0.8$ and Jackson foil profiles. The Jackson profile presented a better convergence to higher angles of incidence and a smaller H distribution near trailing edge, what can be concluded that a sail with the Jackson profile would have less trailing edge separation than a NACA $a = 0.8$.

However, as discussed by Whidden and Levitt [13], real sails have triangular shapes or, section lengths that decrease from foot to top, and a twist in the direction of wind. Because the twist on a triangular sail exists, sailmakers, according to Whidden and Levitt [13], can make sections with their camber gradatively decreased from foot to top, in order to improve the sail performance to the varying angles of incidence caused by the twist.

The objective here is to analyse a sail with the sectional method, using the twist and the variation of section cambers. To do so, a modeller for twisted sails was created for simulating a real sail membrane. The modeller was written in FORTRAN 95, with its code presented in Appendix E and its theory discussed in Appendix B.

The modeller create the sail surface based in three curves: foot curve, leech curve and top. The forehead curve is considered as a straight line. Higher order curves on the forehead edge were not used in this version of modeller, in order to simplify sail modelling. The three curves are quadratic polynomials that use local coordinates that

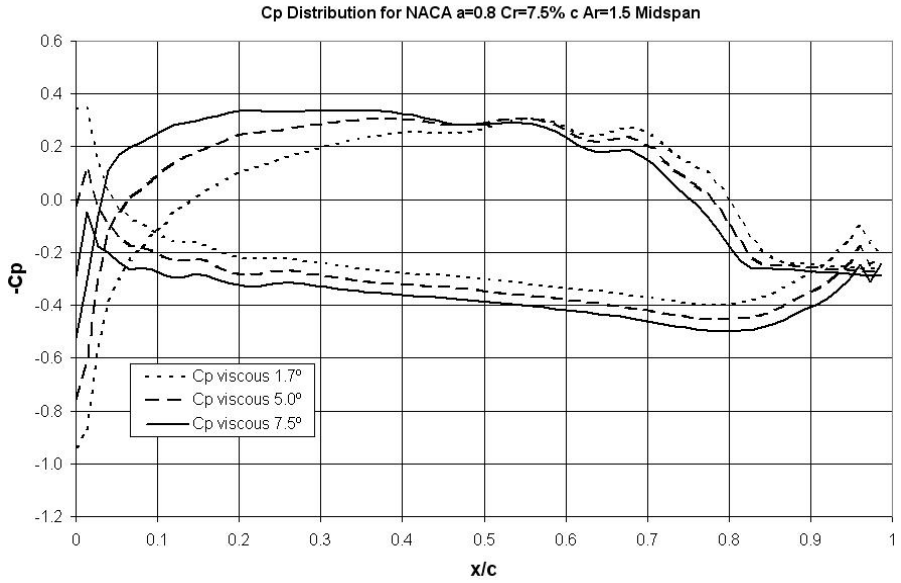

Figure 7.16: C_P to a NACA $a = 0.8$ foil at midspan section at various angles of incidence

vary between 0 and 1. The user inputs the place of maximum chord and the camber in percentage.

The leech curve is controlled by three parameters: Top section angle of incidence, called here as the "differential" angle, shown in Figure B.10; the scale of sections from foot to top making a trapezoidal sailplan profile and the quadratic polynomial that describes trailing edge opening (yz plane) from foot to top.

A schematic illustration of sail membrane modelling is given in Figure B.10.

7.3.2.1 The Control Sail Analysis

A control sail, called "Sail 0", is used to compare with results. This control sail has a constant section camber and no twist. Just its trapezoidal shape is similar to the others with root length of 1.0, top of 35% of root length and $A_R = 1.5$.

The constant section uses a Jackson [12] profile with $\varphi_1 = 21.5^o$ and $\varphi_2 = 17^o$. Flow settings have their values presented in Table 7.5. The incidence angle is 18^o.

Sail 0 does not converge at this angle of incidence because of separation near trailing edge region but, the underconverged results are shown in Table 7.6.

Sail 0 Results	
C_{Li}	0.644
C_{Lv}	0.609
$C_{Di(i)}$	0.195
$C_{Di(v)}$	0.175
C_{Df}	$5.88{\cdot}10^3$
V_{CP}	0.437

Table 7.6: VIX underconverged results for sail 0

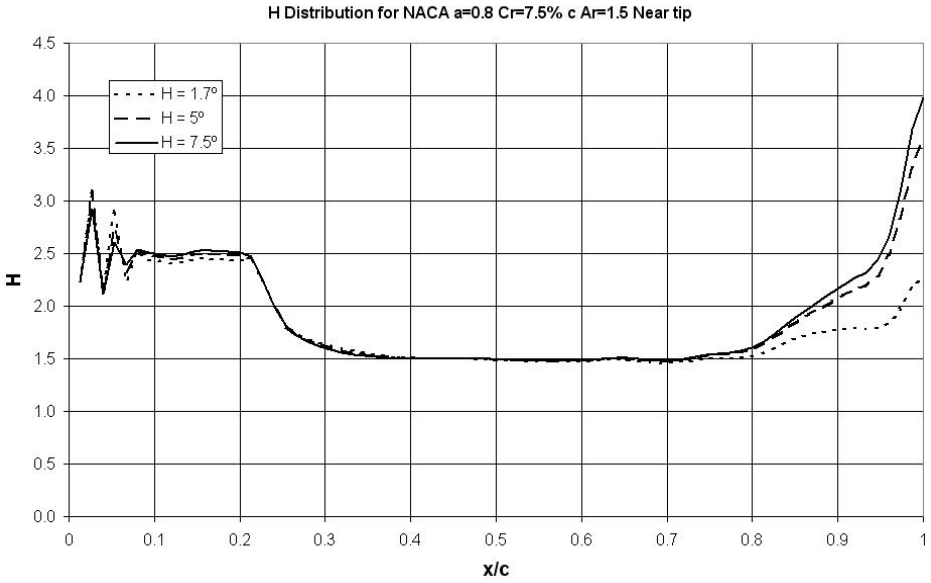

Figure 7.17: H distribution to a NACA $a = 0.8$ foil near tip region

Sail 0 mesh is shown in Figure 7.27.

7.3.2.2 Variation of Twist and Camber

Two sails were created using the modeller:

- Sail 1 with the same sections as sail 0 but, with a twist of 10^o;
- Sail 2 with sections decreasing angles φ_1 and φ_2 in a cubic approximation from foot to top, as given in Table of Figure 7.28, using the same twist as used by Sail 1.

All sails were analysed using $\alpha = 18^o$. Results for sails 1 and 2 are shown in Tables 7.7 and 7.8, with an average convergence of 7 iterations.

Sail 1 Results	
C_{Li}	0.722
C_{Lv}	0.712
$C_{Di(i)}$	0.189
$C_{Di(v)}$	0.184
C_{Df}	$6.65{\cdot}10^3$
V_{CP}	0.423

Table 7.7: VIX results for sail 1

Sail 2 results, shown in Table 7.8, presents inferior results in terms of lifting force, considering that it operates at $\alpha = 18^o$, as sails 1 and 0.

Comparing H distribution on a midspan section, as shown in Figure 7.29, Sail 0, although it did not converge, it presents a high H distribution near trailing edge,

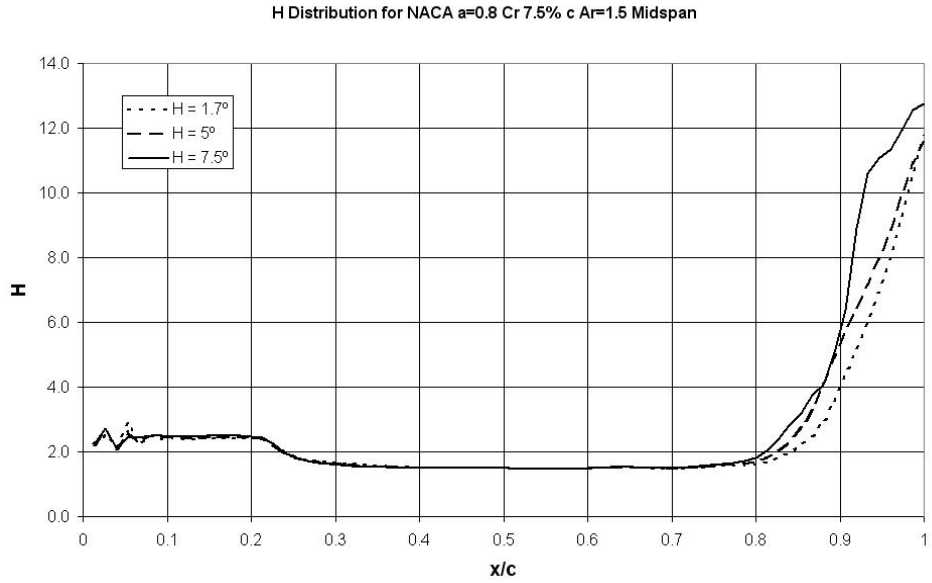

Figure 7.18: H distribution to a NACA $a = 0.8$ foil at midspan section at various angles of incidence

Sail 2 Results	
C_{Li}	0.610
C_{Lv}	0.598
$C_{Di(i)}$	0.164
$C_{Di(v)}$	0.157
C_{Df}	$6.92{\cdot}10^{3}$
V_{CP}	0.387

Table 7.8: VIX results for sail 2

meaning flow separation. Analysing the Sail 1 H distribution, it has a weak trailing edge separation and Sail 2 does not have trailing edge separation on midspan.

Top sections H distribution for sails 1 and 2 are showed in Figure 7.30. By observing these distributions of Figure 7.30, it can be concluded that sail 2 is less susceptible to trailing edge separation.

Hence, the use of a small twist can improve the performance of a sail by minimizing trailing edge separation. The gradative reduction of sail section camber from foot to top allied to twist helps on minimizing flow separation. According to Widden and Levitt [13], this reduction of camber is a common practice applied by most of sailmakers.

In a yacht, the choice of different cambers can even be used to reduce the vertical centre of pressure V_{CP} and improve the equilibrium heeling angle, as long as data of yacht hull and appendages are available.

Comparison to experimental results were not possible in this Section, because there were no data available with this level of detail to three-dimensional rigid sails. However, the analysis performed here are in accordance to the observations of Marchaj [10].

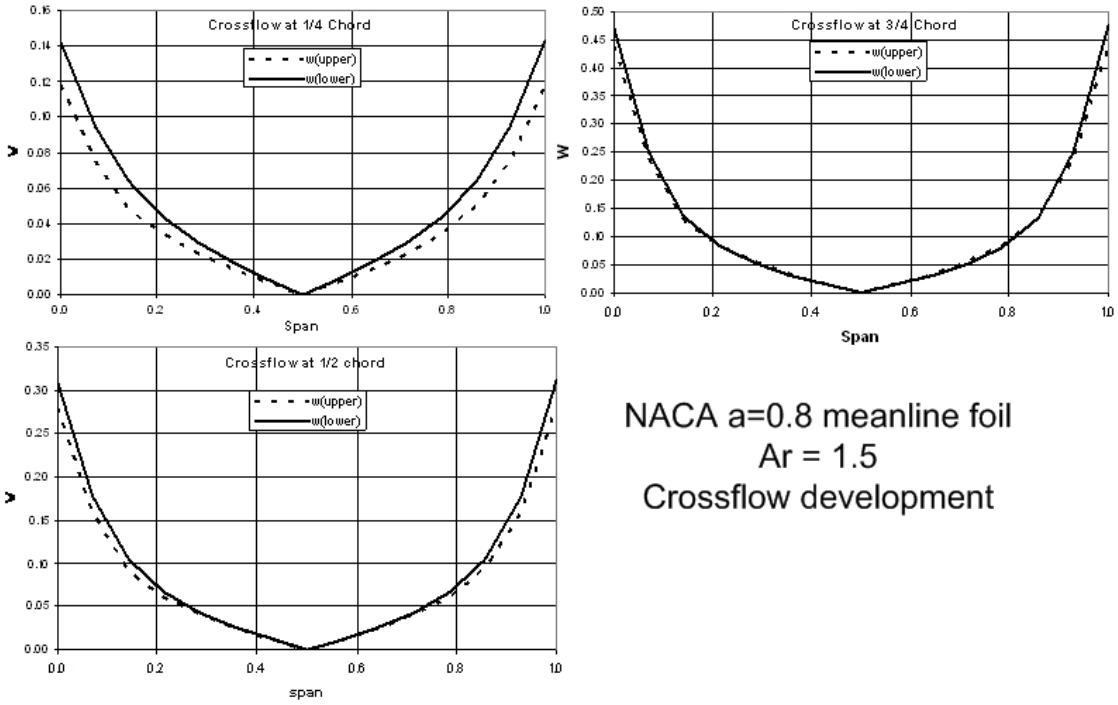

Figure 7.19: Crossflow W development on a NACA $a = 0.8$ foil $A_R = 1.5$ at $\alpha = 5^o$

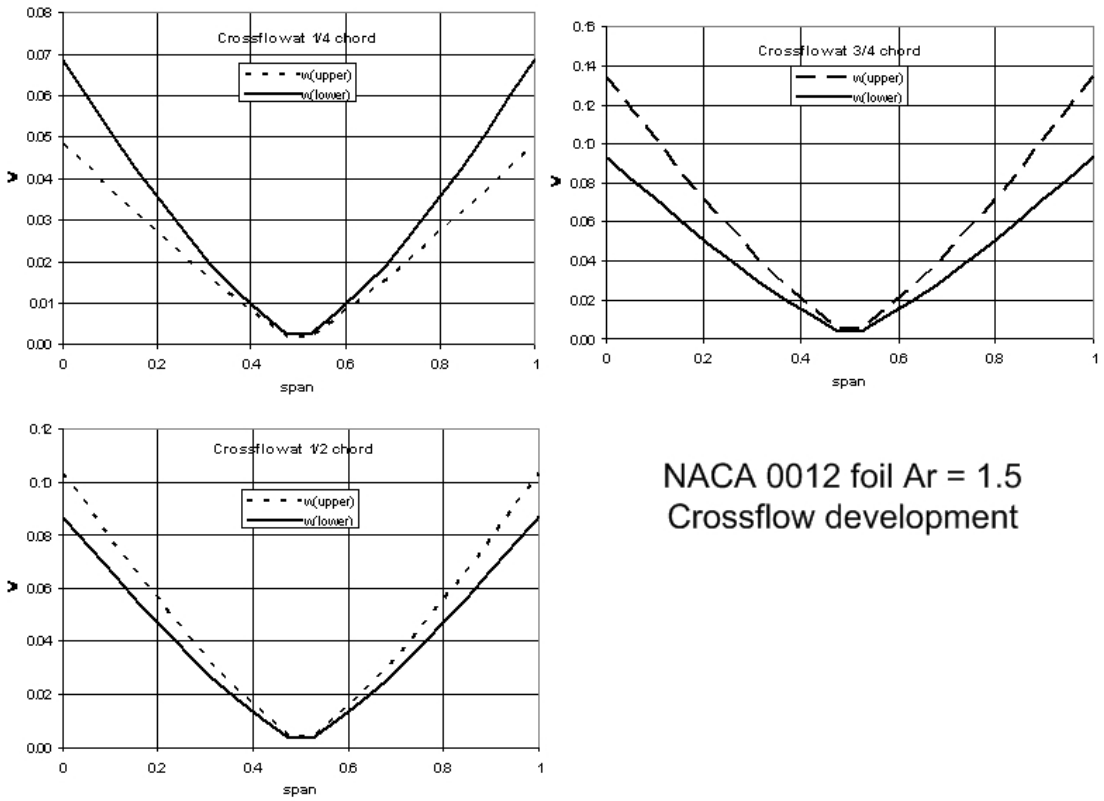

Figure 7.20: Crossflow W development at different stations of a NACA 0012 foil $A_R = 1.5$ at $\alpha = 5^o$

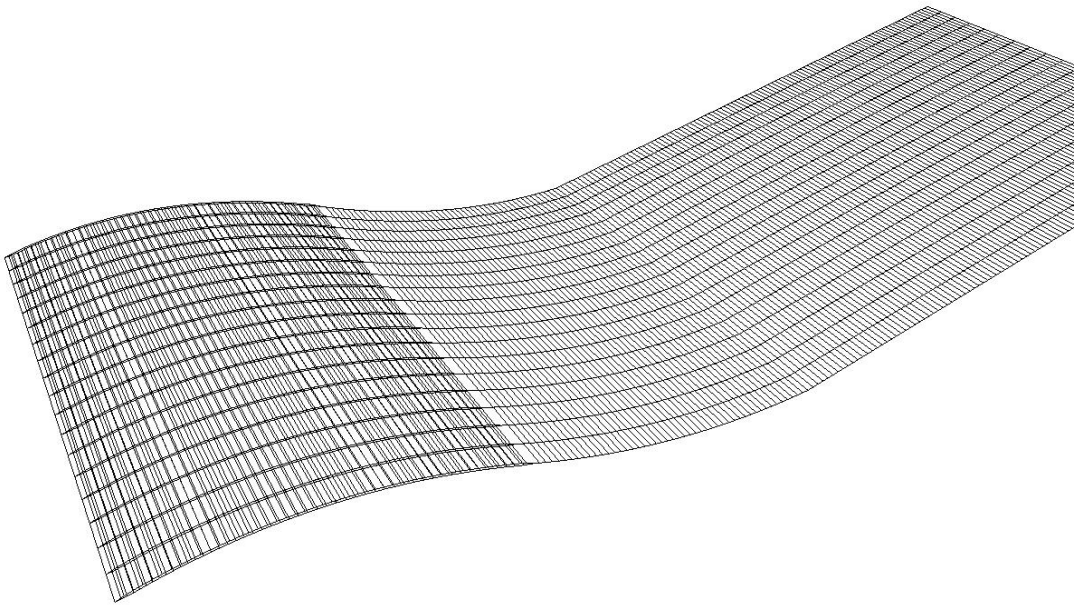

Figure 7.21: Panel mesh of an extruded Jackson profile

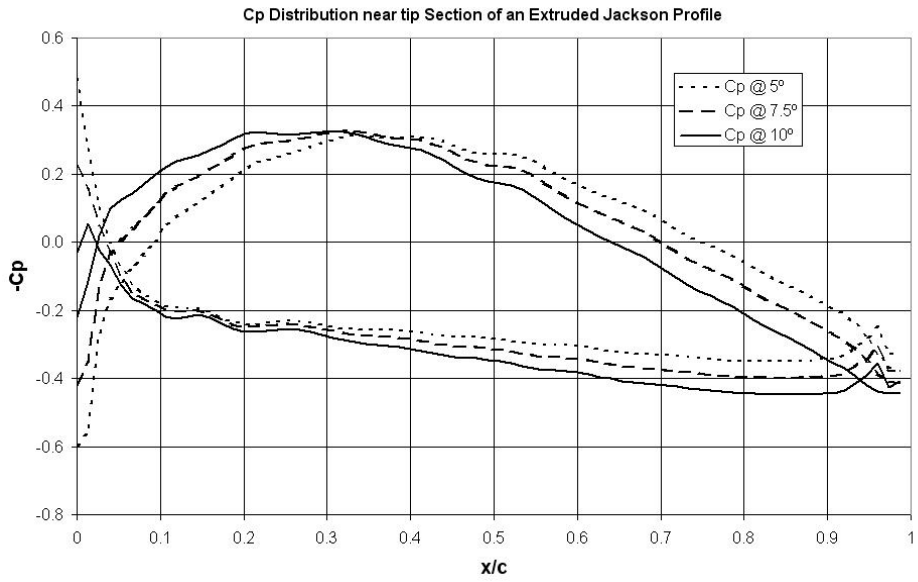

Figure 7.22: C_P distribution on a tip section of an extruded Jackson foil at various angles of incidence

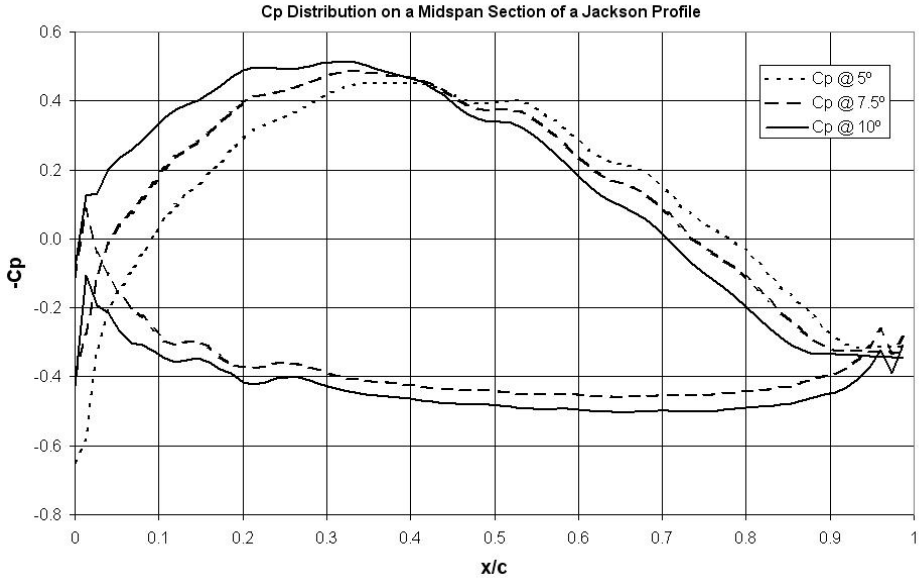

Figure 7.23: C_P distribution on a midspan section of an extruded Jackson foil at various angles of incidence

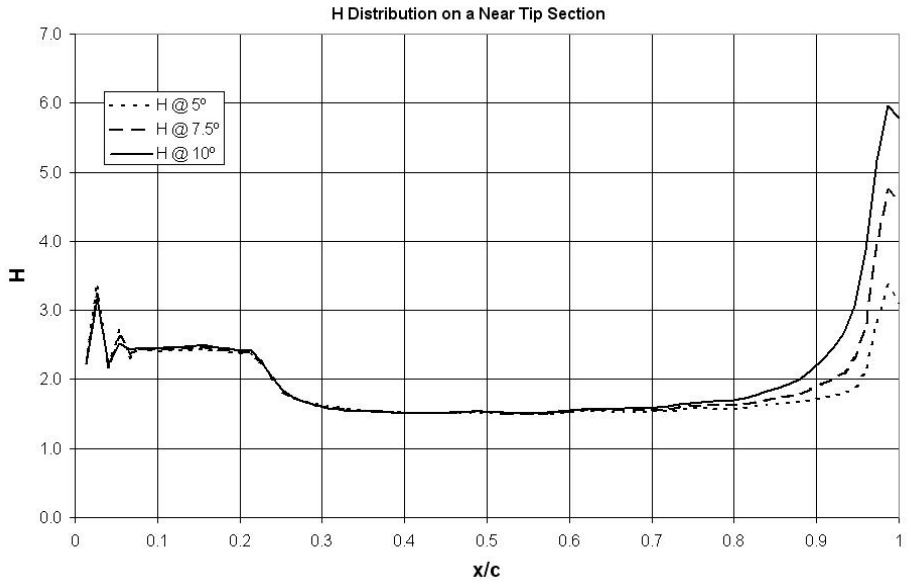

Figure 7.24: H distribution on a tip section of an extruded Jackson foil at various angles of incidence

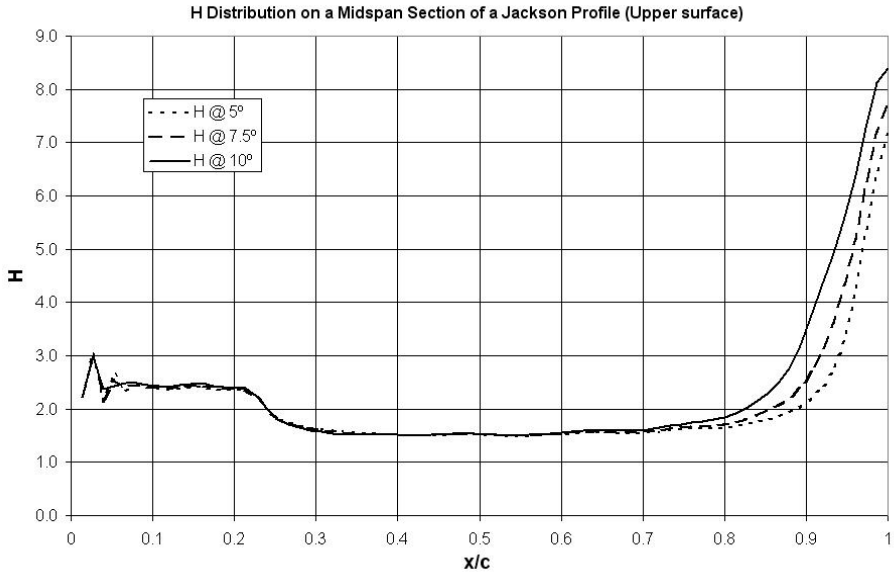

Figure 7.25: H distribution on a midspan section of an extruded Jackson foil at various angles of incidence

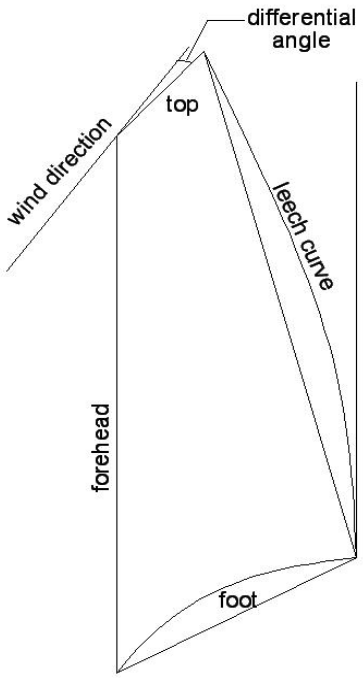

Figure 7.26: Twisted sail modeller scheme

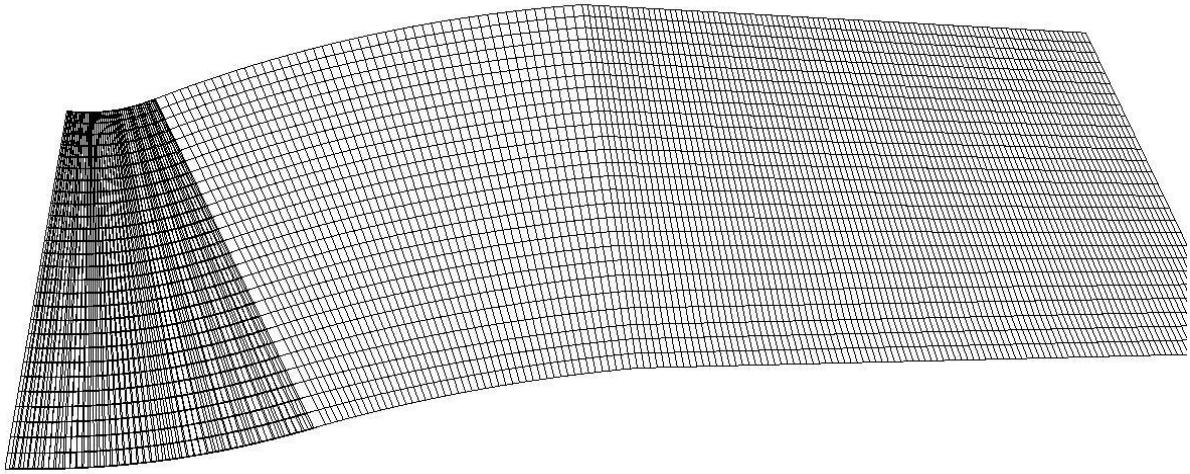

Figure 7.27: Sail 0 panel mesh

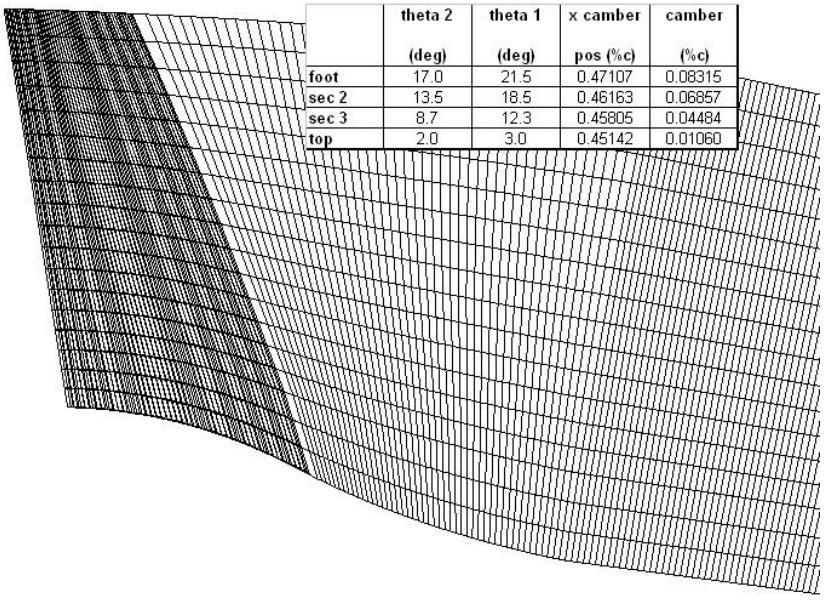

	theta 2 (deg)	theta 1 (deg)	x camber pos (%c)	camber (%c)
foot	17.0	21.5	0.47107	0.08315
sec 2	13.5	18.5	0.46163	0.06857
sec 3	8.7	12.3	0.45805	0.04484
top	2.0	3.0	0.45142	0.01060

Figure 7.28: Twisted sail mesh with a table showing its geometrical data

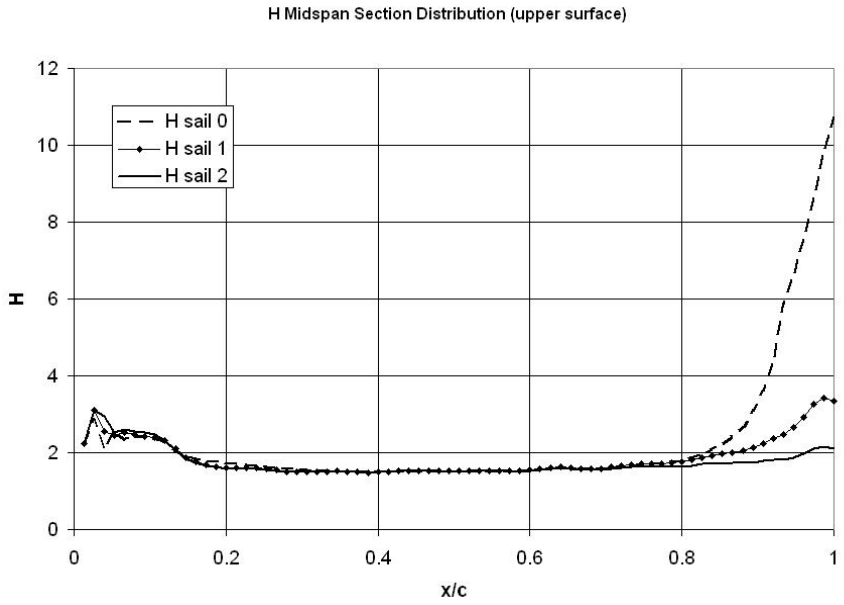

Figure 7.29: H shape parameter (upper surface comparisson between sails 0, 1 and 2

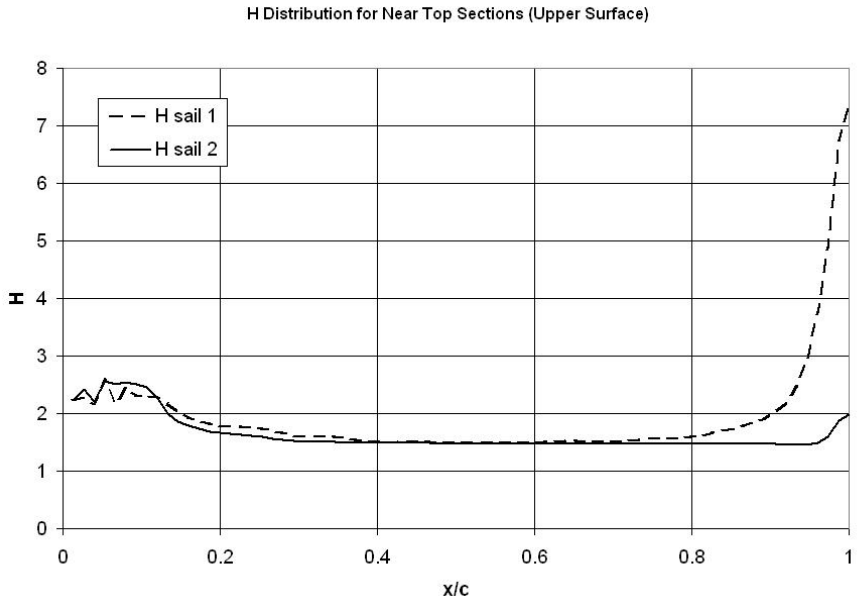

Figure 7.30: H distribution for sails 1 and 2 on near top section

Chapter 8

Conclusion

In this work, it was discussed the development of a surface method for viscous flow analysis applied to sail systems. Flow on sail systems has the characteristic to be low speed, where it lies in the transitional range; low altitude, so viscous effects from the sea waves can influence in viscous flow development.

Sail membranes have the characteristic to be flexible and thin and they only resist to tension on their surfaces so, they need structures at their edges to support the tensions (mast and boom). Wind action can deform the sail, creating a curved shape that will generate lift at small angles of incidence. The curved shape and the interaction with supporting structures create a partially separated flow on sail surface.

Sails can deform and even stretch with wind action, making their flow analysis part of an aeroelastic interaction, as discussed in Chapter 2, where the aeroelastic analysis scheme was showed in Figure 2.8. In this work, sail membrane is considered rigid and the stress-strain analysis is suppressed. This consideration was done because of the following reasons:

- The few experimental data for sails consider rigid sail membranes;
- Characteristics of viscous flow, such as separation, could be better studied and compared maintaining a rigid shape.

The objective of this work was the flow analysis of a sail system using the sectional method. The sail system and flow with their characteristics discussed before, demands an unique flow analysis method that can be added as a module to other multi-parameter analysis, such as aeroelastic, sail shape optimization or global performance analysis.

Methods with heavy computing requirements, such as RANS, cannot be applied properly to the multi-parameter analysis, regarding the high number of interactions and the complex mesh model.

The sectional method is a surface method for viscous flow analysis, based in the viscous-inviscid interaction (VII). The VII, according to Lock and Williams [9], is introduced in the integral boundary layer theory, which has in its momentum equation two parameters, δ^* and θ, related to normal displacement from original surface, in order to create an equivalent inviscid flow.

There were discussed two similar principles for viscous inviscid interaction: the normal displacement of surface panels at a distance δ^* from the original body or, the use of a distribution of transpired sources where their strengths were given by a function of δ^*.

The normal displacement of surface characterized another body geometry, which would have to undergo to the process of mesh modelling and inviscid calculation. In an interactive process, the constant change in body geometry between iterations would be time consuming so, the transpired source principle was chosen.

There are two typical approaches to a VII method: The direct and the simultaneous. The direct approach assumes that initial inviscid velocity is predominant and viscous flow is dependant of a small correction in relation to the initial velocity. Commonly, integral boundary layer methods such as Thwaites and entrainment method are used to evaluate this small correction.

The simultaneous approach assumes the initial inviscid velocity as incorrect and uses a system with the inviscid and viscous equations to simultaneously correct the initial inviscid velocity. Simultaneous approach uses more sophisticated boundary layer methods such as the lag-entrainment and a special closure equation, as discussed in Chapter 4 for transitional flow. Because of the two-equation system, the simultaneous approach is interactive, while the direct approach is normally a one-step process.

The simultaneous approach was chosen due to its independence to the initial inviscid velocity distribution, what makes it more stable and continuous even with separation. Transition is also better treated with a simultaneous approach as it presents a smooth and continuous change from laminar to turbulent flow.

8.1 Contributions of Work

The main contributions of this work to sail system flow analysis are presented here. They are divided in two main subjects: the flow separation and three-dimensional viscous surface flow analysis. Both subjects have a common link that was the treatment partially separated flow on sail systems.

8.1.1 Flow Separation Bubble

Observing the behaviour of boundary layer variables using direct and simultaneous approaches, together with the discussions presented in the works of Wilkinson [4], Gad-el-Hak [1] and Gad-el-Hak and Bushnell [49], it was introduced a classification that divided the flow separation bubble in two types: weak separation and strong separation or, as discussed by Gad-el-Hak [1], long and short bubble behaviours.

In the weak separation, pressure distribution does not present significative differences to the inviscid flow. This distribution on a weak separation is smooth and continuous, so simultaneous approach can converge, presenting a $H > 2.5$ shape parameter distribution on the separated region.

In the strong separation bubble, the pressure distribution has a discontinuous characteristic, presenting a constant pressure on the separated region. Up and downstream out of the separated region, pressure distribution has a close agreement to the inviscid attached flow model. This was identified in experimental test cases in Wilkinson [4] work and in the work of Gad-el-Hak [1]. Simultaneous approach did not converge in strong separation bubbles and in some cases method broke down.

The transition, separation and reattachment in the laminar flow are closely linked, according to Gad-el-Hak [1]. In weak separation cases, this could be shown with the appearance of laminar separation bubbles in H distribution: once in the laminar flow H starts to increase to values above 2.5, there will be a peak and H will fall to turbulent values further downstream. This behaviour of H was observed in all membrane and thick foil shapes cases.

8.1.2 Separation on Mast and Sail Configurations

In the cases of mast and sail configurations studied by Wilkinson [4], separation was classified as strong. In all of Wilkinson's [4] tests, velocity distribution had discontinuous shape, presenting a constant velocity between separation and transition points and recovering to values near the inviscid attached flow velocity distribution downstream from the re-attachment point. The strong separation velocity profile could not be obtained numerically by surface methods.

8.1.2.1 Identification of Transition

Mast and sail configurations were investigated with the direct approach, using Thwaites method. It was considered *a priori* a large laminar flow length that included mast and most part of sail membrane. The investigation adopted the laminar attached flow calculation even downstream of separation point. According to Duncan et al [42], the use of one parameter laminar method, such as Thwaites, downstream of the separation point is not valid in fluid dynamic theory but, it was used with the engineering purpose of estimating the transition point.

The discontinuous shape of the inviscid velocity distribution on a mast and sail configuration, allowed the identification of the following points, with a close agreement to experimental results discussed by Wilkinson [4]:

- The separation point, which was where velocity reached its highest peak;
- The attachment of sail to mast, where inviscid velocity was closer to zero, making a discontinuous region.

The transition point was identified when, downstream of the attachment point of mast and sail, velocity distribution approached the inviscid distribution of the sail membrane alone. Coincidentally with the inviscid distribution, H shape parameter approached turbulent values after the attachment point. The turbulent value, $H = 1.94$,

was observed to change its position in a close agreement to Wilkinson [4] experiments so, the transition point was considered in the place where $H \approx 1.94$.

8.1.2.2 The Re-attachment Point

As discussed by Gad-el-Hak [1], it is difficult to predict with a reasonable accuracy the re-attachment point location. According to Gad-el-Hak [1], even the repetition in experiments conserving the same flow settings does not produce the same results for re-attachment location. Authors, such as Cook and McDonald [68] use empirical approaches to its estimation.

In this work, for mast and sail configurations, the re-attachment point was calculated using a method developed from a statistical study with the numerical results of transition and the experimental data for re-attachment points presented by Wilkinson [4].

The separation, transition and re-attachment points were used to create a matching surface enveloping the separated zone between mast and sail. The initial intention was the flow analysis using viscous-inviscid interaction. However, the application of any surface flow analysis on mast and sail configurations with a matching surface, did not agree to the velocity shape obtained experimentally by Wilkinson [4].

The real flow with strong separation has a discontinuous nature. Surface methods based in panel method could only produce continuous velocity shapes that did not match with the ones obtained in experiments.

An alternative to produce the same experimental velocity distribution using a surface method, is the superposition of a source sheet, forcing their strength to a constant potential on the separated region, as tested by Wilkinson [4].

8.1.3 The Three-dimensional Flow Analysis Using The Sectional Method

8.1.3.1 Independence from Initial Inviscid Velocity Calculation

The development of a simultaneous approach for three-dimensional flow brought the idea, when dividing body into sections, that viscous corrections could be implemented separately to panel method solution. This was possible by using the Dirichlet tangential boundary condition in section source distribution.

However, the use of a Dirichlet boundary condition, imposed a minimum volume inside the foil, in order that the constant potential consideration could be applied. Hence, a minimum numerical thickness had to be adopted in the membrane cases, demanding a more refined mesh for initial panel method and section node distribution, in order to avoid the close approach problem.

The viscous correction module works independently to the panel method. Panel method is only used initially to calculate the inviscid velocity distribution. Initial inviscid velocities are input to the viscous correction module and, with the initial panel mesh, three-dimensional velocity distribution is interpolated onto the body surface

sections. By means of a two-dimensional surface source distribution on each section, the viscous-inviscid coupling is performed.

The independence from the initial panel method solution also allows the possibility to other initial surface velocities distributions to be used in the problem. Other advantage is the choice of a better distribution of nodes on sections, as viscous flow solution demands normally more nodes per section than the original panel mesh can provide.

8.1.3.2 Simultaneous Approach Sensitivity to Separation

Applying the sectional method to three-dimensional sail shapes, H distribution could be obtained to each section where the same criteria of separation ($H > 2.5$) to two-dimensional analysis was adopted. The simultaneous approach, which includes the sectional method, is sensitive to flow separation and, by using the H distribution, it is possible to detect separated flow.

The sectional method could be adopted in aeroelastic analysis of sails, providing details of boundary layer development and flow separation. So, if sail reached a shape where high H values were detected on a region of its surface, designer could take providences to control the separated region.

This idea was shown to be possible in the case where extruded membranes were analysed. The NACA $a = 0.8$ shape was substituted by the Jackson profile, where separation could be better controlled by changing trailing and leading edge angles. In three-dimensional sail shapes, the sectional method could provide information of boundary layer development where it was possible to compare which sail shape would be more susceptible to separation.

In the case of three-dimensional sail geometries, the results presented agreed with Marchaj [10] observations, regarding sail twist and camber regulation to avoid sail trailing edge separation. However, experimental data that allow a quantitative comparison to numerical results obtained are not yet available.

8.2 Further Research

The sectional method and numerical data presented in this work lacked of experimental background to have a better comparison to real flow. Most of experimental data obtained either refer to a two-dimensional profile shape, as in the cases of Milgram [73] and Wilkinson [4] or, it uses a sail system inserted in an experimental environment which is difficult to isolate the effect of sail geometry changes, as in the cases of Campbell [6] and Poor and Sironi [5].

It is recognized here the difficulty on providing experimental detail of boundary layer parameters however, further research in this area would be of great importance to calibrate the surface method developed here.

Other useful research area would be the development of a method which is capable of calculating drag on weak separation. The frictional drag used in the simultaneous

and direct approaches was not accurate with presence of flow separation, as it was showed in Milgram [73] profiles cases.

References

[1] M. Gad el Hak. Control of low-speed airfoil aerodynamics. *AIAA Journal*, 28(9):1537 – 1552, September 1990.

[2] P. Van-Oossanen. Predicting the speed of sailing yachts. *SNAME Transactions*, 101:337 – 397, 1993.

[3] L. Larsson and R. E. Eliasson. *Principles of Yacht Design*. International Marine, Camdem, Maine UK, 1994.

[4] S. L. Wilkinson. *Partialy Separated Flow Around Masts an Sails*. PhD thesis, University of Southampton, U.K., 1984.

[5] C. L. Poor and N. Sironi. The international measurement system. *HISWA 11th International Symposium on Yacht Design and Yacht Construction*, November 1990.

[6] I. M. C. Campbell. Optimisation of a sailing rig using wind tunnel data. *The Thirteenth Chesapeake Sailing Yacht Symposium*, pages 49 – 63, 1997.

[7] J. C. Date. *Performance Prediction of High Lift Rudders Operating Under Steady and Periodic Flow Conditions*. PhD thesis, Dept of Ship Science, University of Southampton, Southampton, U.K., July 2001.

[8] M. Camponneto, A. Castelli, P. Dupont, B. Bonjour, P. L. Mathey, S. Sanchi, and M. L. Sawley. Sailing yacht design using advanced numerical flow techniques. *The 14th Chesapeake Sailing Yacht Symposium*, pages 97 – 104, 1999.

[9] R. C. Lock and B. R. Williams. Viscous-inviscid interactions in external aerodynamics. *Progress in Aerospace Science*, 24:51 – 171, 1987.

[10] C. A. Marchaj. *Sail Performance: Techniques to Maximize Sail Performance*. International Marine, London, UK, 1996.

[11] C. A. Marchaj. *Sailing Theory and Practice*. Granada Publishing Ltd., London, UK, 1964.

[12] P. S. Jackson. A simple model for elastic two-dimensional sails. *AIAA Journal*, vol. 21(1):153 – 155, January 1983.

[13] T. Whidden and M. Levitt. *The Art and Science of Sails: A Guide to Modern Materials, Construction, Aerodynamics, Upkeep and Use*. St. Martin Press, 1990.

[14] T. Sugimoto. A method for optimizing sail design. *Journal of Sports Engineering*, 2(1), 1999.

[15] H. C. Herreshoff. Hydrodynamics and aerodynamics of the sailing yacht. In *Annual Meeting of The Society of Naval Architects and Marine Engineers*, pages 445 – 492. S.N.A.M.E., November 1964.

[16] R. G. J. Flay and P. S. Jackson. Flow simulation for wind-tunnel studies of sail aerodynamics. *Journal of Wind Engineering and Industrial Aerodynamics*, 41(44):2703 – 2714, 1992.

[17] D. B. Peters. Determination of force coefficients for racing yacht sails using actual force measurements. Master's thesis, Ocean Engineering, Masachusetts Institute of Technology, June 1992.

[18] R. G. J. Flay. A twisted flow wind tunnel for testing yacht sails. *Journal of Wind Engineering and Industrial Aerodynamics*, (63):171 – 182, June 1996.

[19] G. D. Mallinson R. G. J. Flay, N. J. Locke. Model tests of twisted flow wind tunnel designs for testing yacht sails. *Journal of Wind Engineering and Industrial Aerodynamics*, (63):155 – 169, June 1996.

[20] L. Larsson. Scientific methods in yacht design. *Annual Review in Fluid Dynamics*, 22:349 – 385, 1990.

[21] B. G. Newman. Aerodynamic therory for membranes and sails. *Progres in Aerospace Science*, vol. 24:1 – 27, 1987.

[22] P. S. Jackson and G. W. Christie. Numerical analysis of three-dimensional elastic membrane wings. *AIAA Journal*, vol. 25(5):676 – 682, may 1987.

[23] M. A. Hobbs. *Aeroelastic Analysis of a Yacht Rig*. Phd thesis, University of Southampton, UK, October 2000.

[24] J.C. Oliver, J.S.Jr. Letcher, and N. Salvensen. Performance Predictions for Stars & Stripes. *Trans. SNAME*, 95:239–261, 1987.

[25] J. Gerritsma, R. Onnink, and A. Versluis. Geometry, resistence and stability of the delft systematic yacht hull series. *Report Technological University Delft*, pages 276 – 297, 1978.

[26] A. E. L. Veiga. *Uma Contribuição Ao Projeto Racional de Veleiros de Regata*. M.sc thesis, COPPE/UFRJ, Brasil, September 2000.

[27] ORC. *User's Guide to The IMS*. Offshore Racing Council, UK, 1996.

[28] P. Couser. Prediction of aerodynamic sail forces for upwind yacht velocity prediction programs. In *Proceedings of the 1st Australian Sailing Science Conference*, Tasmania, Australia, November 1998.

[29] R. Ranzenbach and J. Teeters. Enhanced depowering model for offwind sails. In *Proceedings of The High Performance Yacht Conference*, Auckland, December 2002.

[30] R. Ranzenbach and J. Teeters. Volvo 70 offwind aerodynamic modeling and its impact upon sail inventory design optimization. In *Proceedings of the First Symposium on Yacht Design and Production*, Spain, May 2004.

[31] P. J. Richards K. L. Hedges and G. D. Mallinson. Computer modelling of downwind sails. *Journal of Wind Engineering and Industrial Aerodynamics*, 63:95 – 110, 1996.

[32] S. L. Wilkinson. Static pressure distributions over 2d Mast/Sail geometries. *Marine Technology*, 26(4):333–337, October 1989.

[33] J. H. Ferziger and M. Peric. *Computational Methods for Fluid Dynamics*. Springer, third edition, 2002.

[34] J. Katz and A. Plotkin. *Low-Speed Aerodynamics*. Cambridge University Press, second edition, 2001.

[35] M. Drela and M. B. Giles. Viscous-inviscid analysis of transonic and low reynolds number airfoils. *AIAA Journal*, 25(10):1347 – 1355, 1987.

[36] A. H. Day. Steps towards an optimal yacht sailplan. *Transactions of RINA*, pages 155 – 174, 1993.

[37] D. Foussekis, P. Fraunié, and C. Béguier. Steady and unsteady separated flows arround a profile. application on the wind turbines. *Journal of Wind Engineering and Industrial Aerodynamics*, 39:41 – 49, 1992.

[38] P. Couser. Computational methods for investigating sail forces - a case study. In *Proceedings of Yacht Vision*, Auckland, New Zealand, January 1998.

[39] A. L. Drew D. S. Greeley, K. L. Kirkman and J. Cross-Whiter. Scientific sail shape design. In *Proceedings of the Nineth Chesapeake Sailing Yacht Simposium*, Annapolis, Maryland - U.S.A., 1989.

[40] J. L. Hess. The problem of three-dimensional lifting potential flow and its solution by means of surface singularity distribution. *Computer Methods in Applied Mechanics and Engineering*, 4:283 – 319, 1974.

[41] L. R. C. Eça and J. A. C. Falcão de Campos. Analysis of two-dimensional foils using a viscous-inviscid interaction method. *International Shipbuilding Progress*, 40(422):137 – 163, 1993.

[42] W. J. Duncan, A. S. Thom, and A. D. Young. *Mechanics of Fluids*. Edward Arnold Ltd, London, U K, 1970.

[43] M. Drela. Integral boundary layer for blunt trailling edges. Technical Report 89-2200, AIAA, August 1989.

[44] J. E. Green, D. J. Weeks, and J. W. F Brooman. Prediction of turbulent boundary layers and wakes in compressible flow by a lag-entrainment method. R.A.E. Technical Report 3791, R.A.E. Technical Report, Aerodynamics Dept, R.A.E., Farnborough, U.K., January 1973.

[45] G. S. Hufford, M. Drela, and J. E. Kerwin. Viscous flow around marine propellers using boundary-layer strip theory. *Journal of Ship Research*, 38(1):52 – 62, March 1994. SNAME.

[46] M. Drela and B. Mughal. A calculation method for the three-dimensional boundary layer equations in integral form. *AIAA Paper 93-0786*, January 1993. Paper obtained on Web page of Massachussets Institute of Technology (http://raphael.mit.edu/pubs.html).

[47] C-Y. Hsin. *Development and Analysis of Panel Methods for Propellers in Unsteady Flow*. PhD thesis, Ocean Engineering, Massachusetts Institute of Technology, U.S.A., September 1990.

[48] W. M. Milewski. *Three-Dimensional Viscous Flow Computations Using the Integral Boundary Layer Equations Simultaneously Coupled with a Low Order Panel Method*. PhD thesis, Massachusetts Institute of Technology, U.S.A, June 1997.

[49] M. Gad el Hak and D. M. Bushnell. Separation control: Review. *Journal of Fluids Engineering*, 113:5 – 30, March 1991.

[50] P. A. R. Hoghton. Computer modelling of sail geometry's. 3rd year project, Faculty of Engineering and Applied Science, University of Southampton, May 1996.

[51] J. H. Milgram. Naval architecture technology used in winning the 1992 america's cup match. *SNAME Transactions*, 101:399 – 436, 1993.

[52] D. S. Greeley and J. H. Cross-Wither. Design and hydrodynamic performance of sailboat keels. *Marine Technology*, Vol. 26(4):260 – 281, October 1989.

[53] P. Couser. Validation of SVL vortex lattice code. International report for programme g, task g3 - prediction of aerodynamic forces, Curtin University, Perth, Australia, June 1998.

[54] J. L. Hess and A. M. O. Smith. Calculation of nonlifiting potential flow about arbitrary three-dimensional bodies. *Journal of Ship Research*, pages 22 – 45, September 1964.

[55] S. R. Turnock. *Prediction of Ship Rudder-Propeller Interaction Using Parallel Computations and Wind Tunnel Tests*. PhD thesis, University of Southampton, 1993.

[56] M. B. Giles and R. M. Cummings. Wake integration for three-dimensional flowfield computations: Theoretical development. *Journal of Aircraft*, vol 36(no 2):357 – 365, march 1999.

[57] D. L. Hunt, R. M. Cummings, and M. B. Giles. Wake integration for three-dimensional flowfield computations: Applications. *Journal of Aircraft*, vol 36(no 2):366 – 373, March 1999.

[58] C. E. Elstub. *The Potential Modeling of Multiple Sail Geometries*. B.eng. project, University of Southampton, U.K., May 1995.

[59] N. C. Rycroft and S. R. Turnock. Three-dimensional multiblock grid generation: FLEXIMESH. Ship science report 101, Dept. of Ship Science, Faculty of Engineering and Applied Science, University of Southampton, November 1997.

[60] C-Y. Hsin, J. E. Kerwin, and S. A. Kinnas. A panel method for the analysis of the flow around highly skewed propellers. *SNAME Propeller/Shafting 91 Symposium*, pages 11–1 11–13, September 1991.

[61] I. H. Abbott and A. E. Von Doenhoff. *Theory of Wing Sections*. McGraw Hill, New York, USA, 1949.

[62] M. Drela and H. Youngreen. XFOIL 6.94 user primer. Technical report, MIT Aero Astro, 2001. Document distributed with the GNU program, open source code XFOIL.

[63] T. Cebeci and P. Bradshaw. *Momentum Transfer in Boundary Layers*. McGraw-Hill, London, 1977.

[64] K. Hiemenz. Die grenzschicht an einem in den gleichformigen flussigkeitsstrom eingetauchten geraden kreiszylinder. *Politechnisches Journal*, 21:41, May 1911.

[65] A. D. S. Neto. Fundamentos da turbulência nos fluidos. In *Transição e Turbulência, 1 Escola de Primavera, Mini-Cursos*, pages 1 – 48, Rio de Janeiro, Brasil, september 1998. Coppe/UFRJ, Associação Brasileira de Ciências Mecânicas. In portuguese.

[66] A. R. Wazzan, C. Gazzley Jr., and A. M. O. Smith. H-rex method for predicting transition. *AIAA Journal*, 19(6):810 – 812, 1981.

[67] G. V. Parkinson and T. Jandali. A wake source model for bluff body potential flow. *Journal of Fluid Mechanics*, 40(3):577 – 594, 1970.

[68] P. H. Cook and M. A. McDonald. Wind tunnel measurements in the boundary layer and wake of an aerofoil with a blunt base at high subsonic speeds. Technical Report 84002, Royal Aircraft Stablishment, January, 1964.

[69] F. A. Dvorak, F. A. Woodward, and B. Maskew. A three-dimensional Viscous/Potential flow interaction analysis method for multi-element wing. NASA Technical Report CR 152012, NASA, July 1977.

[70] S. R. Turnock. *PALISUPAN USER GUIDE*. Department of Ship Science, Faculty of Engineering and Applied Science, University of Southampton, 2 edition, 1997.

[71] J. P. Johnston. *Three-Dimensional Turbulent Boundary Layers*. PhD thesis, Gas Turbine Laboratory, M.I.T., 1957.

[72] S. R. Turnock and A. M. Wright. Directly coupled fluid structural model of a ship rudder behind a propeller. *Marine Structures*, 13:53 – 72, 2000.

[73] J. H. Milgram. Effects of masts on the arodynamicas of sail sections. *Marine Technology*, vol. 15(1):35 – 42, January 1978.

[74] S. Harries, C. Abt, and K. Hochkirch. Hydrodynamic modeling of sailing yachts. *The Fifteenth Chesapeake Sailing Yacht Symposium*, March 2001.

[75] D. F. Rogers and J. A. Adams. *Mathematical Elements for Computer Graphics*. McGraw Hill Publishing Co., New York, U.S.A., 2nd edition edition, 1990. ISBN 0-07-053530-2.

[76] W. H. Press, S. A. Teukolsky, W. T. Vetterling, and B. P. Flannery. *Numerical Recipes in C++: The Art of Scientific Computing*. Press Syndicate of The University of Cambridge, Cambridge, U.K., second edition edition, 1992.

Appendix A

Influence Coefficients

A.1 Two-Dimensional Influence Coefficients

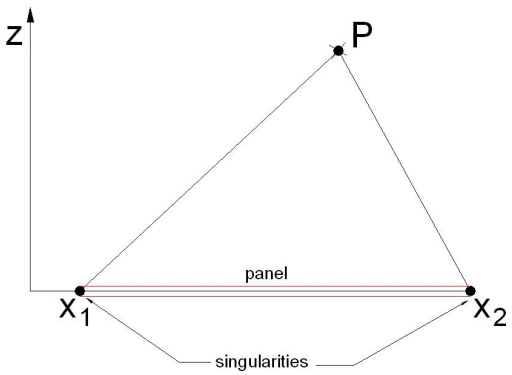

Figure A.1: The two-dimensional panel singularity distribution

Considering a two-dimensional segment showed on figure A.1 defined between edges x_1 and x_2 and with a point P located on (x, z) coordinates from panel, the constant and linear singularities are as given below:

A.1.1 Constant Source Influence in a Collocation Point

$$\phi = \frac{\sigma}{4\pi} \cdot \left[(x - x_1) \cdot \ln r_1^2 - (x - x_1) \cdot \ln r_2^2 + 2z \left(\theta_2 - \theta_1 \right) \right]$$

Where

$$r_k = \sqrt{(x - x_k)^2 + z^2}$$

$$\theta_k = \tan^{-1} \frac{z}{x - x_k}$$

$$k = 1, 2$$

$$\frac{\partial \phi}{\partial x} = -u = -\frac{\sigma}{2\pi} \cdot \ln\left(\frac{r_1}{r_2}\right)$$

$$\frac{\partial \phi}{\partial z} = -v = -\frac{\sigma}{2\pi} \cdot (\theta_2 - \theta_1)$$

Where self influence velocities are:

$$u = 0$$

$$v = \frac{\sigma}{2}$$

A.1.2 Constant Doublet Influence in a Collocation Point

$$\phi = \frac{-\mu}{2\pi} \cdot \left[\tan^{-1}\theta_2 - \tan^{-1}\theta_1\right]$$

$$\frac{\partial \phi}{\partial x} = -u = \frac{\mu}{2\pi} \cdot \left[\frac{y}{r_1^2} - \frac{y}{r_2^2}\right]$$

$$\frac{\partial \phi}{\partial z} = -v = \frac{-\mu}{2\pi} \cdot \left[\frac{x - x_1}{r_1^2} - \frac{x - x_2}{r_2^2}\right]$$

Where self influence velocities are:

$$u = 0$$

$$v = \frac{\mu}{\pi} \cdot \frac{2}{(x_2 - x_1)}$$

A.1.3 Constant Vortex Influence in a Collocation Point

$$\phi = \frac{-\gamma}{\pi} \cdot \left[(x - x_1)\,\theta_1 - (x - x_2)\,\theta_2 + y \cdot \ln\left(\frac{r_1}{r_2}\right)\right]$$

$$\frac{\partial \phi}{\partial x} = -u = -\frac{\gamma}{2\pi} \cdot \left[\tan^{-1}\theta_2 - \tan^{-1}\theta_1\right]$$

$$\frac{\partial \phi}{\partial z} = -v = -\frac{\gamma}{2\pi} \cdot \left[\ln\left(\frac{r_1}{r_2}\right)\right]$$

Where self influence velocities are:

$$u = 0$$

$$v = \gamma \frac{1}{2}$$

A.1.4 Linear Source Influence in a Collocation Point

The linear source influence considers a first solution based on the constant source strength solution σ_0 plus a linear correction for one panel edge to another σ_1.

$$\sigma_0 = \sigma_j$$

$$\sigma_1 = \frac{\sigma_{j+1} - \sigma_j}{x_{_{j+1}} - x_j}$$

The total potential ϕ is as given on equation below for panel coordinates:

$$\phi = \frac{\sigma_0}{4\pi} \left[(x - x_1) \ln r_1^2 - (x - x_2) \ln r_2^2 + 2z (\theta_2 - \theta_1) \right]$$

$$+ \frac{\sigma_1}{4\pi} \left[\frac{x^2 - x_1^2 - z^2}{2} \ln r_1^2 - \frac{x^2 - x_2^2 - z^2}{2} \ln r_2^2 \right.$$

$$\left. + 2xz (\theta_2 - \theta_1) - x (x_2 - x_1) \right]$$

The linear source influence is used in this work for the coupling of a inviscid method to a viscous solution.

A.2 Three-Dimensional Influence Coefficients

A.2.1 Constant Source Influence of a Quadrilateral Panel

$$\phi = \frac{\sigma}{4\pi} \cdot \left\{ \left[\frac{(x - x_1)(z_2 - z_1) - (z - z_1)(x_2 - x_1)}{d_{12}} \cdot \ln \frac{r_1 + r_2 + d_{12}}{r_1 + r_2 - d_{12}} \right. \right.$$

$$+ \frac{(x - x_2)(z_3 - z_2) - (z - z_2)(x_3 - x_2)}{d_{23}} \cdot \ln \frac{r_2 + r_3 + d_{23}}{r_2 + r_3 - d_{23}}$$

$$\left. + \frac{(x - x_3)(z_4 - z_3) - (z - z_3)(x_4 - x_3)}{d_{34}} \cdot \ln \frac{r_3 + r_4 + d_{34}}{r_3 + r_4 - d_{34}} \right.$$

$$+\frac{(x-x_4)(z_1-z_4)-(z-z_4)(x_1-x_4)}{d_{41}}\cdot\ln\frac{r_4+r_1+d_{41}}{r_4+r_1-d_{41}}\Bigg]$$

$$-|y|\cdot\Bigg[\tan^{-1}\left(\frac{m_{12}e_{12}-h_1}{yr_1}\right)-\tan^{-1}\left(\frac{m_{12}e_{12}-h_2}{yr_2}\right)$$

$$+\tan^{-1}\left(\frac{m_{23}e_{23}-h_2}{yr_2}\right)-\tan^{-1}\left(\frac{m_{23}e_{23}-h_3}{yr_3}\right)$$

$$+\tan^{-1}\left(\frac{m_{34}e_{34}-h_3}{yr_3}\right)-\tan^{-1}\left(\frac{m_{34}e_{34}-h_4}{yr_4}\right)$$

$$+\tan^{-1}\left(\frac{m_{41}e_{41}-h_4}{yr_4}\right)-\tan^{-1}\left(\frac{m_{41}e_{41}-h_1}{yr_1}\right)\Bigg]\Bigg\}$$

Where:

$$d_{12}=\sqrt{(x_2-x_1)^2+(z_2-z_1)^2}$$

$$d_{23}=\sqrt{(x_3-x_2)^2+(z_3-z_2)^2}$$

$$d_{34}=\sqrt{(x_4-x_3)^2+(z_4-z_3)^2}$$

$$d_{41}=\sqrt{(x_1-x_4)^2+(z_1-z_4)^2}$$

and

$$m_{12}=\frac{z_2-z_1}{x_2-x_1}$$

$$m_{23}=\frac{z_3-z_2}{x_3-x_2}$$

$$m_{34}=\frac{z_3-z_4}{x_3-x_4}$$

$$m_{41} = \frac{z_1 - z_4}{x_1 - x_4}$$

and

$$r_k = \sqrt{(x - x_k)^2 + (z - z_k)^2 + y^2}$$

$$e_k = (x - x_k)^2 + y^2$$

$$h_k = (x - x_k)(z - z_k)$$

where $k = 1, 2, 3, 4$

$$u = -\frac{\sigma}{4\pi} \cdot \left[\frac{z_2 - z_1}{d_{12}} \ln \frac{r_1 + r_2 - d_{12}}{r_1 + r_2 + d_{12}} + \frac{z_3 - z_2}{d_{23}} \ln \frac{r_2 + r_3 - d_{23}}{r_2 + r_3 + d_{23}} \right.$$

$$\left. + \frac{z_3 - z_4}{d_{34}} \ln \frac{r_3 + r_4 - d_{34}}{r_3 + r_4 + d_{34}} + \frac{z_1 - z_4}{d_{41}} \ln \frac{r_4 + r_1 - d_{41}}{r_4 + r_1 + d_{41}} \right]$$

$$w = -\frac{\sigma}{4\pi} \cdot \left[\frac{x_2 - x_1}{d_{12}} \ln \frac{r_1 + r_2 - d_{12}}{r_1 + r_2 + d_{12}} + \frac{x_3 - x_2}{d_{23}} \ln \frac{r_2 + r_3 - d_{23}}{r_2 + r_3 + d_{23}} \right.$$

$$\left. + \frac{x_3 - x_4}{d_{34}} \ln \frac{r_3 + r_4 - d_{34}}{r_3 + r_4 + d_{34}} + \frac{x_1 - x_4}{d_{41}} \ln \frac{r_4 + r_1 - d_{41}}{r_4 + r_1 + d_{41}} \right]$$

$$v = -\frac{\sigma}{4\pi} \cdot \left[\tan^{-1} \left(\frac{m_{12} e_{12} - h_1}{y r_1} \right) - \tan^{-1} \left(\frac{m_{12} e_{12} - h_2}{y r_2} \right) \right.$$

$$+ \tan^{-1} \left(\frac{m_{23} e_{23} - h_2}{y r_2} \right) - \tan^{-1} \left(\frac{m_{23} e_{23} - h_3}{y r_3} \right)$$

$$+ \tan^{-1} \left(\frac{m_{34} e_{34} - h_3}{y r_3} \right) - \tan^{-1} \left(\frac{m_{34} e_{34} - h_4}{y r_4} \right)$$

$$\left. + \tan^{-1} \left(\frac{m_{41} e_{41} - h_4}{y r_4} \right) - \tan^{-1} \left(\frac{m_{41} e_{41} - h_1}{y r_1} \right) \right]$$

Self influence velocities:

$$u = 0$$

$$w = 0$$

$$v = \frac{\sigma}{2}$$

A.2.2 Constant Doublet Influence of a Quadrilateral Panel

$$\phi = \frac{\mu}{4\pi} \cdot \left[\tan^{-1}\left(\frac{m_{12}e_{12} - h_1}{yr_1}\right) - \tan^{-1}\left(\frac{m_{12}e_{12} - h_2}{yr_2}\right) \right.$$

$$+ \tan^{-1}\left(\frac{m_{23}e_{23} - h_2}{yr_2}\right) - \tan^{-1}\left(\frac{m_{23}e_{23} - h_3}{yr_3}\right)$$

$$+ \tan^{-1}\left(\frac{m_{34}e_{34} - h_3}{yr_3}\right) - \tan^{-1}\left(\frac{m_{34}e_{34} - h_4}{yr_4}\right)$$

$$\left. + \tan^{-1}\left(\frac{m_{41}e_{41} - h_4}{yr_4}\right) - \tan^{-1}\left(\frac{m_{41}e_{41} - h_1}{yr_1}\right) \right]$$

Appendix B

Mesh Generation and Sail Shape Creation Using Three-Dimensional Interpolation Methods

There are many methods today that allow the fast creation of complicated geometry and permits a fast mesh generation to CFD analysis. A remarkable work was developed by Haries et al [74], which generates complex three-dimensional surfaces of yacht hull and appendages to CFD analysis. Their work involves the creation of a shape by varying few parameters. It is a creation phase or, as defined by Rogers and Adams [75], an *ab initio* problem.

In this work, the main problem was the high fidelity reproduction of three-dimensional shapes of sail membranes and masts. The approach using B-spline surfaces and NURBS was not the best option as, there were many parameters to control in order that the surface generated could interpolate the original points obtained.

The accurate representation lead to a development of an in-house method based in cubic spline interpolation of surface. The method is simple and fast, with very little interference from user, which makes modelling of mesh faster, different than other approaches such as NURBS. This in-house method was also adapted to linear interpolation to its inviscid data interpolation on body surface.

Using the in-house interpolation method, it was also developed a three-dimensional sail shape generator using the Jackson [12] sail profiles that contributed to the analysis of sail shapes discussed in Chapter 7.

B.1 Bi-Linear Interpolation

This linear surface interpolation sets up the basis for a higher order interpolation. The basic algorithm is discussed here. This surface interpolation method was employed in VIX and VIMesh interpolation of velocities on body surface, as discussed on Chapter 5. It considers quadrilateral panels but, theory can be extended to any polygonal panel.

Considering that s is in the chord direction and t is on the width direction of a wing,

as exemplified in Figure B.1, the Cartesian coordinates can be expressed as functions of these parameters:

$$x = f_1(s,t)$$

$$y = f_2(s,t)$$

$$z = f_3(s,t)$$

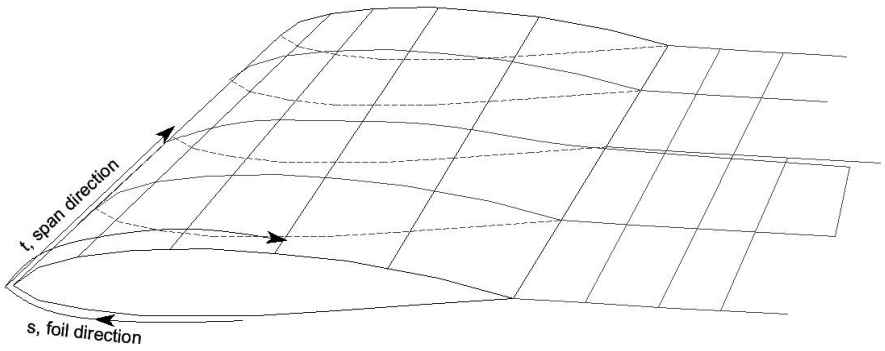

Figure B.1: Scheme of a paneled surface with directions s and t

If a point $p(s,t)$ belongs to surface panel, then it is possible to interpolate its Cartesian coordinates. In order to simplify the explanation, just the x coordinate will be exemplified. The same process can be repeated to the y and z coordinates. The surface linear interpolation to one panel follows the sequence below:

1. Distribution of function values $x[...][...]$ for each panel node.
2. Calculation of s and t surface coordinates for each panel node. s and t should vary from 0 to 1.0.
3. Division of nodes on strips following chordwise and spanwise direction
4. If point p belongs to the panel, showed on figure B.2, considering counter-clockwise distribution of nodes on panel, calculate the normalized coordinates (T,U) by doing:

$$T = (s - s_j)/(s_{j+1} - s_j)$$

$$U = (t - t_k)/(t_{k+1} - t_k)$$

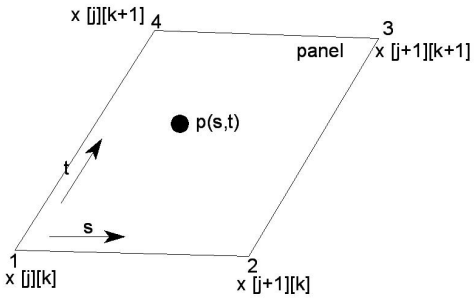

Figure B.2: The transfinite linear interpolation on a panel

5. Calculate weighting coefficients each node influence, following a counter-clockwise order of panel nodes

$$A_1 = (1 - T) \cdot (1 - U)$$

$$A_2 = T \cdot (1 - U)$$

$$A_3 = T \cdot U$$

$$A_4 = (1 - T) \cdot U$$

6. The resulting function x on point $p(s, t)$ will be:

$$x(s, t) = \sum_{i=1}^{4} (A_i \cdot x_i)$$

B.2 The Spline Interpolation Method

The spline method is very well known in computer graphics and mesh generation. It is the equation of an elastic beam simply supported at ends. In computer graphics, the nodes are equivalent to ends of the beam. The momentum M for beam deflection is given on equation (B.1),

$$M(s) = \frac{E \cdot I}{R(s)} \tag{B.1}$$

where E is the elasticity modulus of beam material, I is the sectional inertia and R is the gyradius of beam which is inversely proportional to curvature κ.

Considering E and I constants and a small curvature between ends, gyradius and curvature can be approximated by equation (B.2).

$$\kappa = \frac{1}{R} = \frac{x''(s)}{(1 + x'(s))^{3/2}} \tag{B.2}$$

If the derivatives at nodes are known then, second derivatives on nodes are given by the equation (B.2). Second derivatives vary linearly from one node to another and

the deflection equation of beam will be a cubic polynomial.

$$x''(s) = a \cdot s + b = \frac{M(s)}{E \cdot I} \tag{B.3}$$

The spline method uses this principle for evaluating second derivatives at nodes and establishes a cubic correlation between them. One advantage of using splines is that the polynomial relating any two consecutive nodes of a line will always be cubic. The disadvantage is that, second derivative distribution may not be always continuous in a set of nodes. This discontinuity also varies when curvature increases, reaching high values of second derivatives at isolated nodes.

A high second derivative value may cause an undesired oscillation as exemplified in Figure B.3, where it is shown a typical motorboat station. As the station has a double chine, if few nodes are used, there will be an oscillation showed in Figure B.3. If the number of nodes is increased, showed on the left, this oscillation will decrease. The spline oscillation can decrease even more if more nodes are added on chines.

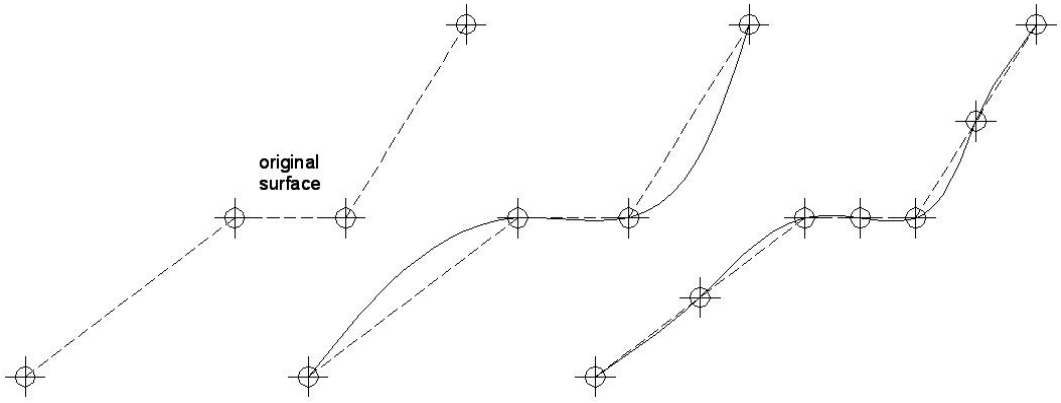

Figure B.3: A typical motorboat station with a spline routine interpolating its nodes

The concentration of nodes reduces the local curvature and the polynomial approximation can be applied with more accuracy. This practice introduces to the vertex multiplication theory, which is the multiplication by a weighting factor of determinate node. It is more used on NURBS surfaces, as exemplified next.

B.3 The B-Spline Surface

B-Spline is a surface generated by a base of splines. For a two-dimensional line, b-spline is defined by equation (B.4) where $N_{i,k}(s)$ is a recursive function given on equation (B.5).

$$P(t) = \sum_{i=1}^{n+1} B_i^h N_{i,k}(t) \tag{B.4}$$

where

$$N_{i,1}(t)\{.0pt1, if x[i] \leq t \leq x[i+1]0, other\ case \tag{B.5}$$

and

$$N_{i,k}(t) = \frac{(t - x\,[i])\, N_{i,k-1}\,(t)}{x\,[i+k-1] - x\,[i]}$$
$$+\frac{(x\,[i+k] - t)\, N_{i+1,k-1}}{x\,[i+k] - x\,[i+1]}$$

A sequence of nodes that satisfy the condition $x[i-1] \leq x[i] \leq x[i+1]$ is an array of parametric nodes that defines the base parametric domain.

NURBS (Non Uniform Rational B-spline Surface) has equation (B.6) in the three-dimensional space,

$$P\,(t) = \frac{\sum_{i=1}^{n+1} B_i h_i N_{i,k}(t)}{\sum_{i=1}^{n+1} h_i N_{i,k}(t)} \tag{B.6}$$

where B_i is the control polygon node defined on Cartesian coordinates. h_i is the weighting function of curve to each node and it is correlated to homogeneous coordinates of control polygon in the four-dimensional space. $N_{i,k}(t)$ is an array of recursive functions for b-spline theory.

Rearranging equation (B.6) it is obtained (B.7)

$$P\,(t) = \sum_{i=1}^{n+1} B_i R_{i,k}(t) \tag{B.7}$$

where $R_{i,k}(t)$ is defined by:

$$R_{i,k}(t) = \frac{h_i N_{i,k}(t)}{\sum_{i=1}^{n+1} h_i N_{i,k}(t)}$$

A b-spline curve does not necessarily interpolates input nodes. It adjusts a control polygon to a smooth surface, as exemplified in Figure B.4.

The weighting function h_i of NURBS can be applied to nodes of control polygon in Figure B.4 where a trial and error sequence is made by user, until curve interpolates or, approximately interpolates, the nodes of the original curve (control polygon).

B.3.1 NURBS Three-dimensional Surfaces

Three-dimensional surfaces uses the same principle as the two-dimensional NURBS. In three-dimensions, base splines are created in two parametric directions of surface. The surface coordinates will be obtained by the torsor of these base spline vectors on parametric directions s and t, as mentioned by Rogers and Adams [75].

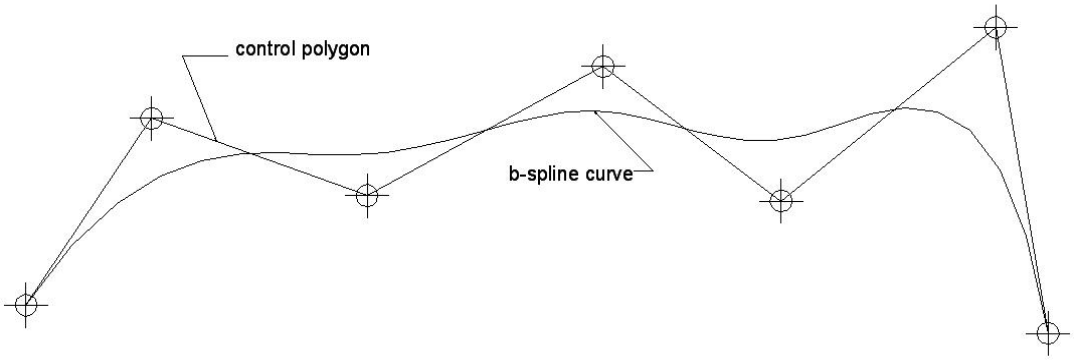

Figure B.4: The b-spline curve with its control polygon

B.4 The Bi-cubic Interpolation

The concept of the linear interpolation lead to a higher order interpolation method. It is used when panel surface presents a significative curvature and it needs its accurate representation, with surface points interpolating exactly the original input nodes. At a first approach, the coordinate x from the previous linear problem on a point $p(s,t)$ is the sum of the linear value plus some curvature correction.

B.4.1 The Surface Curvature

The spline theory is applied for calculating second derivatives along chordwise and spanwise lines, formed by panel edges. On three-dimensional surfaces, the spline function is evaluated at each node and there are two second derivatives distributions: one for $x''(s)$ and another for $x''(t)$, for directions s and t respectively.

The surface curvature varies in both directions but the correction to a point inside panel due to curvature, using the approach made by Rogers and Adams [75] for b-splines, is dependant on just one value that is given by the torsor of both curvature vectors.

B.4.2 The Curvature Correction Procedure

If a point $p(s,t)$ belongs to the panel, the value of the function at this point $x(s,t)$ can be interpolated. But, it needs the curvature effect in order to give accuracy to prediction. Follows then, a similar calculation sequence as the linear method:

1. Distribution of function values $x[...][...]$ for each panel node.
2. Calculation of s and t surface coordinates for each panel node. s and t should vary from 0 to 1.0.
3. Division of nodes on strips following chordwise and spanwise direction

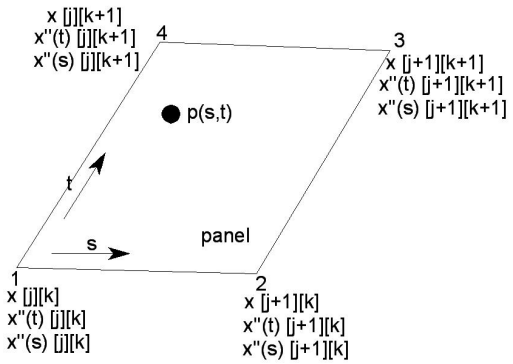

Figure B.5: The bi-cubic transfinite interpolation scheme

4. Calculation of two-dimensional spline second derivatives for each segment of the strip of nodes. The initial and final derivatives should be obtained by single difference on first and last nodes of each strip

5. Distribution of second derivatives of function (here represented as x) $x''(s)[...][...]$ and $x''(t)[...][...]$ on each node.

6. If point p belongs to a panel, shown in Figure B.5, considering counter-clockwise distribution of nodes on panel, calculate the normalized coordinates (T, U) by doing

$$T = (s - s_j)/(s_{j+1} - s_j)$$

$$U = (t - t_k)/(t_{k+1} - t_k)$$

7. Calculate coefficients for normalized linear interpolation on a panel:

$$A_1 = (1 - T) \cdot (1 - U)$$

$$A_2 = T \cdot (1 - U)$$

$$A_3 = T \cdot U$$

$$A_4 = (1 - T) \cdot U$$

A spline is a third order polynomial then, if the second derivatives for this polynomial were calculated at each node of the panel, in both directions (s, t), it means that the variation of the second derivative between nodes of a panel will be linear. The variation of both derivatives is linearly proportional to the torsor of the second derivatives vector on s and t directions.

To the line interpolation case, as discussed by Press et al [76], the value of a function is the summation of the linear interpolation between nodes plus a correction considering

the second derivatives of this nodes in relation to s.

$$x(s) = A \cdot x_i + (1 - A) \cdot x_{i+1} + B_1 \cdot d^2x/ds^2[i] + B_2 \cdot d^2x/ds^2[i+1] \tag{B.8}$$

B_1 and B_2 are weighting functions for curvature of nodes included on each line segment. B_1, for example, is as given on equation (B.8) for line interpolation and is related to node i to $i+1$. B_2 is related from node $i+1$ to i:

$$B = \frac{1}{6}\left(A_i^3 - A_i\right).\Delta s$$

where Δs is the parameter s variation on the segment.

A similar weighting scheme can be applied to the quadrilateral panel but, there are eight parameters B. Four related to direction s at each node and another four related to t at each node.

$$B_{si} = \frac{1}{6}\left(A_i^3 - A_i\right).\Delta s_j$$

$$B_{ti} = \frac{1}{6}\left(A_i^3 - A_i\right).\Delta t_k$$

Where i varies from 1 to 4 (number of edges). If the first node is taken as an example,

$$a = B_{s1} \cdot \left(d^2x/ds^2[j+1][k] - d^2x/ds^2[j][k]\right)$$

$$b = B_{t1} \cdot \left(d^2x/dt^2[j+1][k] - d^2x/dt^2[j][k]\right)$$

$$c = B_{s4} \cdot \left(d^2x/ds^2[j][k+1] - d^2x/ds^2[j][k]\right)$$

$$d = B_{t4} \cdot \left(d^2x/dt^2[j][k+1] - d^2x/dt^2[j][k]\right)$$

there will be two vectors $v1 = (a, b, 0)$ and $v2 = (c, d, 0)$. $v1 \times v2 = a \cdot d - b \cdot c = vn_1$. Applying the same operation to each node of the panel, there is the contribution of each second derivative of nodes at point p, represented by the summation:

$$\sum_{i=1}^{4} vn_i$$

The vn vector estimates the value of the second derivative contribution. Then, the function x at point $p(s,t)$ is the sum of the linear interpolation in relation to each panel node plus the estimated correction based on the second derivative.

$$x(s,t) = \sum_{i=1}^{4}(A_i \cdot x_i + vn_i)$$

B.5 Oscillations on Cubic Interpolation

Any spline method considers a small curvature that equation (B.3) can be applied. Chines on surface or a very high curvature region do not fit to this approximation. One good example are stations of a fast motor boat, as exemplified in Figure B.3.

On chine region there is a need to have more vertices that curvature between segments will be small and line will approach the original surface.

The B-Spline theory, that is generalized on NURBS (Non-uniform rational base spline surfaces), has the facility of the vertex multiplicity. This is similar as the increasing on the number of nodes in a determined region of a surface.

The bi-cubic interpolation scheme is dependent to relatively small curvatures. It is difficult to apply more nodes to a region on an automated modelling scheme as VIMesh but, some geometry representations on three-dimensional space suffer from oscillations.

On a big mesh for CFD application, the accuracy on representation is very important and the user cannot rely on checking all vertex multiplicity on nodes. It is very time consuming.

B.5.1 Correcting Oscillations

One disadvantage of using splines is that the second derivative distribution is not always continuous and smooth on segments between nodes. Applying this consideration to a surface with four distinct nodes, it leads to the conclusion that on a panel, curvature may not be continuous at all and a second derivative in two line directions can present many spikes with high values. Those spikes are responsible for local oscillations in function interpolation. A filtering procedure has to be applied to correct oscillations.

B.5.2 Filtering

It is relatively known in image processing problems the filtering functions. It takes raw data from image and filters possible spikes transforming the original data into a clear image, free of noises and disturbances. There are many methods for smoothing spikes and they vary in complexity.

A very simple method and largely used is the moving window average method. It basically considers a window with a fixed number of nodes (N) and predicts the value of the function f_i, included in the chosen interval (window), by averaging the neighbouring values on nodes. Equation (B.9) is used as central moving window average,

$$\overline{f}_i = \frac{\sum_{k=-int(N/2)}^{k=int(N/2)} f_{i+k}}{N} \tag{B.9}$$

where k, for even numbers, varies from minus the integer division of N by 2 to its positive counterpart. Then, if $N = 5$, $-2 \leq k \leq 2$.

B.6 The Sail Mesh

Considering that a surface has approximately a smooth distribution of points without steps (this excludes hard chinned surfaces), the filtering can be applied to second derivative distributions for any Cartesian coordinate (x, y, z). Sails, for example do not present steps and then, can be a typical case of smooth surfaces.

Because of surface smoothness, sail surface interpolation does not present high oscillations. However, local oscillations on double curvature regions may occur and mesh can be compromised if a filtering procedure is not applied.

Figure B.6 shows the second derivative distribution for coordinate y on a chordwise line ($t = constant$) from a sail model near the top region and compares this distribution with a filtered one. The filtering procedure used a central five nodes window.

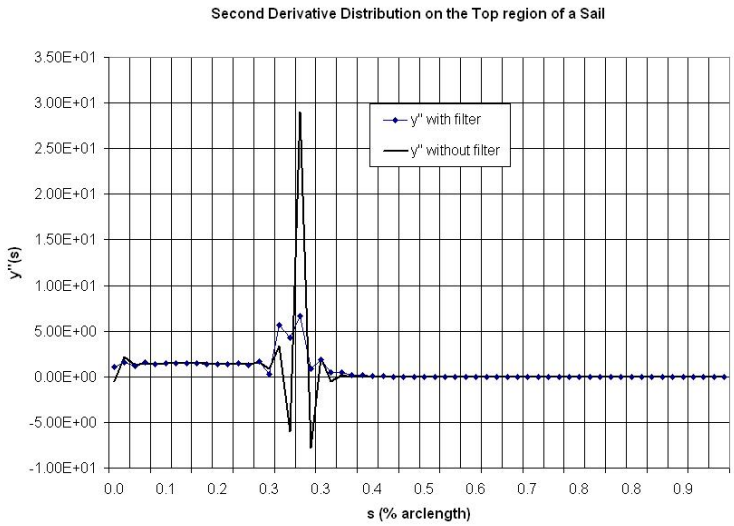

Figure B.6: Second derivative of y on the top region of a sail

The filtered second derivatives have smaller variations and oscillation is reduced, resulting in more accuracy for mesh refinement. The resulting curve could be even more smoother if more points were added to window but, for CFD modelling, the resultant mesh did not present high oscillations on such a way that it could influence flow calculation.

B.6.1 Some Mesh Examples

Figure B.7 shows a sail top region with oscillations that caused an unwanted wake positioning.

Figure B.8 shows the magnified region using the filtering procedure. By filtering, the wake follows the original membrane trailing edge angle at this region.

Figure B.9 shows the y coordinate distribution for the meshes discussed before. Differences are small but the distribution without filter presents a more pronounced

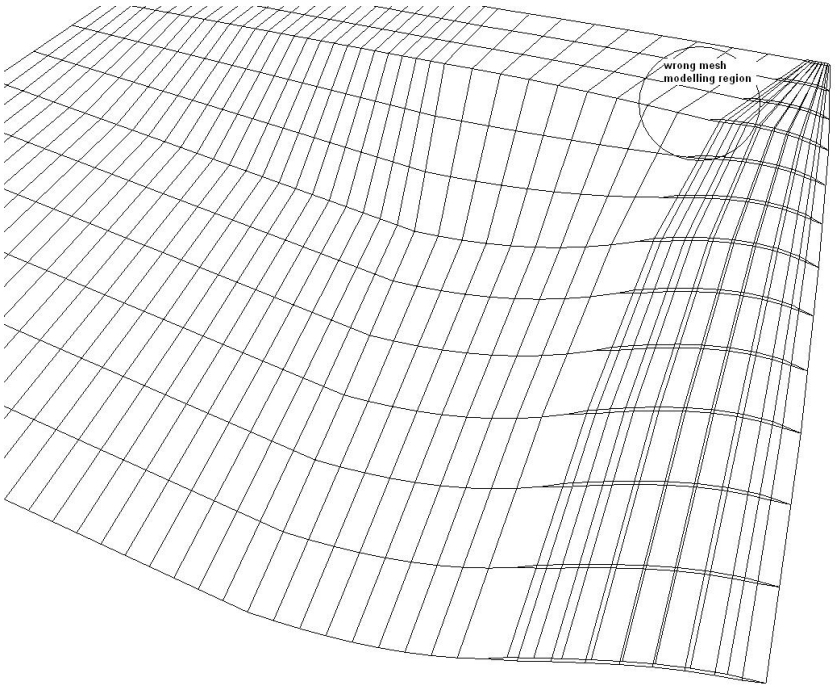

Figure B.7: A sail mesh without filtering with an unexpected wake modelling

oscillation at trailing edge region.

B.7 Sail Membrane Modeller Using Jackson Profiles

In this work, it was created a three-dimensional sail modeller that used Jackson [12] section profiles and a series of curves to model sail with twist, foot curvature, leech curvature and top curvature. The foot, leech and top curvature theories are based on quadratic and cubic polynomials where parameters to generate them are basically camber, in a percentage of chord, and its position on chord length.

For sail twist, this polynomial is rotated to a determinate angle α_{te}. This angle is a function of the differential angle to apparent wind direction, as illustrated in Figure B.10.

B.7.1 The Leech Polynomial Structure

Trailing edge polynomial structure is based on a cubic polynomial. Input parameters are length of camber position ($z_{\max}$) and camber (y_c) in relation to height of leech. Height of leech is given by the line from trailing edge of foot section to trailing edge of top section.

The boundary conditions are the y values at the beginning and end of curve and the $\partial y/\partial z = 0$ at camber $z_{\max}$ position. These boundary conditions make a 4×4 system that is solved by means of a Gauss elimination scheme.

After the curve generation, coordinates y and z at trailing edge are modified and

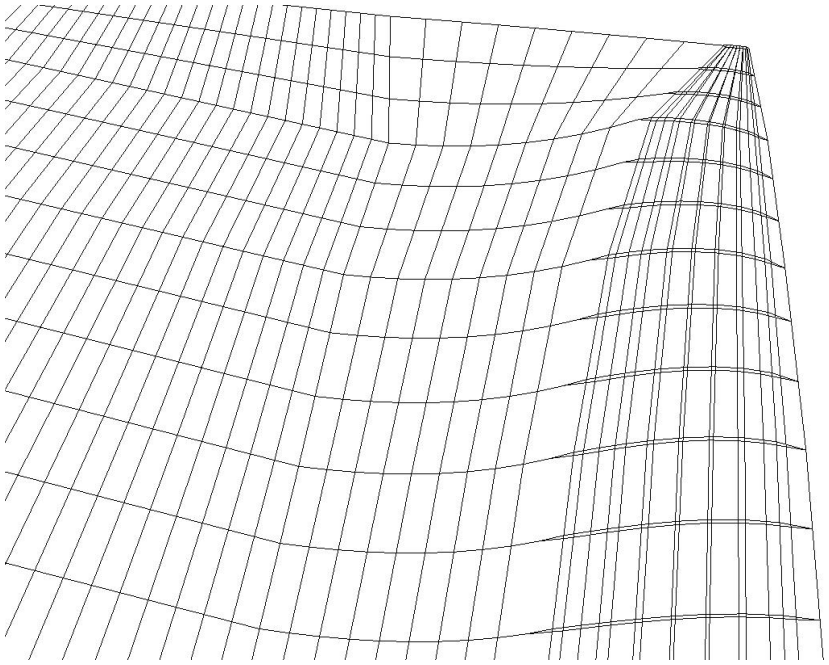

Figure B.8: Sail with its second derivatives filtered and the resulting wake positioning

sections rotated according to polynomial. When the slope given by the rotation of top section in relation to differential angle is calculated, the straight line that links trailing edge points of foot and top, represented in Figure B.10 is rotated in relation to foot trailing edge to a new position given by the rotation of top section on xy plane. Hence, leech is developed from this line and sections rotated again.

Top and foot sections are generated by quadratic polynomials that have boundary conditions on xz planes. It has an initial angle and final angle where curvature is developed.

B.7.2 Program Implementation

The modeller was created using FORTRAN 95 language and its code is described integrally in Appendix E. Sails for Chapter 7 were created using this program. Their data is given by the sets of numbers below:

```
Sail 1 data:
1.50 1.000 4.000
1.000 17 21.5
0.80 17 21.5
0.60 17 21.5
0.40 17.  21.5
0.000 0.000 0.470 0.020
-2.000 -4.000 0.000 0.000
```

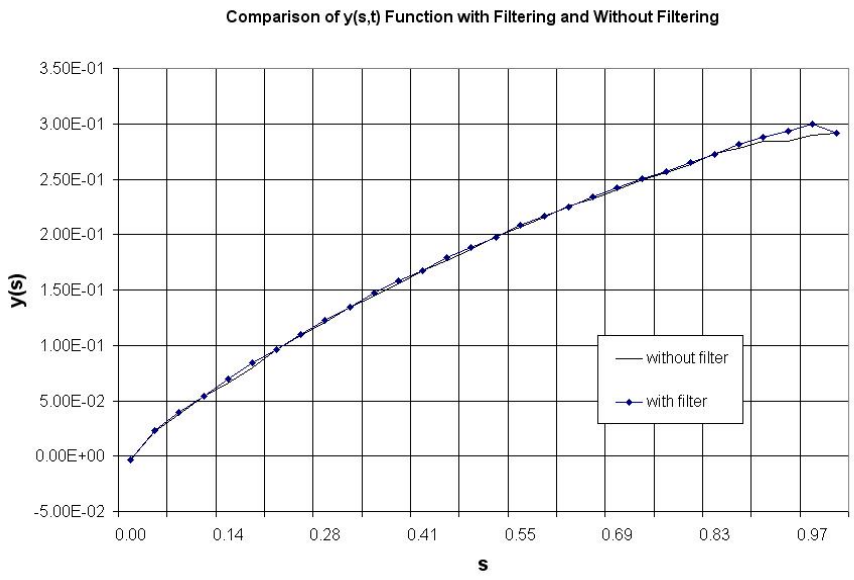

Figure B.9: Top region y coordinate distribution with and without filtering

where first line are parameters for height of mast, foot length and flow incidence (degrees). The second line until the fifth line are: scale factors and Jackson section parameters for the control sections. Sixth line is the transversal translation of foot section trailing edge, leech $z_{\max}$ and y_c. The seventh line have initial and final angles on xz for foot and top sections respectively.

For sail 2, set of sail parameters are shown as below:

```
Sail 2 data:
1.50 1.000 4.000
1.000 17    21.5
0.80 13.5    18.5
0.60 8.7    12.3
0.40 2.0    3.0
0.000 0.000 0.470 0.020
-2.000 -4.000 0.000 0.000
```

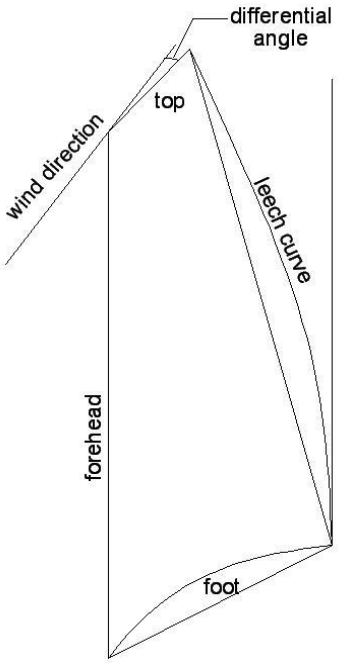

Figure B.10: Scheme of differential angle for sail geometry generation

Appendix C

Lag-Entrainment Closure Relations

Equations:

$$\frac{d\theta}{ds} + \frac{1}{u_e}\frac{du_e}{ds}\theta(H + 2 - M^2) = \frac{C_f}{2}$$

$$\frac{1}{H^*} \cdot \frac{dH^*}{ds} + \left[2H^{**} + (1 - H)\right]\frac{1}{u_e}\frac{du_e}{ds} = \frac{2C_{diss}}{H^* \cdot \theta} - \frac{C_f}{2\theta}$$

$$\frac{\delta}{C_\tau} \cdot \frac{\partial C_\tau}{\partial s} = 4.2 \cdot (C_{\tau_{eq}}^{1/2} - C_\tau^{1/2})$$

or

$$\frac{\partial \tilde{n}}{\partial s}(H_k, \theta) = \frac{\partial \tilde{n}}{\partial Re_\theta}(H_k) \cdot \frac{m(H_k) + 1}{2} \cdot \frac{\ell(H_k)}{\theta}$$

C.1 Laminar Closure

$$H_k = \frac{H - 0.290M^2}{1 + 0.113M^2}$$

For incompressible flow: $H_k = H$

$$H^* = 1.515 + 0.076 \cdot \frac{(4 - H_k)^2}{H_k}, H_k \leq 4$$

$$H^* = 1.515 + 0.040 \cdot \frac{(H_k - 4)^2}{H_k}, H_k > 4$$

$$Re_\theta \cdot \frac{C_f}{2} = -0.067 + 0.01977 \cdot \frac{(7.4 - H_k)^2}{H_k - 1}, H_k \leq 7.4$$

$$Re_\theta \cdot \frac{C_f}{2} = -0.067 + 0.022 \cdot \left(1 - \frac{1.4}{H_k - 6}\right)^2, H_k > 7.4$$

$$Re_\theta \cdot \frac{2C_{diss}}{H^*} = 0.207 + 0.00205 \cdot (4 - H_k)^{5.5}, H_k \leq 4$$

$$Re_\theta \cdot \frac{2C_{diss}}{H^*} = 0.207 + 0.003 \cdot \frac{(H_k - 4)^2}{1 + 0.02 \cdot (H_k - 4)^2}, H_k > 4$$

$$H^{**} = \left(\frac{0.064}{H_k - 0.8} + 0.251\right) \cdot M^2$$

For incompressible flow, $H^{**} = 0$

C.2 Transition Closure

$$\frac{\partial \tilde{n}}{\partial Re_\theta} = 0.01 \cdot \left\{[2.4H_k - 3.7 + 2.5\tanh(1.5H_k - 4.65)]^2 + 0.25\right\}^{\frac{1}{2}}$$

$$\ell(H_k) = \frac{6.54H_k - 14.07}{H_k^2}$$

$$m(H_k) = \left(0.058 \cdot \frac{(H_k - 4)^2}{H_k - 1} - 0.068\right) \cdot \frac{1}{\ell(H_k)}$$

C.3 Turbulent Closure

$F_c = 1$ for incompressible flow

$\mathrm{F}_c \cdot C_f = 0.3 \cdot e^{-1.33 \cdot H_k} \left[\log\left(\frac{Re_\theta}{F_c}\right)\right]^{-1.74 - 0.31H_k}$
$+ 0.00011 \left[\tanh\left(4 - \frac{H_k}{0.875}\right) - 1\right]$

$$H_k = 1.505 + \frac{4}{Re_\theta} + \left(0.165 - \frac{1.6}{Re_\theta}\right) \cdot \frac{(H_0 - H_k)^{1.6}}{H_k}, H_k \leq H_0$$

$$H_k = 1.505 + \frac{4}{Re_\theta} + (H_k - H_0)^2 \left[\frac{0.04}{H_k} + \frac{0.0071 \log(Re_\theta)}{(H_k - H_0 + 4/\log(Re_\theta))^2}\right], H_k \geq H_0$$

$$H_0 = 4, Re_\theta \leq 400$$

$$H_0 = 3 + \frac{400}{Re_\theta}, Re_\theta > 400$$

$$C_{diss} = \frac{C_f}{2} U_s + C_\tau (1 - U_s)$$

$$U_s = \frac{H^*}{2} \cdot \left(1 - \frac{4}{3} \cdot \frac{H_k - 1}{H} \right)$$

$$\delta = \theta \cdot \left(3.15 + \frac{1.72}{H_k - 1} \right) + \delta^*$$

$$C_{\tau eq} = H^* \cdot \frac{0.015}{1 - U_s} \cdot \frac{(H_k - 1)^3}{H_k^2 \cdot H}$$

Appendix D

Wilkinson's Experimental Results

Variables						Experimental Results					
test no	Re x 10^5	Ai (dgrees)	CR	diam. Ratio	mast ang	Xt/c	CPt	Xr/c	CPr	Cpre	Xsep/c
1	3.500	2.500	0.175	0.171	15.000	0.160	-1.500	0.310	-0.900	0.240	0.790
4	3.500	5.000	0.175	0.171	15.000	0.210	-1.700	0.360	-1.000	0.026	0.760
7	3.500	7.500	0.175	0.171	15.000	0.240	-1.700	0.430	-1.100	0.220	0.720
10	3.500	10.000	0.175	0.171	15.000	0.260	-1.700	0.460	-1.300	0.150	0.660
14	6.000	2.500	0.150	0.168	15.000	0.180	-1.600	0.370	-0.900	0.270	0.810
17	6.000	5.000	0.150	0.168	15.000	0.210	-1.700	0.430	-0.900	0.300	0.800
20	6.000	7.500	0.150	0.168	15.000	0.240	-1.800	0.460	-1.000	0.290	0.790
23	6.000	10.000	0.150	0.168	15.000	0.300	-1.800	0.440	-1.200	0.210	0.760
25	6.000	2.500	0.150	0.103	10.000	0.130	-1.400	0.220	-0.800	0.250	0.800
28	6.000	5.000	0.150	0.103	10.000	0.160	-1.700	0.280	-1.100	0.220	0.770
31	6.000	7.500	0.150	0.103	10.000	0.140	-1.800	0.330	-1.100	0.250	0.760
34	6.000	10.000	0.150	0.103	10.000	0.220	-1.900	0.420	-1.100	0.280	0.710
37	3.500	2.500	0.125	0.165	15.000	0.240	-1.600	0.430	-0.800	0.310	0.860
40	3.500	5.000	0.125	0.165	15.000	0.280	-1.800	0.490	-1.100	0.250	0.800
45	10.000	7.500	0.125	0.165	15.000	0.190	-1.800	0.390	-1.100	0.250	0.740
48	10.000	10.000	0.125	0.165	15.000	0.190	-1.900	0.430	-1.200	0.240	0.760
49	6.000	2.500	0.125	0.102	10.000	0.130	-1.500	0.240	-0.800	0.280	0.840
52	6.000	5.000	0.125	0.102	10.000	0.160	-1.700	0.310	-0.900	0.310	0.082
55	6.000	7.500	0.125	0.102	10.000	0.220	-1.900	0.400	-1.000	0.310	0.800
58	6.000	10.000	0.125	0.102	10.000	0.250	-1.700	0.420	-1.200	0.190	0.690
61	10.000	2.500	0.125	0.043	5.000	0.060	-1.400	0.120	-0.500	0.380	0.820
64	10.000	5.000	0.125	0.043	5.000	0.080	-1.900	0.130	-0.900	0.340	0.800
67	10.000	7.500	0.125	0.043	5.000	0.080	-2.200	0.160	-1.200	0.310	0.790
70	10.000	10.000	0.125	0.043	5.000	0.130	-2.300	0.270	-1.300	0.300	0.780
73	6.000	2.500	0.100	0.100	10.000	0.160	-1.500	0.320	-0.900	0.240	0.900
76	6.000	5.000	0.100	0.100	10.000	0.210	-1.600	0.400	-0.900	0.270	0.820
79	6.000	7.500	0.100	0.100	10.000	0.300	-1.500	0.540	-0.900	0.240	0.760
82	6.000	10.000	0.100	0.100	10.000	0.340	-1.400	0.460	-1.200	0.080	0.760
85	6.000	2.500	0.100	0.042	5.000	0.080	-1.600	0.230	-0.700	0.350	0.920
88	10.000	5.000	0.100	0.042	5.000	0.100	-2.000	0.190	-1.000	0.330	0.910
91	10.000	7.500	0.100	0.042	5.000	0.140	-2.100	0.280	-1.200	0.290	0.840
94	10.000	10.000	0.100	0.042	5.000	0.200	-1.800	0.410	-1.100	0.250	0.720
97	10.000	2.500	0.075	0.041	5.000	0.080	-1.600	0.160	-0.800	0.310	0.920
100	10.000	5.000	0.075	0.041	5.000	0.110	-1.900	0.260	-1.000	0.310	0.900
103	10.000	7.500	0.075	0.041	5.000	0.220	-1.700	0.430	-1.000	0.260	0.790
106	10.000	10.000	0.075	0.041	5.000	0.280	-1.500	0.430	-1.100	0.160	0.720

Figure D.1: Results for the body upper part for a sail/mast configuration using NACA a=0.8 mean camber line attached to a circular mast.

Appendix E

FORTRAN 95 Codes